UNIVERSITY OF BIRMINGHAM

Experimental and Numerical Studies of Fuel Spray

By

Daliang Jing

A thesis submitted to

The University of Birmingham

for the degree of

DOCTOR OF PHILOSOPHY

The University of Birmingham

School of Mechanical Engineering

March 2015

ABSTRACT

In modern Internal Combustion (IC) engines, the fuel spray atomization process is known to play a key role in affecting mixture formation, combustion efficiency and soot emissions. Therefore, a thorough understanding of the fuel spray characteristics and atomization process is of great importance. In this study, the fuel spray of modern Gasoline Direct Injection (GDI) engines and diesel engines has been experimentally and numerically studied. At the same time, optimized physical-numerical spray breakup models for the spray simulation have been developed and validated.

In the gasoline spray study, the effects of injection pressure, injection duration and different injector nozzle machining methods on the spray characteristics of the GDI engine have been experimentally studied by using optical approaches such as high-speed photography and a Phase Doppler Particle Analyzer (PDPA) system. The results show that higher injection pressure can increase the penetration length and enhance the atomization process due to its higher injection velocity, stronger turbulence and cavitation phenomenon and greater aerodynamic force. In addition, the laser drilled injector nozzle can also promote the spray atomization performance due to its sharp inlet edge and fine inner surface produced by the laser machining technology. The enhanced turbulence induced by the nozzle's sharp inlet edge plays an important role in accelerating the spray breakup and atomization processes.

In terms of the spray study of the diesel engine, the effects of injection pressure, ambient pressure and different fuels including gasoline, diesel, and their blends – dieseline, on the spray characteristics, have been experimentally investigated. It is shown that for all the test fuels, higher injection pressure and higher ambient pressure will enhance the spray atomization

process due to significant cavitation phenomenon, stronger turbulence effects and greater aerodynamic force. Compared to pure diesel, the recently developed dieseline fuel shows many advantages in terms of enhancing the spray atomization process. Better atomization performances can be achieved by increasing the proportion of gasoline in the dieseline fuel; due to its stronger cavitation phenomenon, higher volatility, lower surface tension and lower viscosity.

According to the different spray characteristics and breakup regimes induced by injector parameters, injection pressures and ambient conditions between the GDI and diesel engines, two different spray breakup models for the gasoline and diesel spray simulations have been respectively proposed in the numerical studies. The breakup model for the gasoline spray simulation is improved by considering the turbulence-induced breakup mechanism in the study. While for the diesel spray simulation, the breakup model is enhanced by accounting for the cavitation phenomenon as well as the turbulence effect into the modelling. Both of the models are implemented in the Computational Fluid Dynamics (CFD) code and validated with the high-speed imaging and PDPA experiments. The simulation results of the proposed models are in good agreement with the experiment data and show significant improvements compared to the results of the current existing spray atomization models.

ACKNOWLEDGEMENTS

First and foremost, I would like to express my sincere gratitude to my supervisor, **Professor Hongming Xu**, for his careful supervision, valuable suggestions and constant encouragement throughout my PhD study. At the same time, I would also like to thank my associate supervisor, Professor Miroslaw Lech Wyszynski, who gave me helpful suggestions.

I am also grateful to **Professor Shijin Shuai**, **Professor Zhi Wang**, Professor Jianxin Wang, Professor Xin He, Senior Engineer Jianhua Xiao, Dr. Xiao Ma and Dr. Zhelin Dong from Tsinghua University for their continual guidance and support in the CFD work during my two years' study at Tsinghua University.

I acknowledge the support of **Jaguar Land Rover (JLR)**, Shell and Advantage West Midlands; without their equipment and financial support, I could not have finished my PhD study. Special thanks go to Dr. Cao Li and Dr. Paul Dunkley from JLR who gave me instructive advice and useful suggestions on my research work.

I am also grateful to all of my colleagues at the **Future Power Systems** group for their support and companionship. In particular, many thanks go to Dr. Yanfei Li and Dr. Xiao Ma, for their guidance during the first year of my PhD study; and to Dr. Fan Zhang, Changzhao Jiang, Powen-Tu and Haichun Ding for their great help in the experiments.

Finally, I would like to extend my gratitude to my beloved **parents and family** who have been assisting, supporting and caring for me all of my life.

I would like to dedicate this thesis to my parents, teachers and friends for their great support through all these years.

CONTENTS

LIST OF ABBREVIATIONS

AC	Alternating Current
ALE	Arbitrary Lagrangian Eulerian
AMD	Average Mean Diameter
ASOI	After the Start of Injection
CDM	Continuous Droplet Model
CEI	Computational Engineering International
CFD	Computational Fluid Dynamics
CO	Carbon Monoxide
CO_2	Carbon Dioxide
CVV	Constant Volume Vessel
DDM	Discrete Droplet Model
DI	Direct Injection
DISI	Direct Injection Spark Ignition
DNS	Direct Numerical Simulation
EACT	Enhanced-Kelvin-Helmholtz-Aerodynamics-Cavitation-Turbulence
ECU	Electronic Control Unit
EIA	Energy Information Administration
EN590	European standard diesel
ERC	Engine Research Centre
EU	European Union
FEM	Finite Element Model

G0	Pure diesel
G100	Pure gasoline
G20	20% gasoline blended dieseline
G50	50% gasoline blended dieseline
G70	70% gasoline blended dieseline
GDI	Gasoline Direct Injection
HC	Unburned Hydrocarbon
IC	Internal Combustion
ICE	Internal Combustion Engine
IMEP	Indicated Mean Effective Pressure
ISFC	Indicated Specific Fuel Consumption
JLR	Jaguar Land Rover
KH-ACT	Kelvin-Helmholtz-Aerodynamics-Cavitation-Turbulence
KHRT	Kelvin-Helmholtz & Rayleigh-Taylor
LDV	Laser Doppler Velocimetry
LIF	Laser-induced Fluorescence
MD	Mean Diameter
NI	National Instruments
NO_x	Nitrogen Oxides
PDA	Phase Doppler Anemometry
PDF	Probability Distribution Function
PDPA	Phase Doppler Particle Analyzer
PIV	Particle Imaging Velocimetry
PM	Particle Matters
PPCI	Partially Premixed Compression Ignition

RT	Rayleigh-Taylor
SI	Spark Ignition
SMD	Sauter Mean Diameter
TAB	Taylor Analogy Breakup
TL-KHRT	Turbulence-Ligament- Kelvin-Helmholtz & Rayleigh-Taylor
ULG95	The 95 octane gasoline
US	United States of America

LIST OF SYMBOLS

a	The droplet acceleration
A_p	Surface area
B_0	Size constant in KH model
B_1	Time constant in KH model
C_0	Size constant in RT model
C_1	Time constant in RT model
Ca	The area contraction coefficient
C_{cri}	The transition switch parameter in EACT model
C_d	The discharge coefficient
$C_{T,CAV}$	Model constant in EACT model
C_u	Turbulence model constant
C_V	The orifice velocity contraction coefficient
D	The nozzle diameter
D_{32}	Sauter Mean Diameter (SMD)
D_i	The droplet size of parcel *i*
D_l	The ligament diameter
d_p	Droplet size
d_s	Surface diameter
d_v	Volume diameter
f_s	The source term due to collision, coalescence, breakup etc
F^s	The rate of momentum gain per unit volume due to the spray

$\hat{g}$	The specific body force vector
I	The specific internal energy (exclusive of chemical energy)
$\hat{J}$	The heat flux vector including turbulent heat conduction and
$K(t)$	The turbulent kinetic energy
K_0	The initial turbulent kinetic energy
K_c	A constant taking into account losses in the contraction corner
k_l	Size constant in TL-KHRT model
K_s	A constant for average turbulent energy dissipation
k_t	The breakup time constant in TL-KHRT model
k_{TL}	Model constant in TL-KHRT model
K_{tw}	Model constant of the turbulence-induced breakup
L	The nozzle length
L_{bu}	The primary breakup length
L_{CAV}	The cavitation-induced breakup length scale
L_{KH}	The aerodynamics breakup length scale
L_t	Turbulence length scale
L_t^0	The initial turbulence length scale
L_{TL}	The characteristic breakup length scale in TL-KHRT model
L_{tw}	The characteristic length scale of turbulence-induced breakup
L_w	Wavelength of surface perturbations
m_s	Parameter in relation to gas density
N_i	The droplet number in parcel *i*
n_s	Parameter in relation to pressure difference
Oh	Ohnesorge number

p	The fluid pressure
P_a	Back pressure
P_{inj}	Injection pressure
p_v	Fuel vapour pressure
Q^c	The source terms due to chemical heat release
Q^s	The source terms due to spray interaction
r	Parent drop radius
R_{CAV}	The effective radius of an equivalent bubble from the nozzle
r_{KH}	Child droplet size in KHRT model
s	The area contraction ratio of the nozzle hole
S_1	Spray penetration length for stage 1
S_2	Spray penetration length for stage 2
t	Time
t_b	The time before breakup
T_p	Droplet temperature
u	The injection velocity
U	The initial liquid velocity at the nozzle exit
$\hat{u}$	Fluid velocity vector
u_{pi}	Droplet velocity
u_r	The droplet relative velocity
V_p	Volume of the particle
We_g	Gas Weber number
We_l	The ligament Weber number
x_i	Droplet position

Δf	The frequency of the intensity signal
Δs	The distance between the fringe
Δt	The flash pulse width
∇	The vector operator

Greek Symbols

μ_l	The dynamic viscosity of the liquid
ε	The dissipation rate of turbulent kinetic energy
v_0'	The average cross stream velocity fluctuation at jet exit
α_s	Parameter in relation to nozzle diameter
β_s	Parameter in relation to time
$\varepsilon(t)$	The turbulent dissipation rate
ε_0	The initial turbulent dissipation rate
θ	Spray dispersion angle
κ	Turbulent kinetic energy
ρ	The total mass density
ρ_a	Ambient gas density
ρ_l	Fuel/Liquid density
ρ_m	The mass density of species *m*
ρ_m^c	Source terms due to chemical reaction
ρ_m^s	Source terms due to spray evaporation
σ	Surface tension
τ_{CAV}	The cavitation-induced breakup time scale
τ_{KH}	The aerodynamics breakup time scale

τ_t	Turbulence time scale
τ_t^0	The initial turbulence time scale
τ_{TL}	The characteristic breakup time scale in TL-KHRT model
τ_{tw}	The characteristic time scale of turbulence-induced breakup
τ_w	Wave growth time

Subscripts and Superscripts

a	Stands for ambient
b	Stands for breakup
c	Stands for chemical reaction
CAV	Stands for Cavitation
d	Stands for discharge
g	Stands for gas phase
inj	Stands for injection
KH	Stands for Kelvin-Helmholtz
l	Stands for liquid phase
p	Stands for parcel
s	Stands for spray
T	Stands for Turbulence
TL	Stands for Turbulence-Ligament
tw	Stands for turbulence wave
^{V}	Stands for volume

LIST OF FIGURES

LIST OF TABLES

LIST OF PUBLICATIONS

Jing, D., Xu, H., Shuai, S., Wang, Z. et al., "A Turbulence and Cavitation-induced Breakup Model for Fuel Spray Modeling," SAE Technical Paper 2014-01-2737, 2014, doi: 10.4271/2014-01-2737.

Jing, D., Xu, H. et al., "Development of a Turbulence-induced Breakup Model for Diesel Spray Simulation." Proceedings of the 17th of Liquid Atomization & Spray Systems - Asia (ILASS-Asia 2014). 2014.

Jing, D., Shuai, S., Wang, Z., Xu, H. et al., "Development of a Turbulence-induced Breakup Model for Gasoline Spray Simulation," SAE Technical Paper 2015-01-0939, 2015, doi: 10.4271/ 2015-01-0939.

Jing, D., Xu, H. et al., "Numerical Modeling of Diesel Spray using TL-KHRT Breakup Model," Ready for Submission.

Jing, D. & Zhang, F., Xu, H., Li, Y., Shuai, S., "Experimental Investigation into the Macroscopic and Microscopic Spray Characteristics of Dieseline," Ready for Submission.

CHAPTER 1
INTRODUCTION

1.1 Background

Internal Combustion (IC) Engines, as the greatest invention of the 19th century, are the most popular thermal engines and widely used in industry, agriculture etcetera since the 1860s [1, 2]. Precisely because of its excellent performance, the IC engine has always been in a leading position in the field of power production and plays an important role in the rapid developments of the world economy, state-building, and people's livelihood [3]. With the increasing demand for energy conservation and environmental protection, further improvements in fuel efficiency and emission reduction in internal combustion engines are urgently required; due to the limited energy reserves, the rising price of crude oil and climate change [4]. Although the electric vehicle exhibits a promising future in recent years due to its environmentally friendly features [5, 6], some inevitable issues such as the high costs, the limited battery range, and the lagging behind of charging technology have greatly hindered its further development[7]. Thus it is predictable that the IC engine will still be the most used power engine in the 21st century.

1.1.1 Energy Demand and Emission Regulations

Energy Demand

With rapid economic development and continuous growth of the population, the increasing demand for energy and the problem of environmental pollution are becoming more and more

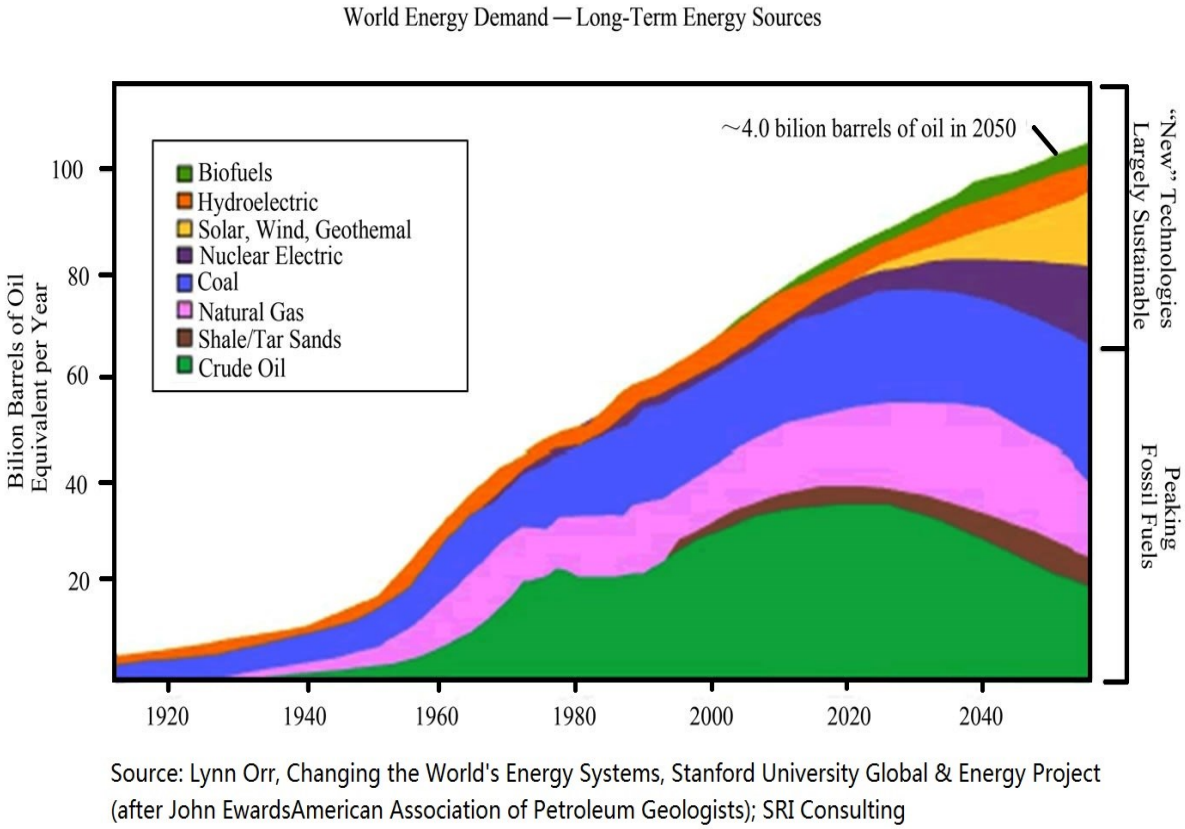

Figure 1-1 World energy demand forecast – long-term energy sources [8]

serious. It is reported by the Energy Information Administration (EIA) in its International Energy Outlook that world energy consumption will rise 56 percent in the next three decades, driven by growth in the developing world [9, 10]. Figure 1-1 illustrates the historical and the forecasted demand for energy of the world [8]. It is shown that the fossil fuels including crude oil, natural gas, and coal will still be the energy source and increase considerably before 2040. After 2040, the renewable sources such as biofuels, hydroelectricity, solar and wind power and geothermal energy will be expected to fulfil the further increasing demand. However, the roles of the fossil fuels are still irreplaceable in the foreseeable future; especially for crude oil, which is the so-called 'blood' of the industry and will still be an indispensable energy source.

From the view of the share of energy consumption by various sectors, the transportation sector consumes a big part of the total energy continuously [11]. Figure 1-2 shows the most recently published report by the EIA in terms of global primary energy consumption by source and sector [12]. It can be seen that 28% of the primary energy is consumed by transportation, which is just second to the percentage (39%) that is consumed by electric power. Furthermore, the transportation sector consumes 71% of the liquid fuel, which has no competition from any other sector. It can be expected that vehicles will still be the main consumer in the foreseeable future; thus, further improvement of fuel efficiency of vehicles is of great importance in slowing down the increasing speed of the energy demand.

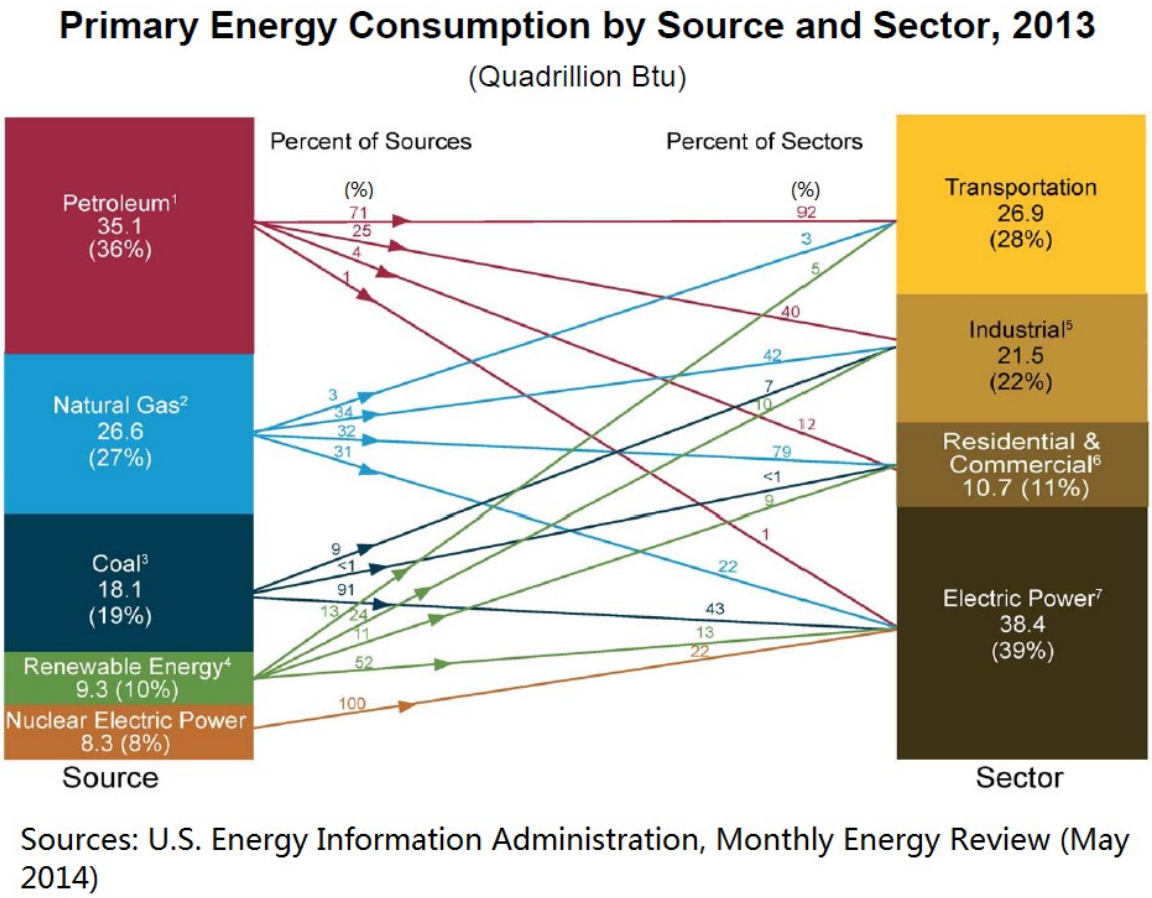

Figure 1-2 Primary energy consumption by source and sector [12]

Emission Regulations

Apart from the increasing energy demand by vehicles, the emissions are another important aspect which has attracted much attention in recent years. As one of the main air pollution sources in cities, the IC engine is facing more and more stringent emission regulations all over the world. The main harmful exhaust emissions such as carbon monoxide (CO), unburned hydrocarbon (HC), nitrogen oxides (NO_x), and soot/ particle matters (PM) have a strong pungent smell and will seriously poison and pollute the air in cities [13]. Figure 1-3 shows an image of the air pollution in Beijing. At the same time, large amounts of carbon dioxide (CO_2) exhausted by IC engines will lead to the greenhouse effect and then result in climate change and global warming [14].

Figure 1-3 An image of the air pollution in Beijing [15]

Many countries have made stringent vehicle emission regulations to limit the exhaust emissions of vehicles. The first emission regulation 'Euro 1' was released by the Europe Union (EU) in 1992. During the past 20 years, the EU emission regulations have been updated several times and have become more and more stringent. The detailed EU emission regulations for passenger cars from the 'Euro 1' stage to the 'Euro 6' stage are listed in Table 1-1. It can be seen that from the year 1992 to 2005, the CO emissions for diesel engines and gasoline engines were forced to be reduced by 82% and 63%, respectively. From the year 2000 to 2014, the HC emissions for gasoline engines have been reduced by 50%; the NO_x emissions for diesel

Table 1-1 European emission regulations for passenger cars [16]

European emission standards for passenger cars (Category M*), g/km								
Tier	Date	CO	THC	NMHC	NOx	HC+NOx	PM	P [#/km]
Diesel								
Euro 1†	1992.07	2.72 (3.16)	-	-	-	0.97 (1.13)	0.14 (0.18)	-
Euro 2	1996.01	1.0	-	-	-	0.7	0.08	-
Euro 3	2000.01	0.64	-	-	0.50	0.56	0.05	-
Euro 4	2005.01	0.50	-	-	0.25	0.30	0.025	-
Euro 5a	2009.09	0.50	-	-	0.180	0.230	0.005	-
Euro 5b	2011.09	0.50	-	-	0.180	0.230	0.005	6×10^{11}
Euro 6	2014.09	0.50	-	-	0.080	0.170	0.005	6×10^{11}
Petrol (Gasoline)								
Euro 1†	1992.07	2.72 (3.16)	-	-	-	0.97 (1.13)	-	-
Euro 2	1996.01	2.2	-	-	-	0.5	-	-
Euro 3	2000.01	2.3	0.20	-	0.15	-	-	-
Euro 4	2005.01	1.0	0.10	-	0.08	-	-	-
Euro 5	2009.09	1.0	0.10	0.068	0.060	-	0.005**	-
Euro 6	2014.09	1.0	0.10	0.068	0.060	-	0.005**	6×10^{11}***

* Before Euro 5, passenger vehicles > 2500 kg were type approved as light commercial vehicles N_1-I
** Applies only to vehicles with direct injection engines
*** 6×10^{12}/km within first three years from Euro 6 effective dates
† Values in brackets are conformity of production (COP) limits

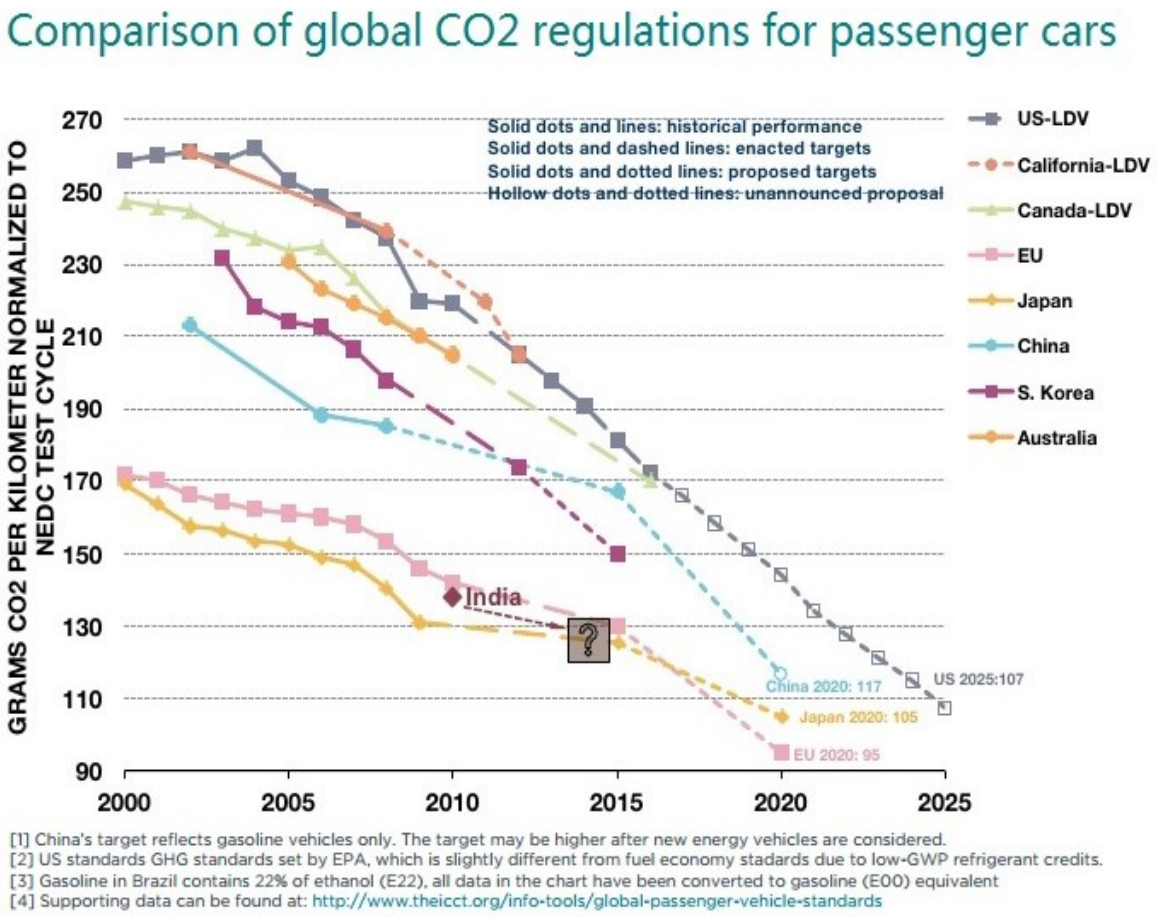

Figure 1-4 Global CO_2 emission regulations for passenger cars [17]

engines and gasoline engines have been reduced by 84% and 60%, respectively; the PM emissions for diesel engines have been reduced by 96%. Similar emission regulations also have been made in China, the United States (US), India etc. In terms of the CO_2 emission legislations, different regulations have been made for the near future. Figure 1-4 illustrates the CO_2 emission regulations for passenger cars in several countries. It is shown that, compared to CO_2 emissions from the year 2000, the US and the EU will reduce them by over 58% and 44%, respectively, by the year 2025. China and India will also make their efforts in decreasing the CO_2 emissions and a 50% reduction will be expected in China.

Obviously, both the energy demand and the emission regulations are the main factors in promoting further improvements in fuel efficiency and a further reduction of the exhaust emissions of the IC engine.

1.1.2 Direct Injection Engines

The design and optimization of the IC engine will greatly rely on the fuel injection system since an advanced fuel injection system can greatly improve the fuel efficiency and combustion quality of vehicles and help to meet the demand for energy saving and the stringent emission regulations [2, 4]. Therefore the optimization of fuel injection technology has attracted more and more attention in recent years. Direct injection technology, which delivers the fuel into the cylinder chamber directly, is proved to be the most effective means in improving fuel efficiency and reducing the emissions for both compression ignition (CI) engines and modern direct injection spark ignition (DISI) engines [4]. Figure 1-5 shows a schematic of the DISI engine cylinder [18].

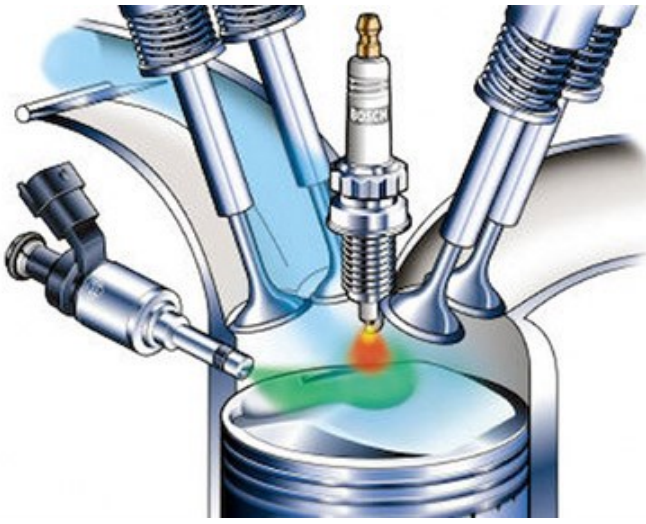

Figure 1-5 Schematic of an DISI engine cylinder [18]

There are several advantages of direct injection technology, especially for the modern DISI engines [19-22]:

- Improving the fuel efficiency: one of the most important objectives during the development of the modern IC engine is to decrease the fuel consumption to meet the requirement of energy saving. Direct injection technology can greatly improve the efficiency of the fuel-air mixing and enhance the atomization quality; and in turn it improves the fuel efficiency.
- Improving the accuracy of the fuel injection: a main feature of the direct injection system is the accurate injection control by the Electronic Control Unit (ECU). It can adjust the injection timing, injection duration and the injection pressure according to the working conditions of the engine; thus it can optimize the accuracy of the fuel injection for different conditions.
- Enhancing engine power: the better air-fuel mixing performance of direct injection technology will lead to a more complete combustion of the fuel; thus it results in a higher efficiency of the power conversion of the fuel, which will directly enhance the power output of the engine.
- Reducing the exhaust emissions: again, the better fuel-air mixing of direct injection technology will result in a more complete combustion of the fuel, so that the CO and HC emissions can be significantly reduced.

However, some problems and drawbacks of the direct injection engine such as the PM emissions at medium or low load, NO_x emissions due to the higher compression ratio and higher heat release rate and other emissions during the cold-start still exist and need further studies [19, 20].

1.1.3 Fuel Spray

The fuel spray atomization process is known to play a key role in affecting mixture formation, combustion efficiency, power output, fuel economy and exhausted emissions in direct injection engines [21]. The spray process is an extremely complicated physical course consisting of fuel spray atomization, droplet breakup, evaporation, collision, coalescence and energy exchange processes. Among them, spray atomization and droplet breakup are the most important physical processes which have attracted a lot of attention in the area of engine research [22]. Figure 1-6 illustrates some images of diesel and gasoline direct injection sprays.

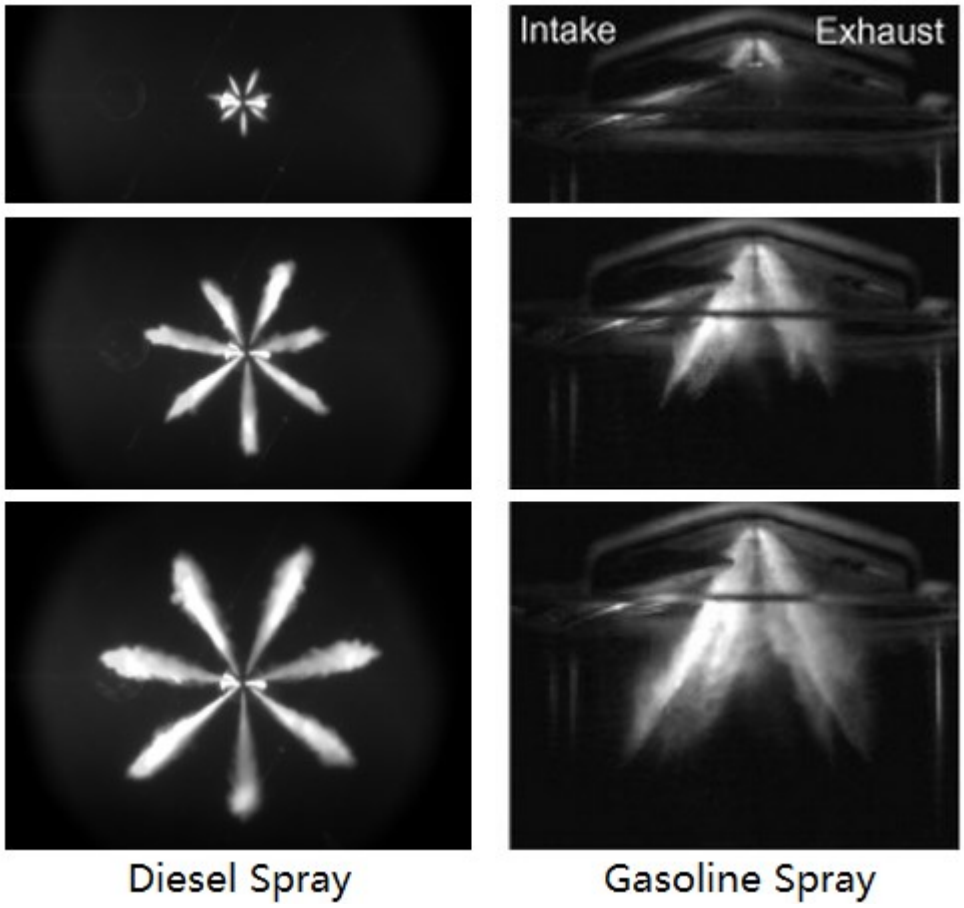

Figure 1-6 Examples of direct injection spray images

The fuel pressured by the fuel supply system and ejected from the injector nozzle will experience primary atomization and secondary breakup processes. The primary atomization process will disintegrate the continuous fuel liquid into numerous droplets with various diameters and velocities. The secondary breakup process will further reduce the droplet size and produce a great number of smaller droplets. In this way, the fuel can be mixed with the air inside the cylinder directly. A better atomization of the fuel spray will increase the fuel-air contact area and then enhance the mixture formation of the engine, which in turn increases the fuel efficiency and reduces the fuel consumption. Furthermore, better atomization quality will result in smaller droplet size, which can effectively reduce soot, as well as other emissions [23].

Thus, a detailed study of the fuel atomization process is of great importance for optimizing the performance of the IC engine. The methodology of combining the experimental investigation and the numerical study can help to achieve a better understanding of the fuel spray, not only in theory, but also in a practical approach.

1.2 Research Objectives

This study aims to achieve a detailed understanding of fuel spray characteristics by using experimental investigation and numerical simulation approaches. The spray characteristics of both the Gasoline Direct Injection (GDI) engine and the diesel engine will be studied; at the same time, optimized physical-numerical spray models for the gasoline and diesel spray simulations will be developed and validated. The main objectives of this study can be described as follows:

- To experimentally study the fuel spray characteristics of the GDI engine and investigate the influence of injection parameters; such as the injection pressure, injection duration and different injector machining methods on the spray characteristics, by using optical approaches including high-speed imaging and PDPA technology.
- To experimentally study the spray characteristics of the diesel engine and compare the differences between the spray characteristics of gasoline, diesel and their blends – dieseline fuel, under various injection and ambient conditions; and then figure out the effects of all the factors on the spray characteristics.
- To numerically study the fuel spray of the GDI engine using CFD modeling technology and deeply analyze the different breakup mechanisms induced by the various injection parameters; and then propose and validate an optimized spray atomization model based on the analysis.
- To numerically study the fuel spray of the diesel engine and improve the current existing spray atomization models by considering the effects of the cavitation phenomenon and turbulence on the spray breakup process; and then validate the proposed model by using the experiment data.

1.3 Thesis Outline

This thesis comprises eight chapters, which are described as follows:

Chapter 1 gives a brief introduction of this study, including the background, the research objectives and the outline of the thesis.

Chapter 2 reviews the fundamentals of fuel spray, including spray characteristics, breakup regimes, spray CFD modelling approaches and spray breakup sub-models used in the spray simulation.

Chapter 3 introduces the research methodologies employed in the fuel spray study, including the experimental and the numerical approaches used in this study. Experimental setups, such as the fuel injection system, the constant volume vessel, the image acquisition system, the Phase Doppler Particle Analyzer (PDPA) system and numerical software, including the calculation code and post-processing program, are introduced in detail.

Chapter 4 studies the spray characteristics of the GDI engine. The effects of injection pressure, injection duration and different injector nozzle machining methods on the spray characteristics have been investigated. It is shown that higher injection pressure can increase the penetration length and enhance the atomization process; due to its higher injection velocity, stronger turbulence and cavitation phenomenon and greater aerodynamic force. The laser drilling nozzle machining method can be an effective means to enhance the spray atomization performance; since this machining technology can provide a sharper inlet edge and finer inner surface to the injector nozzle.

Chapter 5 investigates the spray characteristics of a diesel engine. The effects of the injection parameters such as injection pressure, ambient pressure, different fuels including gasoline, diesel and their blends - dieseline and the gasoline/diesel blending ratio on the spray characteristics have been experimentally investigated. The results show that higher injection pressure and higher ambient pressure will enhance the spray atomization process due to their significant cavitation phenomenon, stronger turbulence effects and greater aerodynamic force.

Compared to pure diesel, the recently developed dieseline fuel shows many advantages in terms of affecting the spray atomization process due to its physical properties; such as stronger cavitation phenomenon, higher volatility, lower surface tension and lower viscosity.

Chapter 6 considers the numerical modelling of gasoline spray. An improved hybrid spray breakup model, named the 'Turbulence-Ligament-KH-RT' (TL-KHRT) model, is developed by considering the turbulence effect and the ligament evolution in the fluid. The improved model is validated with high-speed imaging and PDPA experiments and the simulation result shows a better agreement with the experiment data.

Chapter 7 focuses on the numerical simulation of diesel spray. An enhanced Aerodynamic-Cavitation-Turbulence induced primary breakup model is developed in this study. The improved model is validated with the experiment data of the full-cone diesel spray in a constant volume vessel under non-evaporating and various injection conditions. Simulation results of the improved model exhibit a better agreement with respect to spray penetration, droplet average mean diameter, droplet velocity under all the test conditions and show significant improvements for fuel spray modelling.

Chapter 8 summarizes the studies and gives some recommendations for future work.

CHAPTER 2
LITERATURE REVIEW

This chapter reviews the fundamentals of fuel spray; including spray characteristics, breakup regimes, spray CFD modelling approaches and spray breakup sub-models. The macroscopic characteristics such as spray structure, tip penetration, spray angle and the microscopic characteristics including droplet size and droplet velocity are introduced at first. Then the breakup regimes and their influence factors are analyzed. Finally, the CFD modelling technologies and relevant physical-numerical models are presented.

2.1 Fuel Spray Characteristics

When the liquid fuel is injected into the chamber, a multi-component flow a containing liquid core, liquid droplets, fuel vapour, and air will be formed; this is the so-called spray field. In modern Direct Injection (DI) engines, a multi-hole injector is the most commonly used injector and it provides a desirable atomization performance in the mixture formation process. A widely used means to study the fuel spray characteristics is to focus on one jet of the multi-hole spray or the single hole spray [23].

2.1.1 Spray Structure

In the past, it was supposed that the atomization process would be completed and numerous droplets would be formed once the liquid fuel left the nozzle. However, with the rapid development of optical diagnostic technology, lots of experimental observations indicate that

the atomization process will last for a certain distance and a liquid core exists near the injector nozzle, which is the so-called intact liquid core. For the convenience of study, the spray can be divided into several zones. According to the coupling conditions of the gas phase and liquid phase, Bracco and O'Rourke [24] classify the spray field into four zones by the distance from the nozzle: the churning zone, dense zone, dilute zone and very thin zone. Figure 2-1 [25] shows the schematic of a typical full-cone spray.

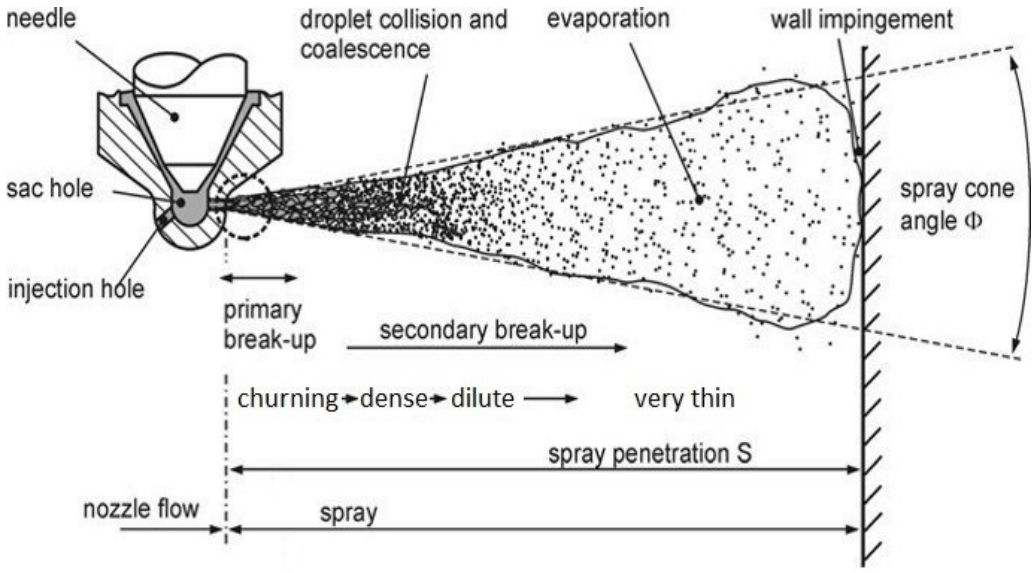

Figure 2-1 Schematic of full-cone spray structure [25]

Liquid Core

A large number of experiments show that the atomization process is incomplete and a liquid core does exist near the nozzle exit. The distance of this intact liquid core is proportional to the nozzle hole diameter. The flow characteristic of this region is similar to the single phase jet flow and can be seen as a continuous phase [26].

Churning Zone

This zone refers to the spray region very close to/around the liquid core, where the continuous liquid starts to breakup into dense droplets or ligaments. However, due to the volume fraction of the liquid phase being equivalent to or even higher than the gas phase, the fuel in this zone is not in the form of discrete droplets. The churning flow is the product of the first step of atomization and it is also the intermediate status between the liquid core and the droplets. The studies of the churning flow are of great importance in revealing the primary breakup mechanisms of the spray.

Dense Zone

The volume fraction of the liquid phase in this zone is still high but relatively lower than the churning flow. The liquid phase is in the form of discrete droplets which disperse in the continuous gas phase. The aerodynamic force induced by the high relative velocity between the droplet and its surrounding air will act on the droplet surface and lead to further breakup, which is known as the secondary breakup. The interaction between droplets cannot be ignored since the space between them is small. Collisions of droplets can lead to droplet deformation, coalescence and breakup; this then can affect the droplet size distribution. O'Rourke [27] carried out a detailed numerical study of the dense spray zone by employing a statistical method which considered collision dynamics, collision probability, collision efficiency etc. A transition function was used to determine the result of coalescence or breakup. On the other hand, the droplet can also affect the dynamic properties of its surrounding air and the air motion will disturb other droplets at the same time; therefore this zone is quite complex and difficult to measure and model.

Dilute Zone

In this zone, the liquid volume fraction is smaller than that of the dense zone. The space between droplets is much bigger than the droplet size, so the interaction between droplets can be ignored. However, the indirect influence of 'droplet-air-droplet' always exists, which means the droplet-induced aerodynamic force will still affect other droplets.

Very Thin Zone

This is the outermost part of the spray field. The liquid volume fraction in this zone is rather low since most of the small droplets have been evaporated during the transportation and the minority of the remaining droplets is distributed in a relatively wide space. The interaction between droplets such as deformation, breakup, collision, coalescence and oscillation becomes weak and can be neglected. The velocity of these droplets is quite low and the transportation is dominated by the turbulent diffusion.

2.1.2 Spray Penetration and Spray Cone Angle

Spray penetration and cone angle are the macroscopic characteristics which have been investigated by many studies over the years. Spray penetration [28] is defined as the distance between the leading edge of the spray and the nozzle exit; while the cone angle [29, 30] is always defined as the angle between the two tangent lines of the side edge of the spray, as is shown in Figure 2-1 in the previous section.

Many empirical equations have been developed in terms of the study of spray penetration [28-31]. Hiroyasu and Arai [28] experimentally studied the temporal evolution of the tip penetration and they found that the spray can be divided into two stages. At the first stage, the penetration length S is proportional to time t and it won't be affected by the ambient density ρ_a. However, the second stage shows a different situation in which the penetration length S is proportional to the square root of time t. By considering the liquid surface properties such as wave fluctuation and breakup; and ambient gas dynamics such as the relative velocity, ambient pressure and density, a more accurate empirical equation can be found; the expression is as below [28]:

$$t_b = \frac{28.65\rho_l D}{(\rho_a(P_{inj} - P_a))^{0.5}} \tag{2-1}$$

$$S_1 = 0.39\left(\frac{2(P_{inj} - P_a)}{\rho_l}\right)^{0.5} t \qquad (0 < t < t_b) \tag{2-2}$$

$$S_2 = 2.95\left(\frac{P_{inj} - P_a}{\rho_a}\right)^{0.25} (Dt)^{0.5} \qquad (t \geq t_b) \tag{2-3}$$

where S_1 and S_2 are spray penetration length for stage 1 and stage 2, respectively; t is the time after the start of injection (ASOI); t_b is the time before breakup; P_{inj} is the injection pressure; P_a is back pressure; ρ_l is fuel density; ρ_a is ambient gas density; and D is the nozzle diameter.

Siebers and Naber [31] investigated the effects of gas density and vaporization on the penetration and dispersion of diesel spray using the Mie-scattering technique over a range of injection conditions. They found that the penetration length decreases with the increase of

ambient pressure or density. The correlations for the tip penetration length are expressed as follows [31]:

$$S_1 = C_v \left(\frac{2(P_{inj} - P_a)}{\rho_l} \right)^{0.5} t \qquad (0 < t < t_b) \tag{2-4}$$

$$S_2 = \left(\frac{C_v C_a^{0.5}}{0.66 \tan \frac{\theta}{2}} \right) \left(\frac{P_{inj} - P_a}{\rho_a} \right)^{0.25} (Dt)^{0.5} \qquad (t \geq t_b) \tag{2-5}$$

where C_V is the orifice velocity contraction coefficient; Ca is the area contraction coefficient; and θ is the spray dispersion angle.

A recent study based on these empirical equations and correlations was carried out by Klein-Douwel et al.[29, 30]. The authors concluded on a general form of the penetration as well as the cone angle for non-vaporizing fuel spray:

$$S \propto \rho_g^{m_s} (P_{inj} - P_a)^{n_s} D^{\alpha_s} t^{\beta_s} \left(\tan \frac{\theta}{2} \right)^{0.5} \tag{2-6}$$

$$\tan \frac{\theta}{2} \propto \rho_g^{m_\theta} (P_{inj} - P_a)^{n_\theta} D^{\alpha_\theta} t^{\beta_\theta} \tag{2-7}$$

where θ is the spray angle; and the exponents m_s, n_s, α_s, and β_s are in relation to gas density, pressure difference, nozzle diameter and time, respectively; they are varied in different conditions, as is shown in Table 2-1.

Table 2-1 Exponents on variables in Equation 2-6 [29, 30]

m_s	n_s	α_s	β_s
-0.23	0.27	0.46	0.54
-0.25	0.25	0.5	0.5
-0.25	0.5	0.5	0.5
-0.32	0.32	0.18	0.64
-0.35	0.25	0.5	0.5
-0.36	0.25	0.5	0.5
-0.406	0.262	0.37	0.568
-0.45	0.25	0.5	0.5
-0.5	0.3	0.59	0.55
-0.5	0.5	0.5	0.5

2.1.3 Droplet Size and Velocity

Droplet size and velocity [32] are two important microscopic characteristics of the fuel spray. Nowadays, advances in optical diagnostic technologies enable a microscopic study of the droplet dynamics. The Phase Doppler Particle Analyzer (PDPA) [33, 34] is an effective means to measure the droplet size and velocity; the details of the PDPA system will be introduced in the next chapter. Figure 2-2 shows a typical result of the spray droplet velocity and size measured by the PDPA system. The measurement point is at a certain distance from the injector nozzle. The blue points plotted are the experiment data acquired and the red curve is the average mean value of the data.

In the left diagram, according to the droplet velocity profile, the spray can be divided into two parts: the ‘spray head’ and ‘spray tail’ [35, 36]. The droplets need some time to arrive at the measuring volume after the start of injection, which is the so-called ‘arrival time’. After this time, the velocity experiences a short decrease and is then followed by a quick increase and a relatively stable period, which together make up the spray head. In the spray head, the droplets in the spray front are firstly decelerated by the drag force and the droplets behind experience

relatively less drag force and show an increase in velocity. As the spray head passes through the measuring volume, a sudden and dramatic velocity drop is observed and this rapid decline process is called the spray tail.

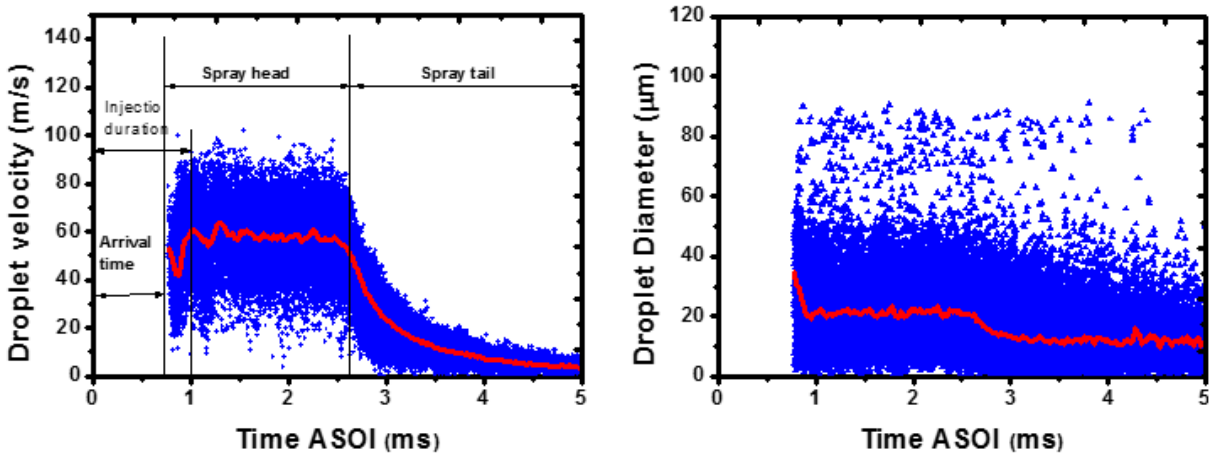

Figure 2-2 Sample of droplet velocity (left) and droplet size (right) of PDPA test [37]

In the right hand diagram, it can be seen that the mean droplet diameter represented by the red curve experiences a quick decrease first and is then followed by a stable trend. At the very beginning, the increase of the droplet velocity enhances the breakup of bigger droplets into smaller droplets; this could be the reason for the decrease of the droplet mean diameter. After this period, the relatively stable velocity leads to a stable breakup rate and this will result in a similar droplet mean diameter.

In the field of internal combustion engines, the most commonly used parameter to evaluate the fuel spray droplet size is the Sauter Mean Diameter (SMD) [38-40], which is defined [41] as the diameter of a sphere that has the same volume/surface area ratio as a particle of interest. To estimate the value of the SMD, the calculation method is expressed as follows:

$$D_{32} = \frac{\sum N_i D_i^3}{\sum N_i D_i^2} \tag{2-8}$$

where D_{32} is the SMD; D_i is the droplet size of parcel i and N_i is the droplet number in parcel i. It indicates that the SMD can also be understood as the ratio of the sum of volume to the sum of surface area.

2.2 Breakup Regimes

The fuel spray atomization and breakup processes are the key links which affect the mixture formation of the internal combustion engine and then influence the combustion efficiency and emissions. For a long time, many researchers [28, 38, 42-55] carried out a large number of studies on the spray field and macroscopic characteristics; however, due to the lack of detailed fluid theories and the limits of the advanced testing technologies, most of these studies emphasized their works on the geometrical characteristics such as spray penetration, cone angle, droplet size, and droplet spatial distributions and very few of them worked on the atomization and breakup regimes.

From the 1970s, with the development of advanced experimental instruments, some researchers [56-64] started to change their focus on the breakup regimes. Since the atomization process is closely related to the linear and non-linear stability theories [65, 66] of fluid dynamics, so the analysis of breakup regimes does not only have important implications in directing internal combustion engine development, but also has great relevance in the field of fluid dynamics. With the further development of the research on breakup regimes, many physical models have been developed during the past few decades.

2.2.1 Breakup Classification

When the liquid is injected into another media, the aerodynamic force, inertia force, viscosity and surface tension will act on the continuous liquid core and force it into separate liquid blocks, ligaments, or droplets. Different injection flows can lead to various breakup regimes due to different injection velocities. In general, the breakup of the round liquid core can be divided into four different regimes according to the velocity gradient: the Rayleigh breakup regime, the first wind-induced breakup regime, the second wind-induced breakup regime, and the atomization regime [57]; as is shown in Figure 2-3 [67]. Figure 2-4 shows the schematic of the four types of breakup.

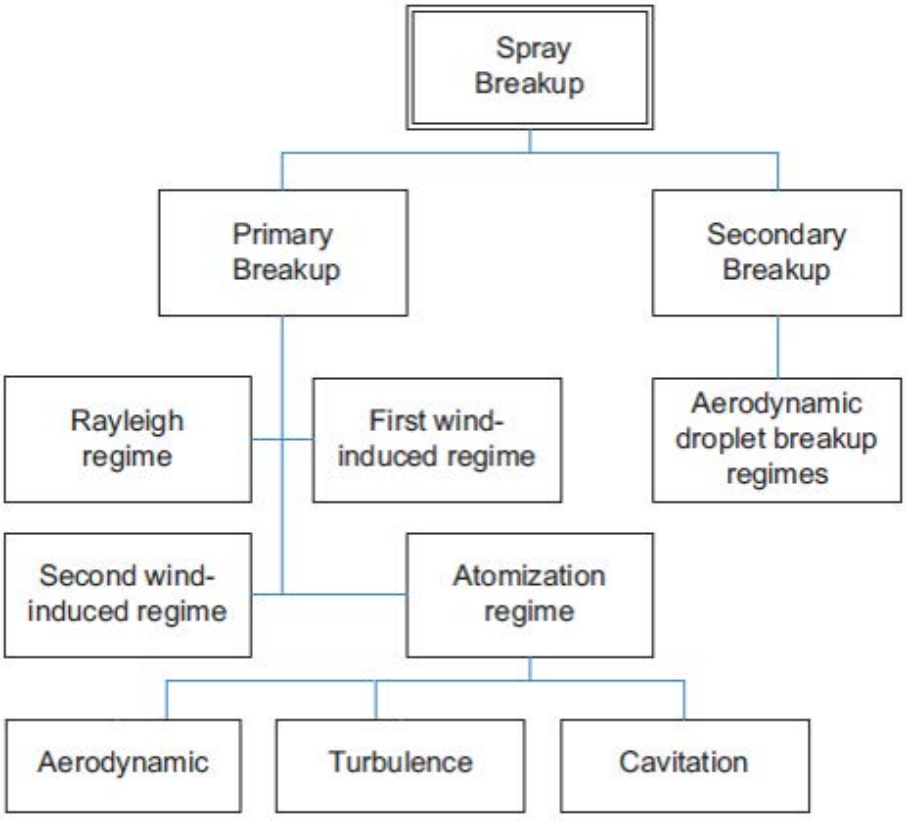

Figure 2-3 The classification of breakup regimes [67]

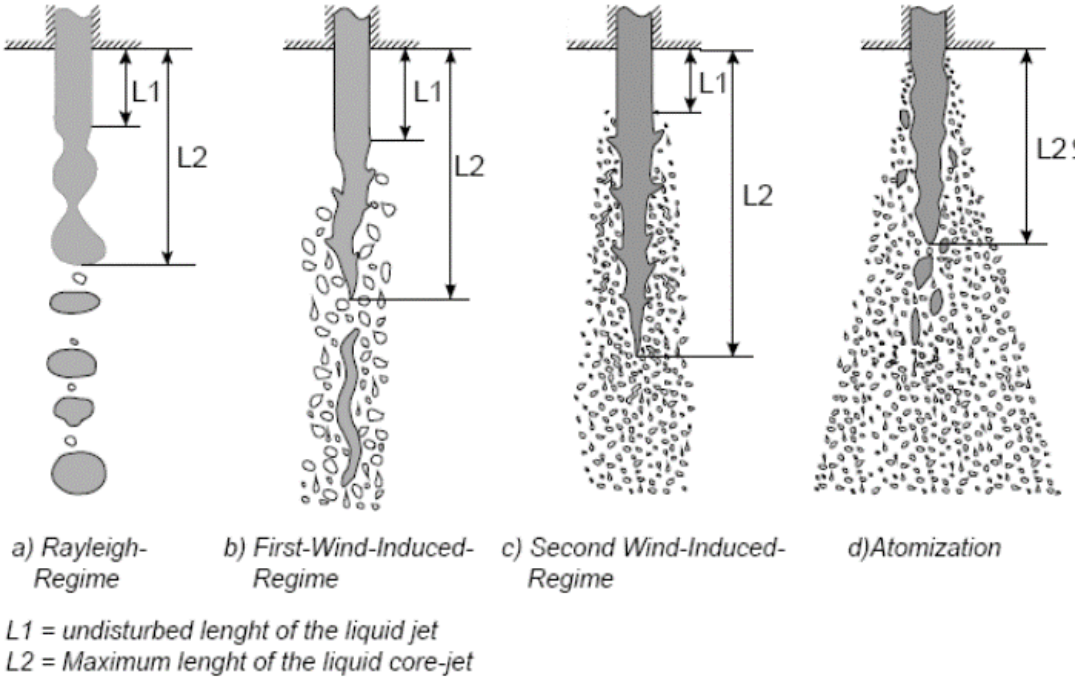

Figure 2-4 Schematic of the four types of breakup: Rayleigh breakup regime, first wind-induced breakup regime, second wind-induced breakup regime and the atomization regime [57]

Rayleigh Breakup Regime

Figure 2-4(a) describes the Rayleigh breakup regime. The liquid core breakups at low jet velocity due to axisymmetric oscillations initiated by liquid inertia and surface tension forces. The size of the produced droplets is greater than the nozzle diameter and the breakup always occurs at a distance far away from the nozzle.

First Wind-induced Breakup Regime

With the increase of the injection velocity, the aerodynamic force induced by the relative velocity becomes significant. Liquid inertia and surface tension forces are amplified by aerodynamic forces and then these forces will lead to the changes of surface curvature and the

uneven static pressure distribution. All of these factors enhance the breakup of the liquid core. The breakup occurs at a distance (shorter than that of the Rayleigh regime) downstream of the nozzle and the produced droplets' size is equivalent to the nozzle diameter.

Second Wind-induced Breakup Regime

The flow inside the nozzle becomes turbulent with a further increase of the injection velocity. The unstable growth of the short wavelength surface waves initiated by the turbulence is amplified by aerodynamic forces. The combined result of the turbulence and aerodynamic forces is the main cause of the breakup. The breakup happens at a short distance away from the nozzle and the produced droplets' size is much smaller than the nozzle diameter.

Atomization Regime

The liquid starts to breakup once it leaves the nozzle. A large number of fine-sized liquid droplets are formed and the droplet size is much smaller than the nozzle size. An intact liquid core exists though the breakup occurs at the nozzle exit. This regime is the main primary breakup mechanism for the sprays of direct injection engines and it has become a focus for engine research; a detailed discussion of this regime will be given later in this chapter.

All of the above classification descriptions are qualitative analyses of fuel spray. Some researchers [28, 56, 68-70] tried to classify these regimes and describe them by quantitative analyses. Ohnesorge [69] suggested a classification method based on the Reynolds number *Re* and the Ohnesorge number *Z* of the liquid:

$$\mathrm{Re} = \frac{uD\rho_l}{\mu_l} \tag{2-9}$$

$$Z = \frac{\sqrt{We_l}}{\mathrm{Re}} = \frac{\mu_l}{\sqrt{\sigma\rho_l D}} \tag{2-10}$$

$$We = \frac{u^2 D\rho_l}{\sigma} \tag{2-11}$$

where u is the injection velocity; D is the nozzle diameter; ρ_l is the liquid density; μ_l is the dynamic viscosity of the liquid; and σ is the surface tension.

The classification of the four regimes can be expressed in the Ohnesorge diagram, as is shown in Figure 2-5.

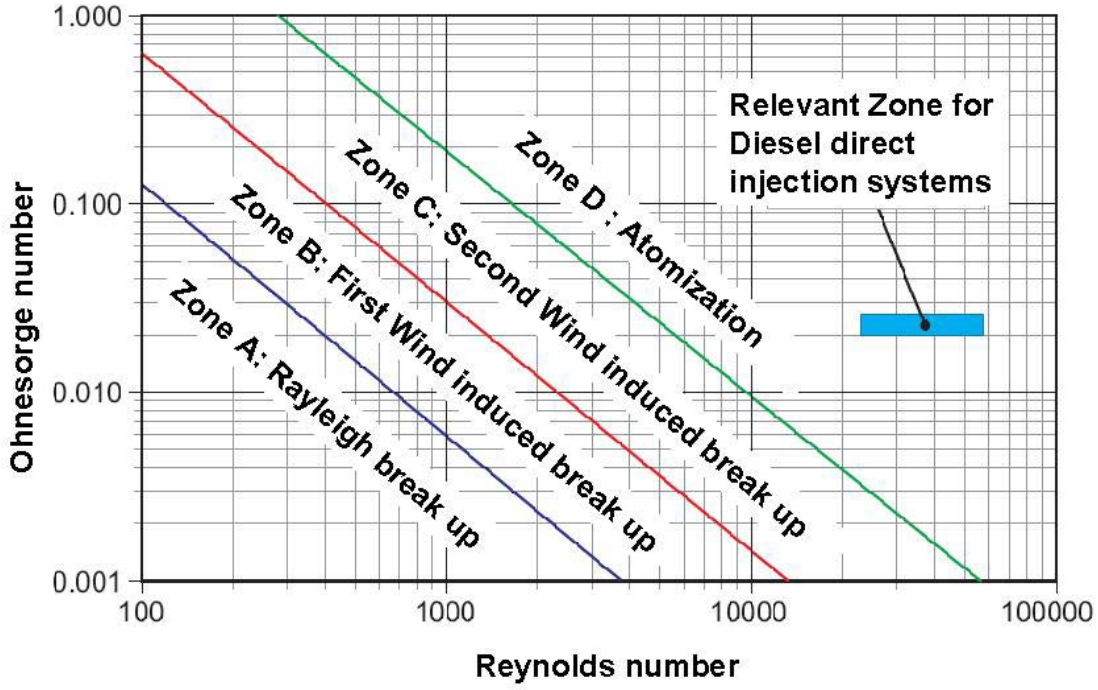

Figure 2-5 Ohnesorge diagram: jet break-up regimes [69]

However, this description did not consider the initial condition of the spray induced by different nozzle geometry and the effect of ambient conditions. Experiments have shown that the ambient gas density also plays an important role in affecting the breakup. Torda [70] corrected this description by considering the influence of the ambient gas density and concluded that higher ambient density can also enhance the atomization process. Ranz [68] also studied the effect of ambient gas density on the breakup regimes and the author believed that the Weber number of the liquid is the dominating parameter in affecting the breakup.

Reitz [56] suggested considering the gas-to-liquid density ratio and extended the two-dimensional Ohnesorge diagram into a three-dimensional description, as is shown in Figure 2-6 [25].

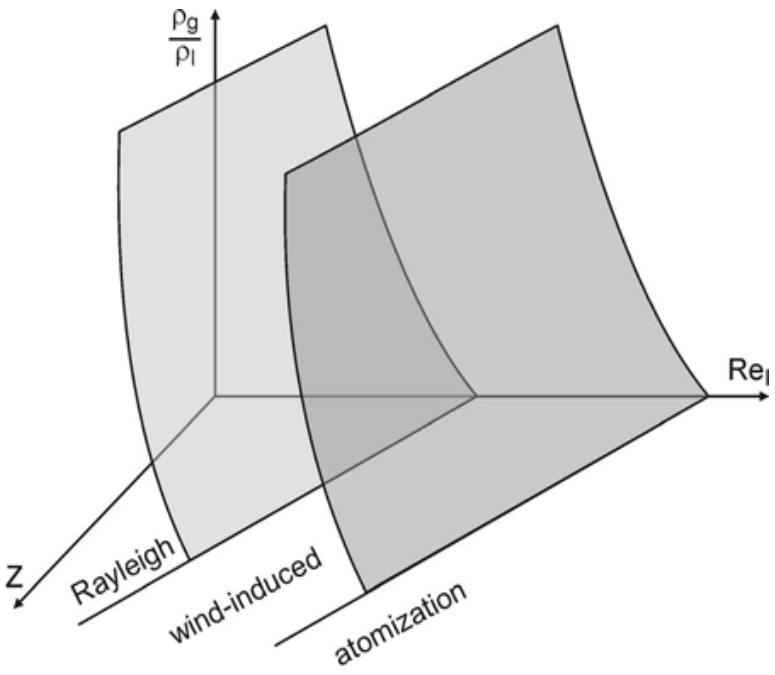

Figure 2-6 Schematic diagram of the 3D classification description of the breakup regimes [25]

It is worth noticing that even the 3D description of the breakup regimes is a better solution; the criterion used for the regimes can be different from one research field to another and all of these descriptions are not absolutely suitable for different situations.

2.2.2 Atomization

Atomization is the typical primary breakup mechanism for the sprays of modern direct injection engines. A series of studies [57] have been carried out to investigate the breakup mechanisms of the atomization process so far and five possible descriptions can be concluded as: aerodynamically-induced breakup, turbulence-induced breakup, cavitation-induced breakup, pressure oscillation induced breakup and breakup due to the relaxation of velocity profile.

Aerodynamically-induced Breakup

Aerodynamically-induced breakup is the most developed mechanism of the spray atomization process. Figure 2-7 shows the schematic of the aerodynamically-induced breakup. This breakup mechanism was initially proposed by Castleman [43] in 1932 and now it has become the most studied and popular description of the fuel spray atomization process. Castleman found that the growth of instable waves on the liquid surface is induced by the aerodynamic interference around the liquid jet. With the increase of the injection velocity, the wavelength of the instable wave continuously decreases until it reaches nanoscale and then the liquid core breakups into ligaments or droplets. By introducing linear perturbation theory into the analysis of the instable surface wave and ignoring the gas viscosity, the wave growth rate and the wavelength can be calculated and the fast growth wave dominates the breakup and the produced droplet size is assumed to be proportional to the wavelength of the fast growth wave. Based on

these analyses, Reitz and Bracco [57] preliminarily modelled the atomization process in the KIVA [71-73] code.

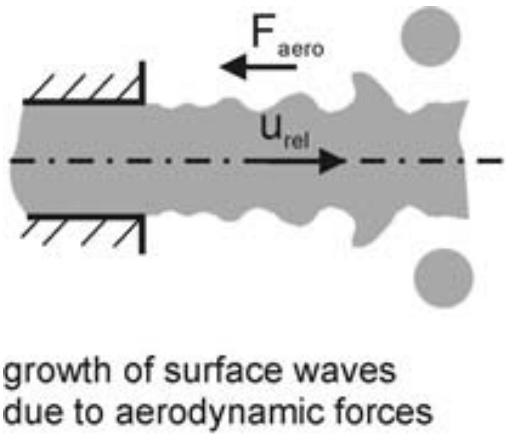

Figure 2-7 Schematic of the aerodynamically-induced breakup [25]

Turbulence-induced Breakup

DeJuhasz [42] studied the atomization process also happening inside the nozzle due to the turbulence of the liquid itself. Schweitzer [74] proposed that the radial component of turbulence velocity will lead to the instability at the nozzle exit which could result in the breakup. Grant [75] and Phinney [76] observed that the flow instability and breakup will be greatly affected by the turbulence at the nozzle exit as well as inside the nozzle hole. Ruff [77], Tseng [78] and Wu [79] found that the turbulence will affect the breakup characteristics when the density ratio of liquid/gas is greater than 500; while the aerodynamic force will dominate the breakup when the ratio is lower than 500.

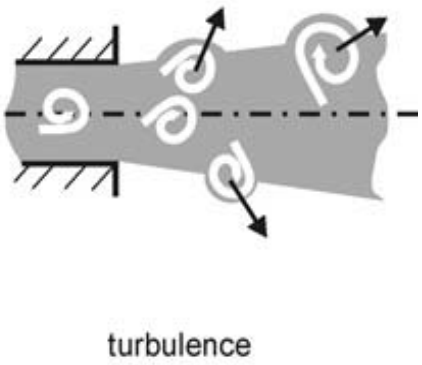

Figure 2-8 Schematic of the turbulence-induced breakup [25]

Figure 2-8 presents a schematic of the turbulence-induced breakup. Compared to the aerodynamically-induced breakup, which has already been well developed, this breakup mechanism is not fully studied due to the lack of detailed turbulence theory. Thus, many assumptions should be made in practical applications. The most popular turbulence model is [80] Huh and Gosman's primary breakup model which will be introduced later in this chapter.

Cavitation-induced Breakup

Bergwerk [81] found that the turbulence is insufficient to cause the atomization phenomenon at certain Reynolds numbers and the main factor is believed to be the cavitation effect inside the nozzle. At high injection pressure, the sharp corner inside the nozzle hole will promote the formation of the cavitation. Hiroyasu [82, 83] also indicated that the main difference between the fully developed spray and the incompletely developed spray is caused by the cavitation effect inside the nozzle. Byung [84] experimentally studied the influence of the fuel temperature on the saturated vapour pressure and cavitation phenomenon; the results in turn

provided the evidence that the cavitation inside the nozzle will enhance the atomization process. The breakup induced by the cavitation phenomenon can be seen in Figure 2-9.

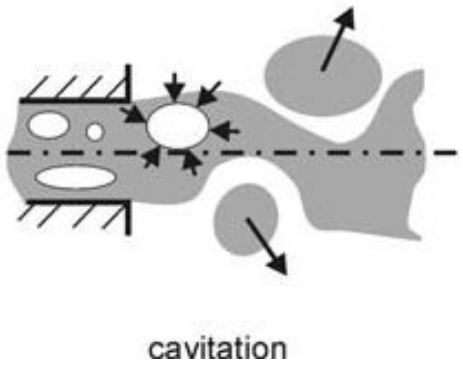

Figure 2-9 Schematic of the cavitation-induced breakup [25]

Pressure Oscillation induced Breakup

Giffen et al. [85] noticed that the pressure oscillation caused by the fuel injection system will also affect the spray atomization process. It is a common phenomenon that the pressure oscillation exists in most injection systems and there is no doubt that this factor is also an important parameter in the atomization process.

Breakup Due to the Relaxation of the Velocity Profile

The boundary conditions experience a sudden change once the liquid fuel leaves the nozzle exit and this is believed by some researchers to be another important factor in affecting the atomization process. Rupe [86] observed that the laminar flow is more unstable than the turbulent flow when the boundary condition changes to free liquid jet flow. The redistribution of the velocity profile induced by the change of boundary conditions will lead to the oscillation of the liquid jet. Figure 2-10 presents a schematic of the relaxation of the velocity profile.

Shkador [87] studied the shear force changes at the interface of the liquid jet and proved that the relaxation of the velocity profile could lead to the short unstable surface wave which may result in the atomization of the liquid jet.

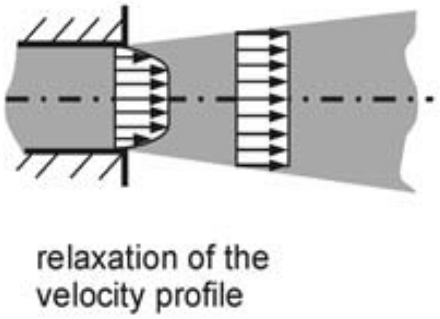

Figure 2-10 Relaxation of the velocity profile [25]

2.2.3 Secondary Breakup

The droplets generated by the primary breakup will undergo secondary breakup due to the aerodynamic force. When the deformation force acting on the droplet exceeds the surface tension, the droplet will then breakup into smaller droplets. Many studies [59, 63, 88] in terms of the droplet breakup have been carried out and the classification of different types of breakup according to gas Weber number is shown in Figure 2-11 [89]. The Weber number of gas We_g is an effective parameter to define the breakup types, the expression of We_g is:

$$We_g = \frac{\rho_g d u_{rel}^2}{\sigma} \tag{2-12}$$

where the subscript g in each term stands for gas.

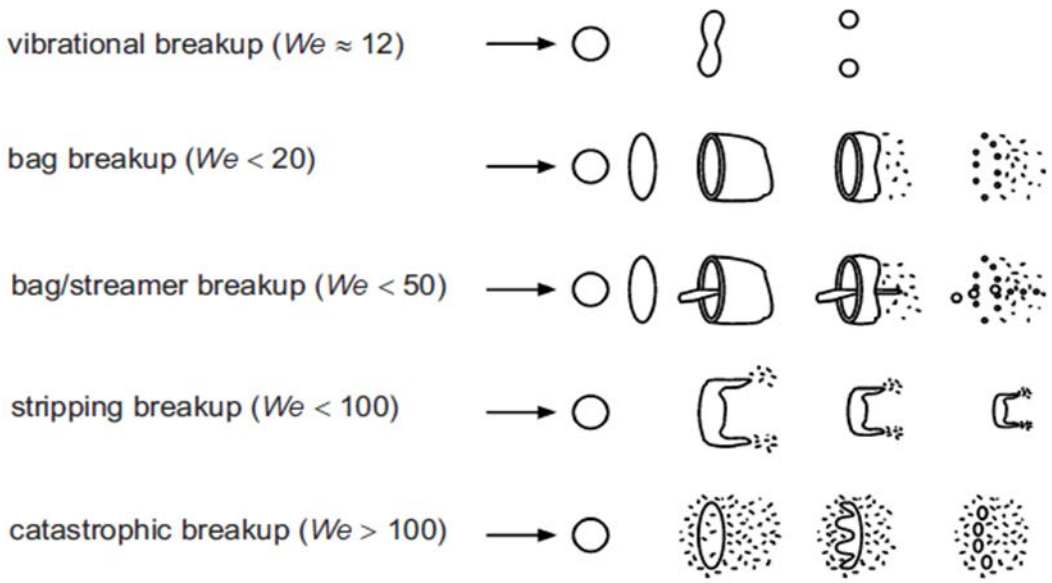

Figure 2-11 The classification of different types of breakup according to gas Weber number [89]

At low Weber number ($We_g<12$), the parent droplet experiences dumbbell-like oscillation and breakups into two small child droplets. With the increase of We_g up to 50, the droplet will firstly experience bag breakup which results in a bag-like deformation and forms small droplets around the bag rim; it then undergoes streamer breakup which results in an umbrella droplet distribution. In the stripping regime ($50<We_g<100$), small droplets are continuously shed off from the liquid surface due to the shear force. The catastrophic breakup refers to the condition of $We_g>100$. The large amplitude wave induced by the deceleration and droplet oscillations leads to a disintegration by means of forming large product droplets; while the small waves with a short wavelength are stripped off and form small child droplets.

In internal combustion engines, the catastrophic breakup is the main form of the secondary breakup due to the high Weber number of the ambient gas; however, all of these breakup regimes may occur because of a reduction of the relative velocity due to drag forces. Based on

these breakup regimes, many physical-numerical models have been developed and will be introduced later in this chapter.

2.3 CFD Approaches for Spray Simulation

The essential outline of the spray simulation is the multidimensional modelling of the gas/liquid two-phase flow and the main task is to simulate the atomization of the continuous liquid jet into droplets. In general, there are two approaches to study the gas/liquid two-phase flow. One approach treats the discrete liquid as an equivalent continuum flow, which assumes that the liquid has continuous velocity, temperature and transport properties; this approach is the so called Continuous Droplet Model (CDM). The other approach is the Discrete Droplet Model (DDM) which treats the liquid as the discrete phase and the liquid droplets or parcels are traced by the Lagrangian description.

2.3.1 Continuous Droplet Model (CDM)

The droplets may possess different sizes d_p, various velocities u_{pi}, different temperatures T_p, and different positions x_i. Thus, a commonly used method [90] to study these complex droplets is to employ a Probability Distribution Function (PDF) to account for the number density of droplets in the ranges of position $\boldsymbol{x_i} \sim \boldsymbol{x_i} + \boldsymbol{dx_i}$, velocity $\boldsymbol{u_{pi}} \sim \boldsymbol{u_{pi}} + \boldsymbol{du_{pi}}$, size $\boldsymbol{d_p} \sim \boldsymbol{d_p} + \boldsymbol{d}(\boldsymbol{d_p})$ and temperature $\boldsymbol{T_p} \sim \boldsymbol{T_p} + \boldsymbol{d}(\boldsymbol{T_p})$ [90]:

$$\frac{probable\ number\ of\ droplets}{unit\ volume} = f(x_i, u_{pi}, d_p, T_p, t)dx_i du_{pi} d(d_p) dT_p dt \qquad (2\text{-}13)$$

The temporal evolution of f is obtained by solving the Spray Equation [91]:

$$\frac{\partial f}{\partial t}+\frac{\partial}{\partial x_i}(fu_{pi})+\frac{\partial}{\partial u_{pi}}(fu_{pi})+\frac{\partial}{\partial d_p}(fd_p)+\frac{\partial}{\partial T_p}(fT_p)=f_s \quad (2\text{-}14)$$

where f_s is the source term due to collision, coalescence, breakup, evaporation etc. Equation 2-14 is also known as the Spray Equation [91].

The CDM approach can describe the flow in a more accurate way; however, the calculation is at a very high level. It can be noticed that the Spray Equation contains 11 independent dimensions, thus it becomes extremely complex to solve.

2.3.2 Discrete Droplet Model (DDM)

Based on the Monte-Carlo method, droplets with the same properties can be simulated as a parcel and then all the droplets in the flow can be represented by a number of parcels. The DDM approach [92] then deals with these representative parcels and traces these parcels in a Lagrangian manner. The following assumptions are made in the DDM approach:

- Ignore the real atomization process and assume that the continuous liquid jet will breakup into droplets/parcels once it leaves the injector nozzle.
- All the droplets in the flow can be represented by a number of parcels and droplets in each parcel have the same properties.
- Ignore the influence between droplets and the behavior of gas/liquid phases is coupled by momentum (droplet velocity is reduced, gas velocity is increased), energy (heat exchange) and mass (evaporated mass passes over to the gas phase) exchanges.

The calculation can be significantly simplified by these assumptions and the result can still meet the engineering requirement, though some details are missing in the DDM approach. Figure 2-12 is the schematic of the DDM method.

Figure 2-12 Schematic of the DDM model and an example of the simulated spray [60]

2.4 Spray Breakup Models

The DDM approach is a commonly used method in most of the engine simulation CFD codes. In this approach, physical-numerical models are required to describe the breakup of the liquid droplet in the parcels during their transportation.

2.4.1 Primary Breakup Models

In the DDM approach, the primary atomization process determines the initial conditions for the calculation of the subsequent droplet breakup process and mixture formation. For the liquid phase, the Lagrangian description requires the existence of liquid drops and the calculation of spray atomization always begins with liquid drops starting to penetrate into the combustion chamber. The primary breakup model is used to predict the initial conditions of these liquid drops, including the initial droplet size and velocity.

Blob Method

Reitz and Diwakar [60, 93] developed a simplified approach to define the initial conditions of the first droplets at the nozzle exit of solid-cone sprays, which is known as the Blob Method. The Blob Method is based on the assumption that atomization and droplet breakup within the dense spray near the nozzle are indistinguishable processes and that a detailed calculation can be simplified by the injection of big spherical droplets with uniform size, which are then subject to aerodynamic-induced breakup.

The diameter of these blobs equals the nozzle hydraulic diameter *D* and the number of drops injected per unit time is calculated from the mass flow rate [94]. The spray angle should be given as an input parameter. Figure 2-13 shows the schematic of the Blob Method. It is of importance to notice that this method is a great simplification of the primary breakup process.

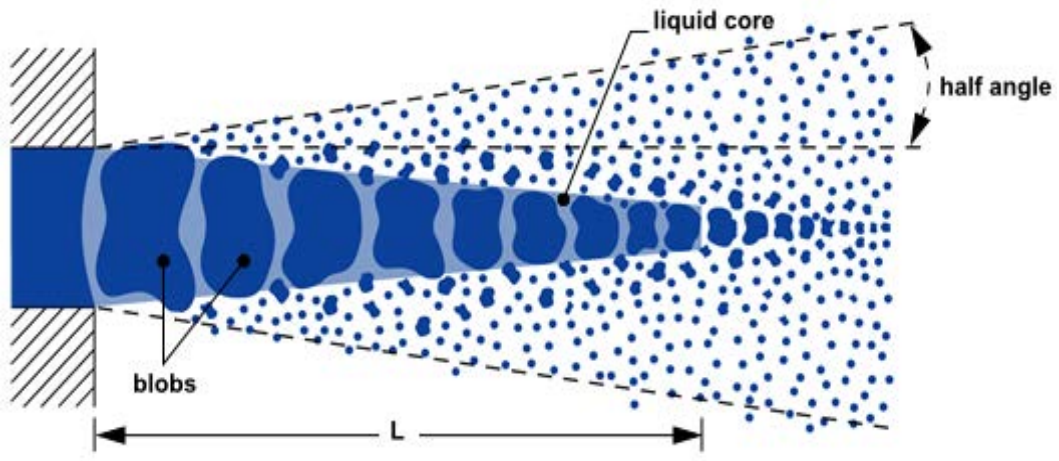

Figure 2-13 Schematic of the Blob Method [93]

Wave Model

Based on the Blob-Method, the KH breakup model proposed by Reitz [56, 57, 60] introduces the KH instability into the breakup model which mainly considers the aerodynamically-induced breakup mechanism. The KH breakup model assumes that the growth of Kelvin-Helmholtz instabilities induces the shearing-off of droplets from the liquid surface. Figure 2-14 shows the schematic of the wave model.

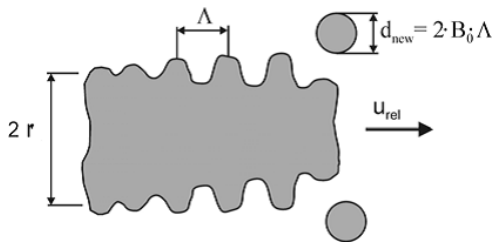

Figure 2-14 Schematic of the wave model [60]

The reduction rate of the parent droplet radius and the resulting child droplet size are related to the frequency (Ω_{KH}) and wavelength (Λ_{KH}) of the fastest growing surface wave, as given below [60]:

$$\Omega_{KH} = \frac{0.34 + 0.385 We_g^{1.5}}{(1+Oh)(1+1.4T^{0.6})}\sqrt{\frac{\sigma}{\rho_l r^3}} \tag{2-15}$$

$$\Lambda_{KH} = \frac{9.02r(1+0.45Oh^{0.5})(1+0.4T^{0.7})}{(1+0.865We_g^{1.67})^{0.6}} \tag{2-16}$$

where r is the parent drop radius; ρ_l is liquid density; σ is liquid surface tension; We_g is the gas Weber number; Oh is the Ohnesorge number and $T = Oh\sqrt{We_g}$.

The radius of the parent droplet decreases continuously according to Equation (2-17) until it reaches the criterion of the KH breakup [60]:

$$\frac{dr}{dt} = -\frac{r - r_{KH}}{\tau_{KH}}, \quad r_{KH} \le r \tag{2-17}$$

The child drop size r_{KH} and breakup time τ_{KH} are [60]:

$$r_{KH} = B_0 \Lambda_{KH} \tag{2-18}$$

$$\tau_{KH} = \frac{3.788 B_1 r}{\Lambda_{KH} \Omega_{KH}} \tag{2-19}$$

where B_0 and B_1 are the model constants.

The KH breakup occurs and a new droplet parcel with drop radius r_{KH} will be created once the shed mass exceeds 5% of the initial parcel mass.

Huh and Gosman Turbulence-induced Breakup Model

Huh et al [80] developed a turbulence induced breakup model for the primary atomization process. In this model, the effects of both aerodynamic-induced instabilities on the jet surface and flow turbulence in the jet are considered. Adopting the Blob Method, the liquid jet is simulated as a train of blob parcels issued from the nozzle and the turbulent fluctuations in the jet flow are an important parameter to produce the initial perturbations on the liquid surface; which grow exponentially due to the KH instability, until they detach as atomized droplets.

Then, the droplets formed after the primary disintegration may undergo further secondary breakups. This model solves the potential problem of the wave model, where the exponential wave growth rate becomes zero at zero perturbation amplitude.

The characteristic length scale L_{tw} and the time scale τ_{tw} of atomization are [80]:

$$L_{tw} = C_1 L_t = C_2 L_w \tag{2-20}$$

$$\tau_{tw} = C_3 \tau_t + C_4 \tau_w \tag{2-21}$$

where L_t, the turbulence length scale, is the dominant length scale and L_w is the wavelength of surface perturbations; and τ_t and τ_w are the turbulence time scale and the wave growth time scale, respectively. The empirical constants C_1 to C_4 are set to 2.0, 0.5, 1.2 and 0.5 respectively, according to [80].

The time-dependent turbulence length and time scales are given as a function of the time and the initial turbulence conditions as [80]:

$$L_t(t) = L_t^0 \left(1 + \frac{0.0828t}{\tau_t^0} \right)^{0.457} \tag{2-22}$$

$$\tau_t(t) = \tau_t^0 + 0.0828t \tag{2-23}$$

The initial turbulence length L_t^0 and time scale τ_t^0 are calculated using average quantities for the turbulent kinetic energy and energy dissipation rate [80]:

$$L_t^0 = C_\mu \frac{k_{avg}^{1.5}}{\varepsilon_{avg}} \tag{2-24}$$

$$\tau_t^0 = C_\mu \frac{k_{avg}}{\varepsilon_{avg}} \tag{2-25}$$

where C_μ = 0.09 and the average quantities are estimated [95] as:

$$k_{avg} = \frac{U^2}{8(L/D)}\left[\frac{1}{c_d^2} - K_c - (1-s^2)\right] \tag{2-26}$$

$$\varepsilon_{avg} = K_\varepsilon \frac{U^2}{2L}\left[\frac{1}{c_d^2} - K_c - (1-s^2)\right] \tag{2-27}$$

where L and D are the hole length and diameter; U is the initial liquid velocity at the nozzle exit; C_d is the discharge coefficient; K_c is a constant, taking into account losses in the contraction corner; K_s is a constant for average turbulent energy dissipation; and s is the area contraction ratio of the nozzle hole. The ranges of these empirical constants are suggested in [80].

Ignoring the surface tension and viscous effects and maintaining only the aerodynamic destabilizing term, the wave growth timescale is calculated as [80]:

$$\tau_w = \frac{L_w}{U}\sqrt{\frac{\rho_l}{\rho_g}} \tag{2-28}$$

The parent drop radius decreases continuously according to the ratio of the atomization length over the time scale [80]:

$$\frac{dr}{dt} = -K_{tw}\frac{0.5L_{tw}}{\tau_{tw}} \tag{2-29}$$

where K_{tw} is the model constant.

The child drop diameter is assumed to be equal to the atomization length scale L_{tw}. A new droplet parcel is then created after the breakup.

Cavitation-induced Breakup Model

Cavitation inside the injector nozzle can reach the nozzle exit and its implosion will enhance spray atomization. It is assumed that cavitation patterns are transported to the jet periphery by the turbulence velocity inside the liquid and they either burst at the periphery or collapse before reaching it. Figure 2-15 shows a schematic of the cavitation phenomenon.

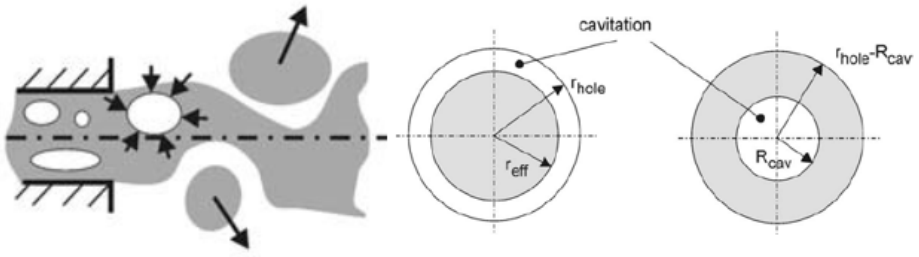

Figure 2-15 Schematic of the cavitation phenomenon [96]

For both cases, a characteristics time scale is calculated, the smaller causing breakup. Following Bianchi, Pelloni, Arcoumanis and Gavaises [96], the characteristic cavitation time scale τ_{CAV} is calculated as:

$$\tau_{CAV} = \min(\tau_{Collapse} : \tau_{Burst}) \tag{2-30}$$

The bubble collapse time is calculated from the Rayleigh Plesset theory as the time taken for a bubble of a given radius *r* to decrease to 0:

$$\tau_{Collapse} = 0.9145 R_{CAV} \sqrt{\frac{\rho_l}{p_v}} \tag{2-31}$$

where, p_v is the fuel vapour pressure; ρ_l is the fuel density; and R_{CAV} is the effective radius of an equivalent bubble from the nozzle:

$$R_{CAV} = r_{hole} \sqrt{(1 - C_a)} \tag{2-32}$$

where C_a is the area reduction coefficient of the nozzle hole.

The average time required for a cavitation bubble to reach the periphery of the jet can be estimated as:

$$\tau_{Burst} = \frac{r_{hole} - R_{CAV}}{u'_{turb}} \tag{2-33}$$

and the turbulent velocity:

$$u'_{turb} = \sqrt{\frac{2K(t)}{3}} \tag{2-34}$$

The length scale for the cavitation induced breakup is:

$$L_{CAV} = R_{CAV} \tag{2-35}$$

When the breakup time reaches the criterion time τ_{CAV}, a new droplet parcel with the drop diameter L_{CAV} will be created.

Hybrid Breakup Model

In fact, the primary breakup process is dominated by a combination effect of the aerodynamically-induced breakup, turbulence-induced breakup and cavitation-induced breakup. Obviously, it's more reasonable to develop hybrid breakup models which could consider all of these effects. Huh and Gosman developed a turbulence-induced breakup model [80] assuming that the turbulent forces within the liquid emerging from the nozzle are the producers of initial surface perturbations, which grow exponentially due to aerodynamic forces and form new droplets. Som et al. [97] developed the KH-ACT model which considered all three effects. A competition between the turbulence, cavitation and aerodynamic-induced breakup mechanisms is carried out to determine the dominant breakup mechanism in the KH-ACT model.

A series of hybrid models have been developed; however, some non-ignorable aspects such as the extent of the impact of these mechanisms and how far downstream the effect lasts are still not fully studied so far. Further studies and understanding on these aspects are still needed and are worth investigation.

2.4.2 Secondary Breakup Models

Taylor Analogy Breakup (TAB) Model

Based on the Blob injection, the TAB model proposed by O'Rourke and Amsden [98] compares an oscillating-distorting droplet to a spring-mass system; where the liquid surface tension, the liquid viscosity and the aerodynamic force on the droplet are analogous to the restoring force, the damping force and external force acting on a mass respectively. Figure 2-16 presents the schematic of the TAB model.

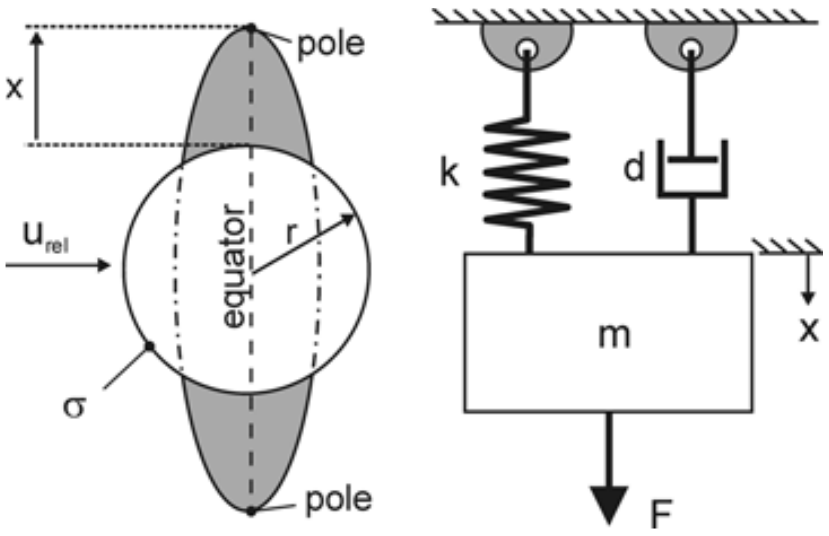

Figure 2-16 Schematic of the TAB model [98]

The distortion parameter *k* is calculated by solving a spring-mass equation:

$$\ddot{k} = \frac{2}{3}\frac{\rho_g}{\rho_l}\frac{u_{rel}^2}{r^2} - \frac{8\sigma}{\rho_l r^3}k - \frac{5\mu_l}{\rho_l r^2}\dot{k} \tag{2-36}$$

where ρ_l, σ and μ are the liquid density, surface tension, and viscosity, respectively; ρ_g is the gas density; and w is the local relative velocity between the droplet and the surrounding gas.

If the value of k exceeds unity, the droplet breakups into smaller droplets with a radius specified in the given distributions. It should be noticed that the TAB model will result in a complete disintegration and the newly formed parcels will not undergo further breakup.

Rayleigh-Taylor (RT) Breakup Model

The RT model [99] is based on the theoretical work of Taylor [100]; who investigated the instability of the interface between two fluids with various densities in the case of an acceleration or deceleration normal to this interface, as is shown in Figure 2-17. This model is always used in combination with the KH model to improve predictions of the secondary breakup process, which is known as the KH-RT model.

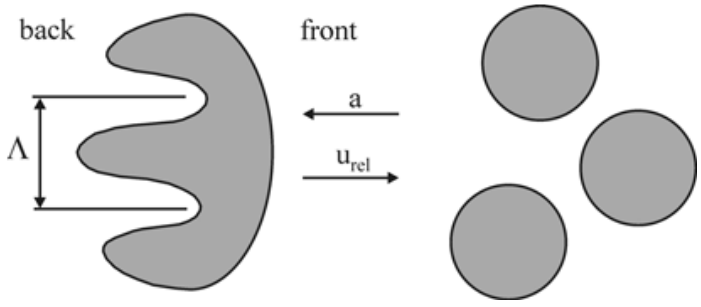

Figure 2-17 Schematic of RT breakup model [99]

The wave growth rate Ω_{RT}, the corresponding wave number K_{RT} and wavelength Λ_{RT} of the fastest growing wave are:

$$\Omega_{RT} = \sqrt{\frac{2\left[a\left(\rho_l - \rho_g\right)\right]^{1.5}}{3\sqrt{3}\sigma\left(\rho_l + \rho_g\right)}} \tag{2-37}$$

$$K_{RT} = \sqrt{\frac{a\left(\rho_l - \rho_g\right)}{3\sigma}} \tag{2-38}$$

$$\Lambda_{RT} = C_0 2\pi / K_{RT} \tag{2-39}$$

$$a = \frac{3}{8} C_d \frac{\rho_g u_r^2}{\rho_l r} \tag{2-40}$$

where C_0 is the model constant; u_r is the droplet relative velocity; and a is the droplet acceleration.

The breakup time scale is:

$$\tau_{RT} = C_1 / \Omega_{RT} \tag{2-41}$$

where C_1 is the model constant.

The RT waves are formed when the droplets' diameter is greater than the wavelength of the fastest growing disturbance and the breakup occurs when the disturbances exceed the elapsed breakup time scale τ_{RT}. It is important to note that no new parcels were created during the RT breakup process and only the droplet is split into smaller droplets with uniform diameters proportional to the wavelength of the disturbances.

Kelvin-Helmholtz-Rayleigh-Taylor (KH-RT) Breakup Model

Based on the wave model, the Rayleigh-Taylor (RT) component has been added to the wave breakup model by Patterson et al. [101] to improve predictions of the secondary breakup process.

As is shown in Figure 2-18, the RT model is applied to spray breakup beyond a certain distance from the nozzle; since its fast breakup rate and a competition between the KH and RT models will be carried out, while within the distance L_b , KH (Wave) model will dominate the breakup process. This model is the most widely used model in most of the engine simulation codes and it has been proved to be an effective spray model.

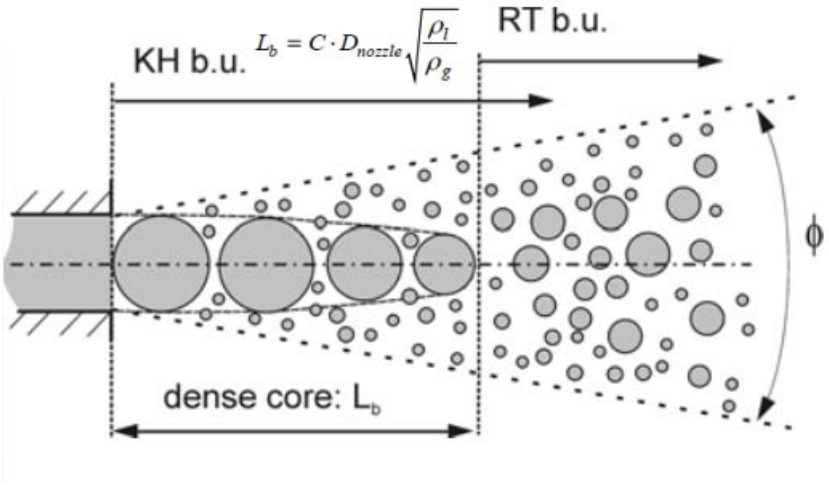

Figure 2-18 KH-RT breakup model [101]

2.4.3 Combined Models

As discussed above, the primary breakup process and the secondary breakup process is dominated by different mechanisms. The former is mainly caused by the combined effect of turbulence fluctuation, cavitation effect and aerodynamic force; while the latter is mostly

induced by the aerodynamic force. Obviously, it's more reasonable to develop combined breakup models which could consider both of the primary breakup models and the secondary breakup models. A summary of the combination studies is shown in Table 2-2.

Table 2-2 Combined breakup models

Studies	"Primary Breakup"	Secondary Breakup
O'Rourke, P.J. and A.A. Amsden [98]	Taylor Analogy Breakup	
Reitz, R.D. [59]	Wave	
Belardini, P., C. Bertoli, and M. Cameretti [102]	Wave	TAB
Beale, J.C. and Reitz [60]	Wave	KH-RT
Arcoumanis, C., M. Gavaises, and B. French [96]	Cavitation-induced model	TAB
Bianchi, G [103]	Cavitation and turbulence-induced model	TAB
Som, S. and S. Aggarwal [104]	KH, cavitation and turbulence-induced model	KH-RT

2.5 Summary

In this chapter, three aspects of the spray study including the fundamentals of spray structure and breakup regimes; the CFD methodology for spray simulation; and the application of the spray atomization and breakup models are reviewed. In the literature, the aerodynamically-induced breakup mechanism has been thoroughly investigated by many researchers. However, the effects of turbulence and cavitation phenomena on a spray atomization process still need to be further studied.

CHAPTER 3
RESEARCH METHODOLOGY

This chapter introduces the research methodologies used in the fuel spray study. The commonly used methodologies including the experimental approach and the numerical method are employed in this study. Experimental setups, such as the fuel injection system, the constant volume vessel, the image acquisition system and the Phase Doppler Particle Analyzer (PDPA) system; and numerical software, including the calculation code and post-processing program, are introduced in detail.

3.1 Experimental Approaches

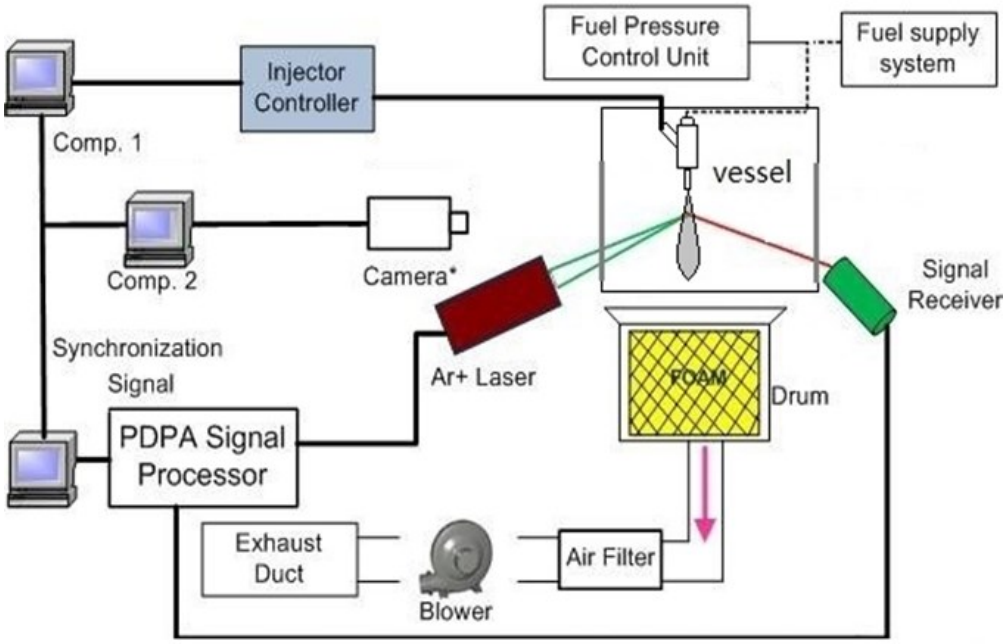

Figure 3-1 Schematic of the experimental setup

The schematic of the experimental setup is shown in Figure 3-1. In general, the experimental setup includes the fuel injection system, the pressure vessel, the image acquisition system, the PDPA system and the ventilation system. The details of each system will be separately introduced in the following sections.

3.1.1 Fuel Injection System

For both diesel and gasoline fuels, the fuel injection system can be divided into two sub-systems for each fuel: the fuel supply system and the injection control units.

Diesel Fuel Supply System

Diesel fuel is pressured by a customized common rail which is demonstrated in Figure 3-2. The fuel from the fuel tank is initially filtered by the rough filter and then pressured by the low pressure pump. The low pressure pump sucks the fuel and provides an initial fuel pressure for the inlet of the high pressure pump. This initial pressure is regulated by a regulator at 0.15 MPa. The high pressure fuel pump is driven by a 5.5 kW 3-phase alternating current (AC) motor and the speed of the motor is controlled by a 3-phase frequency inverter. The fuel can be pressured up to 200 MPa and then it flows into the common rail and is ready to be injected by the injector. The pressure of the fuel in the common rail can be monitored and regulated by the injection control units which will be introduced in the next section. The returning fuel from the injector and the high pressure pump is cooled down by a heat exchanger before returning back to the fuel tank. The coolant is automatically controlled by a solenoid valve according to the fuel temperature.

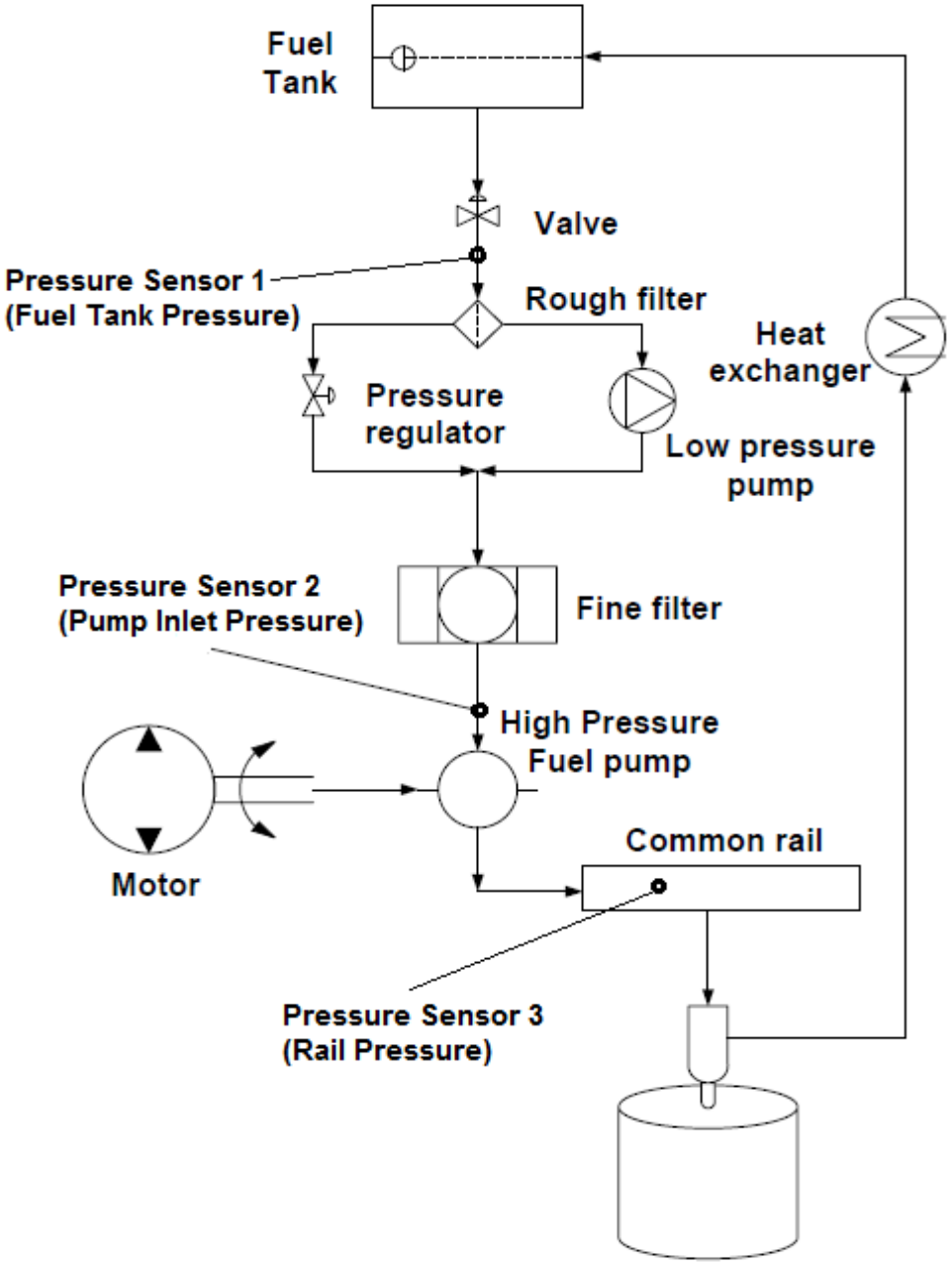

Figure 3-2 Schematic diagram of the diesel common rail

Diesel Fuel Injection Control Units

Figure 3-3 shows a photograph of the injection control units. The unit on the upper left is the common rail pressure control unit, which regulates the fuel pressure by using the feedback

Figure 3-3 Fuel injection control units (left) and injector driver (right)

signal from the pressure transducer on the common rail. The lower left unit is the trigger unit which can realise various customized injection timing signals to the injector driver. The right-hand photograph is the custom-made solenoid injector driver which receives the timing signal from the trigger unit and sends this signal to the injector.

Gasoline Fuel Supply System and Injection Control Unit

Figure 3-4 is a schematic diagram of the gasoline fuel supply system. The gasoline fuel in the accumulator can be pressured up to 200 bar by the compressed nitrogen gas which has a maximum pressure of 235 bar. The fuel pressure is controlled by the regulator of the gas bottle and can be accurate to 1 bar. The injector receives the injection signal from the ECU and drives the nozzle needle to open. The ECU from Jaguar Land Rover (JLR) is a customized injection control unit and is driven by the DAQ PCI 6023E card and the programmable LabVIEW software. With the help of the LabVIEW program, various injection timing and continuous pulse signals can be set. The maximum pulse frequency of the injection signals can be set up to 10 Hz, which is limited to the sensitivity of the injector; however, this is enough

for the spray experiments. Thus many experiments, like the PDPA measurement, can be accomplished in a more automated way.

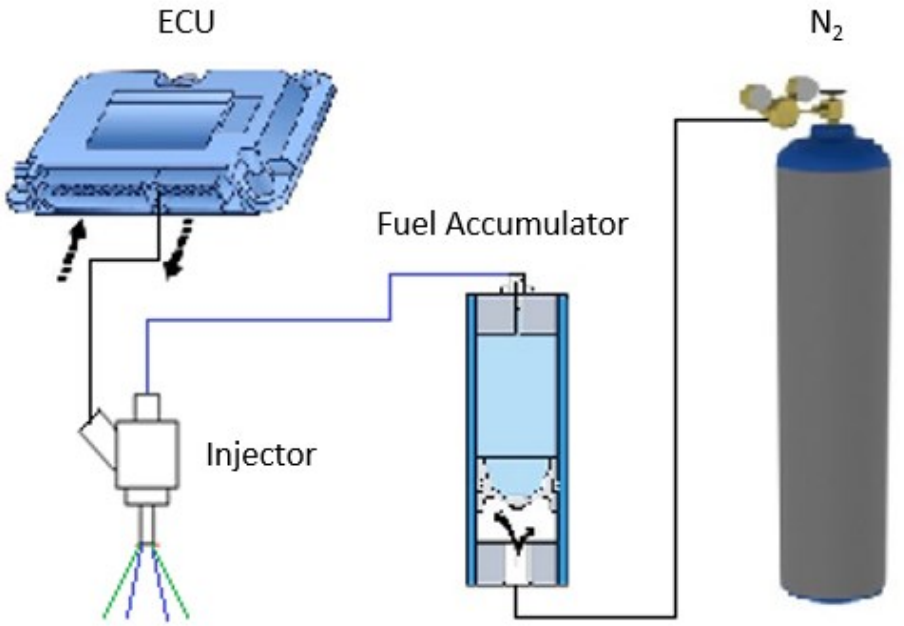

Figure 3-4 Schematic diagram of the gasoline fuel supply system

3.1.2 Pressure Vessel

In this study, two pressure vessels are used to provide various ambient conditions for the spray test. One vessel is a high pressure Constant Volume Vessel (CVV) which can withstand a maximum pressure of 110 bar. The high pressure CVV is mainly used for studies of the macroscopic spray characteristics of the diesel injector. The other is a low pressure CVV which can withstand a maximum pressure of 11 bar. The low pressure CVV has bigger observation windows and is mainly used for studies of the microscopic spray characteristics of the diesel injector and the gasoline injector.

High pressure CVV

An image of the high pressure CVV is shown in Figure 3-5. Figure 3-6 shows the schematic of the vessel design. Four windows are designed for this vessel, three small windows are located on the side and one big window is at the bottom. The size of visible glass on the three small side windows is 40 mm in diameter and the bottom glass is 68 mm in diameter. The optical glass is fixed on the window holders and sealed by heat resistant silicone. The vessel has an 86 mm × 100 mm cylindrical chamber, which aimes to simulate the real cylinder of the diesel engine. Two thermocouples are assembled on the vessel to monitor the chamber temperature.

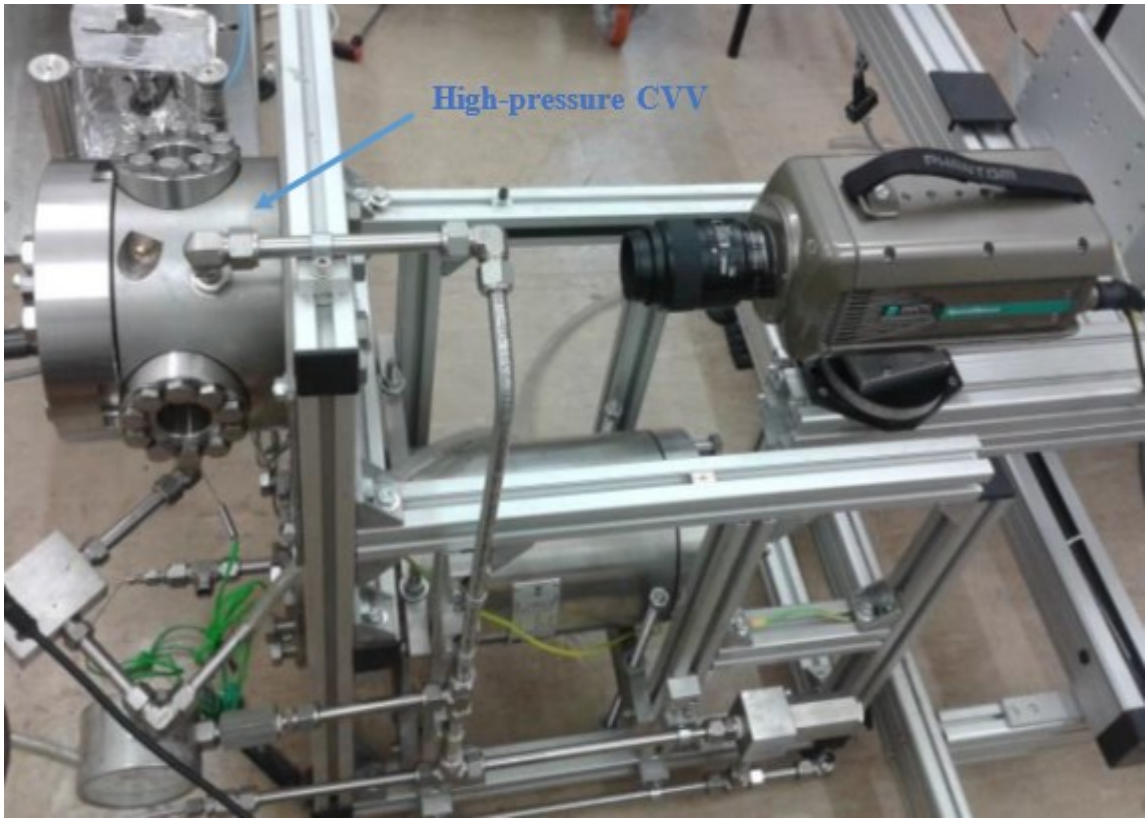

Figure 3-5 Image of the high pressure CVV

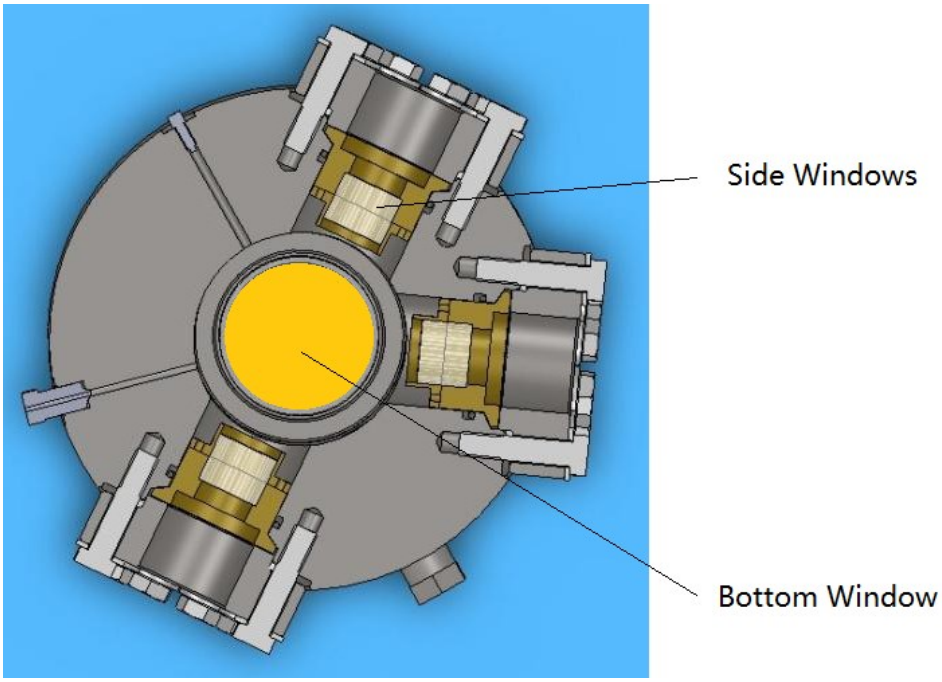

Figure 3-6 Schematic of the high pressure CVV

Various optical diagnostic approaches can be achieved with different combinations of the four windows. For example, with the two in line side windows, the shadowgraph, backlight photography and the schlieren test can be carried out; with the two side windows having an angle of 110 degrees, the PDPA measurement can be utilized to obtain the droplet information of the fuel spray; with the big bottom window and the side windows, Particle Imaging Velocimetry (PIV), Laser-induced Fluorescence (LIF), Mie scattering and high-speed photography can be carried out to study the macroscopic characteristics of the spray.

Depending on the different applications of the vessel, there are three different mounting orientations of the injector, as is shown in Figure 3-7. Figure 3-7a shows an orientation arrangement which enables one to study the macroscopic characteristics of a single spray jet of the multi-hole injector. This design is for the commonly used diesel injector which has a spray angle of 153 degrees and the jet of interest can be at the horizontal direction.

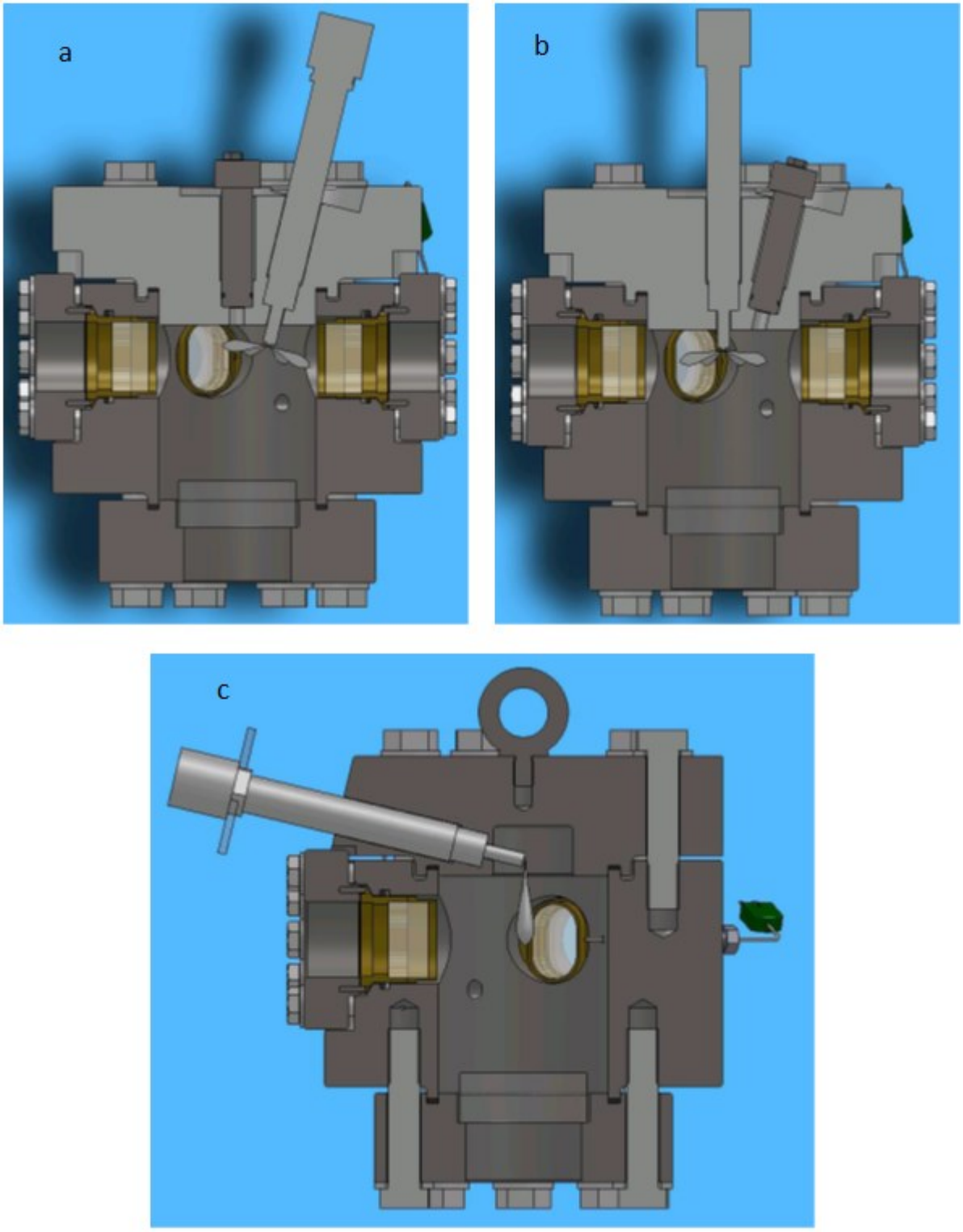

Figure 3-7 Three different mounting orientations of the injector

Figure 3-7b is the vertical mounting and is the common orientation in a diesel engine. In this way, the injector is vertically mounted in the vessel so that the characteristics of the full spray of the multi-hole injector can be obtained from the bottom window. Figure 3-7c indicates the layout of the injector's orientation for the PDPA measurement. In this arrangement, the jet of interest is vertically downwards and the laser passes through the side window. In this study, the mounting methods in Figure 3-7a and Figure 3-7c are used for the high-speed photography and the PDPA measurement, respectively. Figure 3-8 also shows a schematic of the orientation of the vessel for the high-speed photography test.

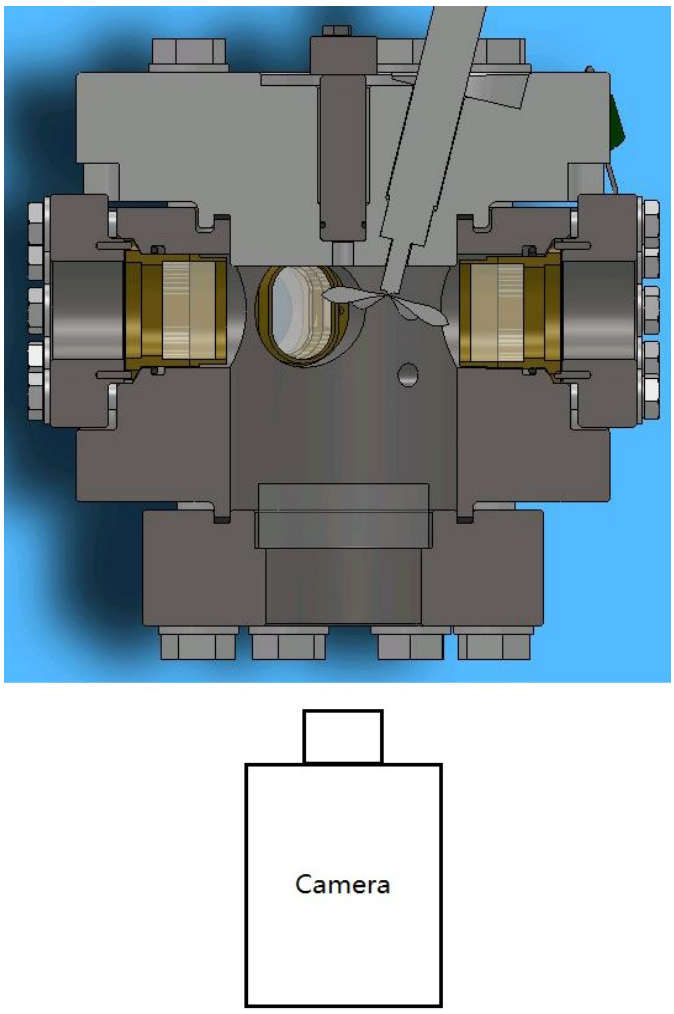

Figure 3-8 Schematic of the high-speed photography setup

Low-pressure CVV

Figure 3-9 shows an image of the low pressure CVV. Compared to the high pressure vessel, this cubic vessel is relatively simple. There are four similar windows on the front, rear, left, and right faces. Each window has a visible diameter of 100 mm. The injector is vertically mounted on the top face and its spray can be captured by the high-speed camera located at the left side of the vessel. The pressure gauge is connected on the vessel to monitor the ambient pressure inside. The intake and exhaust pipes are connected to the bottom face. This vessel is mainly used for studies of the gasoline spray characteristics due to its big visible window and its low rated pressure.

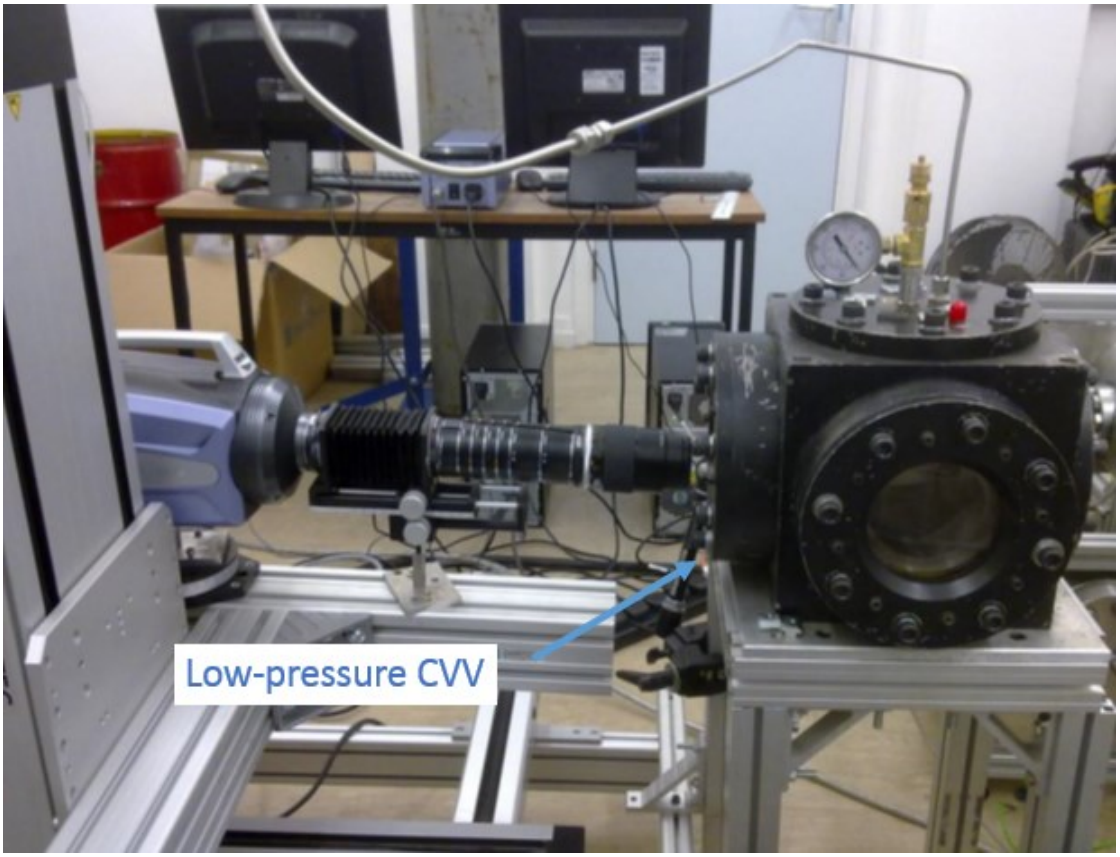

Figure 3-9 Image of the low pressure CVV

3.1.3 Image Acquisition System

High-speed Cameras

Two cameras were available for this study, as is shown in Figure 3-10. The Phantom V12 is a normal high-speed camera, which has flexibility in resolution and speed. This camera benefits from its larger resolution and has the ability to capture the whole spray field; thus this camera is usually used to study the macroscopic characteristics of the fuel spray. The maximum camera speed changes accordingly with the changes of different resolutions of the image. The commonly used configurations of this camera in this study were set at a resolution

Figure 3-10 Image of the high-speed cameras: Phantom V12 (left) and Shimadzu HPV-2 (right)

Table 3-1 Specifications of the Phantom V12 and Shimadzu HPV-2 cameras

Camera	Phantom V12	Shimadzu HPV-2
Imaging Sensor	CCD	CCD
Resolution (pixel)	Up to 1280×720	312×260
Speed (fps)	Up to 1,500,000	Up to 1,000,000
Stored Frames	16 GB	100
Colour Expression	Monochrome 8bit and 12 bit	Monochrome, 10 bit

of 600 pixels × 608 pixels and a speed of 18003 fps. The other camera, the Shimadzu HPV-2 is an ultra-high-speed camera with a maximum speed of up to 1,000,000 fps; while the resolution is constant at 312 pixels × 260 pixels. This camera can capture the initial stage of the fuel spray and provide a detailed observation of the near field spray characteristics. The specifications of these two cameras are listed in Table 3-1.

Image Acquisition Synchronization

In order to synchronize the fuel injection and the camera, a National Instrument (NI) DAQ PCI 6023 card was used in this study. The NI card is controlled by the self-writing program in the LabVIEW platform. The interface of the program is shown in Figure 3-11.

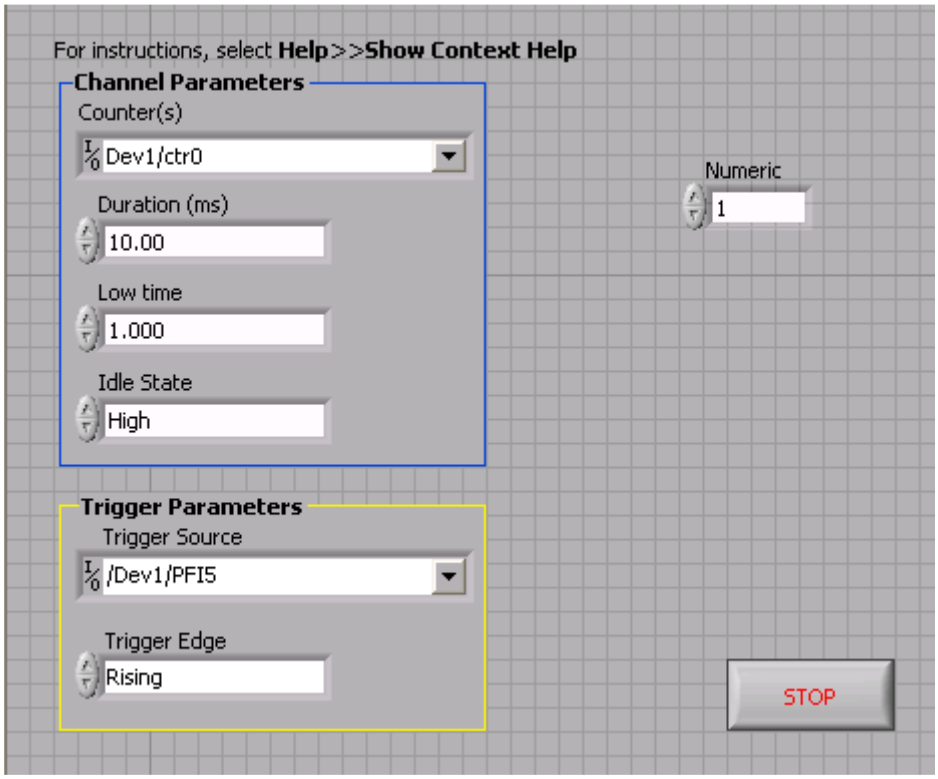

Figure 3-11 LabVIEW interface of the signal synchronization

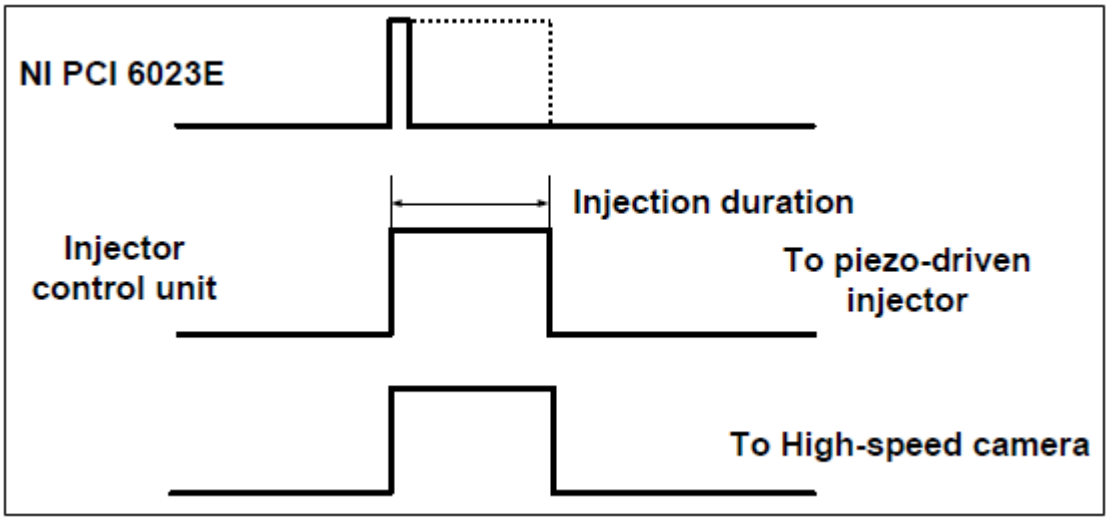

Figure 3-12 The sequence of signals for image acquisition synchronization

Figure 3-12 presents the sequence of signals for image acquisition synchronization. After receiving the command from the LabVIEW program, the NI card will generate a pulse signal and send the signal to the injection control unit (diesel) / ECU (gasoline); and then the injection control unit / ECU will generate the desired pulse driving signal and send it to the injector. In the case of the gasoline spray, the injection duration is controlled from the LabVIEW program directly; while for the diesel spray, the injection duration is controlled by the injection control unit.

Image Post-processing

After the capturing of the spray images, post-processing is necessary and it will provide a quantitative result from these images. One can process these images manually if the number of the images is not too many, however, usually the number of spray images can be up to several thousands. Therefore a customized program in MATLAB is developed to deal with these

images. A flow chart of the MATLAB program is shown in Figure 3-13. After the loading of the data, the image is firstly enhanced to make it easier to recognize its pixels and then the background noise is subtracted and only the spray pixels are left. Then the image is converted into a binary image so that the pixels occupied by the spray can be counted. Finally, the amount of pixels can be correlated with length and angle. With the help of this program, the spray characteristics such as spray penetration, spray angle and tip velocity can be calculated automatically and saved to the spreadsheet.

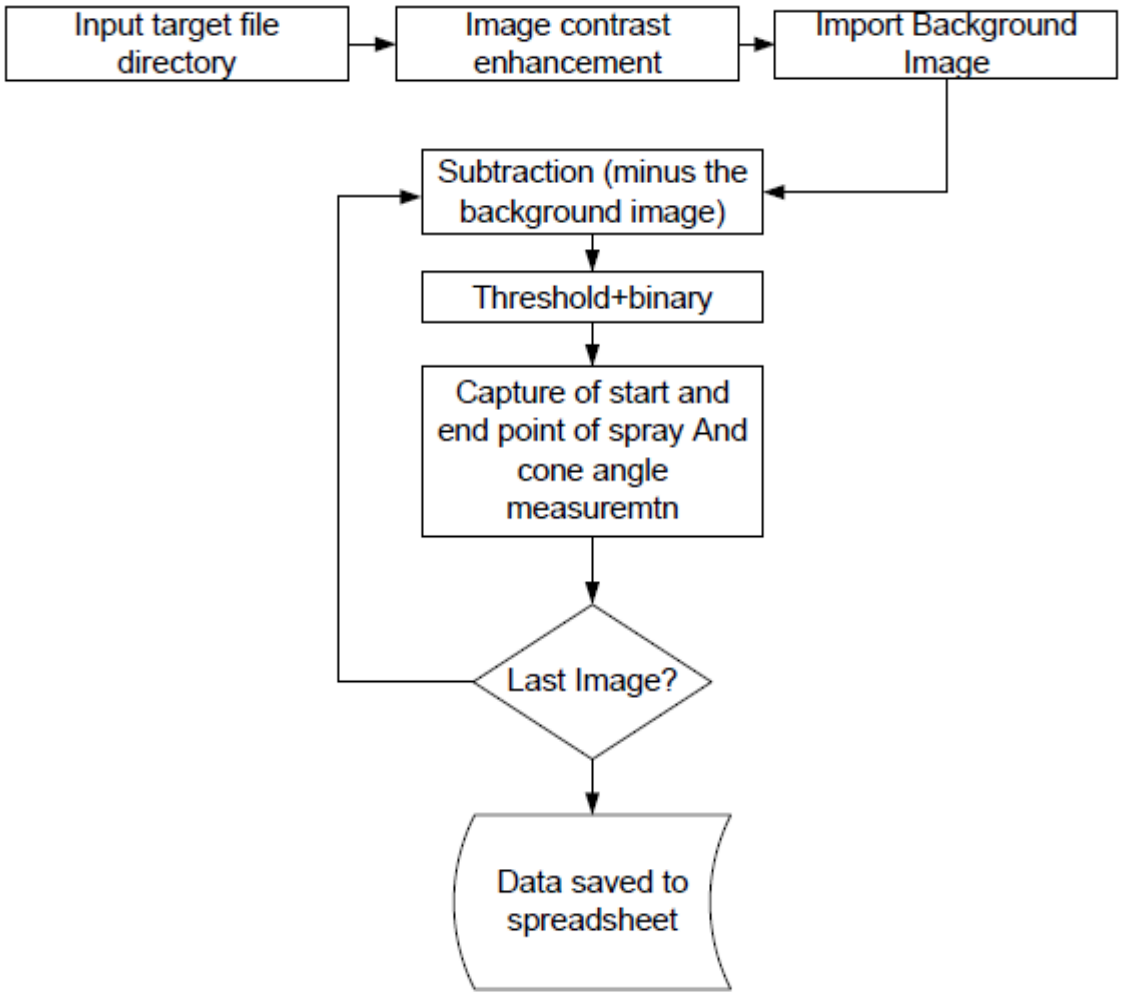

Figure 3-13 Flow chart of the image post-processing

3.1.4 PDPA System

The PDPA system is an accurate, reliable and non-intrusive technique to measure the droplet size and velocity of the fuel spray simultaneously. The characteristics of moving droplets are obtained by utilizing the laser Doppler effect. The image and schematic of the PDPA instrument is shown in Figure 3-14. It consists of laser-based transmitting optics (argon ion laser), photon detectors and signal processers. As an example of the one-dimensional PDPA system: when a moving droplet travels through the measurement volume which is defined by the intersection of two focused laser beams, the laser light will be scattered and its properties will be changed accordingly. The photon detectors will capture the signal which is associated with the temporal and spatial information of the droplet.

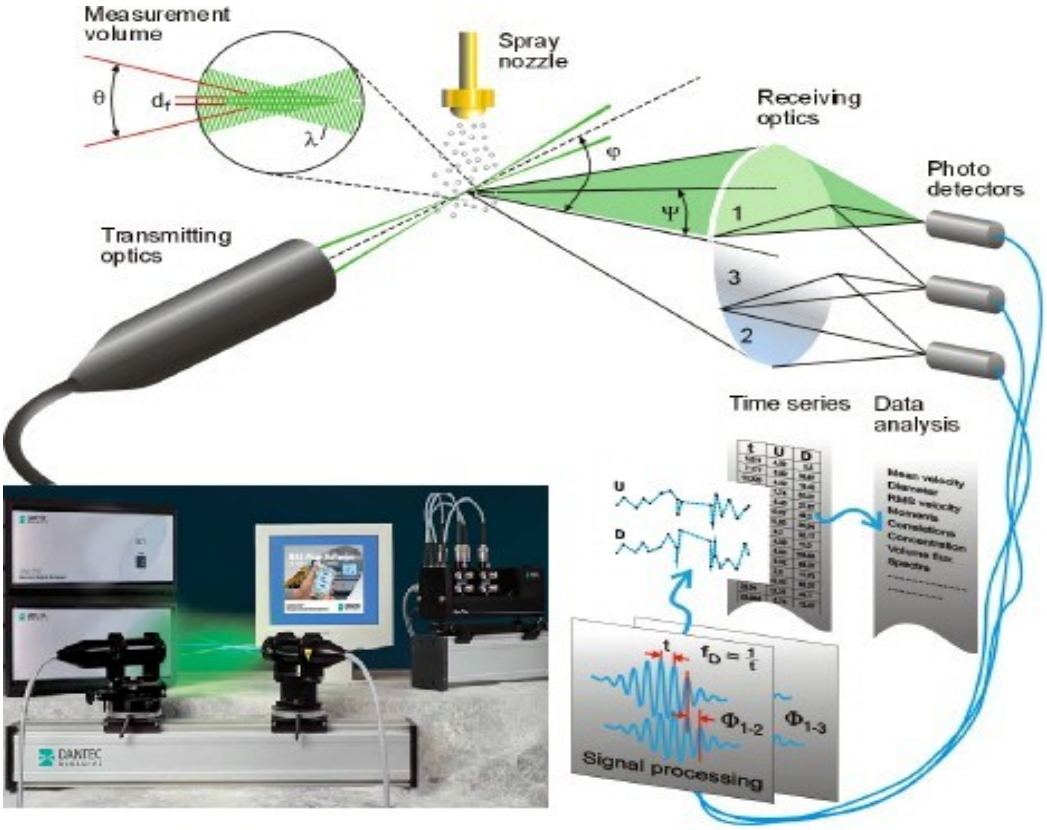

Figure 3-14 Image and schematic of the PDPA instrument [37]

Laser Doppler Velocimetry (LDV)

In the PDPA system, the droplet velocity is measured by the LDV technique. The measurement volume mentioned above is an interference fringe pattern formed by the interaction of two coherent, collimated laser beams. As is shown in Figure 3-15, the formation of the fringe pattern can be illustrated by two "beams" of parallel lines that intersect. At the position where the beams intersect, the wave fronts interact with each other constructively or destructively and form a pattern of horizontal lines. When a moving droplet passes the fringe pattern, it alternately reflects the light and does not reflect light (as it passes through the fringes). A signal detector then picks up these minute flashes / intensity signal of the scattered light.

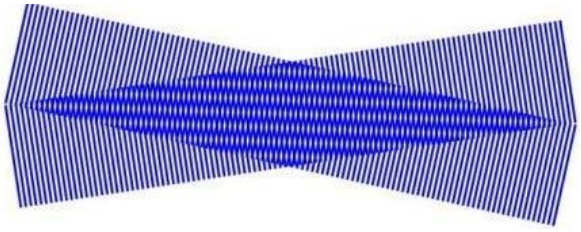

Figure 3-15 Schematic of the formation of the interference fringe pattern

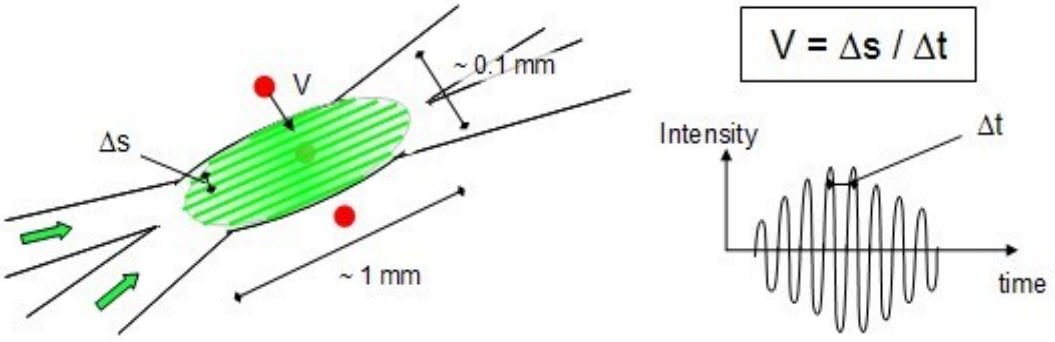

Figure 3-16 Schematic of the principle of the LDV

Once the frequency of the intensity signal of the scattered light is obtained, the droplet velocity v then can be calculated by:

$$v = \frac{\Delta s}{\Delta t} = \Delta s \times \Delta f \tag{3-1}$$

where Δs is the distance between the fringe; Δt is the flash pulse width and Δf is the frequency of the intensity signal.

Phase Doppler Anemometry (PDA)

PDA is an important droplet size measurement technique in the PDPA system. Figure 3-17 shows the schematic of the phenomenon of light scattering on a droplet. When the laser light illuminates the surface of the droplet, part of the light will be reflected from the surface (in the B direction); and another part of the light will be transmitted and refracted in both forward (in the A direction) and backward directions after one internal reflection. The reflected light inside the droplet will again experience the second order refraction (in the C direction). Depending on the purpose of employment, the position (scattering angle) of the receiver must therefore be carefully selected to ensure that one light scattering mode is dominant. For example, the commonly used scattering angle ranges are listed in Table 3-2 below.

Table 3-2 Commonly used scattering angle ranges

A	30° - 70°	Refraction
B	80° - 110°	Reflection
C	135° - 150°	Second order refraction

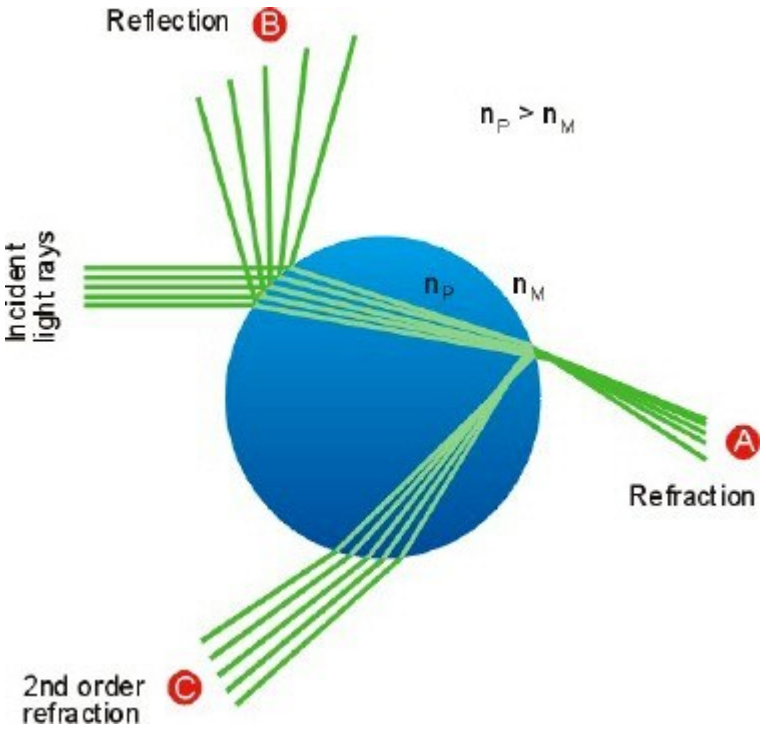

Figure 3-17 Schematic of the phenomenon of light scattering [37]

In this study, the scattering angle is set at 70°, which is in the direction A in Figure 3-17 above. Figure 3-18 shows the signal received from the scattered light and the relationship between the phases difference from the intensity signals. For example, in order to obtain the droplet size of D_1, detector 1 and detector 2 are located at different angles around 110°. The signals received by detector 1 and detector 2 are shown on the right of Figure 3-18. The phase difference between signal 1 and signal 2, due to the different optical paths inside the droplet, is proportional to the droplet diameter. Thus the droplet size can be calculated in this way.

However, the aspect of the 2π ambiguity cannot be ignored in this method. For example, for the smaller droplets D_1 and D_2, there is no problem since the phase difference is

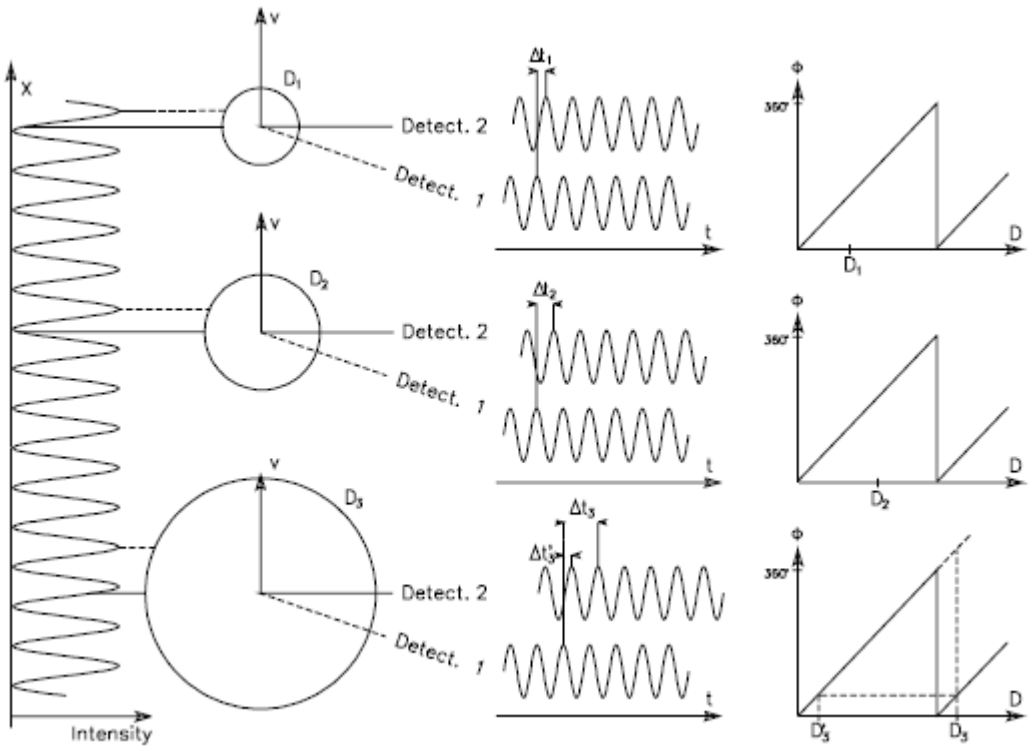

Figure 3-18 The relationship between the phase difference and the droplet size

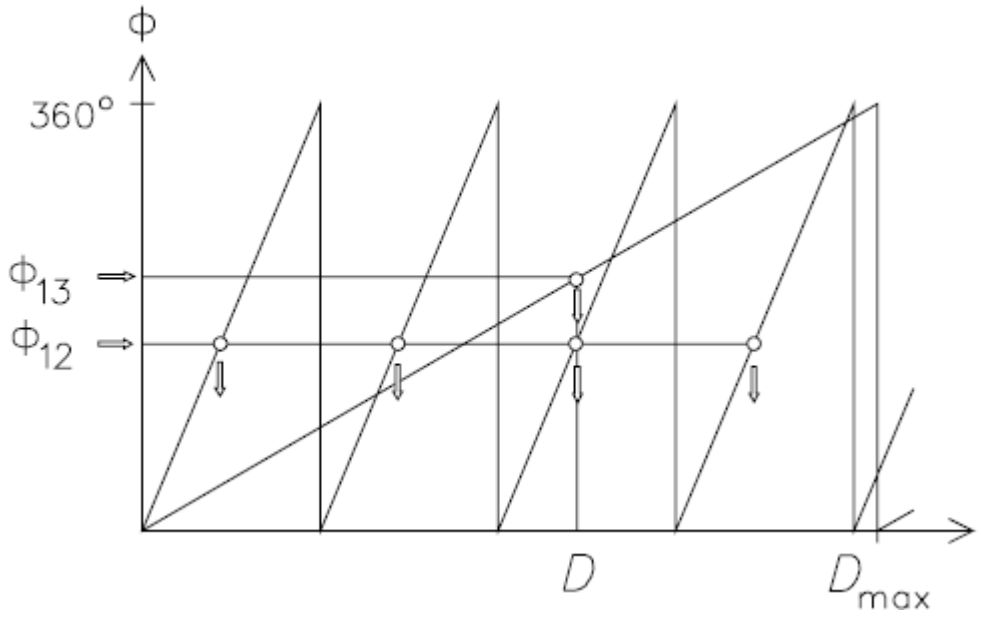

Figure 3-19 The solution of the 2π ambiguity

within the range of 2π. However the situation begins to change when the droplet is bigger. For the droplet D_3, as is shown in Figure 3-18, the phase difference is beyond 2π; it is difficult to tell which one is the true value between D_3 and D_3'. To solve the problem caused by the 2π ambiguity, a third detector is added to the system. Figure 3-19 depicts the principle of the solution. With the help of the third detector, an additional phase difference Φ13 is used to recognize the true value; Φ13 indicates a larger droplet size range, but with a lower resolution; and it can be used to determine in which cycle is the signal phase difference. While Φ12 has a higher resolution, but with a lower size range, it can tell the true value of the droplet size. Thus, with the help of the third detector, the test range can be extended while the resolution is still at a higher level.

LDV and PDA work simultaneously in the PDPA system and the simultaneous measurement of both size and velocity allows correlations to be made between these two quantities.

3.1.5 Ventilation System

The ventilation system, as shown previously in the lower right corner in Figure 3-1, is the last system of the whole experimental setup. It consists of an anti-fire foam drum, an air filter, a blower and an exhaust duct which is designed and assembled to absorb the fuel vapour and droplets. The anti-fire foam is not only used for the precaution of fire, but also used for the stabilization of the inhaled airflow; thus the influence of the ventilation flow on the spray can be ignored. The air filter is employed to filter the fuel in the exhaust gas. With the help of the ventilation system, the spray experiment can be conducted continuously in the lab.

3.2 Numerical Methods

Numerical CFD studies of the fuel spray technology can be an effective means to study and predict spray characteristics such as penetration, droplet size and droplet velocity; and as a consequence, to drastically reduce experimental work during the engine development process. For this reason, an accurate numerical simulation of the spray evolution process is of great importance. In this study, CFD simulations were carried out with the KIVA calculation code and the EnSight post-processing program. The details of the two programs will be introduced briefly in the following sections.

3.2.1 KIVA Calculation Code

KIVA Code

During the past 20 years, KIVA has been a widely used CFD code in the numerical modelling of the flow, mixture formation, spray atomization, combustion and emissions of the internal combustion engine [72, 105, 106]. It is an 'Arbitrary Lagrangian Eulerian (ALE)' based CFD code developed by the Los Alamos National Laboratory. In order to keep up with the rapid development of the internal combustion engine, KIVA has undergone great improvement and enhancement.

The first version of KIVA, initially released in 1985, aimed to study the hydrogen-fluorine chemical system in the design of nuclear weapons. In 1989, the application of KIVA-2 was extended to the studies of the internal combustion engine with the supplementation of the in-cylinder flow model. The valve model was added into the KIVA-3V version in 1997. In 1999,

the fuel wall film model was added into the KIVA-3V-Release2 version. More fuel spray breakup models were then supplemented into the KIVA-3V2 ERC version by the Engine Research Center (ERC) at the University of Wisconsin-Madison in 2001 [13].

In this study, the KIVA-3V2 ERC version was employed. Figure 3-20 shows the images of the interface of the calculation program. The upper left image is an example of the engine cylinder grid, while the upper right image is the main interface of the KIVA solver. The two images below are the examples of the visualization results. A brief introduction of these programs will be given in the following paragraphs.

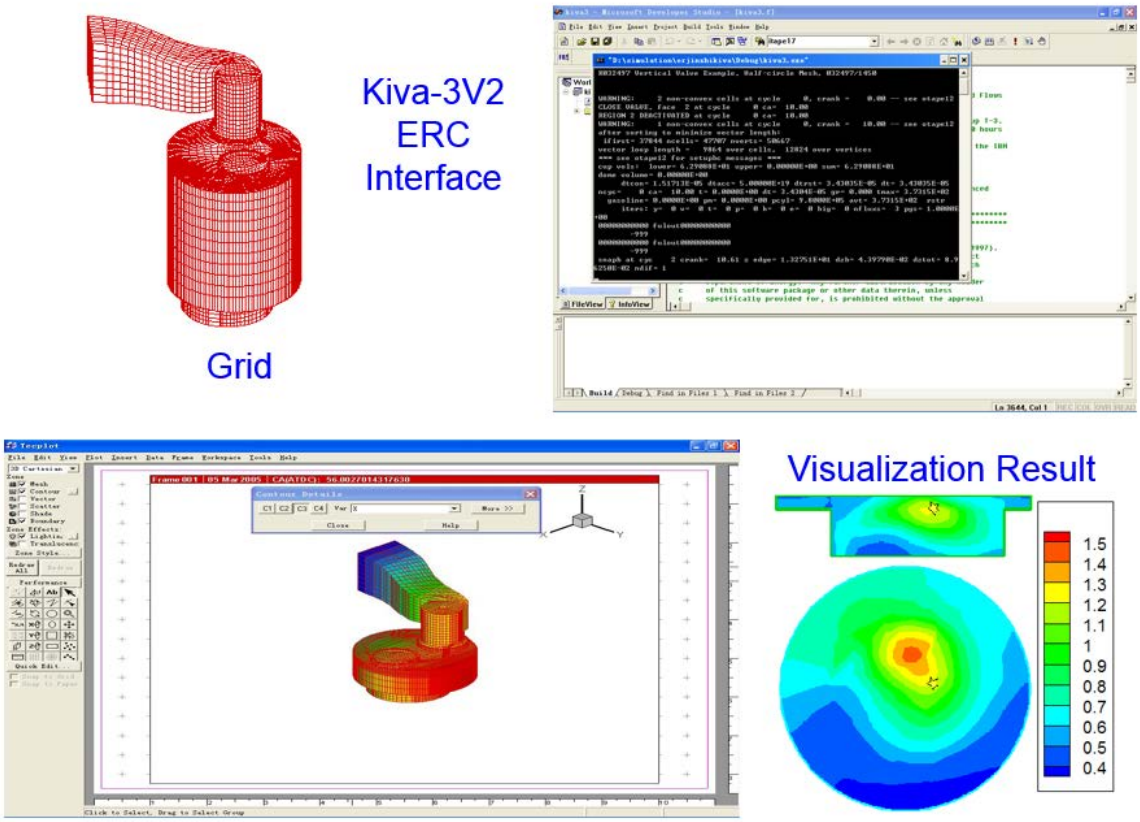

Figure 3-20 Images of the interface of the KIVA-3V2 ERC calculation program

The Structure of KIVA-3V2 ERC

Figure 3-21 shows a flow chart the calculation process of KIVA-3V2 ERC. It consists of three sub-programs: the pre-processing program, the main solver and the post-processing program. All of the files starting with character ‘i’ are the input files while the files starting with character ‘o’ are the output files for each sub-program. The gray blocks are the executable files in each sub-program.

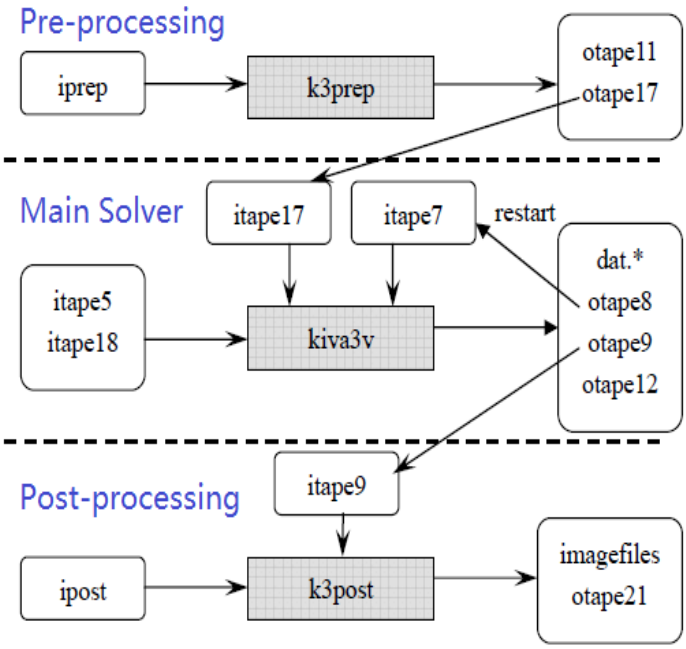

Figure 3-21 Flow chart of the calculation process of KIVA-3V2 ERC

The first gray block ‘k3prep’ in the pre-processing program is the grid generator which generates the desired mesh grid according to the input file ‘iprep’. The output file ‘otape17’ will be the grid file for the main solver after being renamed ‘itape17’. The file ‘otape11’ is a log file. An example of the pre-processing program is shown in Figure 3-22.

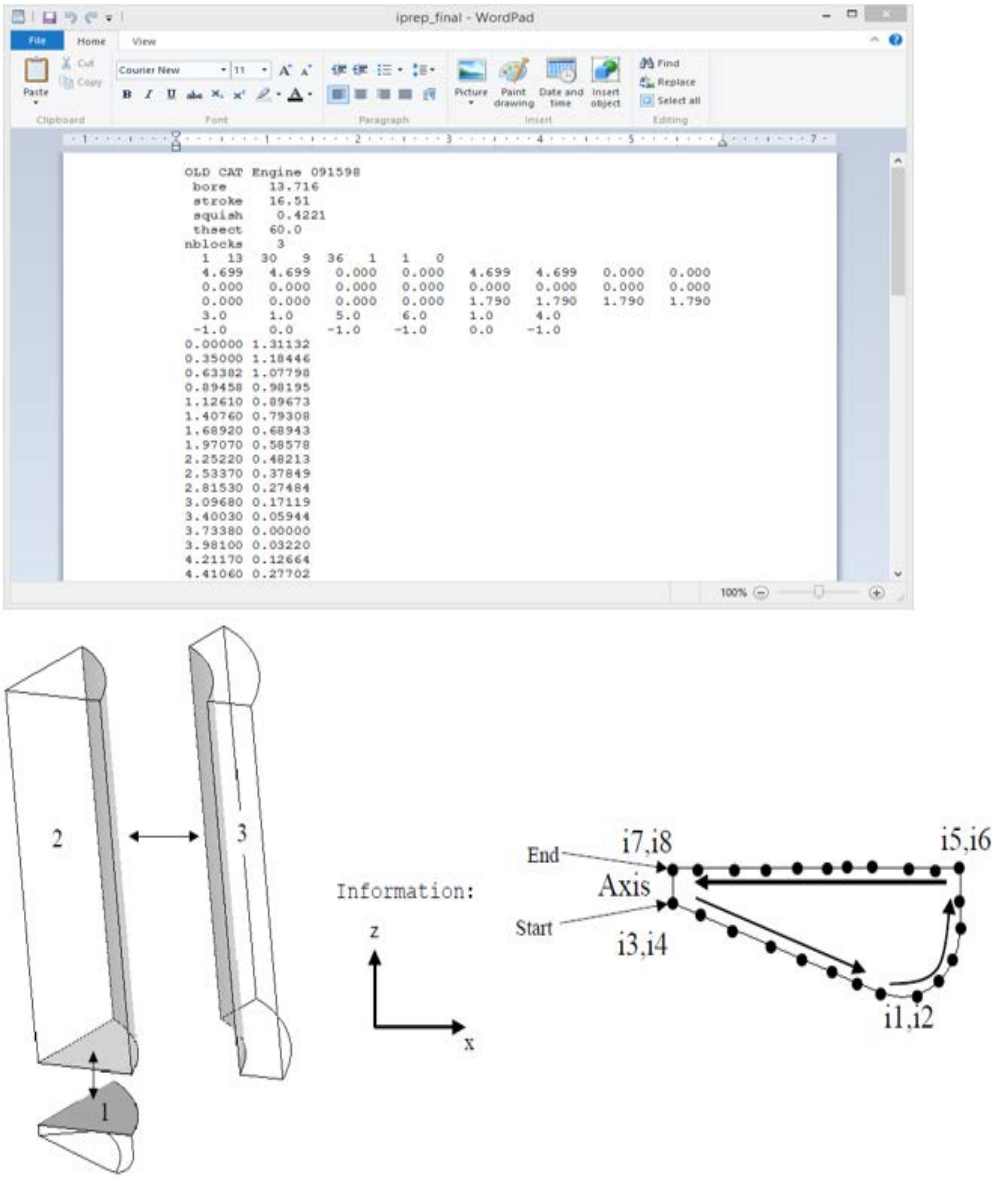

Figure 3-22 An example of the pre-processing program

The second gray block ‘KIVA3v’ is the main solver which reads the input parameters and boundary conditions in ‘itape5’and ‘itape18’ and the grid information in ‘itape17’; and then it calculates the task and saves the visualization result and output in the ‘otape9’ and ‘.dat’ file, respectively. The restart information is saved in ‘otape8’ (renamed to ‘itape7’), which is used to restart the calculation if any break occurs. The file ‘otape12’ is a log file.

According to the requests in the 'ipost' file, the third gray block 'k3post', the post-processing sub-program, can transfer the visualization result file 'itape9' (renamed from 'otape9') into readable documents in a third party post-processing program like EnSight [107] which will be introduced in section 3.2.2.

Governing Equations of KIVA-3V2 ERC

The simulation of the internal combustion engine is multi-dimensional gas-liquid two-phase flow modelling; including gas flow, spray liquid flow and chemical reactions. Taking all physical and chemical effects in internal combustion engines into account, a set of conservation equations for the gas phase describing spray and combustion processes in KIVA can be summarized as follows.

For each chemical species m in a multi-component gas mixture fluid, mass conservation can be expressed by its mass density ρ_m as:

$$\frac{\partial \rho_m}{\partial t} + \nabla \cdot \left(\rho_m \hat{u} \right) = \nabla \cdot \left[\rho D \left(\frac{\rho_m}{\rho} \right) \right] + \dot{\rho}_{m} \quad \dot{\rho}_{m} \tag{3-2}$$

where ρ_m is the mass density of species m; ρ is the total mass density; t is the time; $\hat{u}$ is the fluid velocity vector; D is the turbulent diffusion coefficient; $\dot{\rho}_{m}$ and $\dot{\rho}_{m}$ are source terms due to chemical reaction and spray evaporation, respectively; ∇ is the vector operator given by:

$$\nabla = \frac{\partial}{\partial x}\hat{i} + \frac{\partial}{\partial y}\hat{j} + \frac{\partial}{\partial z}\hat{k} \tag{3-3}$$

In Equation 3-2, the first term on the right hand side is due to mass diffusion, the second and third terms are the source terms due to combustion and spray effects respectively.

In the presence of a liquid spray there can be momentum transfer between the two phases; such that the three gas phase momentum conservation or Navier-Stokes equations become:

$$\frac{\partial \rho \hat{u}}{\partial t} + \nabla \cdot \left(\rho \hat{u} \hat{u} \right) = -\nabla p - \nabla \left(\frac{2}{3} \rho \kappa \right) + \nabla \cdot \overline{\overline{\sigma}} + F^s + \rho \cdot \hat{g} \tag{3-4}$$

where p is the fluid pressure; κ is the turbulent kinetic energy; $\overline{\overline{\sigma}}$ is the (turbulent) viscous stress tensor in Newtonian form; F^s is the rate of momentum gain per unit volume due to the spray;and $\hat{g}$ is the specific body force vector.

The energy conservation equation is:

$$\frac{\partial \rho I}{\partial t} + \nabla \cdot \left(\rho \hat{u} I \right) = -p \nabla \cdot \hat{u} - \nabla \cdot \hat{J} + \rho \varepsilon + \dot{\zeta} \quad \dot{\zeta} \tag{3-5}$$

where I is the specific internal energy (exclusive of chemical energy); $\hat{J}$ is the heat flux vector including turbulent heat conduction and enthalpy diffusion; ε is the dissipation rate of turbulent kinetic energy; $\dot{\zeta}$ and $\dot{\zeta}$ are the source terms due to chemical heat release and spray interaction, respectively.

In terms of the liquid phase, KIVA-3V2 ERC employs the Discrete Droplet Model (DDM) to describe the liquid, which was introduced in Chapter 2. Based on the Monte-Carlo method,

droplets with the same properties can be seen as a parcel and then all the droplets in the flow can be represented by a number of parcels. The DDM approach [92] then deals with these representative parcels and traces these parcels in a Lagrangian manner.

3.2.2 EnSight Post-processing Program

KIVA is an effective CFD solver; however, its post-processing program relies on third party visualization software like EnSight, which was developed by Computational Engineering International (CEI) in 1994. EnSight is a powerful software package for the post-processing, visualization and animation of complex datasets [107]; it has an easy-to-use interface for KIVA.

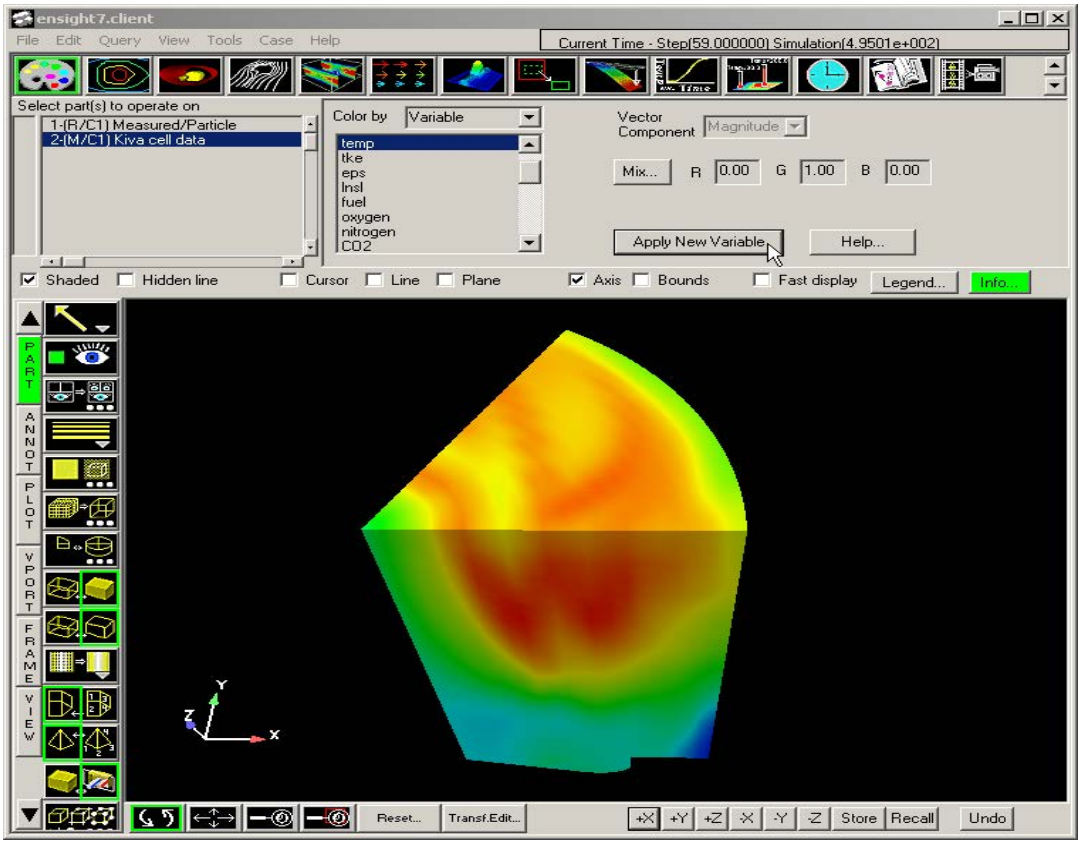

Figure 3-23 Image of the EnSight user interface

Figure 3-23 shows an example image of the EnSight user interface. It allows one to obtain detailed observations of the CFD result of the spray. For example, for the liquid phase the fuel droplet can be zoomed in and out and highlighted and its concentration distribution can be described by various colours; for the gas phase, depending on its concentration distribution, the fuel vapour can also be represented by different colours. The details of the functions of this software can be found in [107]. With the help of the EnSight post-processing program, the morphography and the macroscopic characteristics of the spray can be studied and validated with the experiment data.

3.3 Summary

In this chapter, the research methodologies used in the fuel spray study have been introduced in detail. Two commonly used methodologies which are known as the experimental approach and the numerical method are employed in this study. Experimental approaches such as the experimental setup, including the fuel injection system, the constant volume vessel, the image acquisition system and the Phase Doppler Particle Analyzer (PDPA) system have been introduced and studied. At the same time, numerical methods including the KIVA calculation code and the EnSight post-processing program are briefly reviewed. This chapter is of great importance and provides fundamental knowledge for the following studies.

CHAPTER 4
SPRAY CHARACTERISTICS OF GDI ENGINES

This chapter studies the spray characteristics of Gasoline Direct Injection (GDI) engines. The influence of injection pressure, injection duration and different injector nozzle machining methods on the spray characteristics will be experimentally investigated.

4.1 Introduction

With the increasing demand for energy conservation and environmental protection, further improvement of fuel efficiency and emission reductions in internal combustion engines are urgently required due to the limited energy reserves, the rising price of crude oil and climate change. The GDI engine plays an important role in this area and has undergone a rapid development during the last decade. It can offer many advantages compared to a port fuel injection engine: improved fuel economy, more precise air/fuel ratio control, enhanced transient response and startability, reduced hydrocarbon (HC) and soot emissions in cold start and transient cycles etc. [22, 108-112].

The first generation of production GDI engines included wall-guided and air-guided stratified charge combustion systems as shown in Figure 4-1 [113]. In the wall-guided system, the mixture was prepared with the guidance of the bowl shape geometry piston top and the assistance of in-cylinder swirl and tumble air flow. The issue with this system is that the

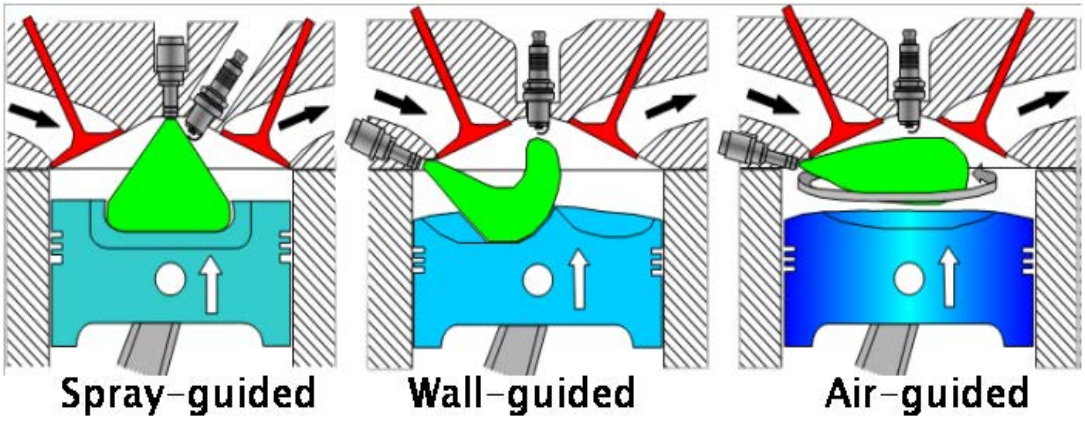

Figure 4-1 The second generation spray-guided and the first generation wall/air-guided stratified charge system [113]

unavoidable wall wetting effect by the fuel spray impingement leads to relatively high soot and HC; and the bowl shape geometry with extra surface area results in extra heat transfer losses and then decreases the power output and fuel economy [114, 115]. In contrast, an air-guided system was designed to reduce the HC and soot emissions by avoiding direct contact between the fuel and the walls of the combustion chamber; which utilised the charge movement to mix the fuel and the intake air. However, the specific swirl or tumble flow movement required to operate this system results in reducing volumetric efficiency and then affects the total performance [116, 117].

In the second generation GDI engines, which are known as spray-guided stratified charge combustion systems [118], the charge movement and the piston geometry are not as important for the mixture formation as in the first generation engines. This offers many benefits compared to the wall/air-guided systems: wall wetting is reduced to the acceptable value which radically reduces the emissions; less heat transfer losses can improve the power output and better atomisation of the fuel spray will provide improved fuel efficiency [19, 119-121].

The design and optimisation of a modern spray-guided GDI engine requires a thorough understanding of the fuel spray characteristics and atomisation process. Spray penetration, spray angle, droplet size and velocity become more crucial since they play extremely important roles in the mixture formation and combustion processes of GDI engines [115]. In this study, the effects of injection pressure, injection duration and different injector nozzle machining methods on the spray characteristics will be investigated. Two types of injectors with the same geometrics but a different manufacturing process will be tested. Both of the two 6-hole injectors are in AJ126 model. The one called LD injector has laser drilled nozzles, while the other titled EDM injector has electric discharge machining holes.

4.2 Experimental Conditions

The experiment was carried out with the experimental system presented in Chapter 3. The low pressure constant volume vessel was used in this study. The specifications of the LD injector and the EDM injector studied are listed in Table 4-1. The injection pressure was controlled by the regulator of the gas bottle and the injection duration was controlled by the LabVIEW program, which sends the injection signal to the ECU. Both of the backlit and PDPA tests were conducted under atmospheric conditions with various injection pressures and durations. The spray image was captured by an ultra high-speed camera with the speed of 18003 frames per second and pixels of 608*600. The main technique specification of the PDPA system is listed in Table 4-2. The test matrix and the schematic test positions for this study are shown in Table 4-3 and Figure 4-2.

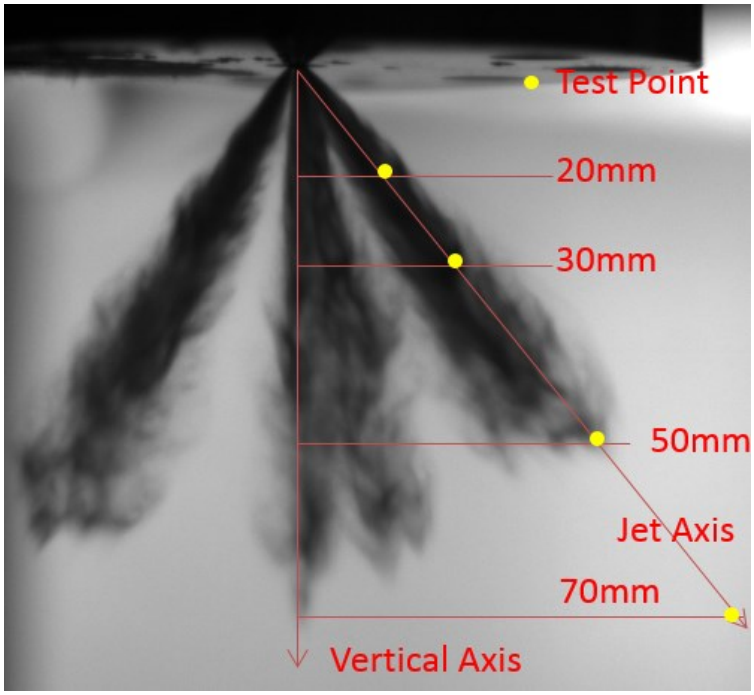

Figure 4-2 Schematic of PDPA test points

Table 4-1 Injector specifications

Injector name	LD injector	EDM injector
Hole manufacturing method	Laser-drilling	Electric discharge machining
Number of holes	6	
Hole diameter	180 μm	
Length to diameter ratio	1.1	
Flow 30s@100bar	17.5 cc/s	

Table 4-2 Specification of PDPA system

Laser energy	1.2 W	Scattering mode	Refraction
Wavelength	514.5/488 nm	Scattering angle	70.0 deg
Beam diameter	2.2 mm	Spherical validation band	15%
Laser expander ratio	1.95	Spatial filter	Slit: 250 μm
Frequency shift	40.00 MHz	Velocity range	-50 m/s ~ 195.10 m/s
Receiver expander	1	Max. particle diameter	79.19 μm

Table 4-3 Test matrix for backlit photography and PDPA test

Injection pressure	50 bar	100 bar	150 bar	200 bar
Ambient pressure	1 bar			
Injection duration	0.3/1/2 ms			
Vertical positions for PDPA test	20/30/50/70 mm			

4.3 Results and Discussion

4.3.1 Spray Morphology Evolution

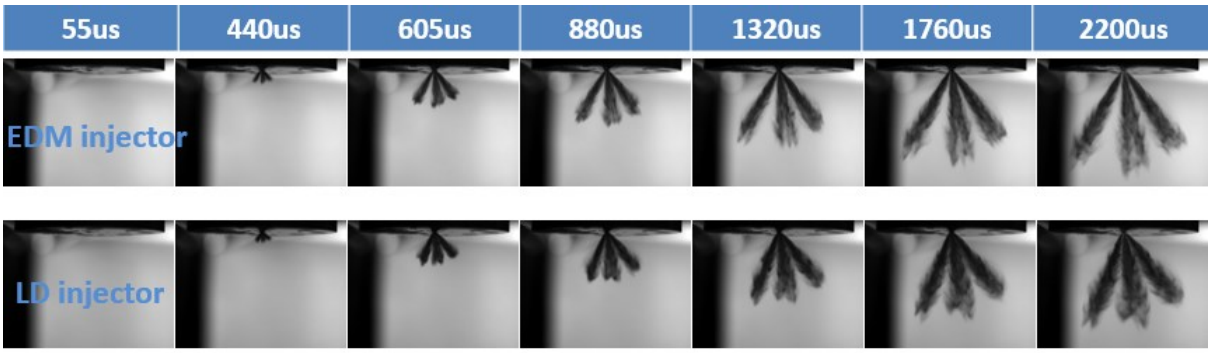

Figure 4-3 Spray evolution at injection pressure of 150 bar and 1 ms duration (Scale: 1:8, *mm*)

Figure 4-3 shows the spray development along with the time ASOI under 150 bar injection pressure and 1 ms injection duration. As is shown in the images, the fuel comes out of the injector at 440 μs ASOI for both injectors. A shorter penetration length and larger spray jet angle for the LD injector can be found at all times. Obviously, the larger spray jet angle of the LD injector will enhance the mixture formation due to the greater interaction area between the fuel spray droplet and the surrounding air. While under the same injection pressure, the LD injector has a shorter penetration length compared to the EDM injector. This will reduce the spray impingement in the cylinder and allow utilizing of higher injection pressures in the engine.

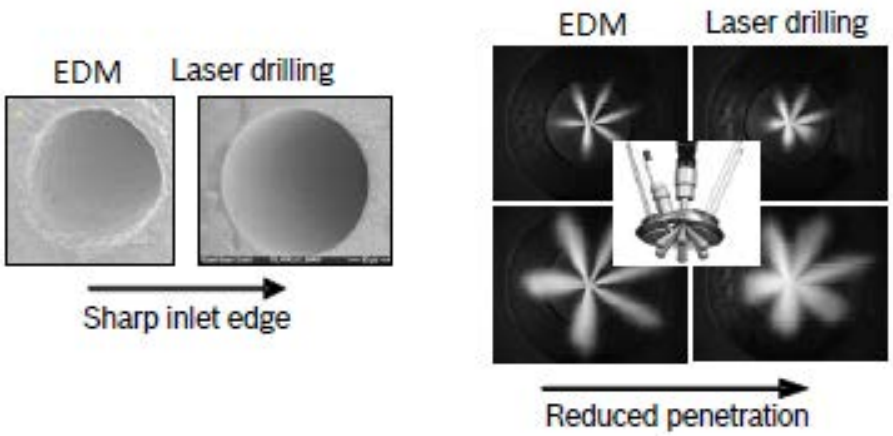

Figure 4-4 Schematic of the sharp inlet edge and sprays of the LD injector

Figure 4-4 shows a schematic of the sharp inlet edge and sprays of the LD injector. Similar findings were also stated in Whitaker's study: the latest laser drilled injector nozzle holes could provide a spray with reduced penetration and improved atomization at the same fuel pressure [122]. These differences may be due to the enhanced turbulence and better spray breakup induced by the sharp inlet edge [123] of the LD injector nozzle. Further analysis will be discussed in detail in the following sections.

4.3.2 Effect of Injection Pressure on Spray Penetration and Spray Angle

Figure 4-5 shows the spray penetration development under injection pressure of 50 bar, 100 bar, 150 bar and 200 bar along with the time ASOI; which are typical injection pressures in homogeneous charge spark ignition engines. In order to study the effect of the injection pressure, the injection durations were fixed at 1 ms for all the injectors and injection pressures. All the other parameters were kept the same so that the only variations were the injection pressure and the different injectors.

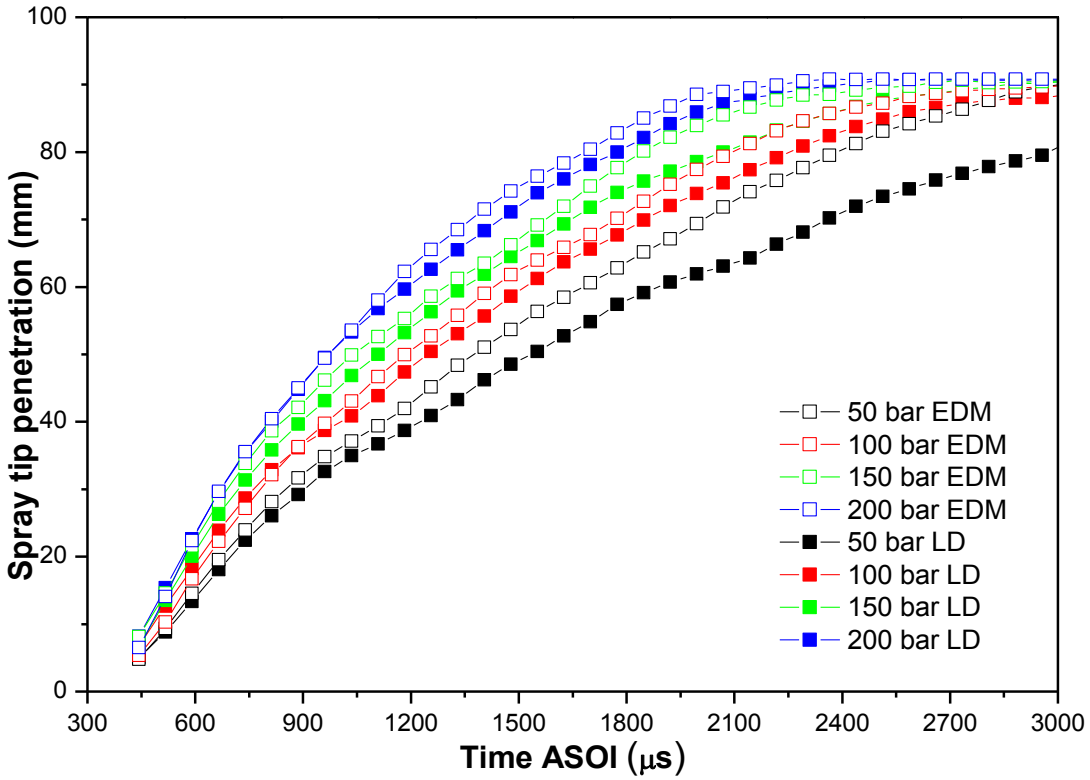

Figure 4-5 Effect of injection pressure on spray penetration (atmospheric back pressure, 1 ms injection duration)

From Figure 4-5, it can be seen that for both of the LD and EDM injectors, the spray penetration length increased gradually with the raising of the injection pressure from 50 bar to 200 bar. This was to be expected since higher injection pressure will result in greater outlet velocity and higher momentum of the spray jet at the nozzle exit. Under the same injection pressure, longer penetration length indicates that the fuel can reach a far distance and have more contact opportunities with fresh air; however, an unavoidable problem along with the longer penetration is the wall impingement, which will significantly increase the soot emissions in the GDI engine. Therefore this is of great importance and should be considered when determining the injection pressure during the engine development [108].

To investigate the effect of different nozzle machining methods on the spray characteristics under different injection pressures, a comparison of the spray penetration between the EDM injector and LD injector was carried out in Figure 4-5. It can be seen that, at the very beginning of the injection, before 600 μs ASOI, the penetration curves of the two injectors under the same injection pressure are quite close. Then the difference appears after 600 μs, for all the injection pressures when the spray penetration length of the EDM injector begins to increase faster than that of the LD injector with the time elapsed.

This is consistent with the morphology comparison and the possible reason is that the sharp inlet edge of the LD injector nozzle could enhance the turbulence intensity of the fuel inside the nozzle [123]. At the same time, the fine inner surface of the LD injector nozzle provides a much greater discharge coefficient of the nozzle flow. Obviously, all these factors will lead to a better spray breakup and a reduced spray penetration. Similar statements can also be found in [122]. On the other hand, the relatively rough surface finishing of the EDM injector nozzle will reduce the flow discharge coefficient and increase the outlet velocity and momentum of the spray jet at the nozzle exit; this then in turn results in a longer penetration length under the same injection pressure.

Figure 4-6 presents the effect of injection pressure on the spray angle. It is shown that for both of the injectors, increasing the injection pressure does not affect the spray angle very much. This finding is consistent with the result in [117]. Mitroglou, Nouri et al. found that the spray angle remains constant and is almost independent of injection pressure [117]. In comparing the spray angle of the two injectors, the EDM and LD nozzle machining methods affect it significantly at all test conditions. The figure indicates that for the same injection pressure, the LD injector has a larger spray angle compared to the EDM at all of the injection conditions.

According to the analysis of the morphology comparison, which shows wide spray jet patterns for the LD injector while narrow jet patterns for the EDM injector, the conclusion can be drawn that the LD injector offers a better atomization performance since the larger spray angle provides more contact area for the spray droplets and the surrounding air.

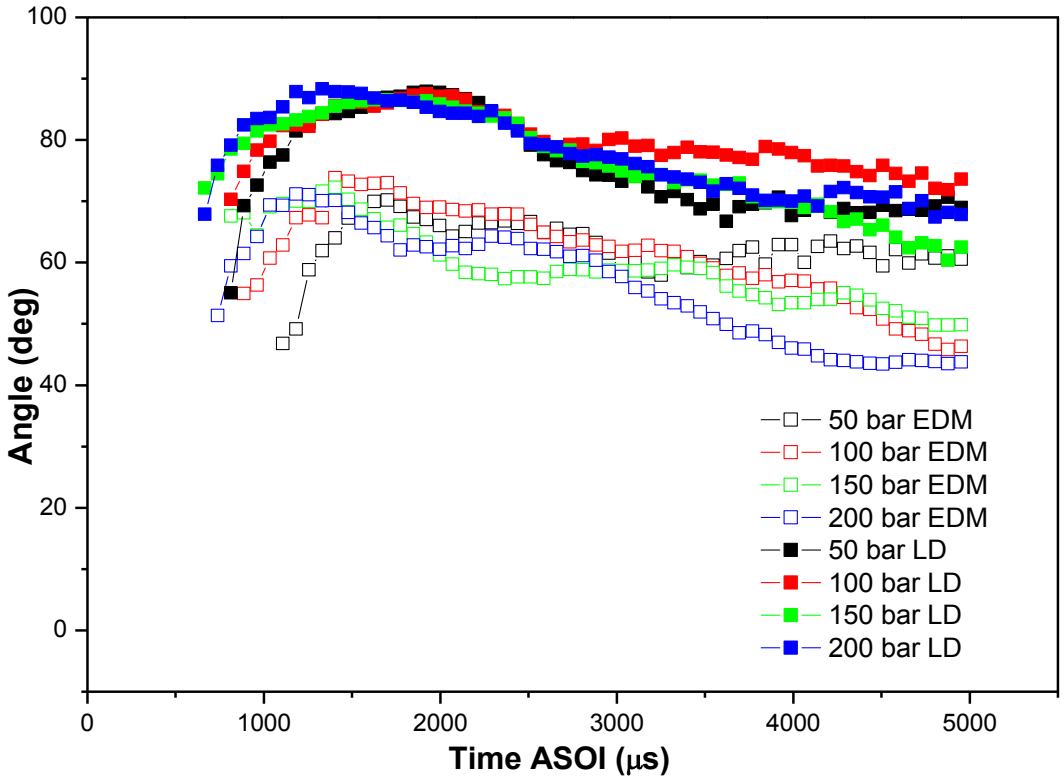

Figure 4-6 Effect of injection pressure on spray angle (atmospheric back pressure, 1 ms injection duration)

4.3.3 Effect of Injection Duration on Spray Penetration and Spray Angle

In order to investigate the effect of injection duration on the spray penetration and the spray angle, the injection pressure was fixed at 150 bar and the injection duration varied from 0.3 ms to 2 ms. Figure 4-7 and Figure 4-8 respectively show the spray penetration and spray angle

under different injection durations. It can be seen that before 1 ms ASOI, the injection duration does not affect the penetration length too much for both injectors; this is because the penetration length is determined by the nozzle outlet velocity only within this period and the same injection pressure led to the same jet velocity at the nozzle exit. After this period, the penetration would be affected by the injection duration since the momentum of the spray jet can be compensated by the help of the longer injection duration. While in the shorter injection duration case, the momentum of the spray jet cannot be compensated after the injection. Thus, compared to the 0.3 ms case, longer penetration can be found for both the 1 ms and the 2 ms cases. However, the difference between the 1 ms case and the 2 ms case is not significant since they reached the observation limit before showing any difference.

When comparing the penetration length of the two injectors under different injection durations, it seems that there is not much difference between the LD injector and the EDM injector for the 0.3 ms case; while a relatively longer penetration length for the EDM injector can be found for both the 1 ms and 2 ms cases. For the much shorter injection duration, the penetration will be more affected by the aerodynamic resistance due to the relatively lower momentum of the spray jet; thus the difference of the spray penetration between the two injectors is not significant.

As for the spray angle, it is shown that it will not change much when increasing the injection duration. It seems that under the same ambient condition, the spray angle is more likely to be dominated by the injector itself, rather than the injection parameters. A greater spray angle for the LD injector at all the conditions can be seen again from Figure 4-8. These findings also support the previous discussion concerning the LD injector performing a shorter penetration and a larger spray angle, compared to the EMD injector.

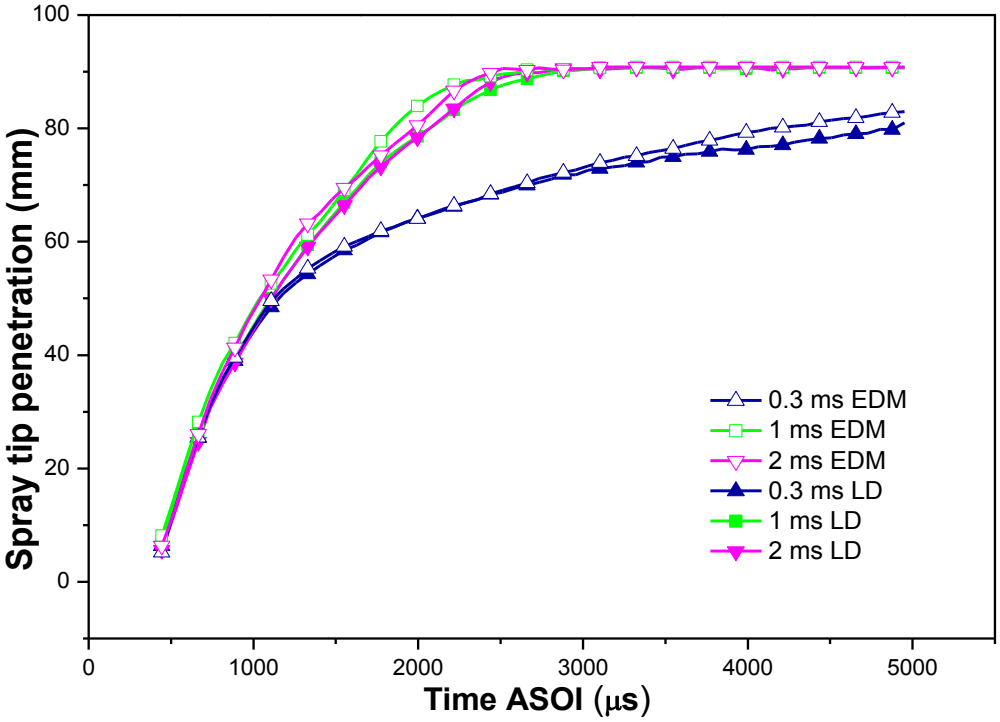

Figure 4-7 Effect of injection duration on spray penetration (atmospheric back pressure, 150 bar injection pressure)

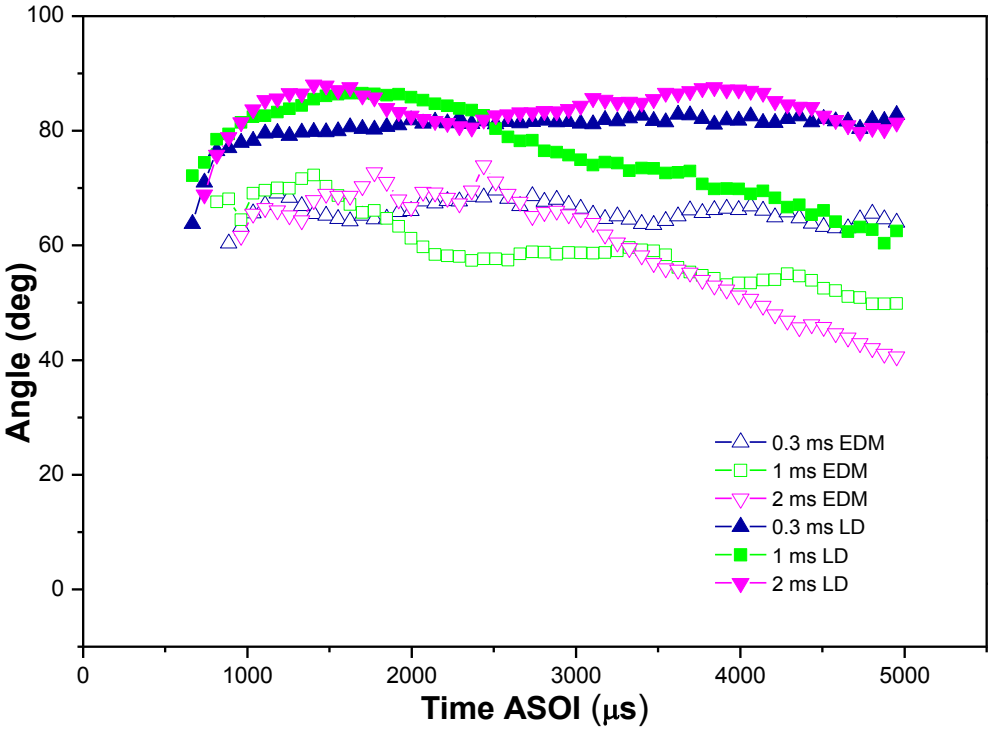

Figure 4-8 Effect of injection duration on spray angle (atmospheric back pressure, 150 bar injection pressure)

4.3.4 Effect of Injection Pressure on Droplet Velocity and Droplet Size

The macroscopic study of the spray characteristics has been reported in previous sections, it provides global spray development through the whole process and qualitative information at different injection conditions. In this section, a microscopic investigation into droplet behaviour by using Phase Doppler Particle Analyser technology has been carried out. Four vertical positions, as shown in Figure 4-2 previously, have been studied here and in order to make the experiment results more accurate, for each vertical position, five test points located on the cross section of the spray axis have been measured. Again the effects of injection pressure and injection duration on the spray droplet size and droplet velocity were investigated.

Figure 4-9 and Figure 4-10 show the droplet velocity evolution in the vertical direction and the horizontal direction respectively: at a vertical position of 30 mm, 1ms injection duration and various injection pressures. As is shown in Figure 4-9, the initial droplet velocity in the vertical direction was not at its peak at the injection pressure of 50 bar, 100 bar and 200 bar for both injectors. The droplet velocity experienced a sudden decrease at the very beginning of the injection and this then was followed by a rapid increase to its peak. The reason for this phenomena is analysed as follows: the droplets in the spray head experienced much more resistance from the surrounding air, which decelerated the velocity of the fuel droplet in the spray head at the very beginning; while the fuel droplets behind the head underwent less resistance from the air and then performed a rapid increase of their velocity. A similar trend of the droplet velocity evolution can be found in the horizontal direction, as is shown in Figure 4-10. The horizontal component of the droplet velocity is lower than the vertical component for all the test cases.

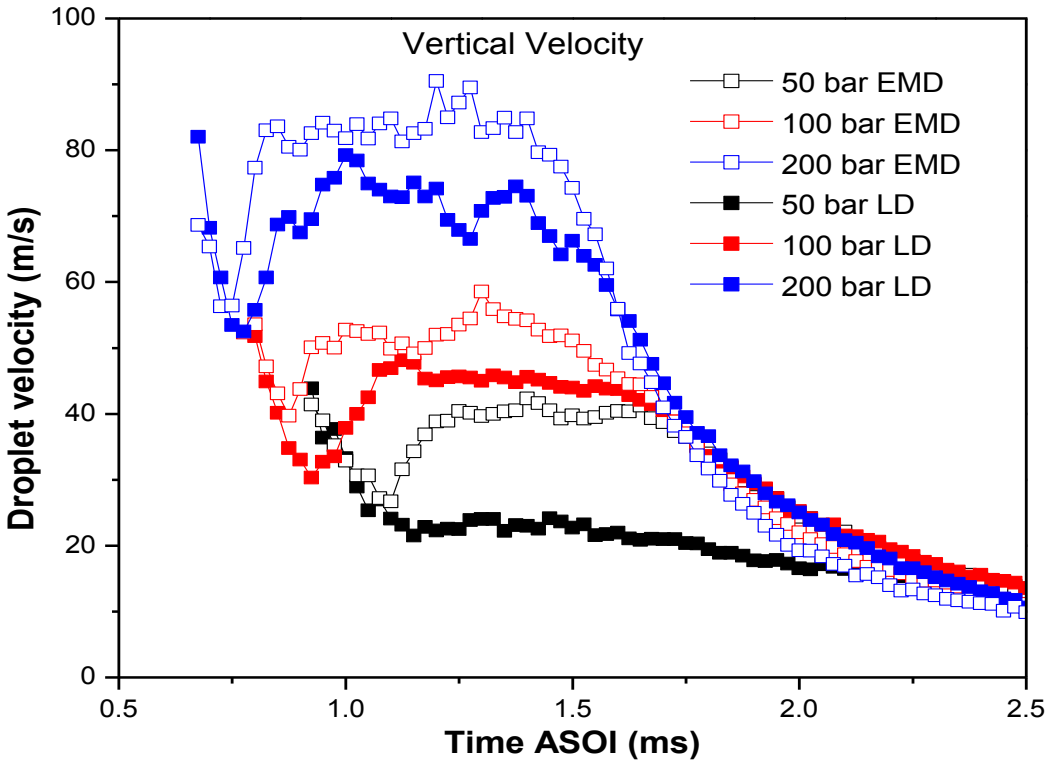

Figure 4-9 Effect of injection pressure on droplet velocity (vertical component, 1 ms injection duration, at a vertical position of 30 mm)

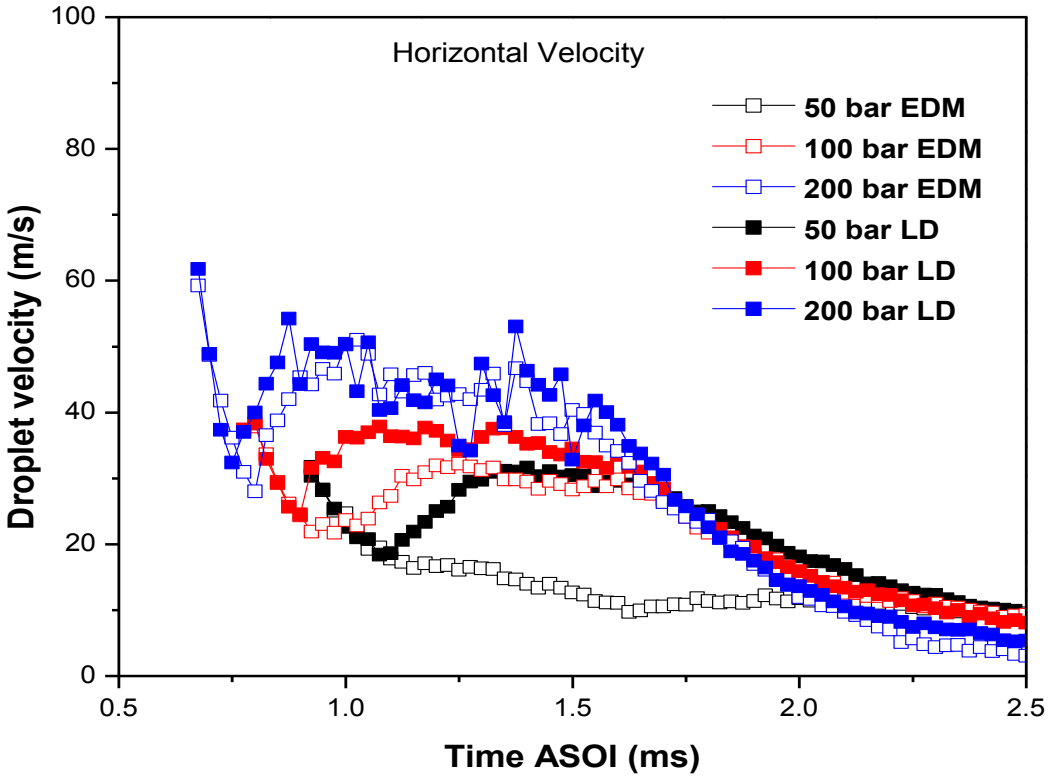

Figure 4-10 Effect of injection pressure on droplet velocity (horizontal component, 1 ms injection duration, at a vertical position of 30 mm)

An obvious trend can be seen in Figure 4-9 where the droplet velocity increases with the increasing of the injection pressure for both injectors; this was expected according to [124]. In addition, it can be seen that a significant lower droplet velocity can be observed for the LD injector at all the different injection pressures. In contrast to the weak acceleration process in the LD injector, especially in the case of 50 bar injection pressure, the EDM injector shows much stronger droplet acceleration. Therefore this also strongly supports the previous penetration comparison where the higher spray velocity of the EDM injector led to a longer penetration length.

Injection pressure is also one of the most important parameters in determining droplet size. Figure 4-11 shows the Sauter Mean Diameter (SMD) at different injection pressures at the vertical distance of 30 mm from the nozzle. The parameter SMD is one of the most important features in the study of the spray atomization process. Although the Average Mean Diameter (AMD) can represent the average droplet size, SMD can avoid the influence of some individual smaller or bigger droplets and provide a more accurate result. In general, the calculation of SMD for a given particle is defined as:

$$SD = D[3,2] = d_{32} = \frac{d_v^3}{d_s^2} \tag{4-1}$$

where d_v and d_s are the volume diameter and surface diameter respectively:

$$d_v = \left(\frac{6V_p}{\pi}\right)^{\frac{1}{3}} \; ; \; d_s = \sqrt{\frac{A_p}{\pi}} \tag{4-2}$$

where A_p and V_p are the surface area and volume of the particle, respectively.

As the injection pressure increases, the SMD is reduced accordingly. This is reasonable because higher injection pressure will lead to stronger turbulence, higher droplet velocity and greater aerodynamic force; and all these factors will boost the breakup of the spray and thus smaller droplets can be obtained.

Another important aspect can be found in Figure 4-11 where the SMD of the spray from the LD injector shows a smaller value at all the injection pressures. As is generally known, a smaller SMD indicates a better atomization performance and a better mixture formation; since the smaller SMD represents a larger total droplet surface being achieved and interacting with surrounding gas, which will enhance the atomization and evaporation processes and in turn promote the mixture formation and combustion quality in the engine [125].

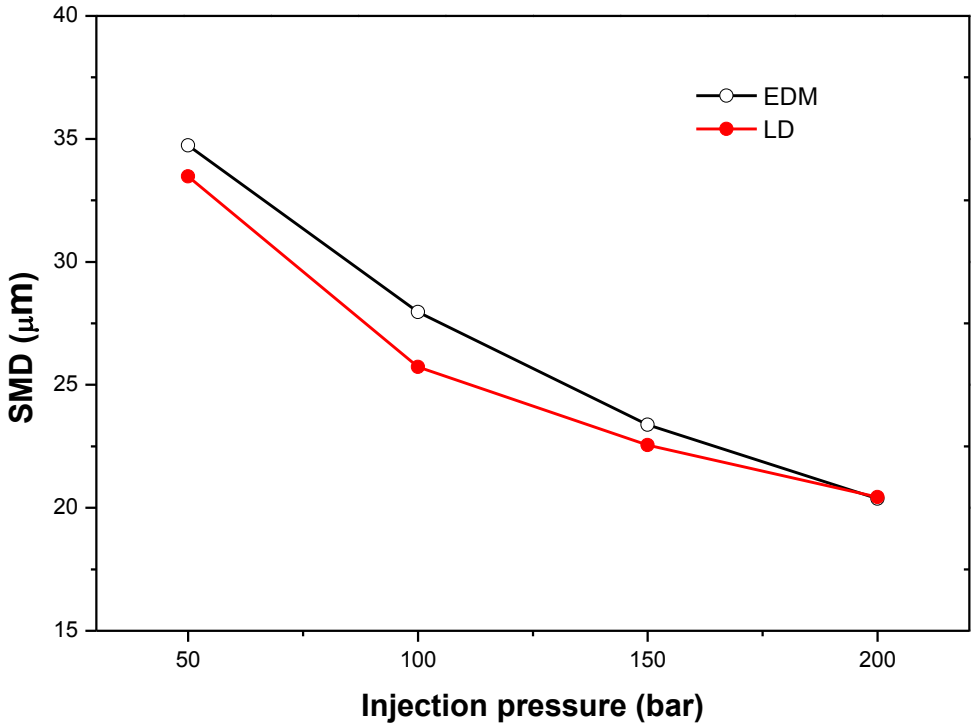

Figure 4-11 Effect of injection pressure on droplet size (1 ms injection duration, at a vertical position of 30mm)

4.3.5 Effect of Injection Duration on Droplet Velocity and Droplet Size

Injection duration is another important parameter when optimising the engine. Figure 4-12 and Figure 4-13 exhibit the evolution of the droplet velocity in the vertical and horizontal direction, respectively, under different injection durations ranging from 0.3 ms to 2 ms and at 100 bar injection pressure. The measurement points are still located at the distance of 30 mm vertically downwards from the nozzle.

It can be seen that for each injector, the droplet velocity will not be affected by the increasing of the injection duration at the very beginning. This is consistent with the previous discussion about the effect of injection duration on the penetration length. At the very beginning of the injection, the same injection pressure will result in an equal outlet velocity at the nozzle exit for all the conditions; thus a similar droplet velocity and penetration length will be obtained. However, after this short period, longer injection duration will continually supplement the momentum of the spray jet due to the newly emerged fuel. Therefore higher droplet velocity can be found for the longer injection duration case, as is shown in the diagram.

At the same time, compared to the EDM injector, the LD injector shows lower droplet velocity at all the injection durations. It is quite possible that the difference is caused by the different surface finishing inside the injector nozzle. The rough inner surface of the EDM injector nozzle can reduce the flow discharge coefficient, which results in the higher droplet velocity. Also the lower turbulence of the flow inside the EDM injector nozzle can reduce the dispersion of the spray jet and then increase the axis speed and spray penetration. This result is again consistent with the previous explanation of the longer penetration length and narrow spray jet angle for the EMD injector.

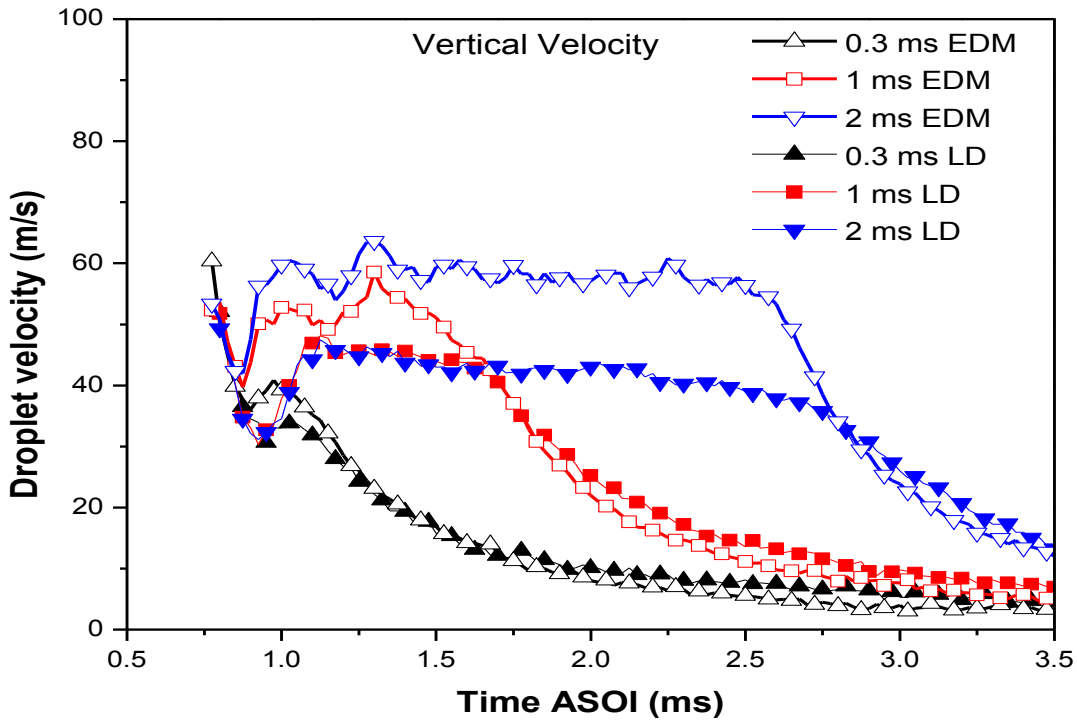

Figure 4-12 Effect of injection duration on droplet velocity (vertical component, 100 bar injection pressure, at a vertical position of 30 mm)

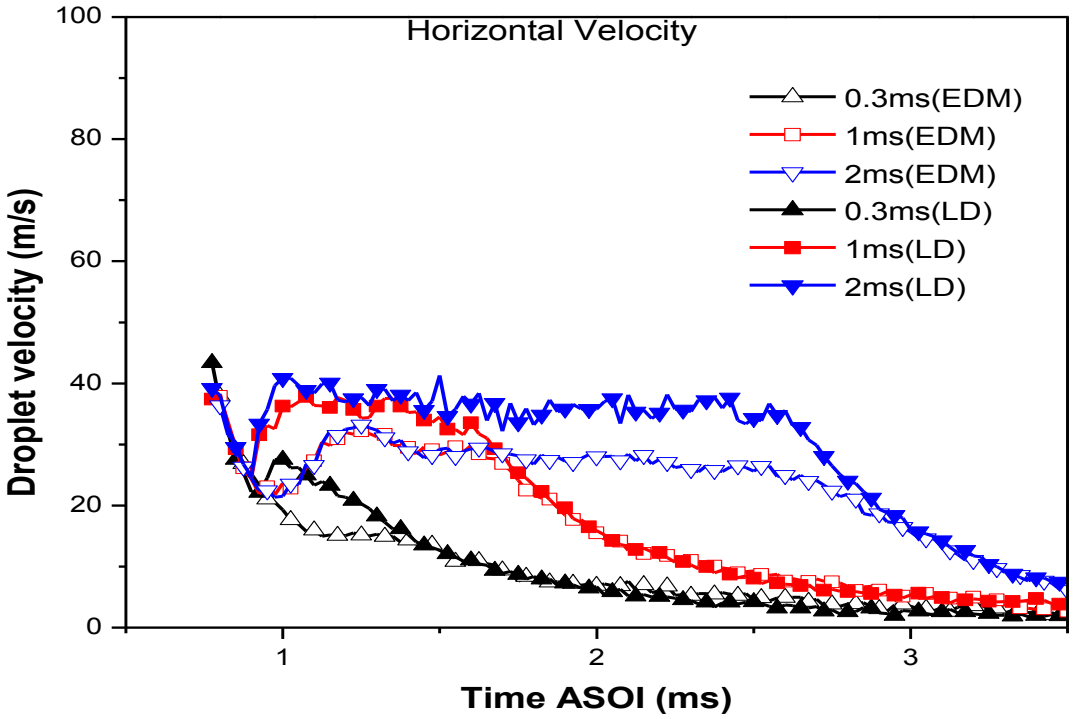

Figure 4-13 Effect of injection duration on droplet velocity (horizontal component, 100 bar injection pressure, at a vertical position of 30 mm)

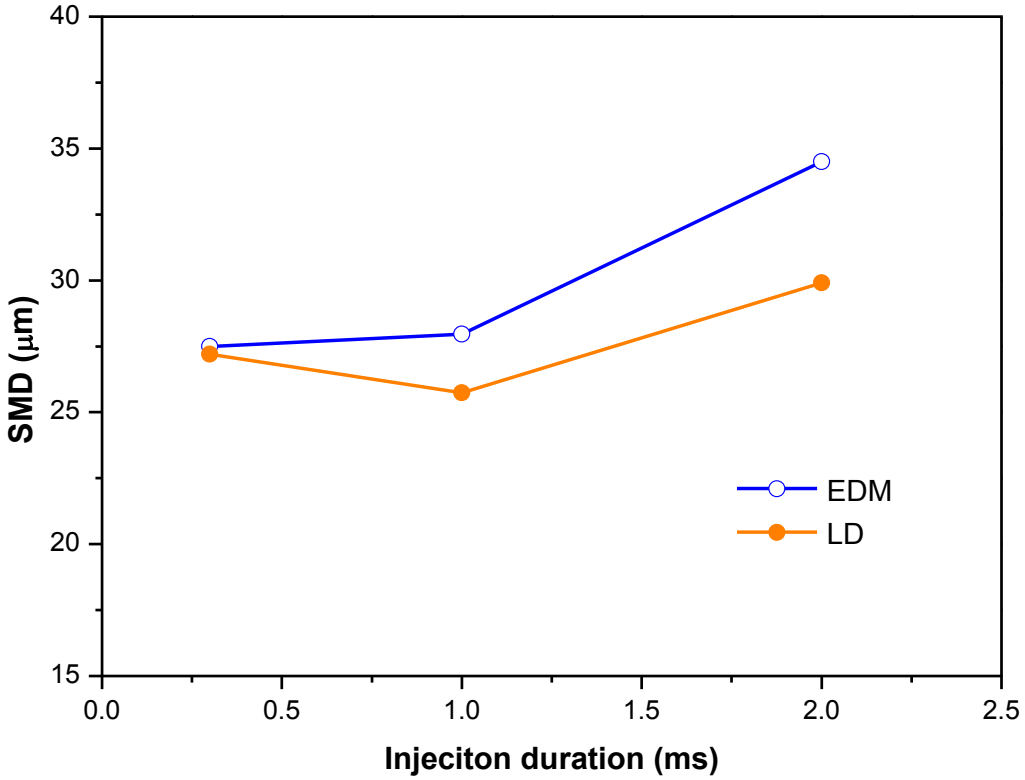

Figure 4-14 Effect of injection duration on droplet size (100 bar injection pressure, at a vertical position of 30 mm)

The effect of injection duration on the SMD at a vertical position of 30 mm has been shown in Figure 4-14. It can be seen that the SMD increases with the rising of the injection duration; this can be attributed to the coalescence of the droplet and the increased fuel amount of longer injection duration will increase the probability of droplet coalescence.

Meanwhile, it also can be seen that the SMD of the EDM injector is more sensitive to the injection duration; which can be increased by up to 30% with the injection duration increasing from 0.3 ms to 2 ms. While for the LD injector, this increment is no more than 10%. In addition, the LD injector has a much lower SMD at all the conditions. This may be futher evidence to show that the LD injector can offer a better atomization performance.

4.3.6 Droplet Velocity and Droplet Size Spatial Distributions

Figure 4-15 shows the droplet velocity evolution in the vertical direction under an injection pressure of 100 bar and injection duration of 1ms. The different evolution curves of four distances downwards of the nozzle: 20 mm, 30 mm, 50 mm and 70 mm are shown in this diagram.

It is shown that the speed decreases with the increase of the distance; this is due to the loss of momentum of the spray droplets during their movement. The aerodynamic resistance force will act on the droplets and slow down their velocity. On the other hand, the breakup of the spray droplets will also consume their kinetic energy and reduce their momentum. Meanwhile, the smaller droplets produced by these breakups can be slowed down more easily during the transportation.

At the distance of 20 mm and 30 mm, the droplet velocity of the LD injector show a lower value compared to those of the EDM injector, the difference can be up to 20 m/s in the distance of 30 mm downwards of the nozzle. While with the further increase in distance, the difference between the two injectors become small. The earlier acceleration process can also be observed for the EDM injector as mentioned previously.

The evolution of the SMD at different distances has been shown in Figure 4-16. The injection pressure and duration are fixed at 100 bar and 1 ms, respectively. With the increase of the distance, the SMD decreases firstly and then rises slightly for both injectors. Likewise, the LD injector shows a relatively lower SMD; which indicates a better atomization for the LD injector compared to that of the EDM.

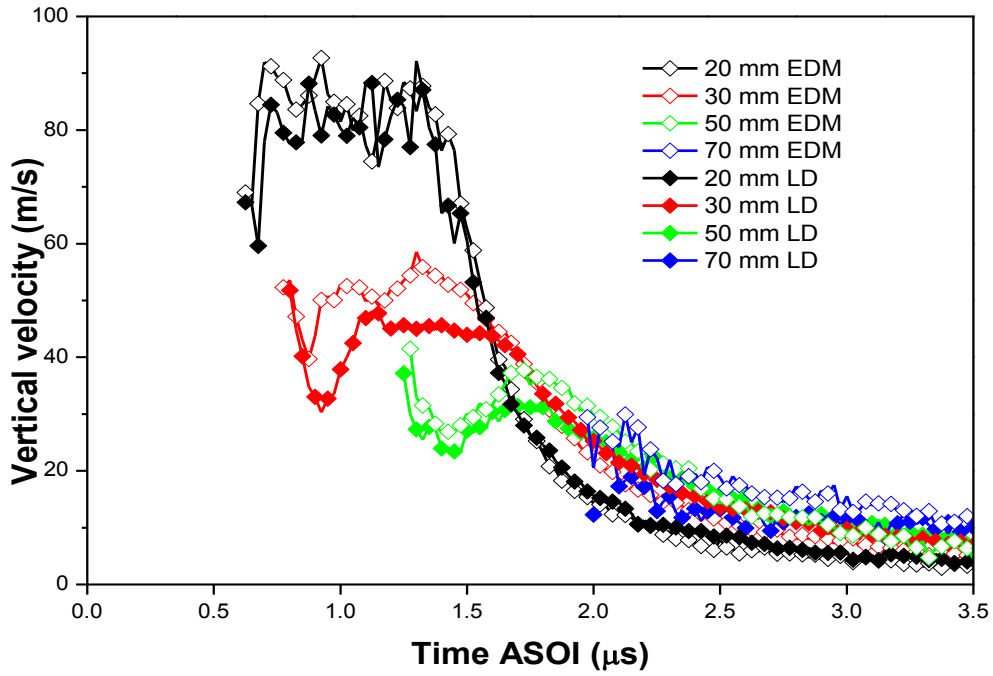

Figure 4-15 Droplet velocity evolution at different vertical positions (100 bar injection pressure, 1 ms injection duration)

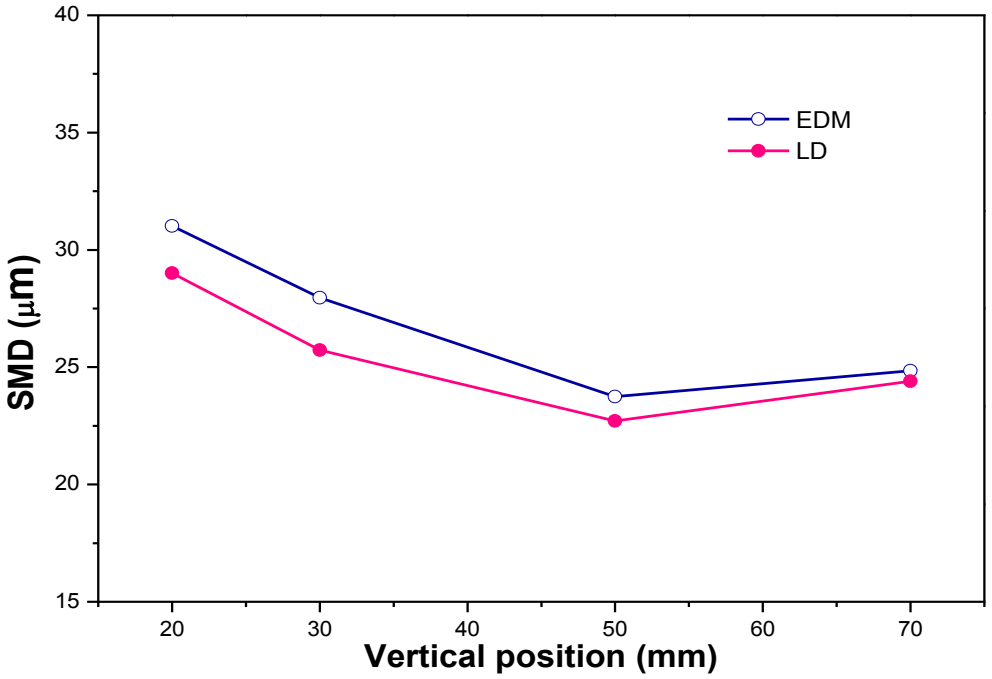

Figure 4-16 Droplet size evolution at different vertical positions (100 bar injection pressure, 1 ms injection duration)

4.3.7 Validations of the Analyses

In order to verify the influence of the sharp inlet of the nozzle and as an extension of this study, a numerical comparison of the flow characteristics has been carried out. With the help of the in-nozzle flow simulation, the flow characteristics such as the turbulence intensity and the outlet velocity of the flow at the nozzle exit can be obtained. These flow parameters can sufficiently provide evidence and help to explain the difference between the spray characteristics of the two injectors.

Figure 4-17 shows a schematic of the two different inlet edges of the nozzle, the sharp inlet edge is represented by 'R/D=0' (left-hand side), where R is the radius of the inlet corner and D is the diameter of the nozzle. While for the blunt edge, R is set to R=0.1D (right-hand side). The gasoline fuel inside the injector was pressured by 150 bar injection pressure and then it flowed through the nozzle. This simulation was carried out on the advanced CFD software – ANSYS Fluent with the *k-ε* Reynolds Averaged Navier-Stokes (RANS) approach.

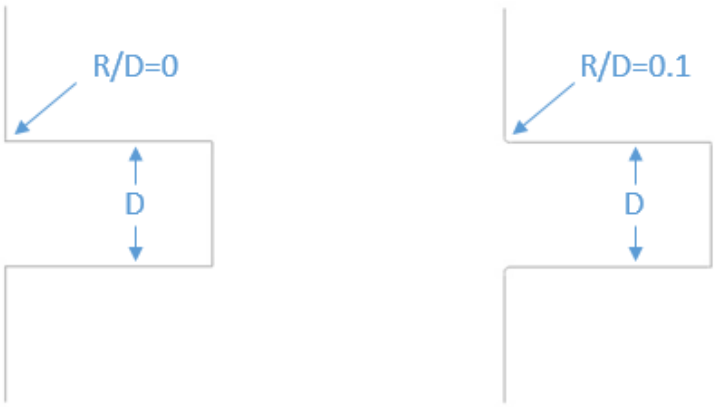

Figure 4-17 Schematic of the sharp inlet edge of the nozzle

Figure 4-18 compares the turbulence kinetic energy inside the nozzle of the two injectors. It can be seen that for the sharp inlet edge nozzle, higher turbulence kinetic energy can be found near the wall and at the nozzle exit. This confirms the previous discussion that the sharp inlet edge of the LD injector nozzle will enhance the turbulence phenomenon and then benefit the spray breakup once the fuel leaves the nozzle.

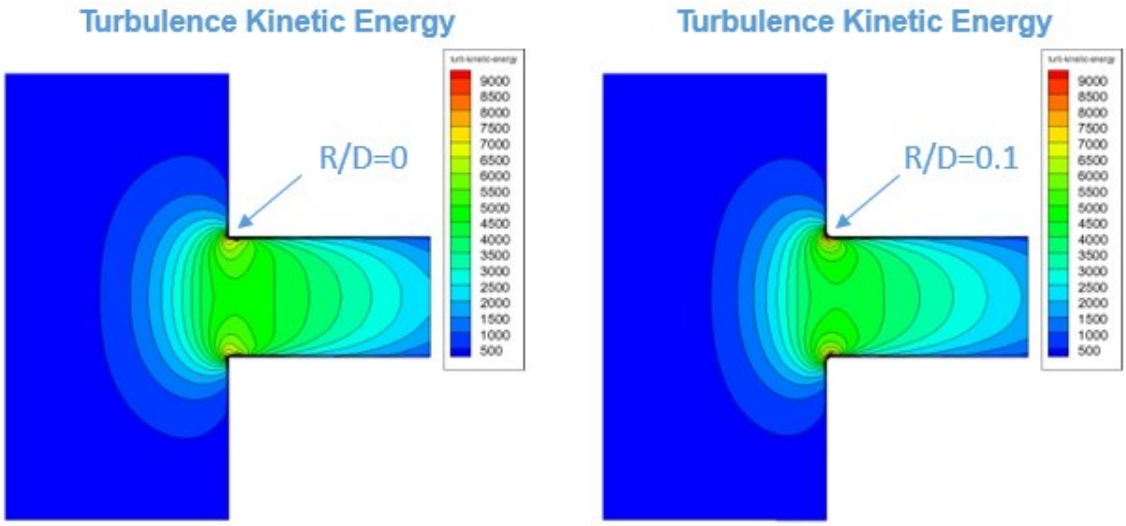

Figure 4-18 The comparison of the turbulence kinetic energy inside the nozzle

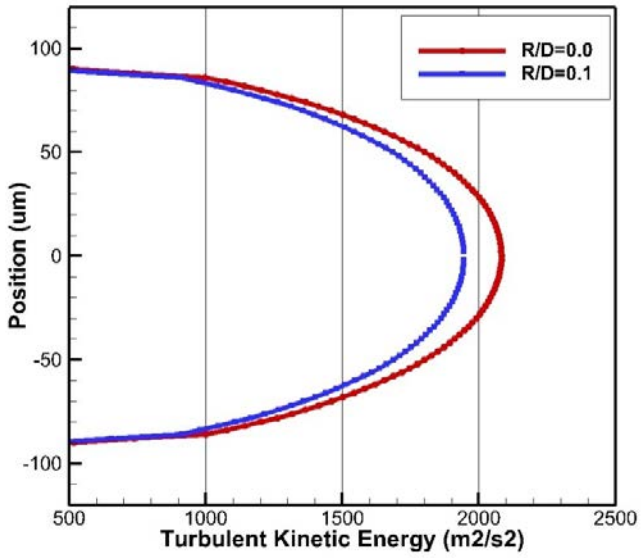

Figure 4-19 The comparison of the turbulence kinetic energy at the nozzle exit

Figure 4-19 presents the quantitative comparison of the turbulence kinetic energy at the nozzle exit. It is shown that the turbulence kinetic energy of the sharp inlet nozzle, which is represented by the red curve in the diagram, is higher than the other nozzle at all positions in the radial direction. Again, this result supports the previous analysis that the turbulence induced by the sharp inlet edge is one of the most important parameters to affect the spray characteristics and atomization performance.

Figure 4-20 shows the comparison of the velocity distribution inside the nozzle. A significant difference in the velocity distribution can be found where the nozzle with the sharp inlet edge exhibits a relatively much lower fluid velocity, compared to the nozzle without the sharp inlet edge near the wall. This provides further evidence to support the analysis as to why the LD injector has a shorter penetration length compared to that of the EDM.

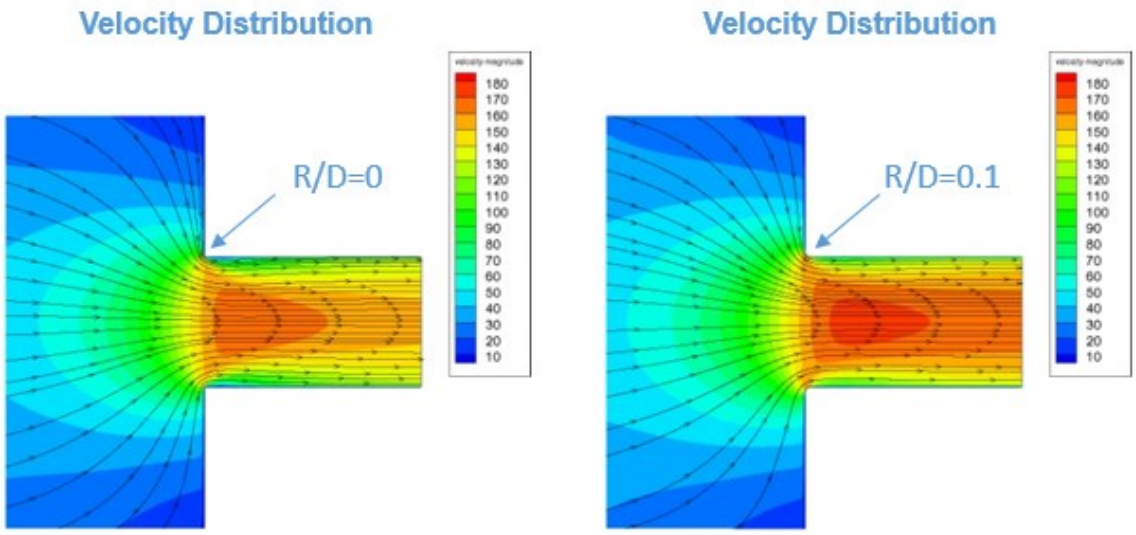

Figure 4-20 The comparison of the velocity distribution inside the nozzle

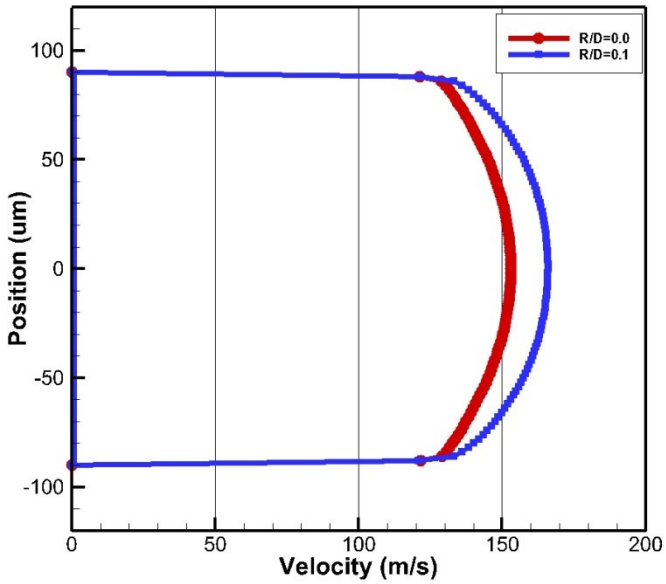

Figure 4-21 The comparison of the velocity distribution at the nozzle exit

Again, as is shown in Figure 4-21, the comparison result of the velocity distribution at the nozzle exit between the two nozzles indicates that the nozzle with the sharp inlet edge exhibits a lower fluid velocity, which is also consistent with the penetration comparison result.

In terms of the effect of the fine inner surface of the LD injector nozzle, Echouchene [126] investigated the wall roughness effects in his study. He found that the discharge coefficient and the turbulent kinetic energy will decrease with the increasing of the wall roughness inside the nozzle. These findings sufficiently support the previous discussion and explain that the fine inner surface of the LD injector nozzle is another important factor which will enhance the spray atomization performance.

4.4 Summary

The influence of injection pressure, injection duration and different injector machining methods on the gasoline spray characteristics have been investigated in this study. The experimental comparison of the spray characteristics of the same injectors made from different manufacturing processes has been studied in terms of spray penetration, spray angle, droplet velocity and droplet size. Differences in the spray characteristics have been found due to the sharp inlet edge and fine inner surface of the LD injector nozzle. The main conclusions are as follows:

1. The injection pressure plays an important role in affecting the spray penetration. Higher injection pressure will increase the penetration length and enhance the spray atomization process. However, the spray angle is almost independent of the injection pressure.

2. The injection pressure also significantly affects the droplet size and droplet velocity. With the increase of the injection pressure, the droplet velocity increases while the droplet size decreases accordingly.

3. The injection duration does not affect the spray penetration at the initial stage of the injection; however, after this period, longer penetration length can be found with the increase of the injection duration. The spray angle is almost independent of the injection duration.

4. The injection duration is another factor which affects the droplet velocity and droplet size. With the increase of the injection duration from 0.3 ms to 2 ms, a similar droplet velocity can

be found at the initial stage of the injection; however, after this period, longer injection duration will lead to higher droplet velocity and greater droplet size.

5. With the increase of the distance downwards of the nozzle, the droplet velocity decreases gradually; while the droplet size decreases first and then increases slightly at a far distance.

6. Compared to the EDM injector, the LD injector shows a reduced penetration, larger spray angle and smaller spray droplet size at all test conditions. Obviously, the adoption of the LD injector will improve the atomization quality due to the sharp inlet edge and fine inner surface of the LD injector nozzle. It is believed that the sharp inlet edge can enhance the turbulence of the flow and in turn promote the spray breakup and atomization performance.

CHAPTER 5
SPRAY CHARACTERISTICS OF DIESEL ENGINES

This chapter investigates the spray characteristics of diesel, gasoline and dieseline fuel in the diesel engine. The main objectives of this study are to investigate the effects of injection pressure, ambient pressure and different fuels including gasoline, diesel, and their blends – dieseline, on the spray characteristics; and furthermore to try to understand the different behaviours of the spray atomization process of pure diesel and the recently developed dieseline fuel. The comparisons in terms of spray macroscopic and microscopic characteristics of different dieseline blends will be experimentally carried out in this study.

5.1 Introduction

Compression Ignition (CI) diesel engines have high thermal efficiency but produce a lot of nitrogen oxides (NOx) and soot emissions. In recent decades, there is an increasing concern regarding the environmental impact of emissions from internal combustion engines (ICE). Furthermore, the emission standard is becoming increasingly stringent in recent years. To meet the emission legislation, diesel engines have to be equipped with a high pressure common rail injection system and costly after treatment equipments. On the other hand, although the harmful exhaust emissions from Spark-ignition (SI) gasoline engines can be reduced by the implementation of a costly effective three-way catalyst, however, the thermal efficiency of gasoline engines is lower than diesel engines.

Much research has shown that the smoke emissions of diesel engines can be significantly reduced by fuelling the engines with gasoline or gasoline/diesel blends; while the reduction of NO_x can also be facilitated by increasing the exhaust gas recirculation ratio [127-132]. Kalghatgi *et al.* [127] successfully tested a gasoline fuelled partially premixed compression ignition (PPCI) engine and showed that even at high loads of 15.95 bar indicated mean effective pressure (IMEP), almost zero smoke emissions and a low indicated specific fuel consumption (ISFC) of 179 g/kWh was obtained. Similar findings were also demonstrated by Ciatti et al. [128] and Manente et al [129].

At the University of Birmingham, researchers investigated the idea of altering fuel characteristics through blending gasoline with diesel and the resulting fuel was named '***Dieseline***' [130-133]. According to the experimental results, dieseline has great advantages over diesel for smoke reduction when being used in both PPCI and conventional diesel engines. Weall and Collings [134] found that the PPCI operating range can be extended by using the dieseline fuel. It was demonstrated by Han et al. [135] that the usage of dieseline fuel reduced the dependence of smoke reduction on high injection pressure.

Both the chemical and physical properties of fuel can affect the combustion performance and emissions of diesel engines. Compared to pure diesel, the lower cetane number of gasoline and dieseline, which increases the ignition delay and mixing time, has definitely contributed to their low smoke emissions [136]. The investigations of diesel-like fuels show that the spray characteristics also play an important role in the emission formations of diesel engines [137, 138]. For example, over-penetration can cause piston bowl/cylinder wall wetting and thus increase particle, UHC and CO emissions; particle emissions can be effectively reduced with better spray atomization. Payri et al. [139] found that there was little difference between diesel

and gasoline in terms of momentum flux and penetration length (steady region) in a high pressure common rail injection system, independently of the nozzle diameter. This study compared the macroscopic and microscopic spray characteristics of different dieseline blends. The objective is to understand the behaviour of the injection and atomization processes of diesel and dieseline fuel.

5.2 Experimental Conditions

The experimental system has been introduced in Chapter 3. The spray experiment was carried out with a 7-hole common rail diesel injector in the two constant volume vessels under non-evaporation and various injection conditions. The solenoid AJ200 diesel injector with 7 holes and a nozzle diameter of 0.15 mm was used in the experiments. The injector was fuelled with diesel and dieseline controlled by electrical pulses, which were generated from the injection trigger unit and amplified by a driver. Five fuels including pure diesel (G0), 20% (G20), 50% (G50), 70% (G70) gasoline blended dieseline and pure gasoline (G100) were tested in this study. The pure diesel and pure gasoline used in the test were the European standard diesel (EN590) and 95 octane gasoline (ULG95). The physical properties of all the five fuels are shown in Table 5-1.

Table 5-1 Fuel properties of dieseline fuels

Test Fuel	Diesel	G20	G50	G70	Gasoline
Density (g/ml at 15 °C)	0.84	0.82	0.79	0.763	0.73
Viscosity(mm^2/s at 40 °C)	2.90	2.08	1.12	0.72	0.5
Surface tension (mN/m at 20 °C)	28.9	-	-	-	21.6
Vapour pressure (kPa at 20 °C)	<0.01	-	-	-	30-90

The rail pressure and the ambient conditions are listed in Table 5-2. The fuel pump can provide a high rail pressure up to 2000 bar, however, with the increased ratio of gasoline in dieseline, the injection system can not achieve its maximum injection pressure since the pump was designed for diesel and it had a lower performance for gasoline. So the maximum injection pressure for G100 was 1000 bar.

Table 5-2 Test conditions for dieseline spray

Test Fuel	P_{inj}(bar)	P_{back}(bar)	Ambient Density (kg/m^3)	Injection Duration(μs)
Diesel	500/750/1000/1250/1500	1/15/30	1.25/17.8/35.6	600
G20	500/750/1000/1250/1500	1/15/30	1.25/17.8/35.6	600
G50	500/750/1000/1250	1/15/30	1.25/17.8/35.6	600
G70	500/750/1000/1250	1/15/30	1.25/17.8/35.6	600
Gasoline	500/750/1000	1/15/30	1.25/17.8/35.6	600

The spray photography tests were carried out in the high pressure CVV which is pressurized by compressed nitrogen gas; while the PDPA tests were carried out at atmospheric pressure in the low pressure CVV, since it was difficult to obtain valid data in the high pressure vessel due to its limited optical access area. Spray images were taken from the bottom window of the high pressure CVV with has a visible diameter of 68 mm. The settings of the camera configurations are shown in Table 5-3. The speed of 18003 fps offered a good enough resolution of 608×600 for the high-speed imaging measurement and the average time interval for each frame was 55 μs.

Table 5-3 Configurations of Phantom V710 camera

Resolution	600×608
Speed	18003 fps
Colour expression gradations	Monochrome 8 bit and 12 bit
Lens	Nikon, 105 mm focus length
Image device	1280×800 CMOS sensor

The configurations of the PDPA system are shown in Table 5-4. The details of the PDPA techniques were introduced in Chapter 3.

Table 5-4 PDPA specifications and operating parameters

Wave length	514.5 mm
Beam diameter	2.2 mm
Transmitter optics	310 mm
Receiver optics	310 mm
Expander ratio	1.950
Beam spacing	37 mm
Frequency shift	4.00 MHz
Receiver type	112 mm Fiber PDPA
Scattering Mode	Refraction
Spatial filter	0..025 mm
Laser power	1.2 w

Figure 5-1 shows the sampling positions of the PDPA test. The positions of 10 mm, 20mm, 30 mm, 40 mm, and 50 mm vertically downstream of the nozzle were measured under different injection pressures. In order to investigate the variations of the spray characteristics in the radial direction, several points beside the spray jet axial have been tested. As shown in the figure, the red points are on the jet axial, while the green points are located beside the jet axial. In addition, to minimize the injection variations and ensure the accuracy of the measurement, 200 injections have been tested at each sampling position and the averaged results are presented throughout this study.

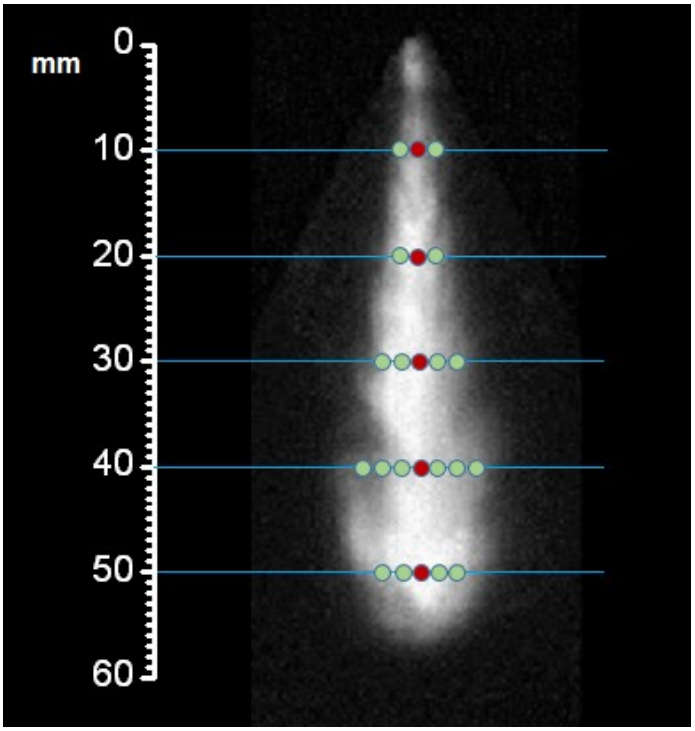

Figure 5-1 PDPA testing positions for dieseline

5.3 Results and Discussion

5.3.1 Macroscopic Comparison of Diesel and Dieseline Sprays

Figure 5-2 is the morphography comparison of diesel, G50 and G100 at an injection pressure of 500 bar and back pressure of 15 bar. It can be seen from the images that the propagation of the spray tip decreases with the increasing of the gasoline blending ratio. The main reason for this is believed to be the higher viscosity and higher density of diesel. Higher viscosity of the liquid makes it more difficult to breakup and lose mass; while higher density gives it bigger initial momentum [28]. Compared to diesel, gasoline has lower density and lower viscosity and thus it results in a shorter penetration length for the higher gasoline blending ratio.

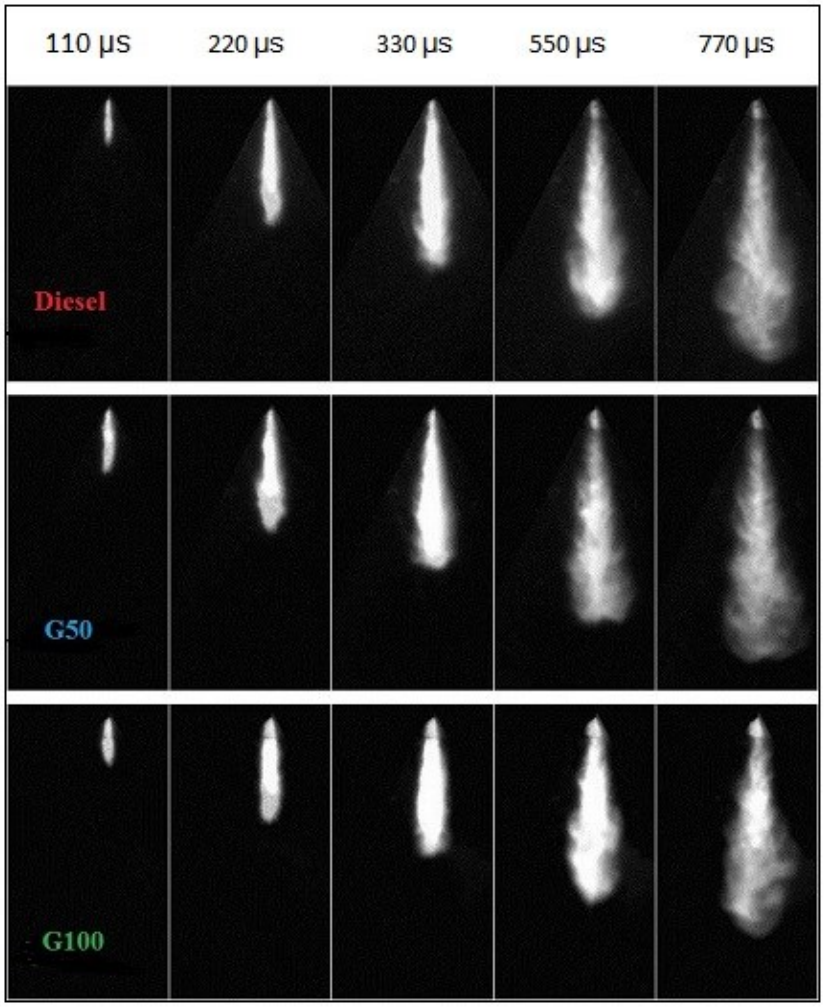

Figure 5-2 Spray images of diesel, G50 and G100, injection pressure 500 bar, back pressure 15 bar (Scale:1:1, *mm*)

5.3.2 Penetration Comparison of Diesel and Dieseline Sprays under Different Gasoline/Diesel Blending Ratios

The comparison of the penetration length of different fuels has been qualitatively discussed in section 5.3.1 and the quantitative comparison is presented in this section. As is shown in Figure 5-3, the same trend can be found for all the injection conditions: the penetration length decreased with the increase of the gasoline blending ratio. The difference is not significant before 200 µs ASOI for each injection condition due to the similar initial tip velocity induced

by the same injection pressure for all fuels. However, after this time point, the situation becomes different and the atomization and breakup reduced the kinetic energy of the fluid and at the same time, the aerodynamic resistance slowed down the droplet velocity. Thus it can be seen in Figure 5-3, beyond the initial stage, the penetrations of different fuels differ much as time goes on. For example, at 15 bar ambient pressure and 500 bar injection pressure, with the increasing of the gasoline/diesel blending ratio, the penetration reduced gradually. The maximum difference of the spray penetration between G0 (pure diesel) and G100 (pure gasoline) is about 6 mm.

As discussed previously, it is believed that the physical properties of gasoline enhances the atomization and breakup processes of the spray and results in the shorter tip penetration due to the kinetic energy loss during the breakup. In addition, the cavitation effect becomes more and more significant with the increase of the gasoline blending ratio; due to the much higher vapour pressure of gasoline. There is no doubt that the cavitation effect plays an important role in accelerating the atomization process [140] and this could be an important factor affecting the penetration length.

To compare the penetration length between the conditions of 15 bar and 30 bar ambient pressure, it can be seen that the penetration difference is more significant at lower ambient pressure; while at higher ambient pressure, this difference becomes weak. Another phenomenon is that the penetration of pure gasoline (G100) is less sensitive to the increase of ambient pressure compared to that of pure diesel. A similar trend can be found in terms of increasing the injection pressure. The possible reasons and details of these differences will be discussed in the following sections.

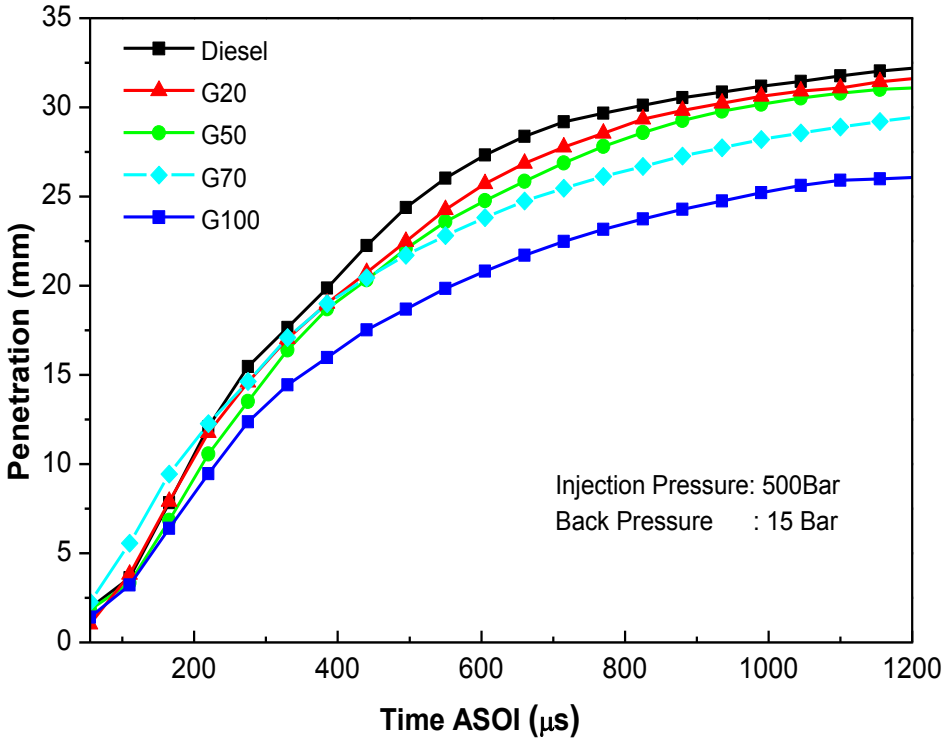

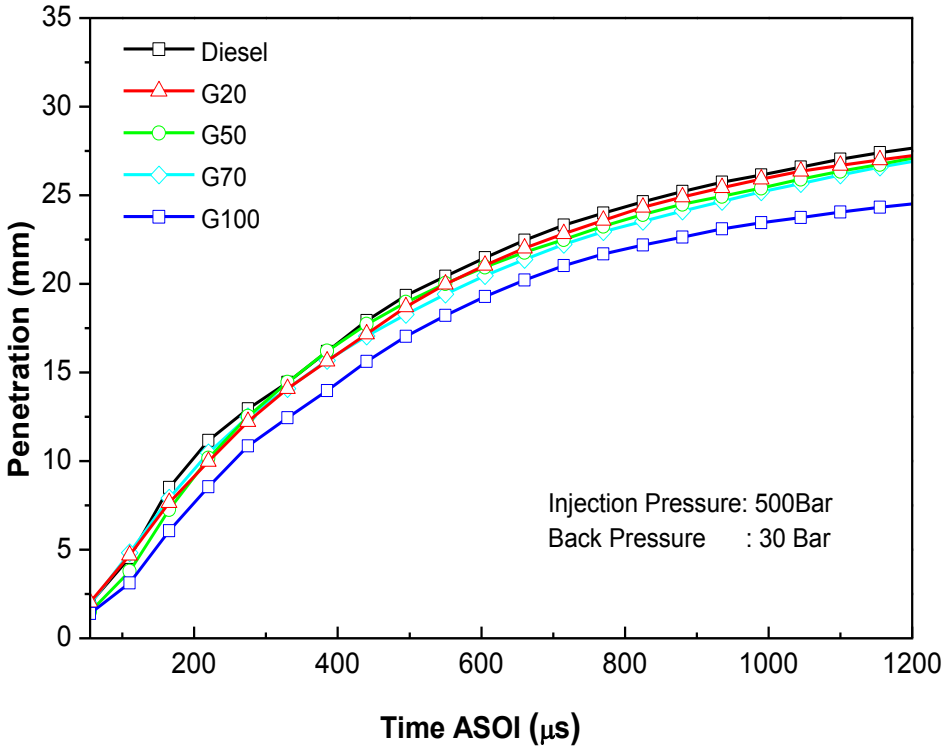

Figure 5-3 Effect of gasoline/diesel blending ratio on penetrations of diesel and dieseline sprays (500 bar injection pressure)

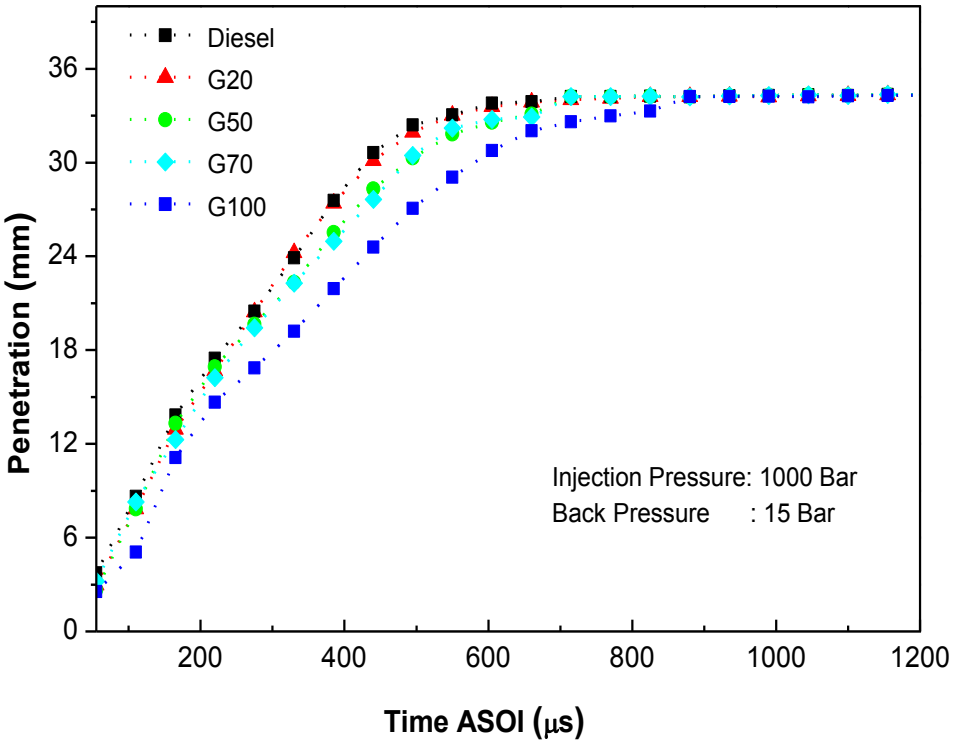

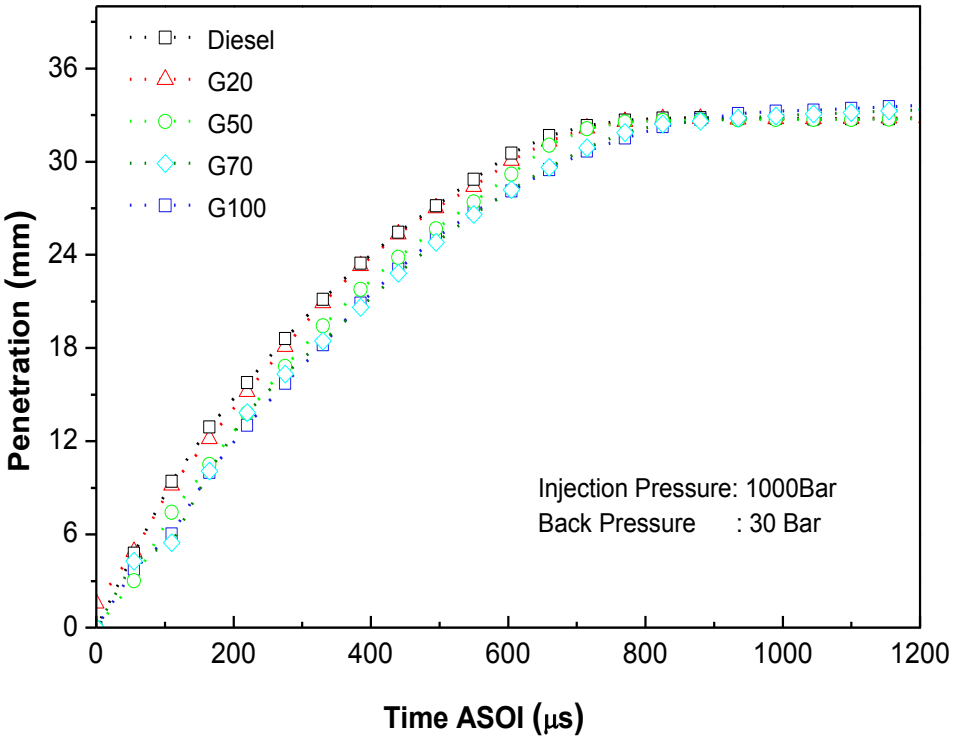

Cont. Figure 5-3 Effect of gasoline/diesel blending ratio on penetrations of diesel and dieseline sprays (1000 bar injection pressure)

5.3.3 Penetration Comparison of Diesel and Dieseline Sprays under Different Injection Pressures and Ambient Pressures

Figure 5-4 presents the effect of ambient pressure on penetrations of diesel, dieseline (G50), and gasoline (G100) sprays. As discussed above, the increase of ambient pressure has little effect on penetration length at the initial stage where the spray is dense; this may be due to the much higher injection pressure, compared to the ambient pressure, dominating the fluid behaviour at the dense spray region. Therefore the effect of the ambient pressure can be neglected at this region. So the initial penetration is determined by the initial liquid velocity, instead of the ambient conditions. After this time, the spray becomes thin and the effect of aerodynamic force gradually increases, which means the fluid properties will be affected by the ambient conditions increasingly beyond this time.

This can be explained by the droplet velocity being slowed down by the drag force, since there is a higher contact probability for droplets and the surrounding gas in the diluted spray region. There is no doubt that higher ambient pressure will result in higher ambient density and which will in turn lead to greater drag force. So the result presented in Figure 5-4 is expected: higher ambient pressure decreases the penetration length significantly after the initial stage. However, compared to diesel and G50, pure gasoline (G100) experiences less influence when increasing the ambient pressure. The most likely reason is as follows: the gasoline spray is easier to be atomized and the atomization and breakup processes mainly occur at the dense spray region, so the droplet of the gasoline spray will experience fewer breakups in the later stage. While the diesel and dieseline sprays will not only experience the drag force, but also will lose kinetic energy due to further breakups.

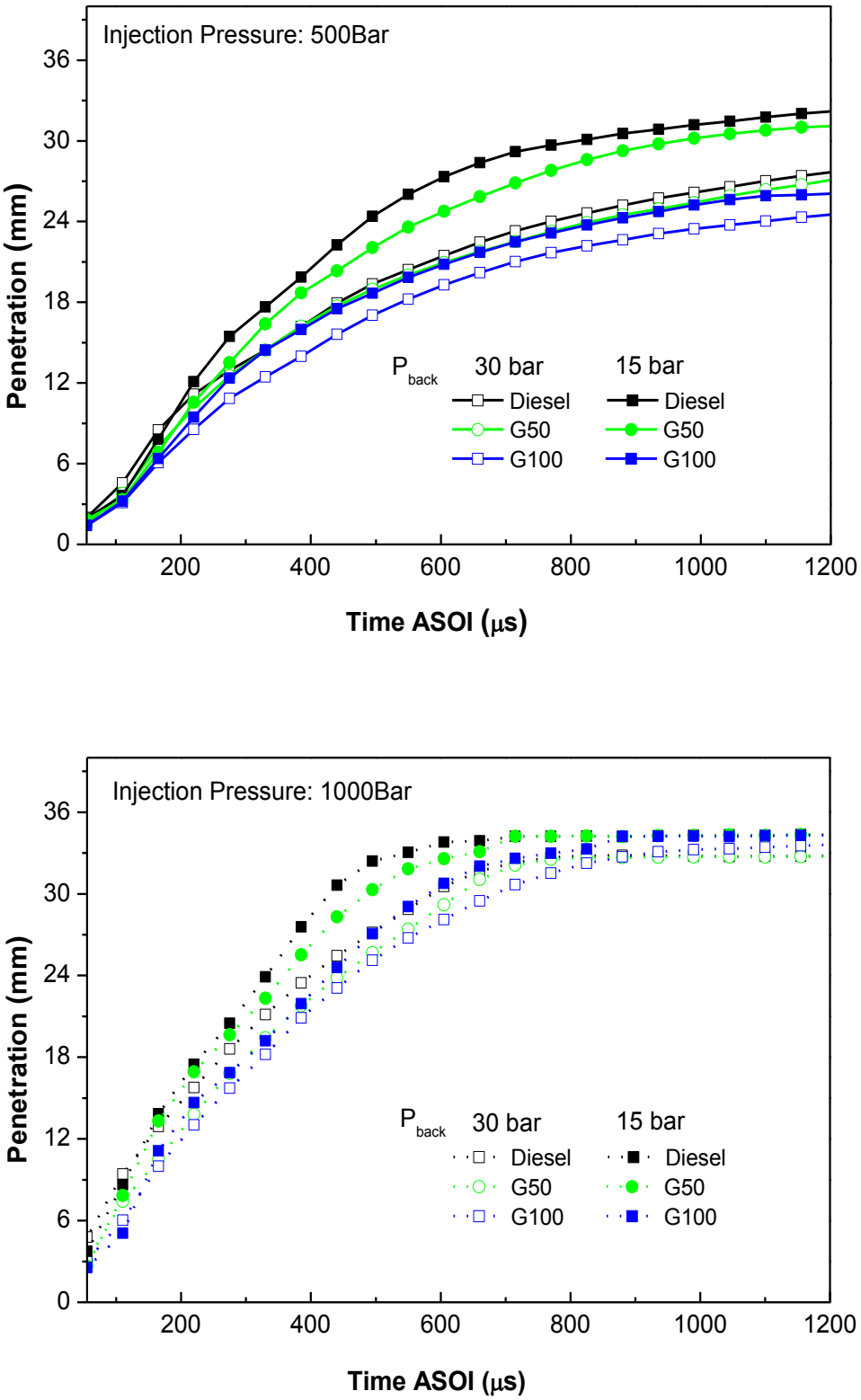

Figure 5-4 Effect of ambient pressure on penetrations of diesel, dieseline (G50), and gasoline (G100) sprays under different injection pressures

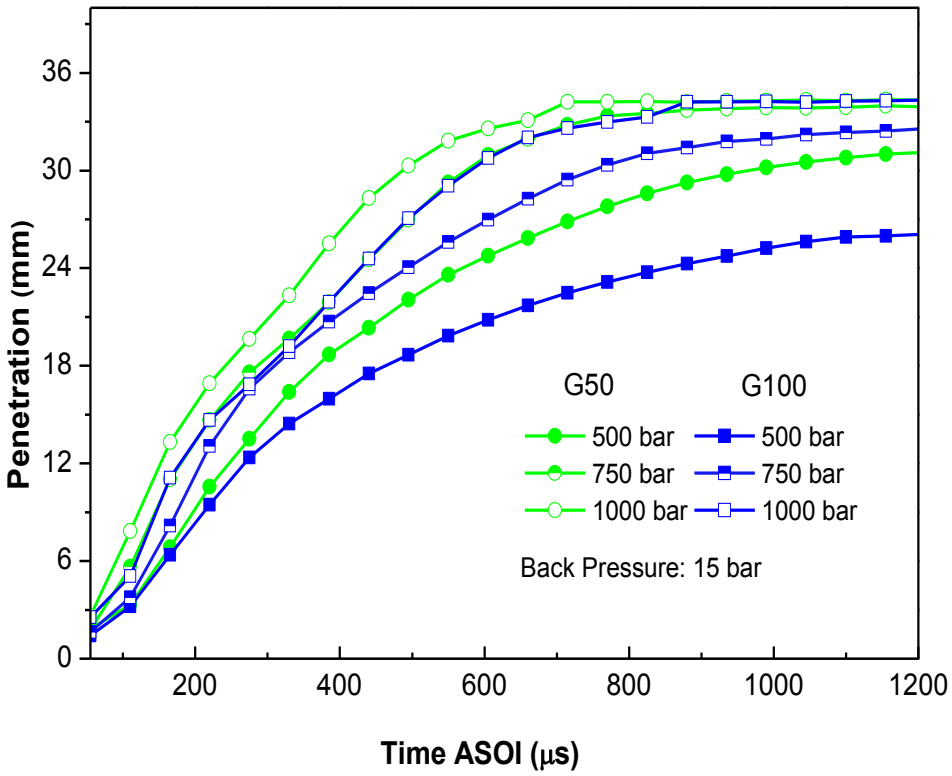

Figure 5-5 Effect of injection pressure on penetrations of dieseline (G50) and gasoline (G100) sprays (15 bar ambient pressure)

As is shown in Figure 5-5, increasing the injection pressure will gradually increase the penetration length for both G50 and G100. Compared to the effect of ambient pressure presented in Figure 5-4, injection pressure plays a more important role in affecting gasoline's penetration length under the presented testing conditions. This is due to the injection pressure directly affecting the initial liquid velocity and momentum; a higher injection pressure will have a positive effect on the penetration length. In other words, for a certain injector, the initial velocity of the spray tip is determined by the injection pressure rather than the ambient condition. The ambient pressure can only affect the spray behaviour at a later stage compared to the injection pressure.

5.3.4 Droplet Size and Velocity Comparison of Diesel and Dieseline Sprays under Different Gasoline/Diesel Blending Ratios

The effect of the gasoline/diesel blending ratio on the droplet mean diameter (MD) is shown in Figure 5-6, where the test position is set at 40 mm downstream of the nozzle and the test ambient condition is atmospheric. It can be seen from this diagram that the mean diameter decreases gradually with the increase of the gasoline/diesel blending ratio at all injection pressures. This result is consistent with the penetration analysis. The lower density and viscosity of gasoline make it more favourable to enhance the atomization process and form smaller droplets. In addition, gasoline may have stronger cavitation than diesel inside the injector and thus better spray atomization at the injector exit. Furthermore, gasoline has a higher vapour pressure which indicates a higher evaporation rate than diesel at a given temperature. This will also contribute to its smaller droplet size.

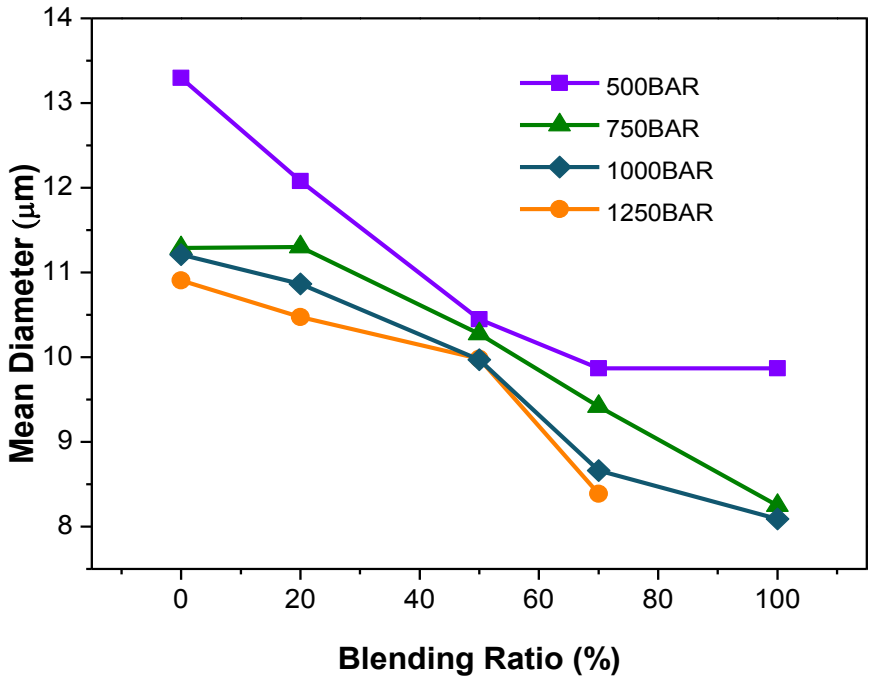

Figure 5-6 Effect of gasoline/diesel blending ratio on droplet mean diameter (MD) under different injection pressures (position of 40 mm, 1 bar ambient pressure)

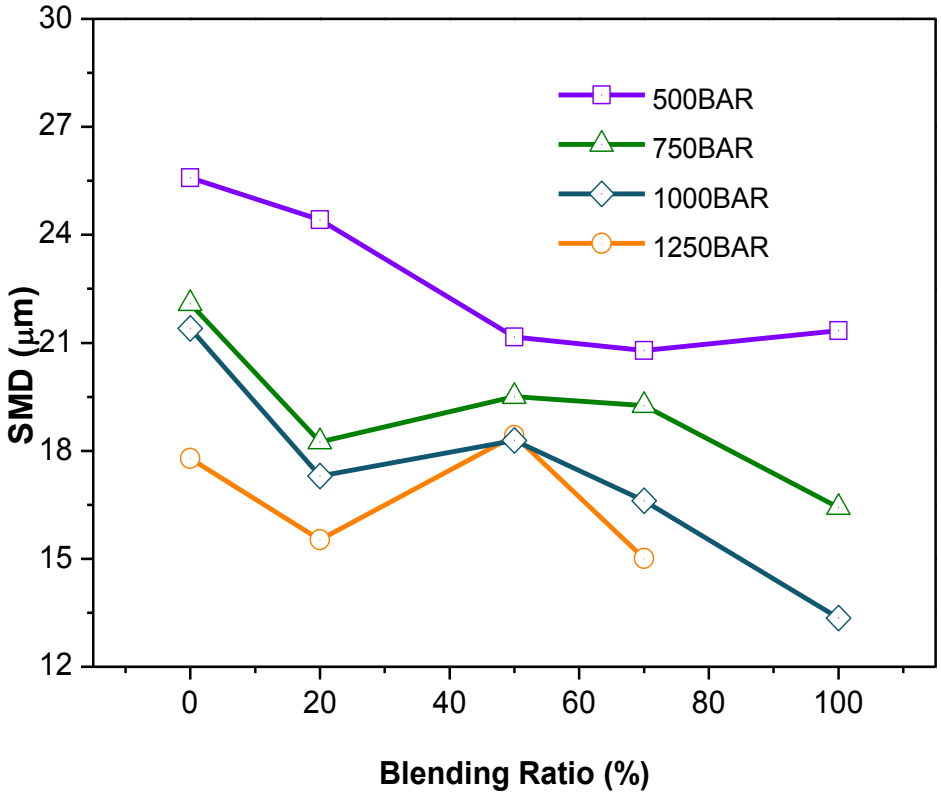

Figure 5-7 Effect of gasoline/diesel blending ratio on droplet Sauter Mean Diameter (SMD) under different injection pressures (position of 40 mm, 1 bar ambient pressure)

A similar trend can be found in Figure 5-7, which indicates the Sauter Mean Diameter (SMD) evolution with the increase of gasoline/diesel blending ratio; the test position and conditions are the same as those in Figure 5-6. As discussed in the previous chapter, the SMD indicates the volume/surface ratio and it is an intuitive parameter to evaluate the spray atomization and evaporation qualities, which in turn affect the fuel/air mixing and combustion of engines. Overall, the SMD decreases with the increase of gasoline/diesel blending ratio at all injection pressures, despite slight fluctuations at some certain blending ratios. This result again proves that the gasoline component in dieseline helps to achieve better atomization of the fuel spray and better mixture formation performance of engines.

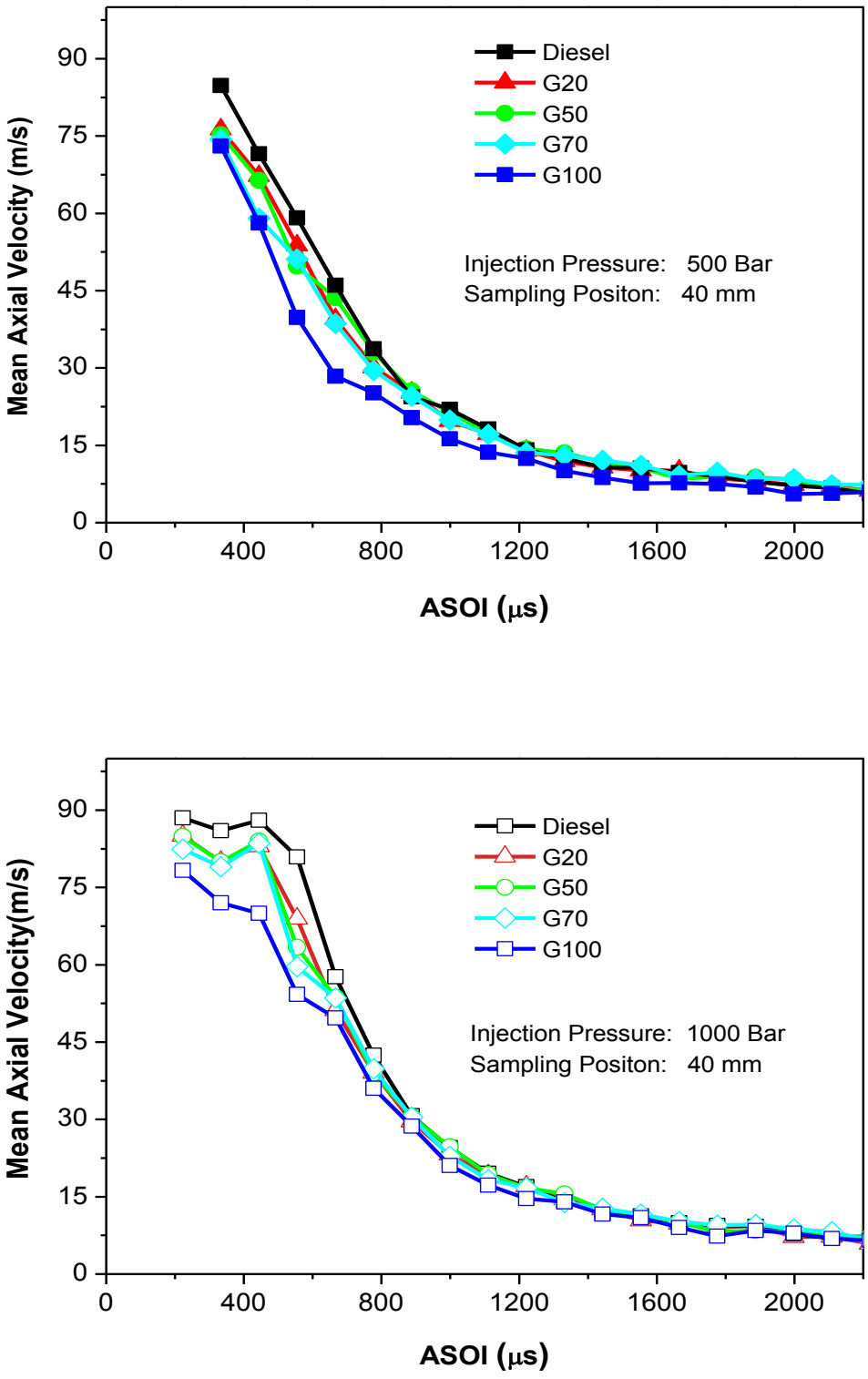

Figure 5-8 Effect of gasoline/diesel blending ratio on mean droplet velocity under different injection pressures (position of 40 mm, 1 bar ambient pressure)

Figure 5-8 shows the effect of gasoline/diesel blending ratio on droplet mean velocity at 40 mm downstream of the nozzle and at an atmospheric ambient condition. As expected, increasing gasoline/diesel blending ratio decreases the droplet mean velocity. This is again consistent with the penetration and droplet size analysis. As analysed above, the existence of the gasoline component in dieseline fuel enhances the atomization and breakup processes. Thus the kinetic energy of the liquid droplet continuously decreases due to the breakups and drag resistance and then the energy loss in turn slows down the droplet velocity. It can be seen that, compared to the result at 500 bar injection condition, the droplet mean velocity experiences less influence from the gasoline/diesel blending ratio at higher injection pressure. In other words, the effect of injection pressure plays a more important role than the gasoline/diesel blending ratio and increasing the injection pressure will weaken the difference caused by the gasoline/diesel blending ratio.

5.3.5 Droplet Size Comparison of Diesel and Dieseline Sprays under Different Injection Pressures

The effects of injection pressure on droplet mean diameter and Sauter Mean Diameter are shown in Figure 5-9 and Figure 5-10, respectively. In Figure 5-9, with the increase of injection pressure, the mean diameter decreases significantly at the very beginning (from 500 bar to 750 bar) and then experiences a slow decline beyond this pressure. However, in terms of the SMD, as is shown in Figure 5-10, the droplet size decreases gradually as injection pressure increases. The possible reason for the different trends between the MD and SMD may be summarised as follows: the increase of injection pressure narrows the range of the droplet diameters, which means the droplet size distribution is forced towards to a uniform distribution and the portions of the largest and smallest droplets are reduced. At low injection pressure, the mean diameter

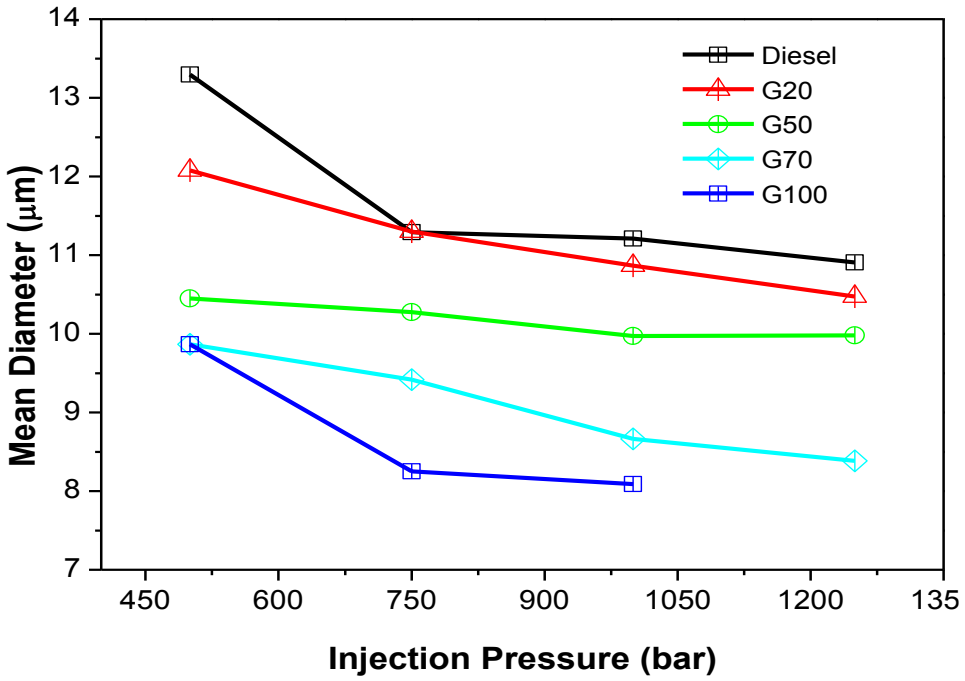

Figure 5-9 Effect of injection pressure on droplet mean diameter (MD) under different gasoline/diesel blending ratios (position of 40 mm, 1 bar ambient pressure)

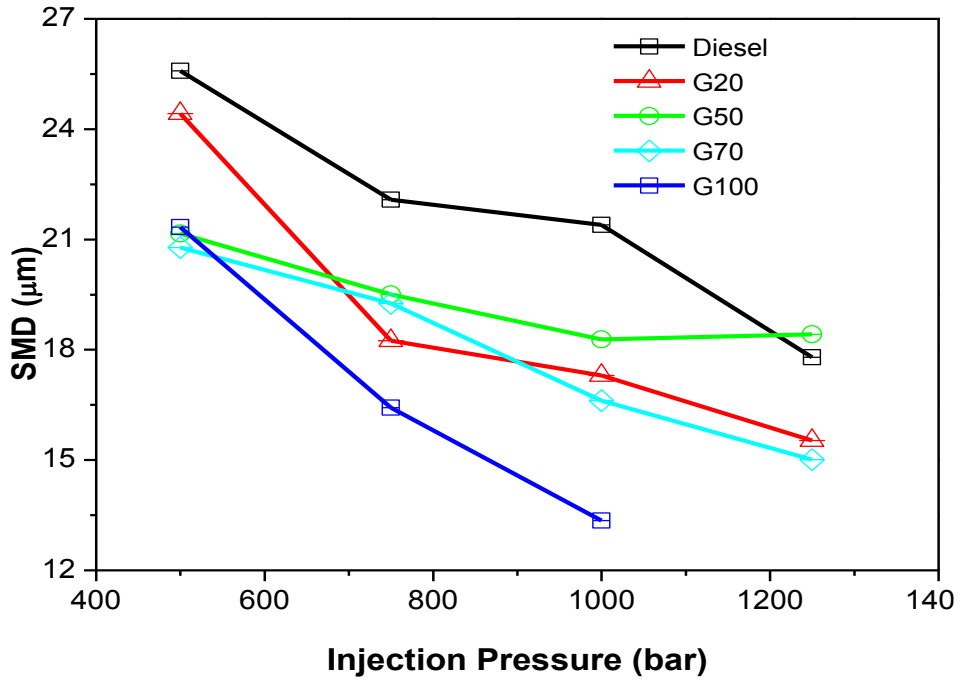

Figure 5-10 Effect of injection pressure on droplet Sauter Mean Diameter (SMD) under different gasoline/diesel blending ratios (position of 40 mm, 1 bar ambient pressure)

can be affected by the individual large droplet easily; while at high injection pressure, the droplet size distribution becomes more uniform and the mean diameter experiences less impact from the large droplets. Thus the droplet mean diameter is more sensitive to the injection pressure at the lower pressure range. While the SMD represents the volume/surface ratio and will not be affected by the individual large or the small droplet as much as the MD, therefore it is a more representative parameter to evaluate the spray atomization performance. The increase of injection pressure is favourable for decreasing the SMD and enhances the atomization of the spray. Another phenomenon which can be found in these two figures is that increasing the gasoline/diesel blending ratio will also benefit the atomization of the spray, despite the small fluctuation of G50. This is also consistent with the previous analysis of the effect of gasoline/diesel blending ratio on the droplet size.

5.3.6 Fuel Droplet Size and Velocity Distribution

To have a holistic view of the atomization characteristics of dieseline throughout the spray region, fuel droplet size and velocity distribution along the spray axis are investigated in this section. Figure 5-11 and Figure 5-12 show the droplet mean diameter distribution and SMD distribution along the spray axis of dieseline (G50), pure gasoline (G100) and pure diesel under 750 bar injection pressure and atmospheric conditions. It can be seen that, for all of the three fuels, the droplet mean diameter for each fuel does not change much and experiences a slight increase along the spray axis. However, the SMD distribution along the spray axis shows a slightly different trend: it decreases significantly when the sampling position moves from 10 mm to 20 mm downstream and then does not change much beyond this distance. The reason for this difference is as follows: the smaller droplets are slowed down by the drag force or evaporated gradually during the transition, so some smaller droplets cannot reach a far distance.

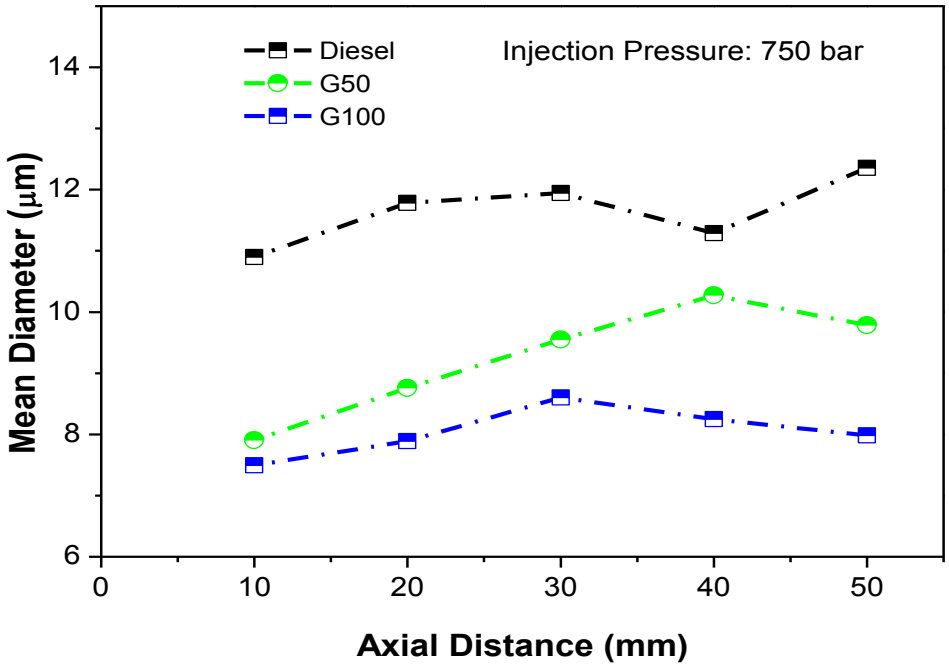

Figure 5-11 Droplet mean diameter (MD) distribution along the spray axis (750 bar injection pressure, 1 bar ambient pressure)

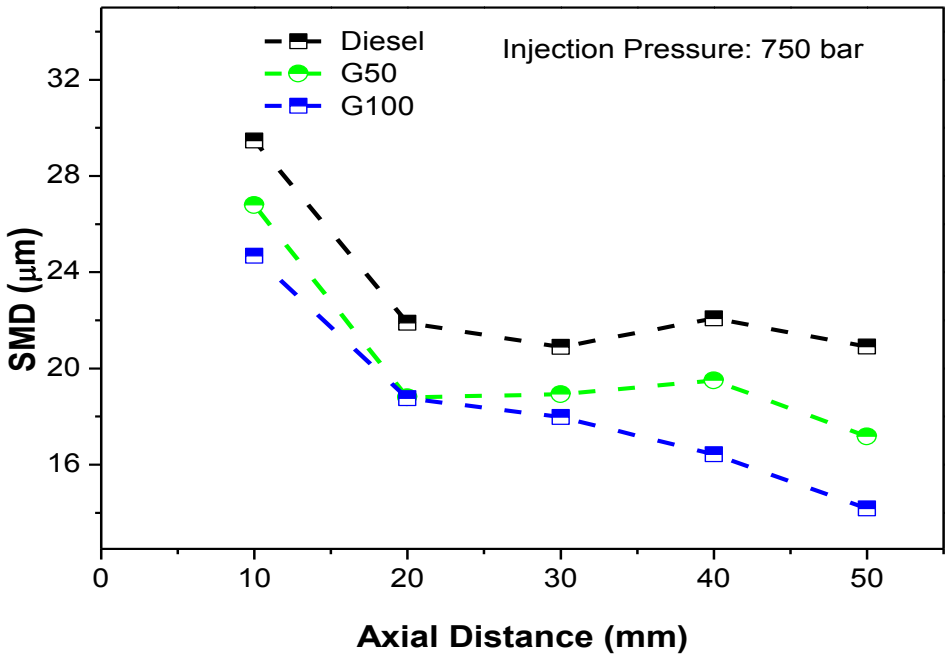

Figure 5-12 Droplet Sauter Mean Diameter (SMD) distribution along the spray axis (750 bar injection pressure, 1 bar ambient pressure)

As disscussed previously, the mean diameter is much more easily affected by the individual larger droplet so that a slight increase can be seen in the diagram; while the SMD will not be influenced by the individual larger or smaller droplet easily, so the SMD distribution shows a different trend to the distribution of the mean diameter.

Figure 5-13 depicts the droplet mean velocity evolution of dieseline (G50) at different sampling positions under 750 bar injection pressure and atmosphere conditions. As is shown in the diagram, the droplet mean velocity increases at the very beginning and then decreases rapidly with time. This is due to the initial droplets at the spray tip experiencing more drag force and being decelerated by the surrounding gas; the following droplets have less contact with the surrounding gas and thus show a higher velocity. As compared to downstream of the spray, the droplet peak velocity upstream is higher but decelerates quicker. The higher deceleration

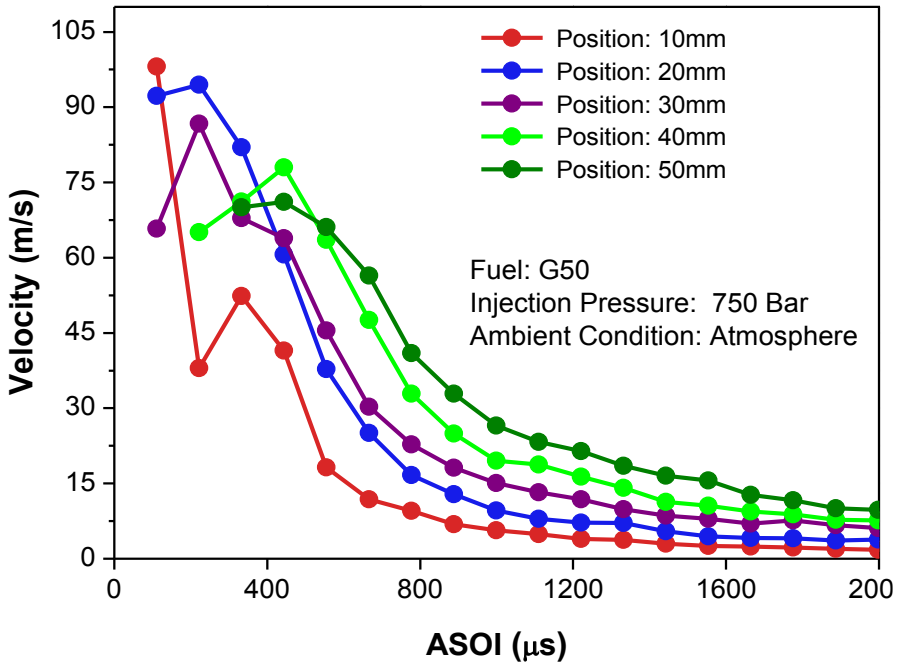

Figure 5-13 Droplet mean velocity of dieseline (G50) at different positions (750 bar injection pressure, 1 bar ambient pressure)

can be associated to the greater drag force induced by the higher droplet velocity. In addition, the spray is much denser near the nozzle and thus more collisions may occur. Similar phenomena also can be found for other fuels at various injection pressures.

Figure 5-14 shows the droplet SMD distribution of diesel, dieseline (G50) and gasoline (G100) under the 750 bar injection pressure and 1 bar ambient pressure. It can be seen that for all the three fuels, the droplet size at the centre of the spray jet is smaller than that at the periphery. These findings are consistent with the study in [141-143]. The most possible explanations for this are as follows:

Firstly, the droplet velocity and the turbulence at the centre of the spray jet are at a much higher level compared to that at the periphery; this will result in a greater spray breakup rate and produce smaller droplets within this centre zone. Meanwhile, the droplets at the periphery of the spray jet experience a much lower breakup rate due to their lower velocity and show a bigger droplet size distribution.

Secondly, the vortex motion of the surrounding air, which is induced by the relative movement of the spray, will bring some large droplets to the periphery of the spray jet. On top of that the density of the droplets number at this area is quite low; a bigger droplet SMD then appears at the periphery of the jet.

Thirdly, the density of the droplets number at the centre of the spray jet is very high and may excess the measurement limit of the PDPA system. If too many small droplets enter the measurement volume at one time, the PDPA will reject the measuring result.

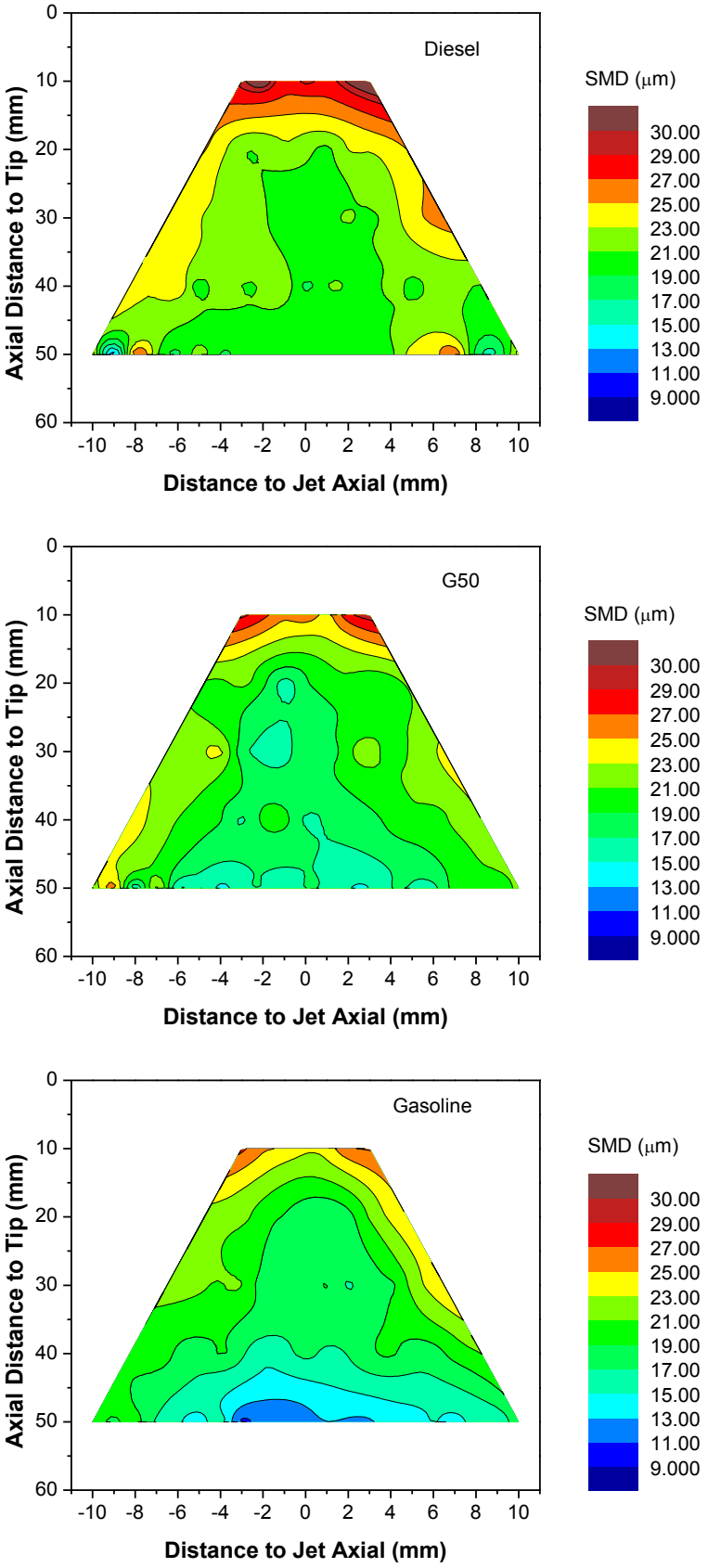

Figure 5-14 Droplet size distribution of diesel, G50, and gasoline (750 bar injection pressure)

5.4 Summary

In this study, the spray characteristics of the diesel engine have been experimentally investigated by using optical approaches such as high-speed photography and PDPA measurement. The effects of injection pressure, ambient pressure, different fuels, including gasoline, diesel and their blends – dieseline and the gasoline/diesel blending ratio on the spray characteristics have been studied in detail. The conclusions drawn from the experimental results are as below:

1. Higher ambient pressure decreases the spray penetration length due to the higher ambient density increasing the aerodynamic drag force and enhancing the atomization and breakup quality. As compared to diesel, the penetration length of gasoline (G100) is less sensitive to the change of ambient pressure.

2. For all the tested fuels, higher injection pressure led to a longer penetration length and improved the atomization and breakup performance. Higher injection pressure results in stronger turbulence, cavitation and aerodynamic force, which helps to enhance the atomization process. Thus the injection pressure is one of the dominating parameters in affecting the fuel spray.

3. The gasoline/diesel blending ratio plays an important role in affecting the spray penetration length. With the increase of the gasoline/diesel blending ratio, the penetration length decreases gradually at low injection pressure and low ambient pressure conditions. While at high injection pressure and high ambient pressure, this trend becomes less significant.

4. With the increase of the gasoline/diesel blending ratio, the droplet SMD decreases significantly at all test conditions, which indicates a better atomization quality can be achieved by increasing the proportion of gasoline in the dieseline fuel. The droplet mean velocity can be also decreased as this ratio increases, which is consistent with the result of the spray penetration.

CHAPTER 6
GASOLINE SPRAY MODEL DEVELOPMENT AND VALIDATION

In this chapter, a numerical study of gasoline spray characteristics has been carried out and a hybrid spray breakup model, named as the 'Turbulence-Ligament-KH-RT' (TL-KHRT) model, was proposed based on the analysis of the turbulence and ligament evolutions. The new model was validated with high-speed imaging and the PDPA experiments. The TL-KHRT model is an effective supplement to the original KHRT breakup mechanism and helps to achieve accurate CFD modelling of the fuel spray and mixture formations.

6.1 Introduction

In GDI engines, the fuel spray atomization process is known to play a key role in affecting mixture formation, combustion efficiency and soot emissions. Therefore, a thorough understanding of the fuel spray characteristics and atomization process is of great importance. The spray atomization and breakup processes are typical two-phase flow phenomena which are affected by turbulence fluctuation, vortices, cavitation effect and aerodynamic force [80, 97, 144-147]. As a combined result of these effects, the injected liquid fuel is disintegrated into liquid segments and ligaments and then smaller droplets will be shed off from these discontinuous liquid elements to form the atomized spray. According to the previous study in Chapter 4, the turbulence is believed to be a most important factor in affecting the primary breakup.

A series of numerical models based on these mechanisms under a Lagrangian framework have been developed by researchers to simulate the spray atomization process in direct injection engines. Some earlier studies [56, 60, 98, 148] do not distinguish the primary breakup and the secondary breakup process and only adopt a single mechanism into the breakup model to simulate the spray atomization process. However, the primary breakup process and the secondary breakup process are dominated by different mechanisms. The former is mainly caused by the combined effect of turbulence fluctuation, cavitation and aerodynamic force; while the latter is mostly induced by the aerodynamic force. Obviously, it is more reasonable to develop hybrid breakup models which could simulate the two breakup processes separately. In the literature, Reitz et al [99] developed a widely used hybrid model which distinguished the primary breakup and the secondary breakup processes by adopting Kelvin-Helmholtz and Rayleigh-Taylor (KH-RT) breakup theories respectively[149]. Nevertheless, this model is still based on the aerodynamically-induced breakup mechanism only. Huh et al [80] developed a turbulence-induced breakup model for the primary atomization process and considered both the turbulence effect and the aerodynamic force in their study. Som et al [104] developed the Kelvin-Helmholtz-Aerodynamics-Cavitation-Turbulence (KH-ACT) model, which improved the primary breakup by considering cavitation and turbulence. Li et al [150] proposed the Huh-Gosman-KH-RT hybrid breakup model in their gasoline spray study by considering the turbulence effect.

However, most of the above mentioned spray models are proposed for high pressure diesel spray and only Li's Huh-Gosman-KH-RT model is validated with the gasoline spray data. As is generally known, the lower injection pressure, fuel properties, sac design, lower L/D aspect ratios of the nozzle and stronger spray jet interactions make the turbulence, vortices and cavitation of the fuel spray of the GDI engine differ from those of the diesel engine [151].

Therefore, more work on the investigations of the gasoline spray is required and this study focuses on the effect of turbulence on the spray atomization process.

Studies [152-154] show that the primary breakup of a turbulent liquid jet was mainly associated with the formation of ligaments along the liquid surface. In this study, a hybrid breakup model, called the 'Turbulence-Ligament-KH-RT' (TL-KHRT) model was developed based on the analysis of the ligament evolution. The comparison of the simulation results of the TL-KHRT model and the KHRT model shows that the TL-KHRT model is an effective supplement to the original KHRT breakup mechanism and helps to achieve accurate CFD modelling of the fuel spray and mixture formations..

6.2 Gasoline Spray Model Development

6.2.1 TL-KHRT Breakup Model

As discussed in Chapter 4, the primary breakup process of the fuel spray of the DISI engine is mainly affected by the turbulence effect and aerodynamic force, which agrees with the findings in [150, 152]. Other studies [155-157] show that the cavitation phenomenon is also another important factor to affect the primary breakup process; however, most of the numerical studies on the fuel spray of the DISI engine neglect the effect of cavitation due to the uncertainty of the injector parameters, such as the sac structure and the nozzle inlet R/D ratio and the relatively low injection pressure compared to that of the diesel spray [150]. Therefore, it is assumed in this work that the primary breakup process of the DISI engine spray is mainly induced by the turbulence and aerodynamic force.

Sallam et al [153] and Brusiani et al [152] studied that the primary breakup of a turbulent liquid jet was associated with the formation of ligaments along the liquid surface. Figure 6-1 shows the simplified ligament along the flow surface. In general, the ligament can be described by three parameters: ligament diameter D_l, ligament length L_l and ligament angle Φ; D_l is found to be proportional to the characteristic size λ_l of the ligament eddy; and λ_l can be calculated by equating the kinetic energy of the ligament eddy to the surface tension energy required to form the ligament itself, which can be described as follows:

$$\rho_l \upsilon_\lambda^2 \lambda_l^3 \sim \sigma \lambda_l^2 \tag{6-1}$$

The characteristic eddy velocity v_λ:

$$\upsilon_\lambda \sim \upsilon_0' \left(\frac{\lambda_l}{D/8} \right)^{1/3} \tag{6-2}$$

where v_0' is the average cross stream velocity fluctuation at the jet exit and D is the nozzle hydraulic diameter.

Then the ligament diameter can be obtained by combining Equation (6-1) and Equation (6-2) along with the assumption that the ligament diameter at the onset of ligament formation is proportional to the characteristic eddy size at the onset of ligament formation [153] :

$$D_l = k_l \cdot \left(\frac{U}{\upsilon_0'} \right)^{6/5} We_l^{-3/5} \frac{D}{8} \tag{6-3}$$

where k_l is the size constant; We_l is the ligament Weber number calculated as:

$$We_l = \rho_l U^2 \frac{D}{8} / \sigma \tag{6-4}$$

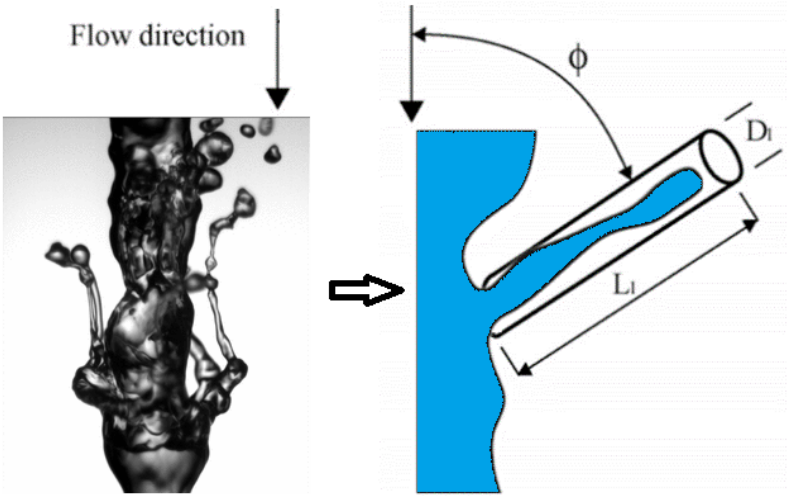

Figure 6-1 A simplified ligament along the flow surface [152, 153, 158]

Based on the ligament breakup mechanism, the characteristic breakup length scale L_{TL} is assumed to be equal to the ligament diameter D_l:

$$L_{TL} = D_l \tag{6-5}$$

It has been found in [152, 153] that Rayleigh breakup at the ligament tip is the dominant breakup mechanism during turbulent primary breakup. So the Rayleigh breakup time required to form a full-length ligament that is ready to produce a drop can be estimated as:

$$\tau_{TL} = k_t \sqrt{\frac{\rho_l D_l^3}{\sigma}} \tag{6-6}$$

where k_t is the breakup time constant.

Within the primary breakup length L_{bu} [159], a competition between the turbulence-ligament and aerodynamically-induced breakup mechanisms is carried out to determine the dominant

primary breakup mechanism in this model. The maximum ratio of length/time scale determines the dominant model during the breakup process:

$$\frac{L_A}{\tau_A} = \max\left\{\frac{L_{KH}}{\tau_{KH}}, \frac{L_{TL}}{\tau_{TL}}\right\} \tag{6-7}$$

where $L_{KH} = r - r_{KH}$ and τ_{KH} are the aerodynamic breakup length and time scales in the KH breakup model.

If $L_A/\tau_A = L_{KH}/\tau_{KH}$, then the KH model is employed. Otherwise the TL model dominates the breakup. The parent droplet size decreases according to Equation (6-8):

$$\frac{dr}{dt} = -k_{TL}\frac{0.5L_{TL}}{t_{TL}} \tag{6-8}$$

where k_{TL} is the model constant.

The child droplet parcels with the drop diameter D_l are created by the turbulence-induced breakup once the shed mass exceeds 5% of the initial parcel mass. Beyond the primary breakup length, the secondary breakup model is employed.

The secondary breakup process is mainly dominated by the aerodynamically-induced breakup mechanism. The KH-RT breakup model, which was introduced previously, is employed to manage the size reduction of the secondary droplets generated by the primary breakup process, as well as the droplets beyond the breakup length [159]. The KH-RT secondary breakup model is closely coupled with the TL primary breakup model in this study.

6.2.2 Model Computing Process

The detail of the computing process of the TL-KHRT model is shown in Figure 6-2.

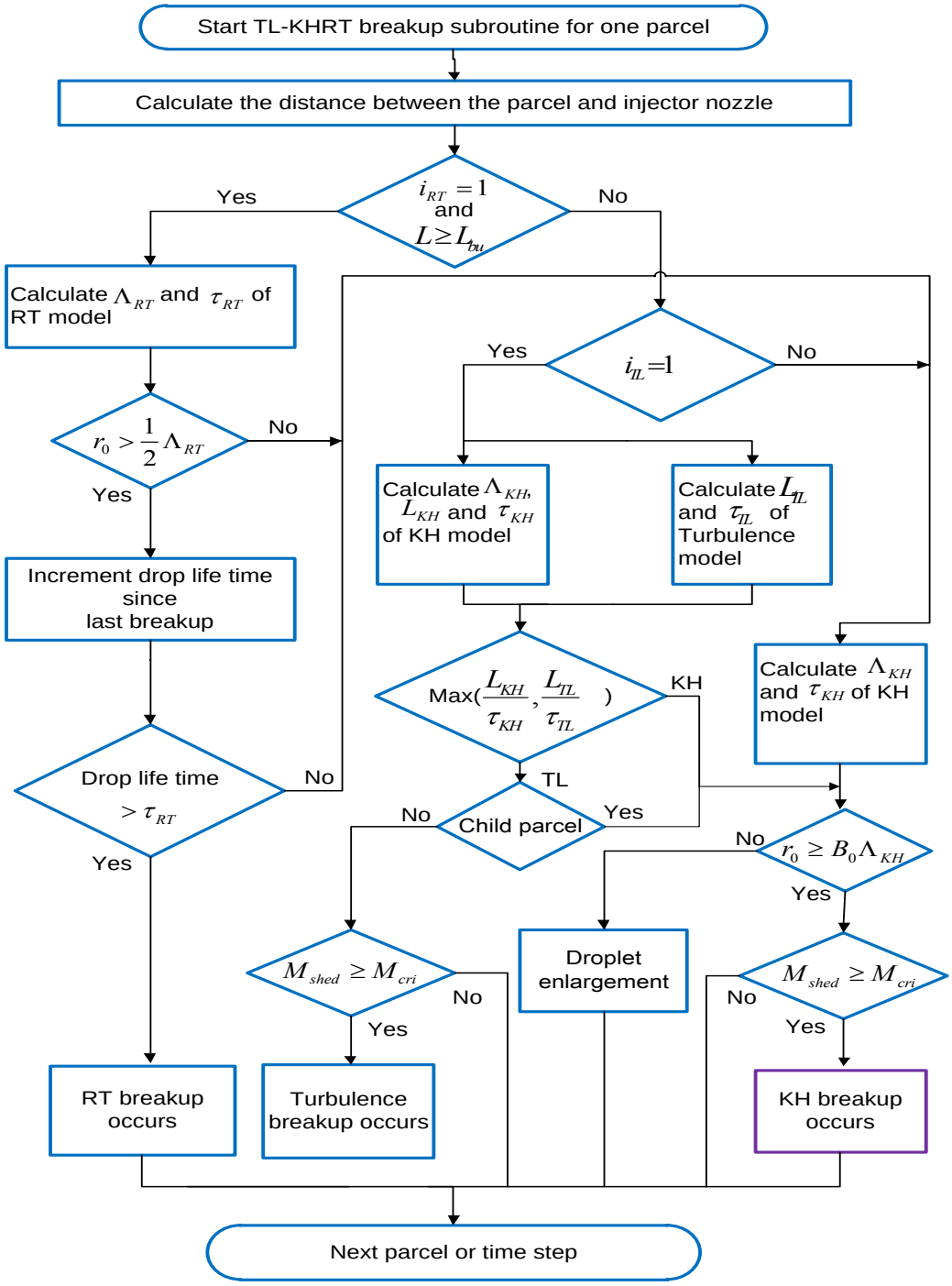

Figure 6-2 Flow chart of the proposed TL-KHRT model

6.3 Simulation Settings

Figure 6-3 shows a cylindrical numerical grid with 40 mm diameter and 100 mm depth. The average cell size of the grid is set to 1.0 mm and the total cell number is 38591. The injector tip is located at the top centre of the cylinder and in order to simplify the modelling process, only one jet (shown in Figure 6-4) of the spray is simulated vertically downwards along the cylinder axis.

In order to compare the accuracy of the spray breakup simulation by using the proposed TL-KHRT model and KHRT model, all the injection parameters and model constants used in the two different models are fixed the same in the whole study and the values of these constants are set as suggested in the literature [57, 60, 99, 152, 153]. Table 6-1 shows some of the key model constants used in this study.

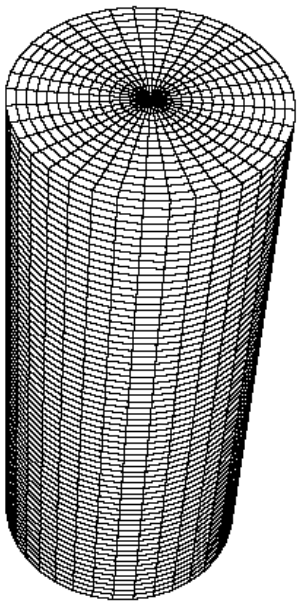

Figure 6-3 Numerical grid for the gasoline spray simulation

Table 6-1 Model constants settings for the gasoline spray simulation

KH		RT		TL		
B_0	B_1	C_0	C_1	k_l	k_t	k_{TL}
0.61	30	1.0	0.35	10	5	1.0

6.4 Validation Experiment

The spray experiment was carried out with a multi-hole GDI injector in the low pressure constant volume vessel under atmospheric conditions and various injection pressures. The schematic of the experiment system [35] has been showed in Chapter 3. A BMW GDI injector with 6 holes and a nozzle diameter of 0.18 mm were used in the experiments. The injector was fuelled with gasoline and controlled by electrical pulses from the Electronic Control Unit (ECU). Spray images were taken from the side view window of the vessel.

Both of the high-speed photography tests and the PDPA tests were carried out at atmospheric pressure (1 bar) and room temperature (298 K). The tests specifications are shown in Table 6-2. Spray images were captured by the ultra-high speed camera with a speed of 18003 frames per second and pixels of 608*600. Figure 6-4 shows a typical image of the full spray.

Table 6-2 Test specifications of gasoline spray validation experiment

Test	T (*K*)	$P_{injection}$ (bar)	P_{back} (bar)	Ambient Density (kg/m^3)	Duration (μs)
Spray Photography	298	100 / 200	1.0	1.29	1000
PDPA	298	100 / 200	1.0	1.29	1000

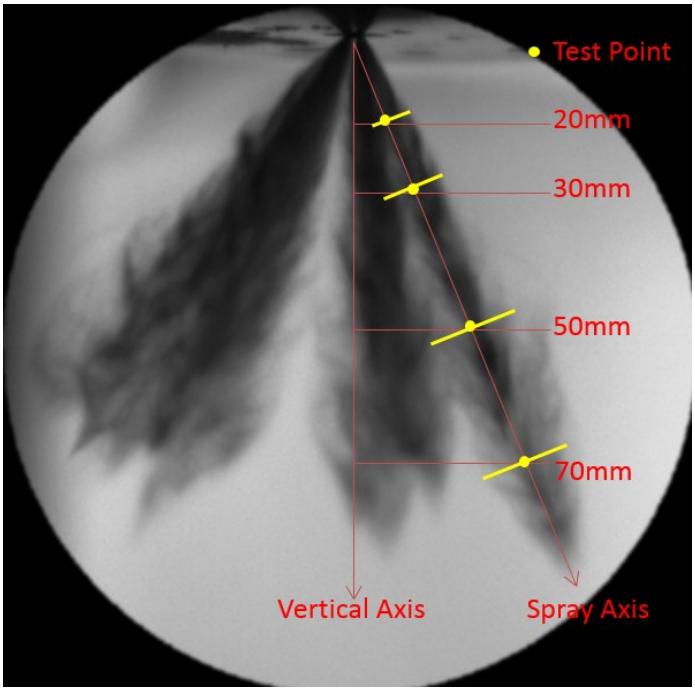

Figure 6-4 Schematic of the PDPA test positions of gasoline spray validation experiment

For the PDPA test, jet 1 is selected to be measured in this study. Four positions including 20, 30, 50 and 70 mm down the vertical axis (approximately 25.4 mm, 38 mm, 63.5 mm and 88.8 mm along the jet axis, respectively) are measured in the test, as is shown in Figure 6-4.

6.5 Validations and Discussion

6.5.1 Spray Penetration

Penetration is one of the most important spray characteristics in the spray study and is always calibrated first when doing the engine simulations. Thus an accurate prediction of the spray penetration made by the spray models is of great importance. The following paragraphs will focus on the spray penetration validation.

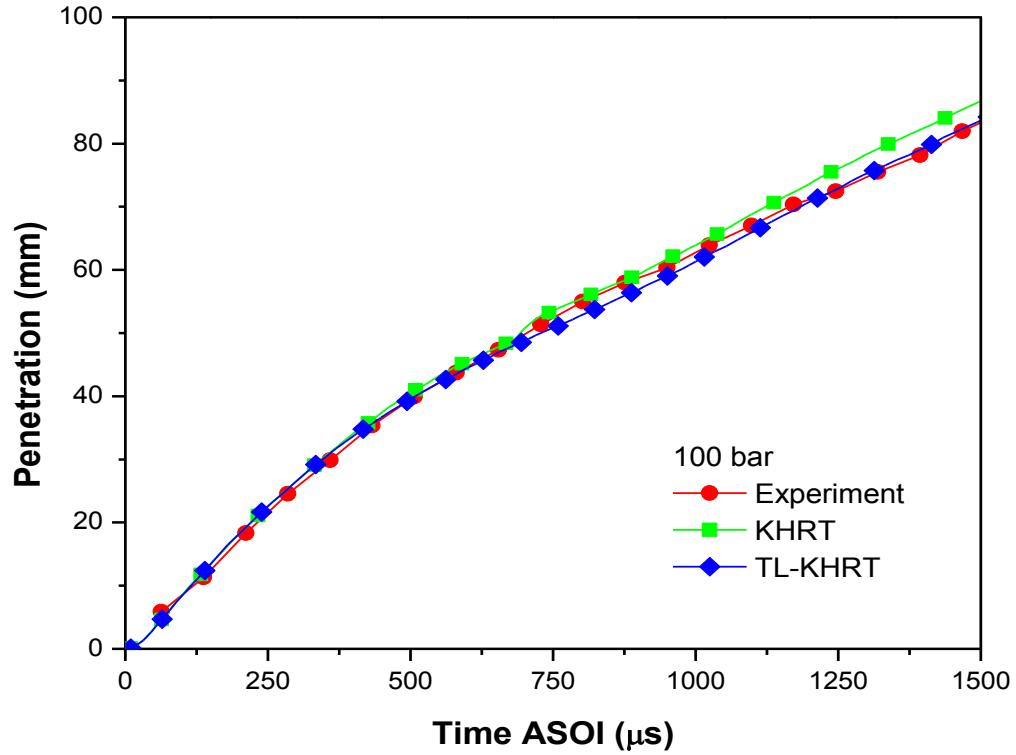

Figure 6-5 Comparison of the effect of different breakup models on gasoline spray penetration (100 bar)

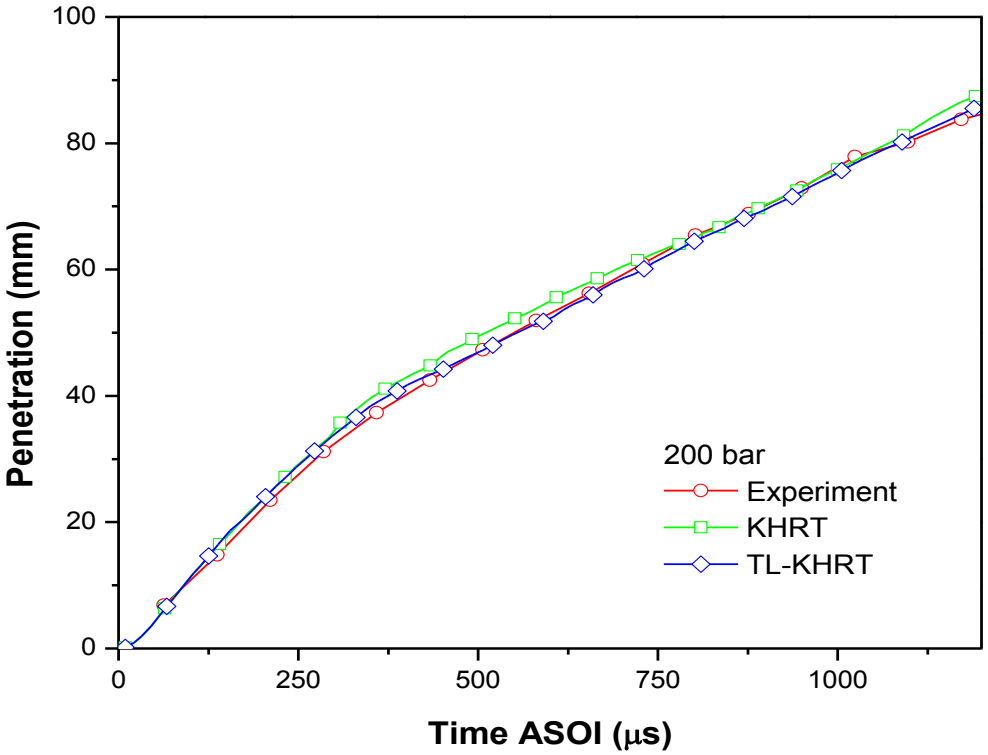

Figure 6-6 Comparison of the effect of different breakup models on gasoline spray penetration (200 bar)

Figure 6-5 and Figure 6-6 present the temporal evolution of the spray penetration of the experiment data and simulation results using KHRT and TL-KHRT breakup models under 100 bar and 200 bar injection pressure, respectively.

For the condition of 100 bar injection pressure, the curves show that both of the models predict the penetration length in good agreement with the experimental data until 750 μs after the start of injection (ASOI). After this time, the divergence of the simulated penetration between the two models starts to increase until the maximum penetration can be captured by the experiment. The penetration length estimated by the TL-KHRT model shows a better agreement with the experiment data all the time, despite some slightly lower values between 750 μs and 1200 μs, which are difficult to distinguish. Conversely, the KHRT model predicts a slightly longer penetration length compared to the experiment data; however, the increment is not significant and is still acceptable.

With the raising of the injection pressure from 100 bar to 200 bar, the spray penetration length shows a trend of increase and reaches its maximum value much earlier. A similar trend can be found in the 200 bar injection condition, as is shown in Figure 6-6. The penetration predicted by the TL-KHRT model is shown to achieve a better agreement with the experimental data during all the injection period; while the KHRT model predicts a slightly longer penetration length compared to the experiment data beyond 250 μs ASOI.

This small discrepancy between the two models can be explained by Figure 6-7, which compares the spray morphography and droplet size simulated by the two models. It can be seen that a larger droplet size is predicted by the KH-RT model and a smaller droplet size is estimated by the TL-KHRT model in both injection conditions, according to the color displayed.

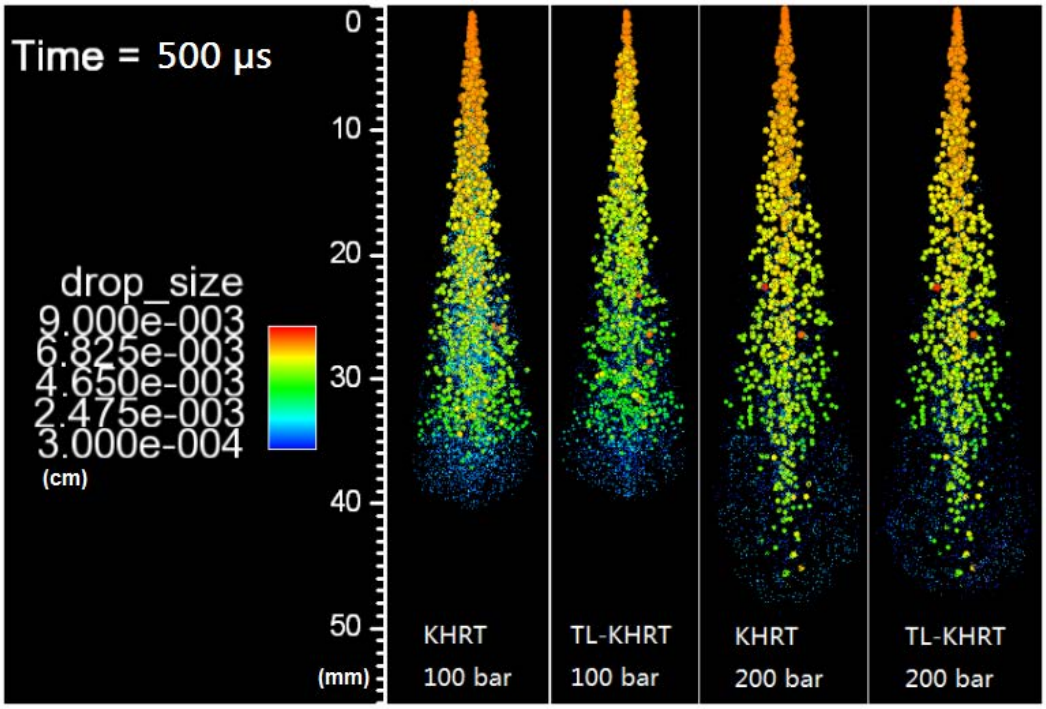

Figure 6-7 Comparison of the effect of different breakup models on the gasoline spray morphography (100 bar and 200 bar)

It is believed that larger droplet size indicates a slower breakup process and a higher droplet velocity, while smaller droplet size indicates a rapid breakup process and a lower droplet velocity; and the different droplet velocities will lead to the longer and shorter penetration lengths, respectively.

6.5.2 Droplet Velocity

Figure 6-8 and Figure 6-9 depict the temporal evolution of the mean droplet velocity in the axial direction at the distance of 38 mm downstream of the nozzle exit. The experiment droplet velocity in the axial direction is calculated by combining the vertical component and the horizontal component measured by the PDPA system.

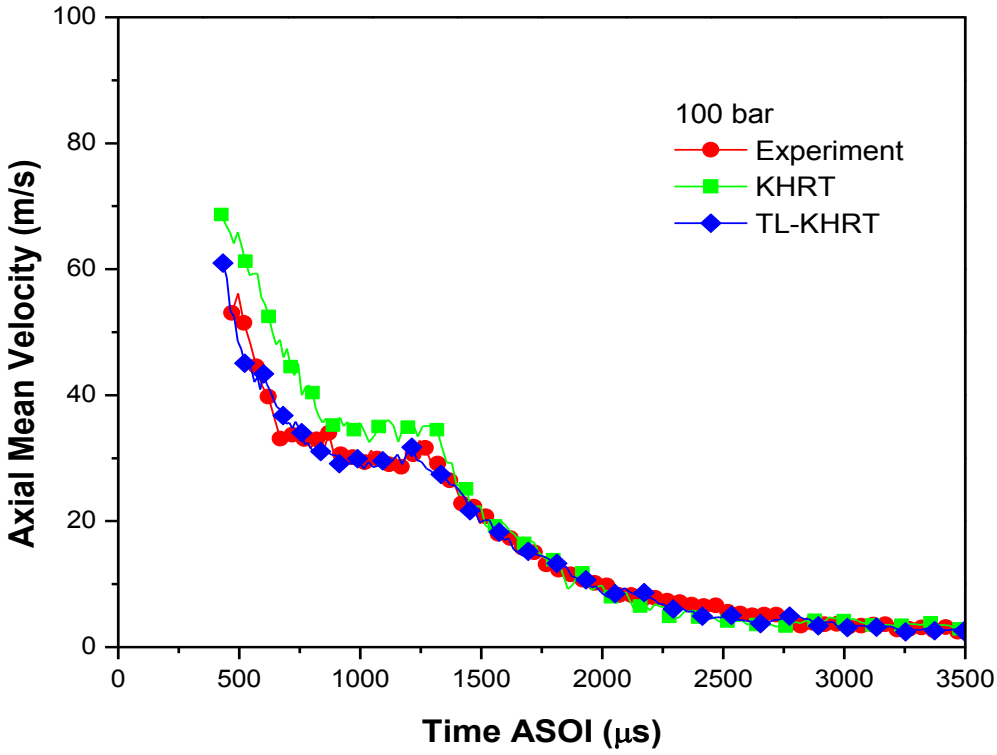

Figure 6-8 Comparison of the effect of different gasoline spray breakup models on droplet axial mean velocity (100 bar, 38 mm)

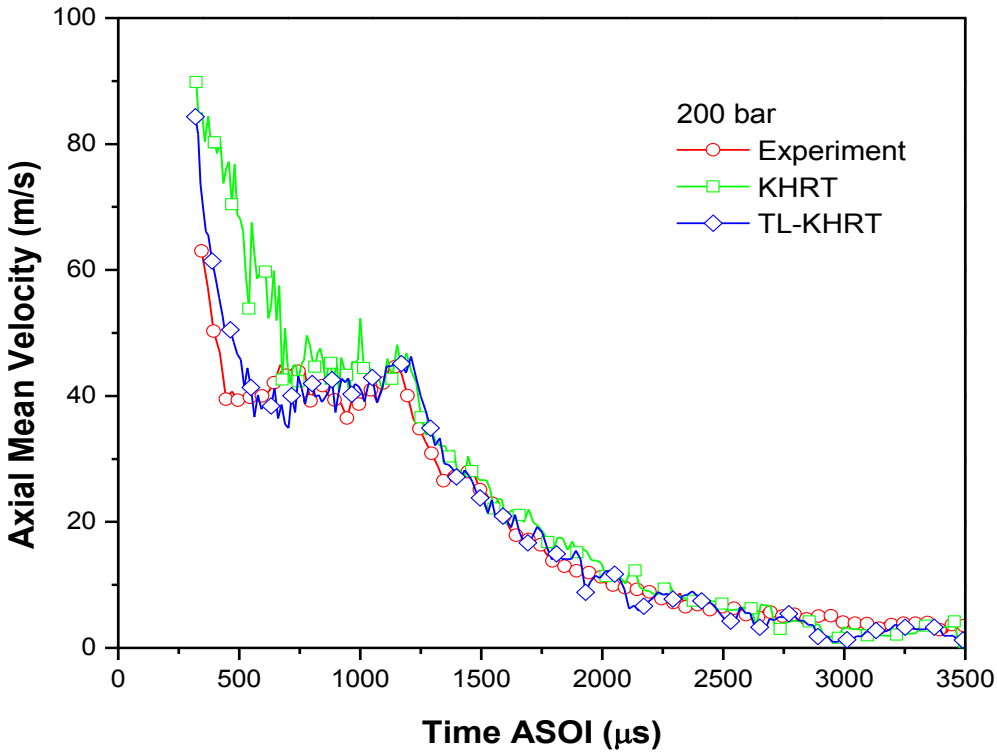

Figure 6-9 Comparison of the effect of different gasoline spray breakup models on droplet axial mean velocity (200 bar, 38 mm)

According to the literature [35, 36], the droplets need some time to arrive at the measurement position after the start of injection, which is the so-called 'arrival time'. After this time, the droplets enter the test volume and the dynamic properties will be captured by the PDPA system. As time goes on, the droplet velocity experiences a quick decrease first and is then followed by a slight increase and a relatively stable period, which together make up the 'spray head'. In the spray head, the droplets in the spray front are firstly decelerated by the drag force and the droplets behind experience relatively less drag force and show a slight increase of velocity. As the spray head passes through the measurement point, a sudden and dramatic velocity drop is observed and this rapid decline process is called 'spray tail'.

The mean axial velocity predicted by the TL-KHRT and KHRT models under 100 bar and 200 bar injection pressure are compared and validated with the PDPA experiment data in Figure 6-8 and Figure 6-9 respectively. The curves in the two figures show that higher injection pressure leads to greater droplet velocity and shorter 'arrival time' in both the simulation results and the experiment data. This indicates that either the new proposed TL-KHRT model or the original KHRT model can capture the trend caused by different injection pressures.

However, not all of the models can predict the velocity in good agreement with the experiment data. In Figure 6-8, it can be seen that the KHRT model over predicts the droplet velocity through all the 'spray head' period and the TL-KHRT model estimates a more accurate result despite some slight fluctuations. Similarly, the same trend can be found in Figure 6-9, under 200 bar injection condition. The droplet velocity simulated by the KHRT model is much higher than the experiment data, especially at the very beginning of the 'spray head'. While the result of the TL-KHRT model is still a good match with that of the PDPA experiment.

This may due to the relatively slower droplet breakup in the KHRT model and the rapid breakup in the TL-KHRT model leading to the droplet's different kinetic energy losing. This is consistent with the analysis in the penetration comparison, in which the higher axial velocity leads to longer penetration length in the KHRT model and the lower axial velocity leads to shorter penetration length in the TL-KHRT model. Obviously, the TL-KHRT model owns the ability to control the droplet velocity properly.

6.5.3 Droplet Size

Droplet size is the characteristic of most concern in the fuel spray simulation since it will represent the performance of the spray atomization directly. Figure 6-10 and Figure 6-11 show the comparison of the temporal evolution of the Average Mean Diameter (AMD) between the simulation results and the PDPA experimental data under 100 bar and 200 bar injection pressures respectively.

As time goes on, the AMD experiences a dramatic decrease at the beginning and then decreases slowly until the end of the 'spray head'. It is believed that the collision and coalescence of the droplets in the spray head lead to a larger AMD in the spray front. A similar result can be found in [160]. To compare Figure 6-10 and Figure 6-11, it can be seen that both of the spray models can predict the trend that the AMD decreases with the raising of the injection pressure.

Similar to the droplet velocity discussed previously, the AMD estimated by the TL-KHRT model is in good agreement with PDPA data while the result predicted by the KHRT model is over predicted significantly in both of the injection conditions.

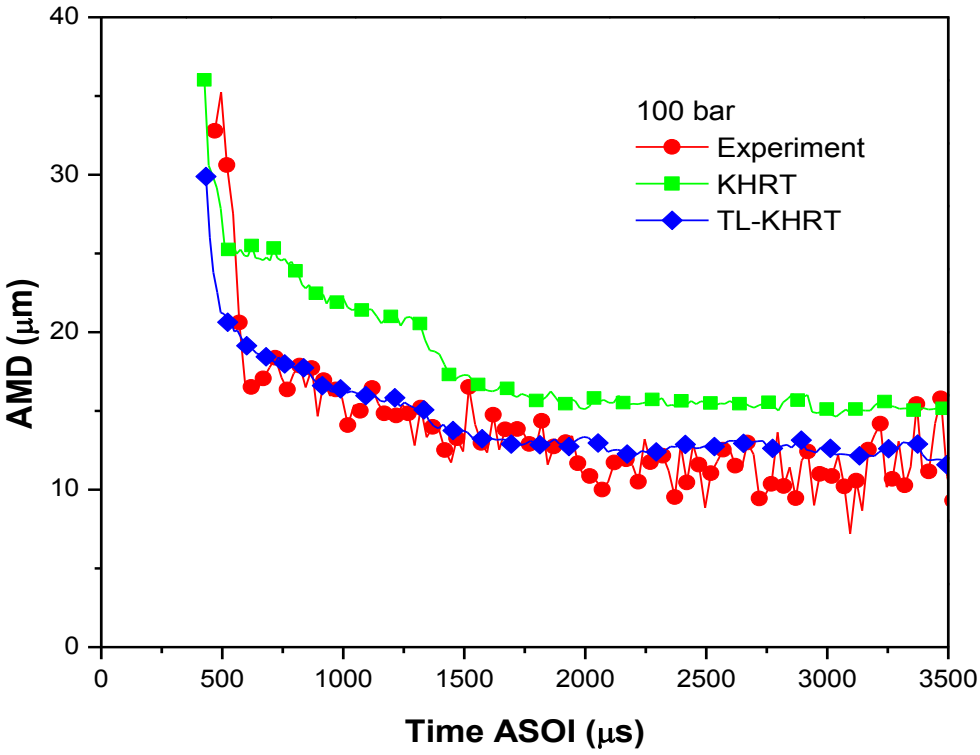

Figure 6-10 Comparison of the effect of different gasoline spray breakup models on droplet AMD evolution (100 bar, 38 mm)

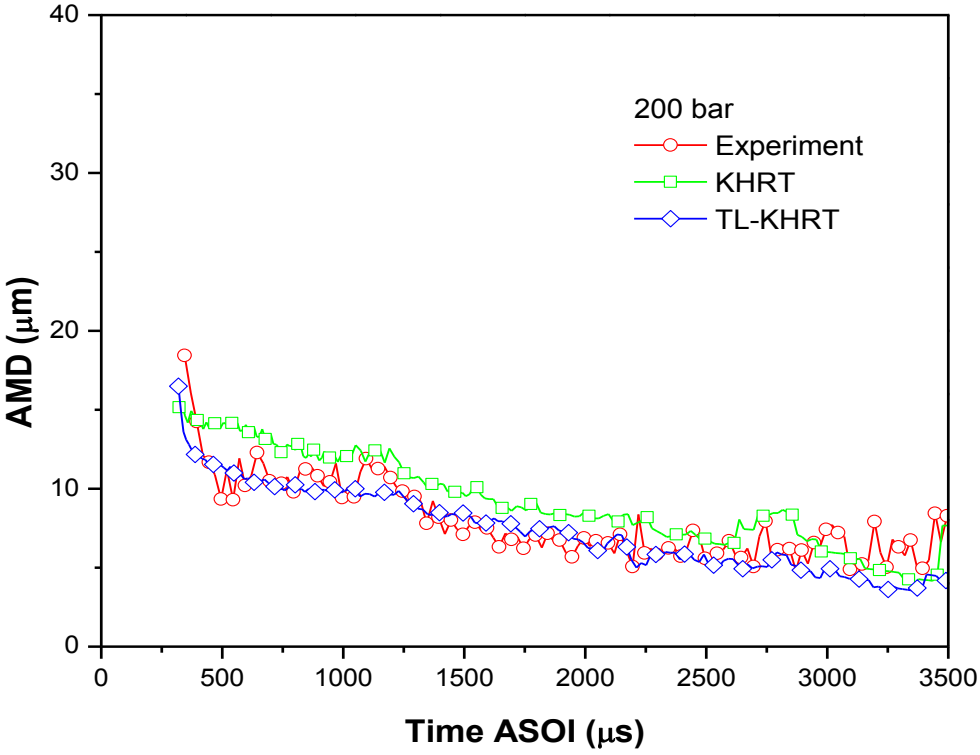

Figure 6-11 Comparison of the effect of different gasoline spray breakup models on droplet AMD evolution (200 bar, 38 mm)

Figure 6-12 and Figure 6-13 present the spatial evolution of the droplet Sauter Mean Diameter (SMD) at the distance of 20 mm, 38 mm, 60 mm and 80 mm downstream of the nozzle exit. The simulation results are compared with the experimental data at 25.4 mm, 38 mm, 63.5 mm and 88.8 mm along the jet axis which have been described in the previous section.

With the increasing of the axial distance from the nozzle, the SMD reduces significantly in the first 40 mm and then keeps a relatively stable trend after this distance. It even shows a slight increase of the SMD in the far distance. The reason for this phenomenon is that the continuous breakups will reduce the droplet size before 40 mm; however, after this distance, the total number of the breakups will be significantly reduced due to the lower droplet velocity. At a far distance, the evaporation of the smaller droplets will result in an increase of the SMD. This agrees with the findings in [161]. Compared to Figure 6-12, Figure 6-13 indicates a smaller SMD value due to its higher injection pressure. This is as expected since higher injection pressure will enhance the breakup process.

Again, the SMD estimated by the TL-KHRT model is in good agreement with PDPA data; while the result predicted by the KHRT model over predicted for both injection conditions. This result is consistent with the spray penetration analysis and droplet velocity analysis again. There are two possible reasons which lead to a better simulation result by the proposed TL-KHRT model. The first is attributed to the turbulence phenomenon inside the liquid enhancing the atomization process and inducing a faster breakup rate of the big droplets. The second is the child droplet size predicted by the new model based on the ligament analysis being closer to the actual value in the spray. The combination of the results will lead to the lower and more accurate SMD prediction of the new model.

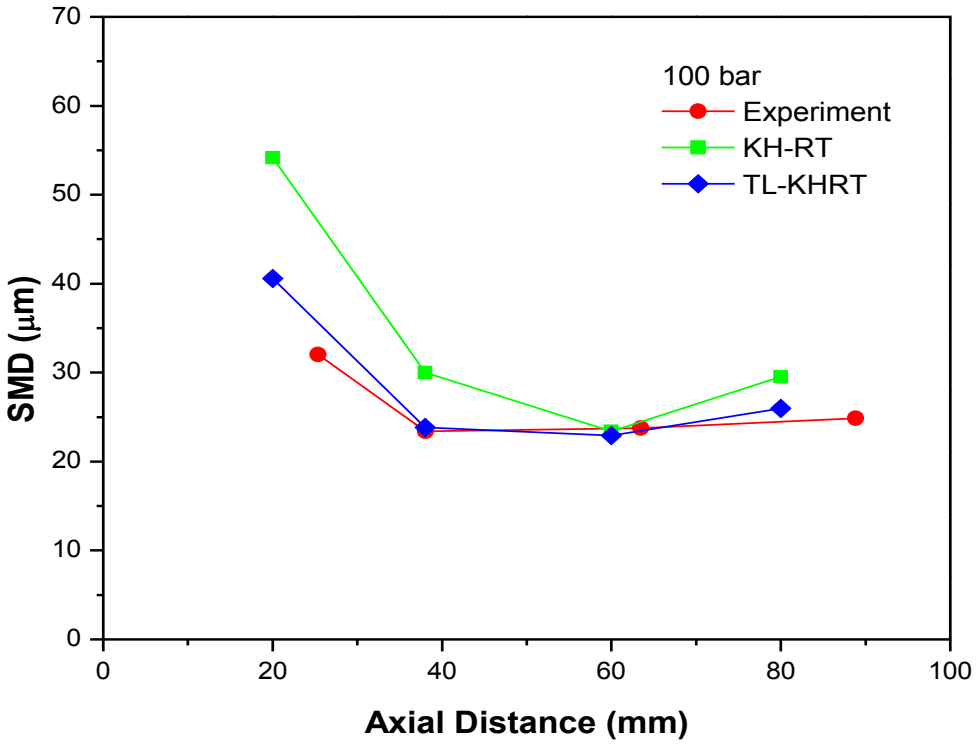

Figure 6-12 Comparison of the effect of different gasoline spray breakup models on droplet SMD evolution (100 bar, 38 mm)

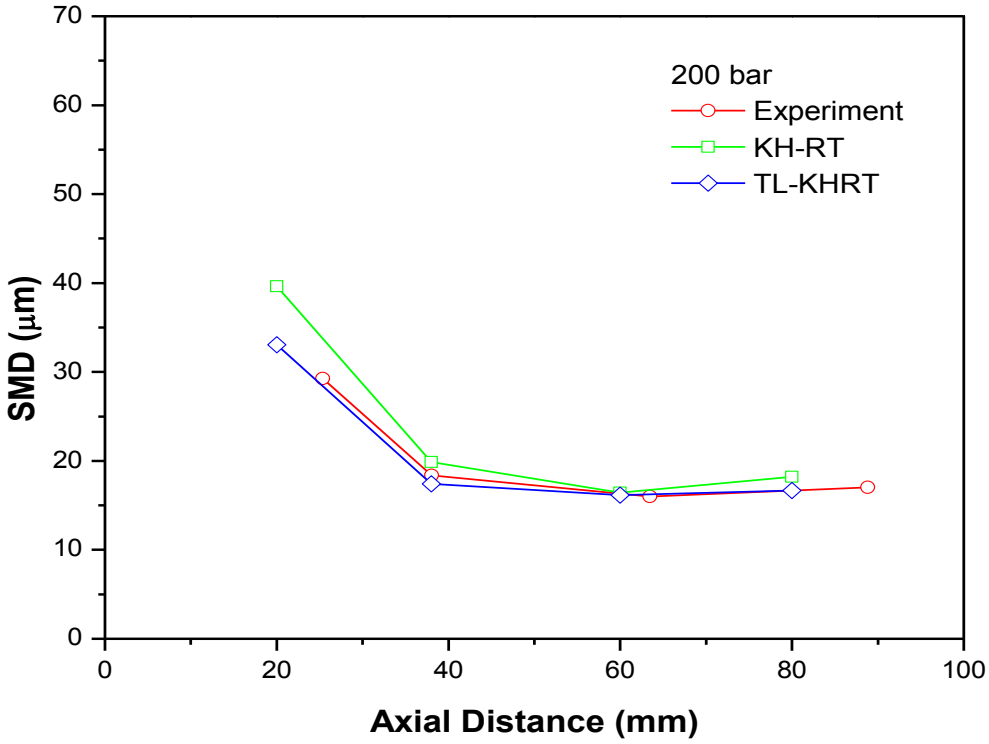

Figure 6-13 Comparison of the effect of different gasoline spray breakup models on droplet SMD evolution (200 bar, 38 mm)

6.5.4 Breakup Statistical Analysis

Spray penetration, droplet velocity, droplet AMD and droplet SMD are the analyses of the macroscopic and microscopic characteristics of the fuel spray which directly exhibit how accurate the prediction can be estimated by the spray models. However, the details of the contribution of each breakup mechanism in the new TL-KHRT model have not been well understood. Figure 6-14 and Figure 6-15 show the breakup statistical results for 100 bar injection and 200 bar injection respectively. The total breakup number and the number of each type of breakup are plotted in the diagram.

It can be seen in both figures that the turbulence-induced breakup dominates the primary breakup process at the beginning of the spray injection and the RT model is the main breakup mechanism for the later secondary breakup process. Before 1000 μs, the number of the turbulence-induced breakup increases gradually. After this period, the RT breakup number will continually increase while the turbulence-induced breakup number will not change much. This is consistent with the previous discussion that the turbulence phenomenon inside the liquid will enhance the primary atomization process.

Another phenomenon can be observed by comparing the two figures: the total breakup number decreases with the raising of the injection pressure from 100 bar to 200 bar. This may due to the fact that higher injection pressure will speed up the decrease rate of the parent droplet size and produce a greater number of child parcels at one time during the breakup. This agrees with the previous discussion of the droplet size evolution, where the droplet size decreases more quickly when increasing the injection pressure.

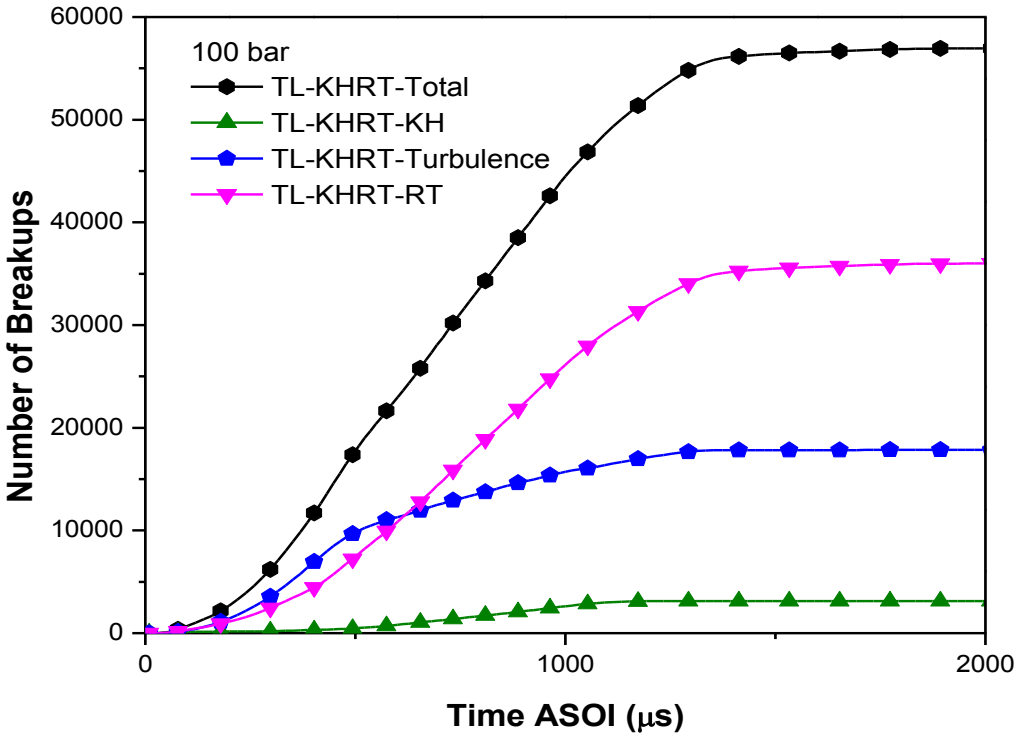

Figure 6-14 Breakup statistical analysis of the TL-KHRT model (100 bar)

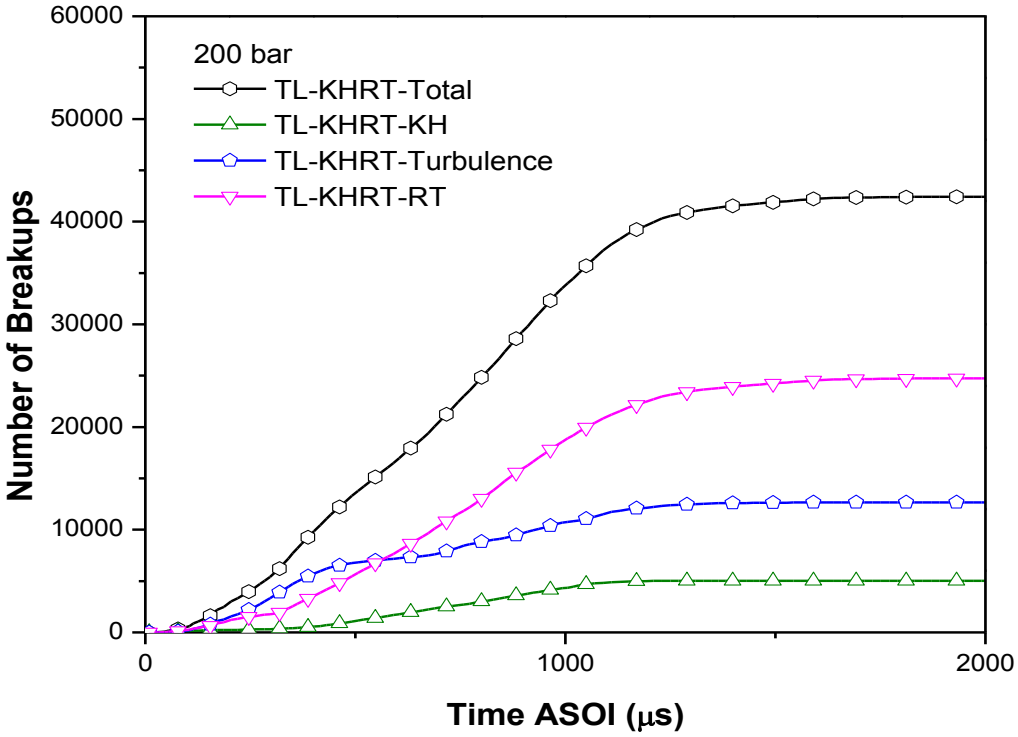

Figure 6-15 Breakup statistical analysis of the TL-KHRT model (200 bar)

6.6 Summary

A turbulence-induced breakup mechanism coupled with aerodynamic instability was developed in this study. The proposed TL-KHRT model improves the simulation accuracy by employing a new droplet breakup mechanism based on the research that the droplet formation is mainly linked to the ligament evolution during the turbulent breakup process. The new model is validated with the high-speed imaging and PDPA experiments and the simulation result shows a good agreement with the experimental data. Conclusions can be drawn from this study as follows:

1. Turbulence from the nozzle has been proved to play an important role in spray breakup and enhance the spray atomization process. By applying the turbulence-ligament breakup mechanism into the spray model, significant improvements in the spray simulation can be achieved.

2. Ligament formation and breakup due to the turbulence-induced instability along the liquid surface are the main causes which result in the primary breakup of the fuel spray. By employing the new droplet generation mechanism based on the ligament evolution, the child droplet size of the new breakup model is proved to be closer to the experimental data than that of the original KHRT model.

3. The spray characteristics such as spray penetration, droplet velocity, droplet AMD and SMD can be clearly predicted by the proposed TL-KHRT model. The simulated spray penetration length of the new model shows better agreement with the high-speed photography data when compared to the slightly longer penetration predicted by the KHRT model. Likewise,

the droplet velocity and droplet size simulated by the TL-KHRT model also present better agreements with the PDPA data.

4. The proposed TL-KHRT model is an effective supplement to the original KHRT breakup model by considering the turbulence and ligament evolution during the spray aromatization process. The development of this model helps to achieve an accurate spray simulation in GDI engines.

CHAPTER 7
DIESEL SPRAY MODEL DEVELOPMENT AND VALIDATION

This chapter focuses on the numerical modelling of diesel spray. In this study, an enhanced Aerodynamic-Cavitation-Turbulence-induced primary breakup model is proposed. The proposed model improves the primary breakup accuracy by optimizing the turbulence induced breakup process; controlling the transition process of the primary and secondary breakups; and employing a new child droplet size function and a new parent droplet size reduction rate. The aerodynamic secondary breakup model has been modified to incorporate with the proposed model and they have been coupled together to simulate the complete spray evolution and better predict the secondary droplet size and velocity. This new model will be validated with the high-speed imaging and Phase Doppler Particle Analyzer (PDPA) experimental results of the full-cone diesel spray in a constant volume vessel under non-evaporating and various injection conditions.

7.1 Introduction

Unlike the gasoline spray modelling, the diesel spray atomization models have experienced more developments since the earlier utilization of direct injection technology in a diesel engine. Various models have been implemented to simulate the spray atomization process in the literature. Some studies do not distinguish the primary breakup and the secondary breakup processes and only employ one model to simulate the spray atomization process.

Allocca O'Rourke et al [98, 148] simulated the breakup process by using a Taylor Analogy Breakup (TAB) model only. Some early studies [56, 60] employed a Wave model only. The later research of Reitz et al [99] distinguishes the primary breakup and the secondary breakup processes by using Kelvin-Helmholtz and Rayleigh-Taylor (KH-RT) models. Other researchers combine the primary breakup and secondary breakup models in their studies by using various approaches, as shown in Table 7-1 [162]. Som et al [104] developed the Kelvin-Helmholtz-Aerodynamics Cavitation Turbulence (KH-ACT) model, which improved the primary breakup model by considering cavitation and turbulence effects along with aerodynamically induced breakup.

A series of recent studies [104, 150, 163] indicates that cavitation and the turbulence phenomenon play an important role in the primary breakup process of diesel spray. Compared to the gasoline spray, the cavitation effect is taken into account in these studies. However, some non-ignorable aspects such as the extent of the impact of these mechanisms and how far downstream these effects last are still not fully understood. According to Som's study [104], these effects seem to be significant up to 10 mm downstream of the nozzle, which is about 60 nozzle diameters. After this distance, the primary breakup process is dominated by the KH breakup model in the KH-ACT model. Li, Zhi-Hua et al [150] employed a Huh-Gosman-KH-RT hybrid breakup model in their gasoline spray study; it can be estimated from their results that the primary breakup process is dominated by the turbulence-induced mechanism up to 30 mm downstream. Obviously, a 30 mm distance will cover the KH breakup length in the KH-RT model, which means that the primary breakup is determined by the turbulence breakup only. Moreover, the influence of these models on some spray atomization characteristics such as droplet size and droplet velocity has not been fully investigated in the studies [104, 150].

Table 7-1 Breakup models

Primary Breakup	Secondary Breakup	
TAB		[98,
Wave		[56, 60]
Wave	TAB	[102]
Wave	KH-RT	[99]
Cavitation	TAB	[96]
Cavitation and Turbulence	TAB	[103]
KH, Cavitation and Turbulence	KH-RT	[104]

In this study, a new hybrid Enhanced KH-ACT (EACT) breakup model is developed to improve the accuracy of the spray breakup simulation [164]. A new criterion is introduced to control the influence of cavitation and the turbulence phenomenon on the primary breakup process and the transition process of the primary and secondary breakups. A new child droplet size distribution function and a new parent droplet size reduction function are employed to better control the creation of the child droplet parcels. The model is validated with the high-speed imaging and Phase Doppler Particle Analyzer (PDPA) experimental results of the full-cone diesel spray in a constant volume vessel under non-evaporating and various injection conditions.

7.2 Diesel Spray Model Development

7.2.1 KH-ACT Breakup Model

Based on the turbulence and cavitation induced primary breakup models, Som et al [104, 165] developed the Kelvin-Helmholtz-Aerodynamics-Cavitation-Turbulence (KH-ACT) model, which improved the primary breakup model considering cavitation and turbulence effects along

with aerodynamically induced breakup. In the KH-ACT model, the length and time scales of aerodynamically induced breakup, cavitation induced breakup and turbulence induced breakup are based on the Kelvin-Helmholtz and Rayleigh-Taylor instability; the bubble collapse and burst times; and the k-ε model, respectively.

The maximum ratio of length/time scale determines the dominant model during the breakup process:

$$\frac{L_A}{\tau_A} = \max\left\{\frac{L_{KH}}{\tau_{KH}}, \frac{L_{CAV}}{\tau_{CAV}}, \frac{L_T}{\tau_T}\right\} \tag{7-1}$$

where $L_{KH} = r - r_{KH}$ and τ_{KH} are the aerodynamics' breakup length and time scales in the KH breakup model [60]; L_{CAV} and τ_{CAV} are the cavitation breakup length and time scales in the cavitation-induced breakup model [96] introduced previously.

The turbulence breakup length scale L_T and time scale τ_T are calculated as:

$$L_T(t) = C_\mu \frac{K(\mathrm{t})^{1.5}}{\varepsilon(t)} \tag{7-2}$$

$$\tau_T(t) = C_\mu \frac{K(\mathrm{t})}{\varepsilon(t)} \tag{7-3}$$

where $K(t)$ and $\varepsilon(t)$ are the turbulent kinetic energy and dissipation rate respectively and can be estimated as follows:

$$K(t) = \left\{ \frac{K_0^{C_\varepsilon}}{K_0(1 + C_\mu - C_\mu C_\varepsilon) + \varepsilon_0 t(C_\varepsilon - 1)} \right\}^{1/(C_\varepsilon - 1)} \tag{7-4}$$

$$\varepsilon(t) = \varepsilon_0 \left\{ \frac{K(t)}{K_0} \right\}^{C_\varepsilon} \tag{7-5}$$

where K_0 and ε_0 are the initial values at the nozzle exit, calculated from the nozzle flow simulations [166].

According to Equation (7-1), if the KH breakup model dominates the breakup process, then the KH model is employed. Otherwise the breakup rate will follow the law:

$$\frac{dr}{dt} = -C_{T,CAV} \frac{L_A}{\tau_A} \tag{7-6}$$

where $C_{T,CAV}$ is the adjustable model constant.

The new droplet parcel with the drop diameter L_A will be created accordingly and these child parcels may undergo further secondary breakups.

7.2.2 EACT Breakup Model

As already stated in the previous section, a new hybrid Enhanced KH-ACT (EACT) breakup model was developed in order to optimize the effects of turbulence and cavitation induced breakup on the spray atomization characteristics. In the proposed EACT model, a drop size based criterion r_{cri} was introduced to control the influence of cavitation and the turbulence

phenomenon on the primary breakup process and the transition process of the primary and secondary breakups. The criterion drop radius r_{cri} is set to:

$$r_{cri} = C_{cri} r_0 \tag{7-7}$$

where C_{cri} is the transition switch parameter expected to be investigated in this study.

While the radius of the parent droplet r is greater than r_{cri}, the primary breakup process follows the similar law as in the KH-ACT model continually until r is reduced to r_{cri}:

$$\frac{L_A}{\tau_A} = \max\left\{\frac{L_{KH}}{\tau_{KH}}, \frac{L_{CAV}}{\tau_{CAV}}, \frac{L_{tw}}{\tau_{tw}}\right\} \tag{7-8}$$

where L_{KH}, $\tau_{KH,}$ L_{CAV} and τ_{CAV} are the same as those in the KH-ACT model; L_{tw} and τ_{tw} are the turbulence breakup length and time scales in the original Huh-Gosman turbulence-induced breakup model.

Similarly in the KH-ACT model, if the KH breakup model dominates the breakup process, then the KH model is employed; otherwise, the breakup rate will follow Equation (7-6). However, the difference of the implementation of Equation (7-6) between the KH-ACT model and the EACT model is in the parent droplet parcel breakup rate, if turbulence induced breakup is the dominant mechanism. Instead of L_T and τ_T used in KH-ACT model, the EACT model employs L_{tw} and τ_{tw} in the original Huh-Gosman turbulence-induced breakup model to offer a new parent droplet size reduction function.

Once the parent drop radius r is reduced to r_{cri}, the KH-RT model will be employed for the primary breakup process, as is shown in Figure 7-1(c) [167]. With this approach, the issue regarding the extent of the impact of these mechanisms and how far downstream the effects of the turbulence and cavitation phenomenon on the primary breakup lasts, are then turned into a drop size-determined problem to be studied.

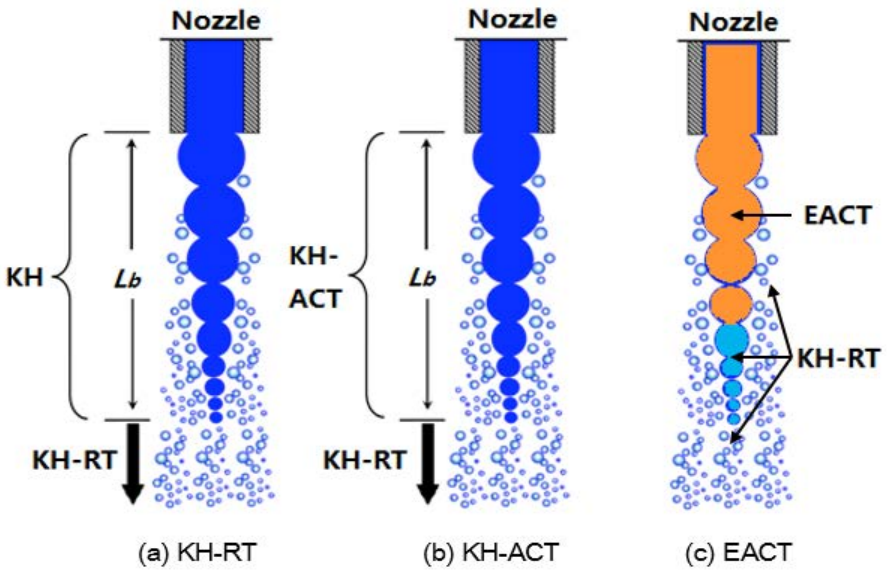

Figure 7-1 Comparison of KH-RT, KH-ACT and EACT models

In order to improve the accuracy of the simulation of the child droplet size, the EACT model also employs a new child droplet size function from the ligament evolution analysis proposed in [152, 153] for the turbulence induced breakup process. The details of the ligament based breakup mechanism have been discussed in Chapter 6. By employing the new child drop size function in the proposed EACT model, the child droplet parcels with drop diameter D_a or L_{CAV} are created by the turbulence or cavitation induced breakup accordingly. Then, these child parcels may undergo KH-RT secondary breakup.

7.2.3 Model Computing Process

The computing process of the EACT model is shown in Figure 7-2; the green block is the main work in this study.

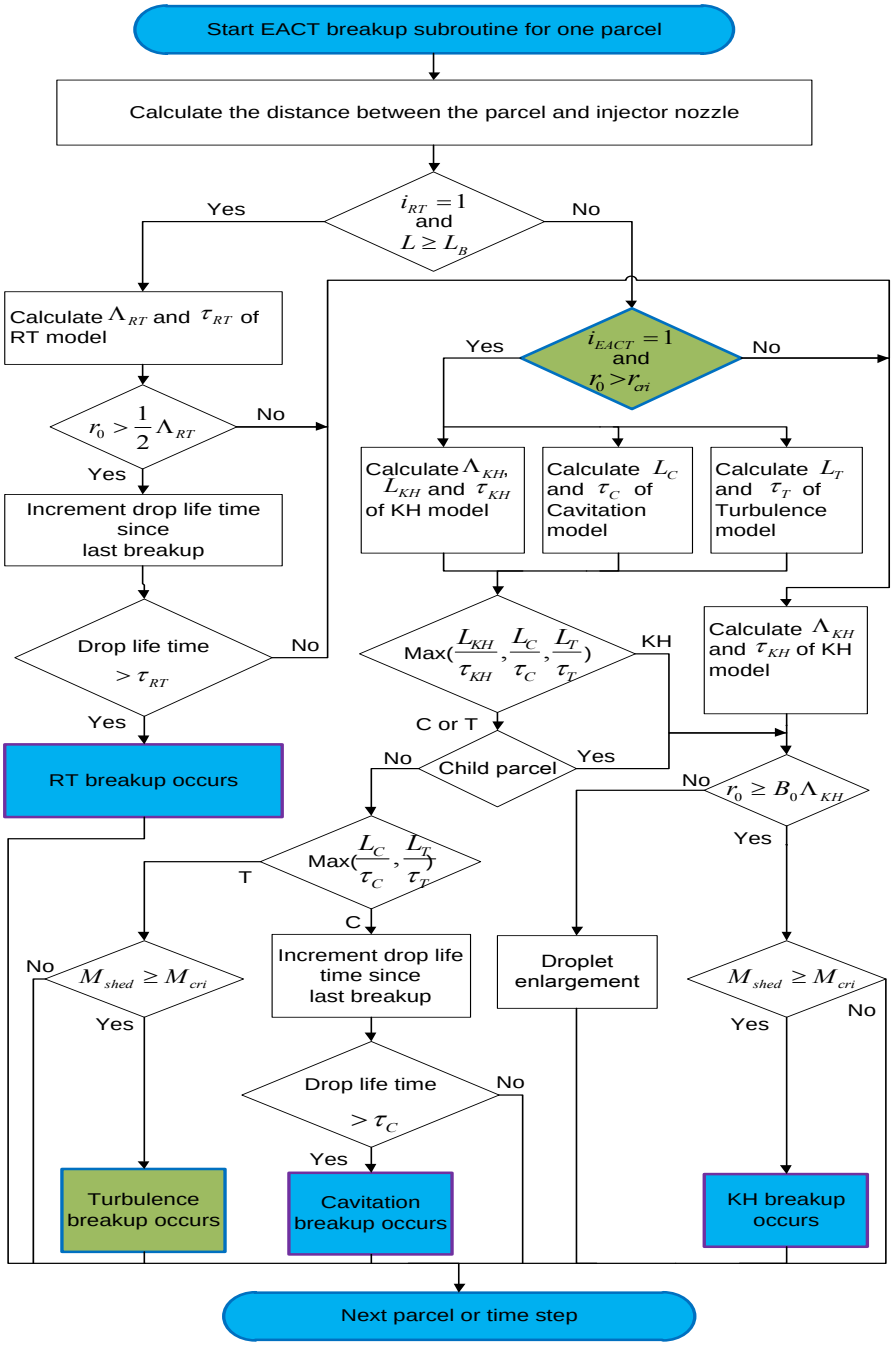

Figure 7-2 Flow chart of the EACT model

7.3 Simulation Settings

A cylindrical numerical grid with an 80 mm diameter and 100 mm depth is generated in this study. Figure 7-3 shows a 180° section view of the numerical grid. The injector tip is located at the top centre of the cylinder and one jet of the spray is simulated vertically downwards along the cylinder axis. The average cell size of the grid is set to 1.0 mm in the upper 60 mm depth, which is refined for the main test region. The boundary conditions are set the same as the experiment specifications.

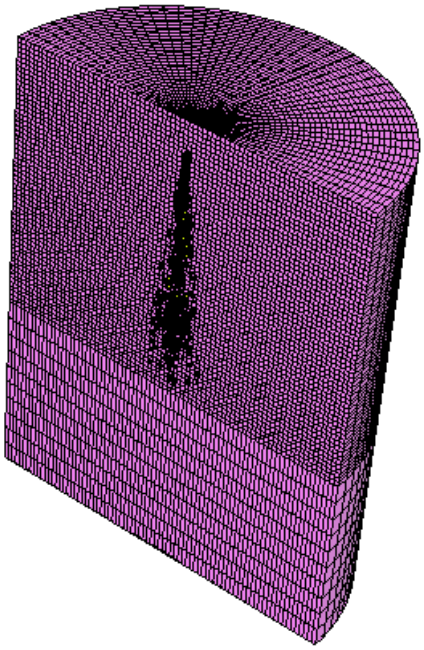

Figure 7-3 Numerical grid of diesel spray simulation

In order to compare the accuracy of the spray breakup simulation by using the proposed EACT model, KH-RT model and KH-ACT model, all the injection parameters and model constants used in the three different models are fixed and the values are set as suggested in the literature

[56, 104, 163, 168-170], except for the transition switch parameter C_{cri}. In order to investigate the influence of the switch parameter C_{cri} on the breakup process, four different C_{cri} values are studied: 0.3, 0.5, 0.7 and 0.9. Both of the 1000 bar and 1500 bar injection pressure conditions are simulated and validated in this study and only the results of 1000 bar injection pressure are shown here for the sake of brevity.

7.4 Validation Experiments

The spray experiment was carried out with a 7-hole common rail diesel injector in the two constant volume vessels under non-evaporation and various injection conditions. The experiment system has been introduced in Chapter 3. A solenoid DENSO injector with 7 holes and a diameter of 0.15 mm was used in the experiments. The injector was fuelled with diesel and controlled by electrical pulses, which were generated from an injection trigger unit and amplified by a driver. The spray photography tests were done in the high pressure CVV pressured by nitrogen; while the PDPA tests were carried out at atmospheric pressure in the low pressure CVV, since it was difficult to obtain valid data in the high pressure vessel due to its limited optical access area. Spray images were taken from the bottom window of the high pressure CVV, with a visible diameter of 68 mm. The tests specifications are shown in Table 7-2.

Table 7-2 Diesel spray experiment specifications

Test	Fuel	Temp-erature	$P_{injection}$ (bar)	P_{back} (bar)	Density (kg/m^3)	Injection Duration
Photography	Diesel	300 *K*	1000/1500	15.0	17.8	600 μs
PDPA	Diesel	300 *K*	1000/1500	1.0	1.29	600 μs

7.5 Validations and Discussion

7.5.1 Spray Morphography Comparison

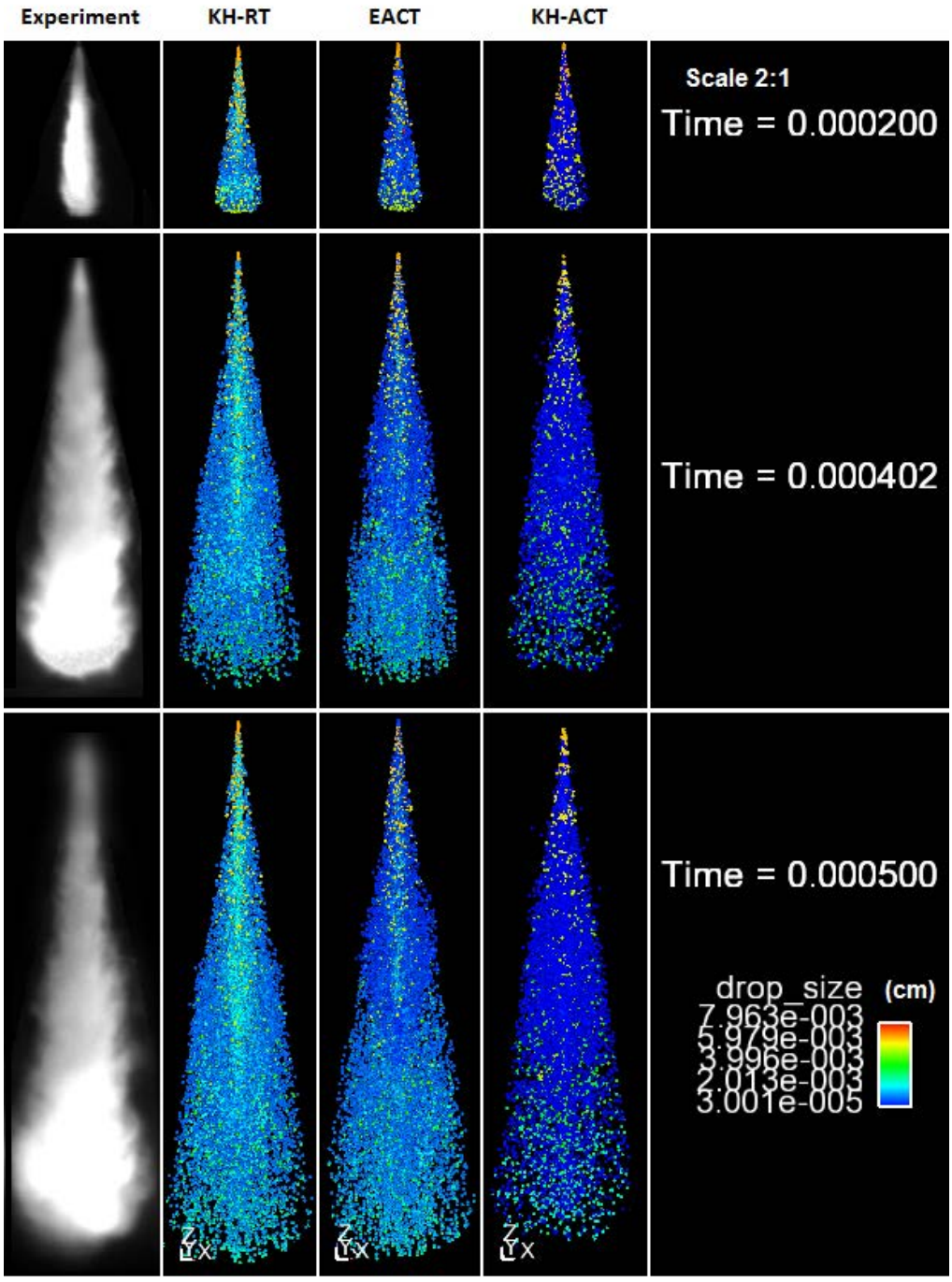

Figure 7-4 Comparison between experiment and simulated spray shape evolution (Scale 2:1)

The comparisons between the experimental and simulated spray shape evolution are shown in Figure 7-4. It can be seen from the visualization results that the KH-RT model predicts a slightly longer penetration and the KH-ACT model predicts a shorter penetration in comparison with the experimental image. According to the color scale, it is noteworthy that the result of the KH-ACT model presents more small droplets distributions than the other two models and the result of the EACT model indicates a moderate sized distribution among the three models.

This is reasonable since the breakup is enhanced by turbulence induced and cavitation induced breakup in the KH-ACT model and the EACT model; and the switch parameter C_{cri} in the EACT model is a most effective drop size-based parameter to control the extent of the inclusion of the turbulence and cavitation models. The detailed discussion of the droplet size validation will be examined in the following sections.

7.5.2 Spray Penetration

Spray penetration is a macroscopic characteristic which is always considered firstly by fuel spray researchers. Figure 7-5 shows the temporal evolution of spray penetration of the experimental data and simulation results using KH-RT, KH-ACT and EACT breakup models. It can be seen that all of the three models provide a penetration trend in good agreement with the experiments until 300 μs after the start of injection (ASOI), which indicates a similar jet velocity at the very beginning of the injection. After this point, the divergence of the simulated penetration between different models starts to increase until the maximum penetration can be captured by the experiment.

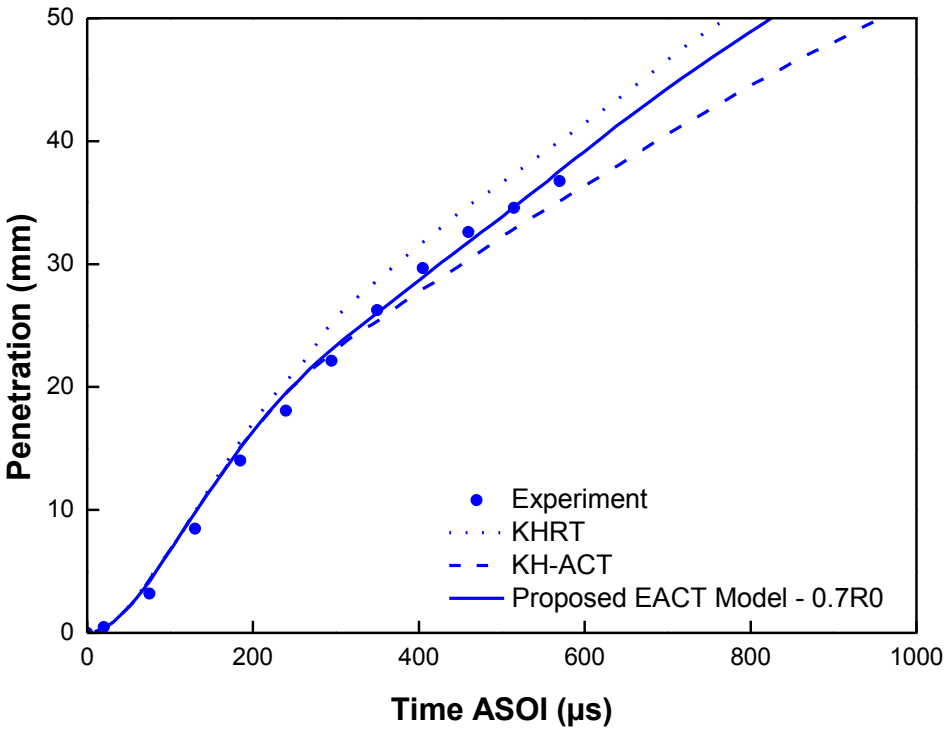

Figure 7-5 Comparison of the effect of different breakup models on spray penetration

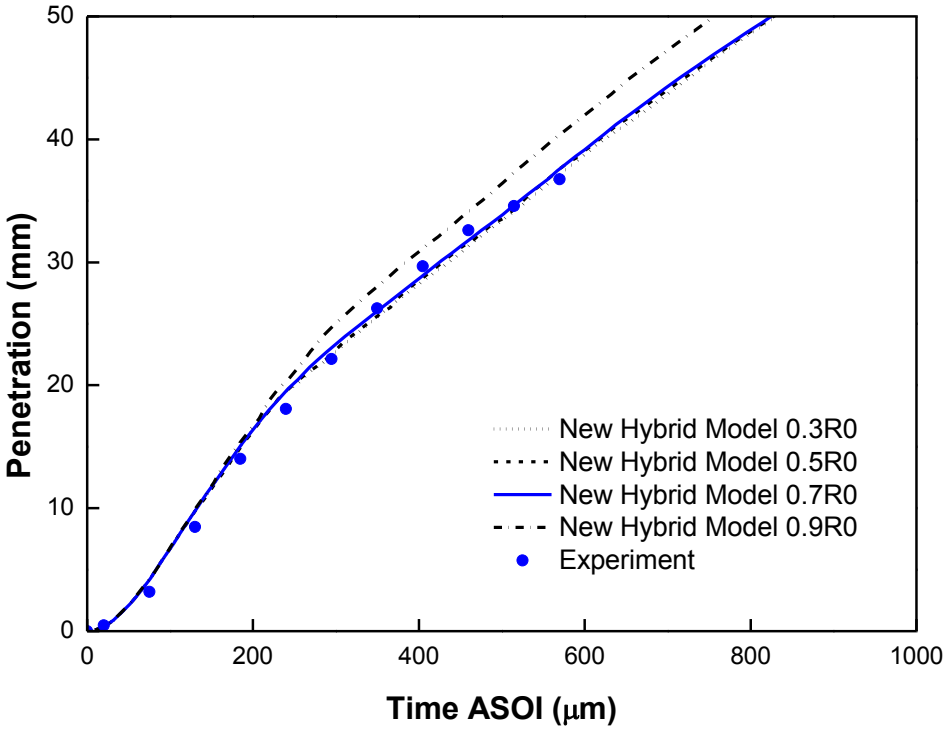

Figure 7-6 Comparison of the effect of different *Ccri* values on spray penetration

The penetration of the EACT model is shown to achieve a better agreement with the experimental data during all of the injection period; while the KH-RT model predicts a slightly longer penetration length and the KH-ACT model predicts a shorter penetration length, compared to the experiment data beyond 300μs ASOI. This discrepancy can be explained by the fact that the larger droplet size and higher droplet velocity predicted by the KH-RT model and smaller droplet size and lower droplet velocity predicted by the rapid breakup with the KH-ACT model, lead to a longer and shorter penetration length respectively.

Figure 7-6 presents the effect of the switch parameter C_{cri} on spray penetration simulation. The experimental trend seems to be clearly predicted by all the cases even if a comparison between the four profiles can be made after 300μs ASOI, where the penetration length is slightly longer with the higher C_{cri} value 0.9.

7.5.3 Droplet Velocity

Droplet velocity is an important microscopic characteristic of the fuel spray. Figure 7-7 presents the temporal evolution of the mean droplet velocity in the axial direction at the distance of 30 mm downstream from the nozzle exit. The axial mean velocities predicted by the KH-RT, KH-ACT and EACT models are compared with the PDPA data.

It can be seen in Figure 7-7, the axial mean velocity predicted by the EACT model is in good agreement with the PDPA data despite some slightly higher values at some points; while the KH-RT model significantly over predicts the axial velocity at the spray head region and the KH-ACT model predicts a much lower axial velocity compared to the PDPA data. This is due to the relatively slow droplet breakup in the KH-RT model and the rapid breakup in the KH-

ACT model, which results in the inaccurate kinetic energy loss of the droplet. This is consistent with the analysis in the penetration validation section, where the higher axial velocity leads to longer penetration length in the KH-RT model and the lower axial velocity leads to shorter penetration length in the KH-ACT model. Obviously, the EACT model has the ability to control the droplet velocity properly.

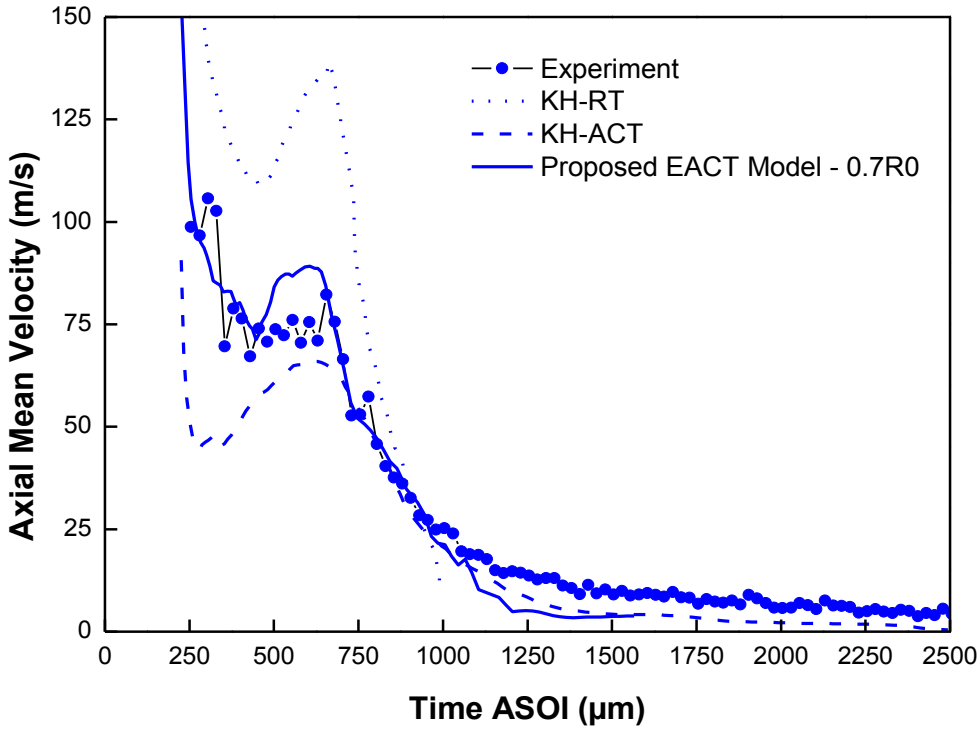

Figure 7-7 Comparison of the effect of different breakup models on droplet axial mean velocity

Figure 7-8 depicts the effect of switch parameter C_{cri} on droplet axial mean velocity. With the increase of the C_{cri} value, the axial mean velocity evidently shows an increasing trend. It can be observed that the case marked 0.9R0 (which means $C_{cri} = 0.9$) over predicts the axial mean velocity significantly and the cases marked 0.3R0 and 0.5R0 under predict the axial mean velocity slightly. This means more droplets will undergo the EACT breakup with a lower C_{cri}

value. The case marked 0.7R0 shows a better prediction in both the spray head and spray tail regions, despite the slightly higher velocity in the spray head which is in an acceptable range.

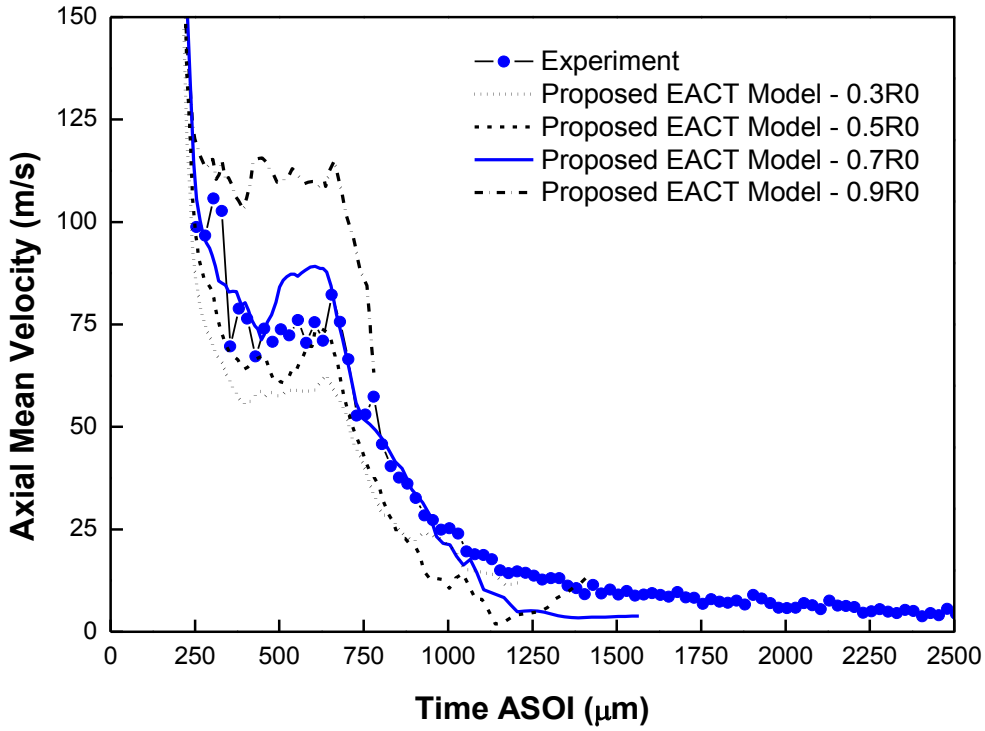

Figure 7-8 Comparison of the effect of different *Ccri* values on droplet axial mean velocity

7.5.4 Droplet Size

Droplet size is another microscopic characteristic in fuel spray studies. Figure 7-9 and Figure 7-10 show the spatial evolution of the droplet Sauter Mean Diameter (SMD) at the distance of 10 mm, 20 mm, 30 mm, 40 mm and 50 mm downstream of the nozzle exit. The SMD values are generally over estimated by simulations [152] in some literature; the same phenomenon can be observed in this study. However, the SMD simulated by the EACT model is much closer to the PDPA data compared to the other two models; the value predicted by the

KH-RT model is over predicted and the value predicted by the KH-ACT model is under predicted significantly.

This is consistent with the spray penetration analysis and droplet velocity analysis: the turbulence and cavitation induced breakup enhance the atomization process and produce greater numbers of child parcels. Again, the C_{cri} parameter plays an important role in controlling the extent of the inclusion of turbulence and cavitation models, as is shown in Figure 7-10; the SMD increases with the increasing of the C_{cri} value.

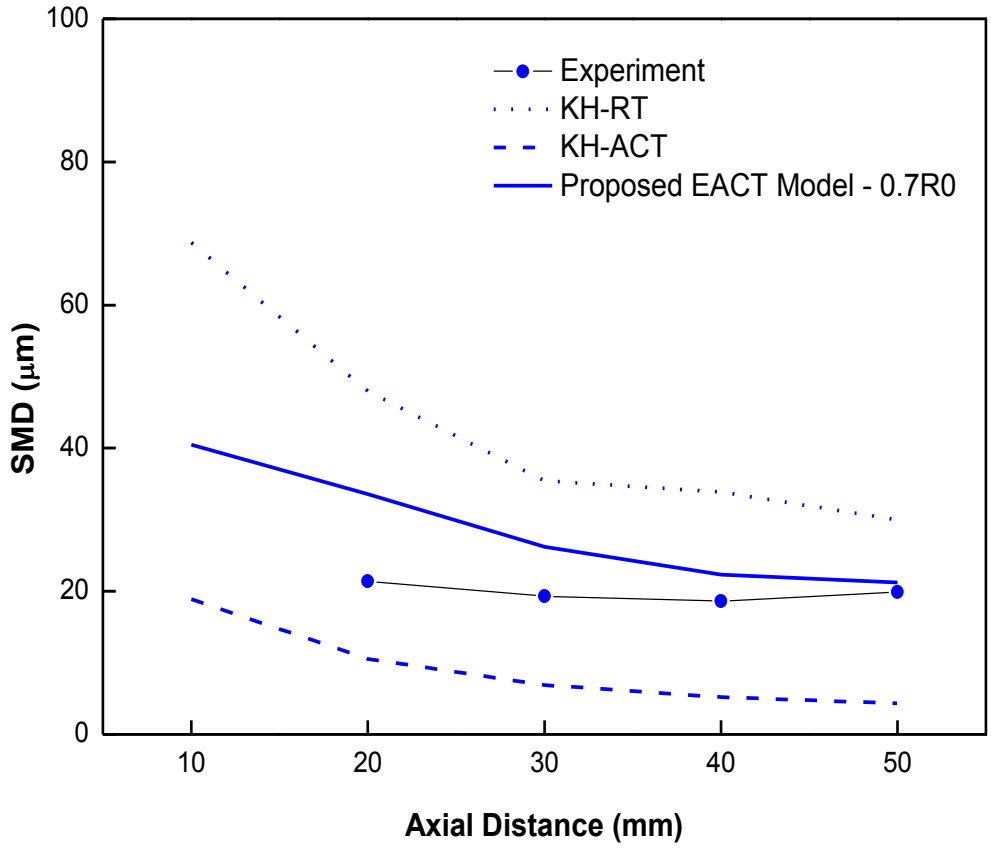

Figure 7-9 Comparison of the effect of different breakup models on droplet SMD

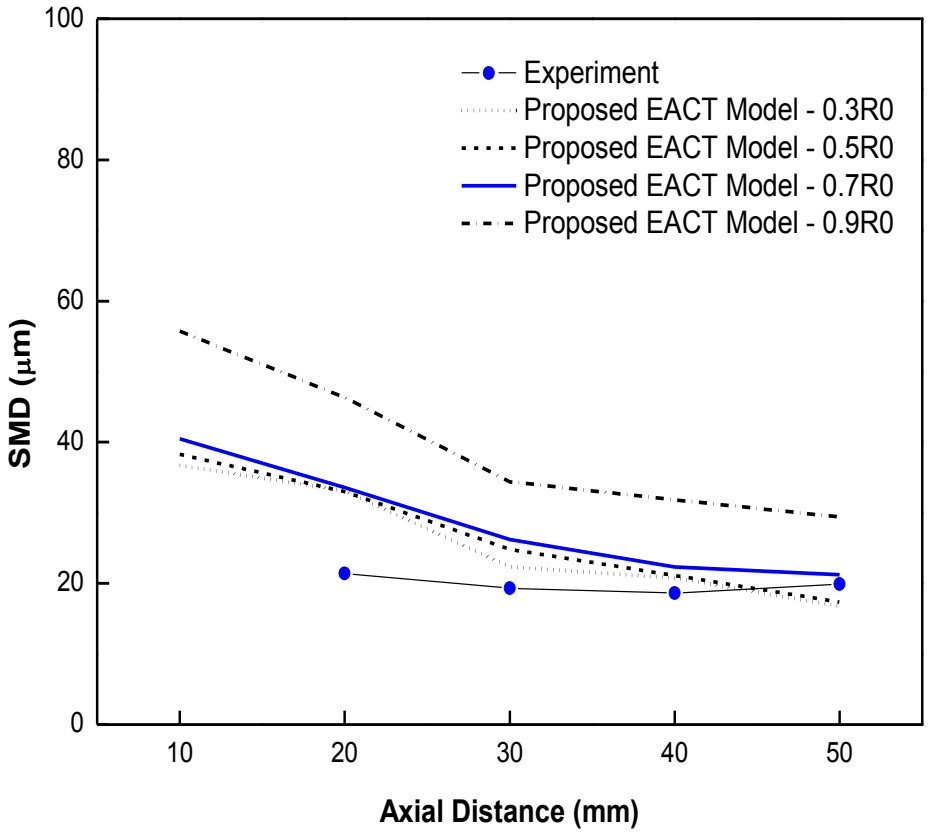

Figure 7-10 Comparison of the effect of different *Ccri* values on droplet SMD

7.5.5 Breakup Statistical Analysis

Spray penetration, droplet axial mean velocity and droplet size are the simulation results of the macroscopic and microscopic characteristics of the fuel spray which directly exhibit how accurate the prediction can be estimated by the EACT model. However, the details of the contribution of each breakup mechanism and the influence of the switch parameter C_{cri} on the contribution have not been well understood.

In order to quantify these details, the total breakup amount and the number of each individual mechanism are shown in Figure 7-11. It can be seen that both of the numbers of the

aerodynamically induced (KH) breakup and the number of the RT breakup increase with the rise of the C_{cri} value; while the number of the turbulence induced breakup is inhibited by a higher C_{cri} value as expected.

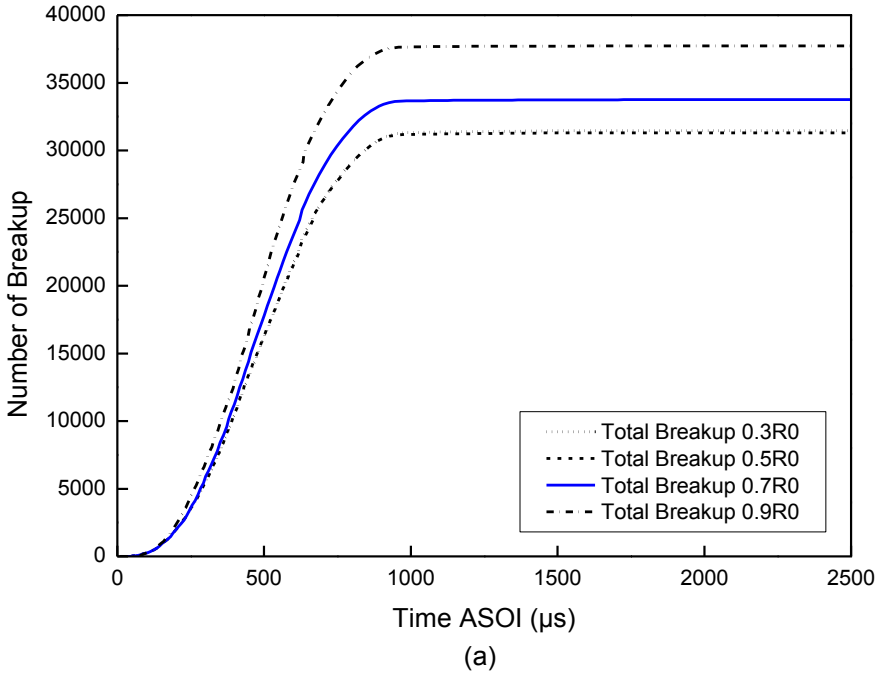

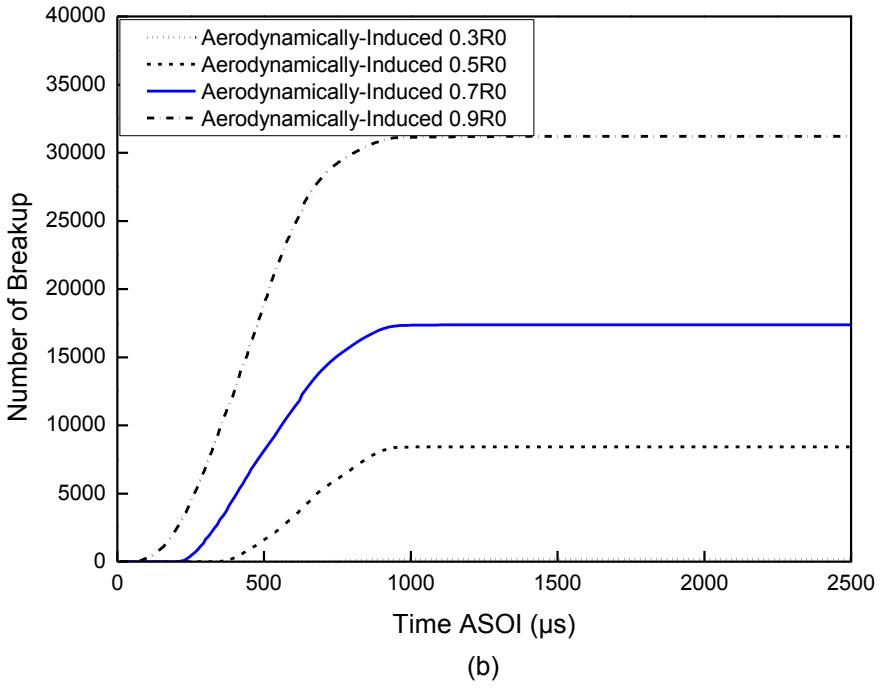

Figure 7-11 Breakup counting in each sub-mechanism of EACT model (a, b)

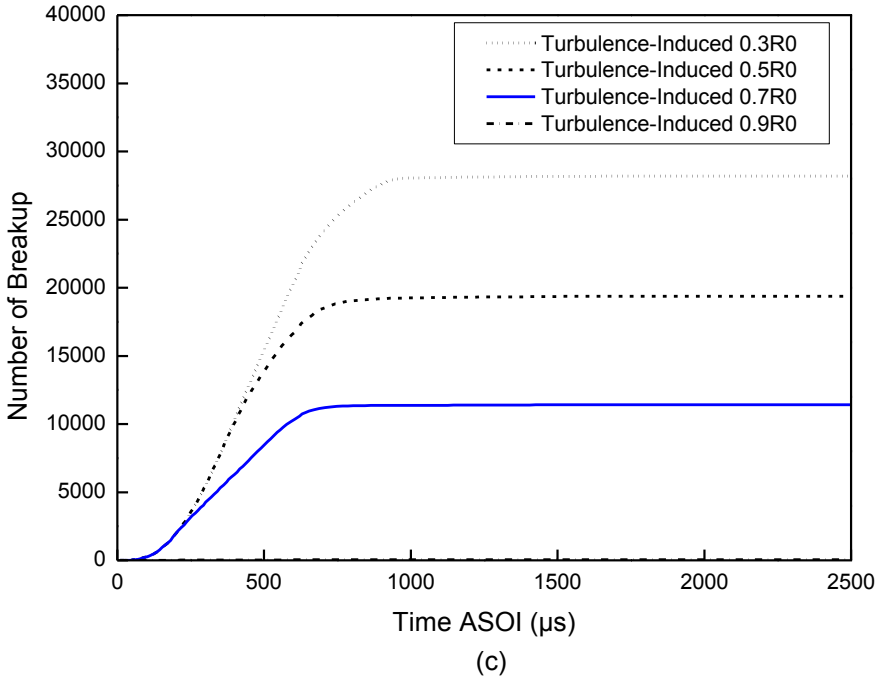

(c)

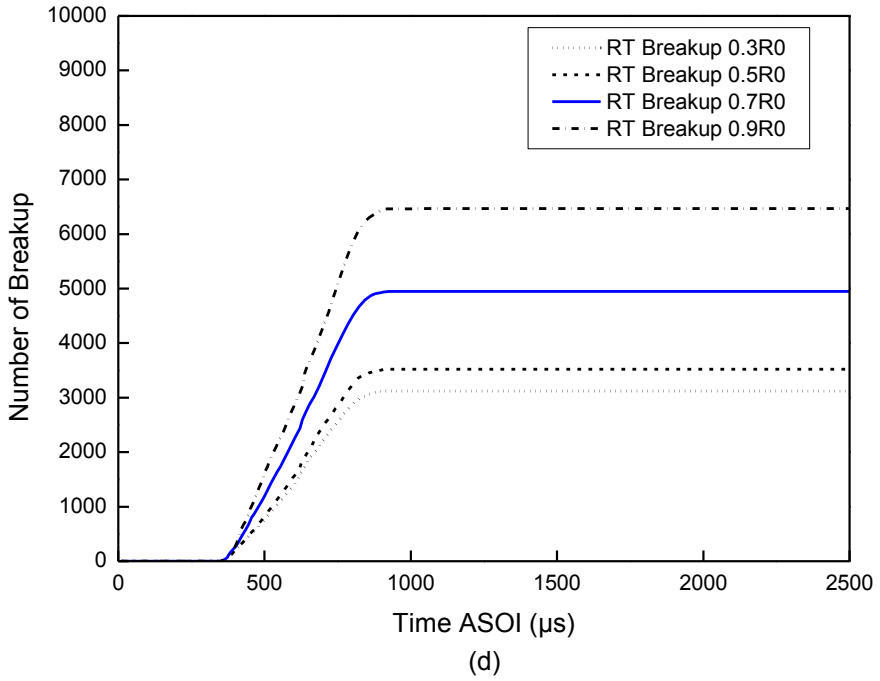

(d)

Figure 7-11 Breakup counting in each sub-mechanism of EACT model (c, d)

The number of the cavitation induced breakup is not plotted here due to its much lower value; and this is not beyond expectation since the amount of cavitation generated from the nozzle is rather low, which can be studied in the literature [97, 169]. Turbulence from the nozzle is proved to play an important role on spray breakup and leads to a rapid atomization process of the spray. The optimization of the extent of the turbulence induced breakup can be realized by controlling the switch parameter C_{cri}.

7.6 Summary

An enhanced turbulence and cavitation induced primary breakup model combined with an aerodynamic breakup mechanism is proposed. The new EACT model improves the primary breakup accuracy by optimizing the turbulence induced breakup mechanism; controlling the primary and secondary breakup process; employing a new child droplet size function and a new parent droplet size reduction function; and introducing a new size-based criterion to control the extent of the EACT model. This new model is validated with the high-speed imaging and Phase Doppler Particle Analyzer (PDPA) experimental results. The conclusions can be drawn from this study as follows:

1. The spray penetration can be clearly predicted by the proposed EACT model with a proper *Ccri* value and the result shows better agreement with the high-speed photography data, compared to the slightly higher value simulated by the KH-RT model and the slightly lower value simulated by the KH-ACT model.

2. The droplet velocity and droplet size simulated by the EACT model present good agreement with the PDPA data, despite the higher SMD value which is generally over estimated by other

spray breakup models. This means that the optimized turbulence breakup rate and the new child droplet size function in the EACT model offer a more accurate simulation of the fuel spray.

3. Turbulence from the nozzle is proved to play an important role in spray breakup and enhances the atomization process of the spray; while the influence of cavitation generated from the nozzle is relatively weaker compared to the turbulence induced breakup.

4. The breakup switch constant *Ccri* is an effective parameter to optimize the extent of the effect of turbulence induced breakup; higher *Ccri* value moves the breakup trend towards the similar results of the KH model and slow down the breakup process. A proper C_{cri} value helps to achieve an accurate simulation of the fuel spray of diesel engines.

CHAPTER 8
CONCLUSIONS AND RECOMMENDATIONS

This chapter summarizes the conclusions for the research work carried out in this thesis and gives some recommendations for future study.

8.1 Conclusions

The research work in this thesis focuses on the experimental and numerical studies of the fuel spray characteristics of direct injection engines. The macroscopic and microscopic characteristics of the fuel spray have been studied by using optical diagnostic technologies and numerical approaches. Improved physical-numerical spray models have been developed and validated. The main conclusions of this study are stated in the following paragraphs.

8.1.1 Spray Characteristics of GDI Engines

The effects of injection pressure, injection duration and different injector nozzle machining methods on the spray characteristics of the GDI engine have been investigated in this study. The results show that higher injection pressure will increase the penetration length and enhance the spray atomization process. However, the spray angle is almost independent of the injection pressure. The injection duration does not affect the spray penetration and atomization performance at the initial stage of the injection. However, after the initial stage, longer penetration length, higher droplet velocity and greater droplet size are found with the increase of the injection duration. The spray angle is almost independent of the injection duration. With

the increase of the distance downwards of the nozzle, the droplet velocity decreases gradually, while the droplet size decreases first and then increases slightly at a far distance. Compared to the EDM injector, the LD injector shows a reduced penetration, larger spray angle and smaller spray droplet size at all test conditions. The laser drilled injector nozzle can promote the spray atomization performance due to its sharp inlet edge and fine inner surface produced by the laser machining technology. The enhanced turbulence effect induced by the nozzle's sharp inlet edge plays an important role in accelerating the spray breakup and atomization processes. From this study it is believed that the turbulence effect plays an important role in affecting the spray breakup and atomization in GDI engines.

8.1.2 Spray Characteristics of Diesel Engines

The spray characteristics of the diesel engine have been experimentally investigated by using optical approaches such as high-speed photography and PDPA measurement. The effects of injection pressure, ambient pressure, different fuels including gasoline, diesel and their blends – dieseline; and the gasoline/diesel blending ratio, on the spray characteristics have been studied in detail. It is shown that for all the tested fuels, increasing the ambient pressure will decrease the spray penetration and enhance the atomization and breakup quality; while raising the injection pressure will increase the penetration length and improve the atomization and breakup performance. It is believed that higher injection pressure and ambient pressure will lead to stronger turbulence, cavitation and aerodynamic force; which will promote the spray atomization process. Compared to pure diesel, the recently developed dieseline fuel shows many advantages in terms of enhancing the spray atomization process. It is found that a reduced penetration and a better atomization quality can be achieved by increasing the proportion of

gasoline in the dieseline fuel; due to its stronger cavitation phenomenon, higher volatility, lower surface tension and lower viscosity.

8.1.3 Gasoline Spray Model Development and Validation

The injection parameters, fuel properties, sac design, lower L/D aspect ratios in the nozzle hole and stronger spray jet interactions make the turbulence and vortices of the fuel spray of the GDI engine differ from those of the diesel engine. The proposed TL-KHRT model improves the simulation accuracy by employing a new droplet breakup mechanism based on the research that the droplet formation is mainly linked to the ligament evolution during the turbulent breakup process. The new model is validated with the high-speed imaging and PDPA experiments; the simulation result shows good agreement with the experiment data. Turbulence from the nozzle has proved to play an important role in spray breakup and enhances the spray atomization process. By applying the turbulence-ligament breakup mechanism into the spray model, significant improvements of the spray simulation can be achieved. Ligament formation and breakup, due to the turbulence-induced instability along the liquid surface, are the main causes of the primary breakup of the fuel spray. By employing the new droplet generation mechanism, the child droplet size of the new breakup model is proved to be closer to the experimental data than that of the original KHRT model. The spray characteristics such as spray penetration, droplet velocity, droplet AMD and SMD can be precisely predicted by the proposed TL-KHRT model. The proposed TL-KHRT model is an effective supplement to the original KHRT breakup model as it considers the turbulence and ligament evolution during the spray aromatization process. The development of this model helps to achieve an accurate spray simulation in GDI engines.

8.1.4 Diesel Spray Model Development and Validation

Compared to the fuel spray of the GDI engine, the cavitation effect cannot be ignored and thus should be taken into account in the modelling of the fuel spray of diesel engines. An enhanced turbulence and cavitation-induced primary breakup model combining with an aerodynamic breakup mechanism is proposed. A new drop size-based criterion to control the extent of the EACT model has been introduced into this model. The spray penetration can be precisely predicted by the proposed EACT model and the result shows better agreement with the high-speed photography data, compared to the slightly higher value simulated by the KH-RT model and the slightly lower value simulated by the KH-ACT model. The droplet velocity and droplet size simulated by the EACT model present good agreement with the PDPA data, despite the higher SMD value which is generally over estimated by other spray breakup models. This means that the optimized turbulence breakup rate and the new child droplet size function in the EACT model offer a more accurate simulation of diesel spray.

8.2 Recommendations

Based on the research work in this thesis, several recommendations for future work can be proposed as described in the following paragraphs.

8.2.1 Detailed Modelling of Fuel Spray

The current study in this thesis, as well as that of most of the commercial CFD codes, is based on the DDM approach which is a simplification of detailed spray modelling. Although this reasonable simplification can reduce the workload of the simulation and obtains a result which

is enough to meet the requirement for engineering product development, the detailed modelling of the spray is still meaningful so that the simulation result can be more precise and needs less calibration. For example, with the rapid development of the calculation capacity of the future computer, Direct Numerical Simulation (DNS) [171] can be employed and a more detailed modelling of the fuel spray can be achieved. Figure 8-1 shows an example of the DNS result of the liquid spray jet [172].

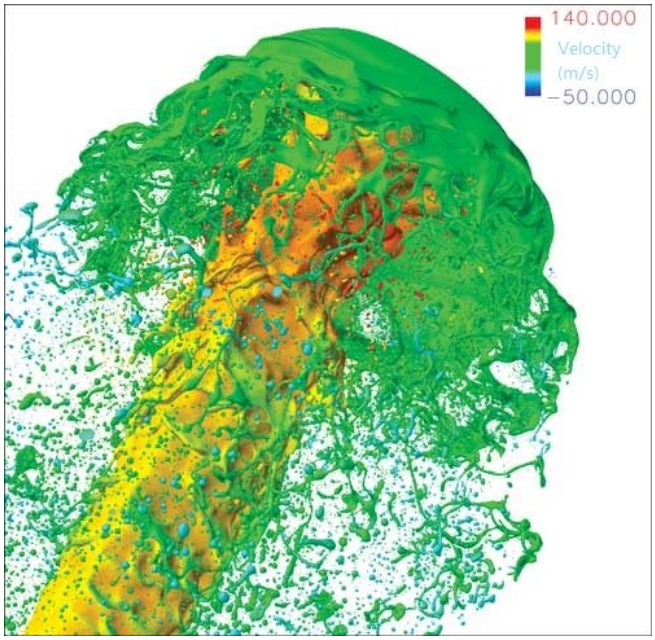

Figure 8-1 An example of the DNS result of the liquid spray [172]

8.2.2 Engineering Simplification of Fuel Spray Modelling

On the contrary, if the fuel spray modelling is only for engineering product development, more simplification can be made by ignoring the complex primary breakup process and only employing secondary breakup models in the simulation, with the help of the available

experiment data. For example, the spray droplet size and velocity measured by the PDPA system can be used as the input for the engine simulation; thus the primary breakup process can be replaced by these experiment data. In this way, the saved computation power can be used for the secondary breakup process, combustion and emissions modelling.

8.2.3 Supercritical Spray Modelling

With the development of the concept of a high density combustion engine [173], supercritical spray has started to become of concern recently. An example of supercritical spray is shown in Figure 8-2. However, the modelling of the spray under a supercritical condition is distinctly different from that of the traditional spray, due to the special property of the fuel; the classical spray atomization and the breakup theory under this particular condition are questionable [174].

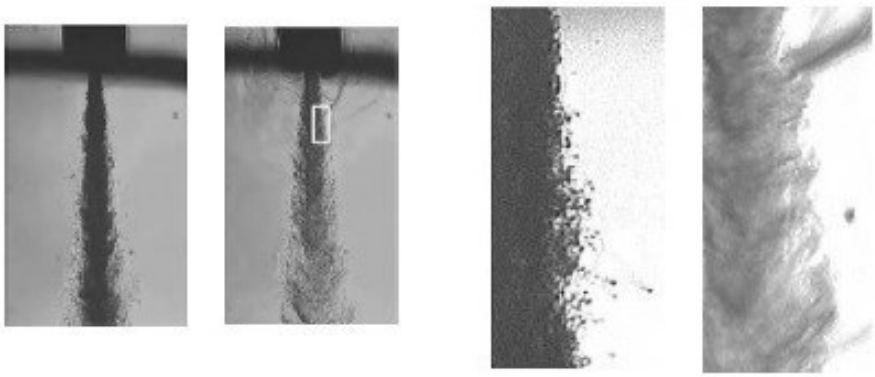

Figure 8-2 An example of supercritical spray [135]

APPENDIX A

Model Parameters of the TL-KHRT model:

itapeTL-KHRT - Notepad

File Edit Format View Help

```
1                !itl, Swith of the TL-KHRT Breakup Model, 1=on, 0=off
1                !itl, Swith of the EACT Breakup Model, 1=on, 0=off
1.0              !cnstact, 0.025 is used by S.SOM
0.45             !acttkec,0.45,S.SOM,losses in the contraction corner
0.01             !acttkes, 0.01, S.SOM,area ratio at the nozzle contraction
0.27             !acttdrc, 0.27,S.SOM,average turbulent energy dissipation
0.09             !cnsttke, 0.09 is used by Huh Gosman
1.92             !cnsttdr
0.8264463        !cnstca,area occupied by the liquid fuel/area at nozzle exit
0.085            !holel, hole length
0.7              !actswt
1                !SMDposition on/off
1.0              !SMDposition,in cm
2.0              !SMDposition,in cm
3.0              !SMDposition,in cm
4.0              !SMDposition,in cm
5.0              !SMDposition,in cm
0.0              !atiltxy, equals tiltxy in itape5
0.0              !atiltxz, equals tiltxz in itape5
0.05             !actmkh, KH shed mass to breakup, should be in itapeERC
10.0             !cligml, ligment size constant
```

itapeERC - Notepad

File Edit Format View Help

```
1                !  KH breakup model
0.61             !balpha
0.188            !cnst1
1.732            !cnst21
40.0             !cnst22  !40.0  standard
1                !  RT breakup model
0.4              !cnst3rt   !0.1  standard
1.0              !cnst2b  !1  standard
0.9              !distant   !1.9  standard
0                ! Sheet spray model
0                ! LISA spray model
1                !  Droplet deformation
10.0             !csubd
8.0              !csubk
0.08333          !cfocbck
1                !Discharge Coefficience
0.8              !Discharge Coefficience value
```

APPENDIX B

Tracing droplet breakup in the original KH-RT model:

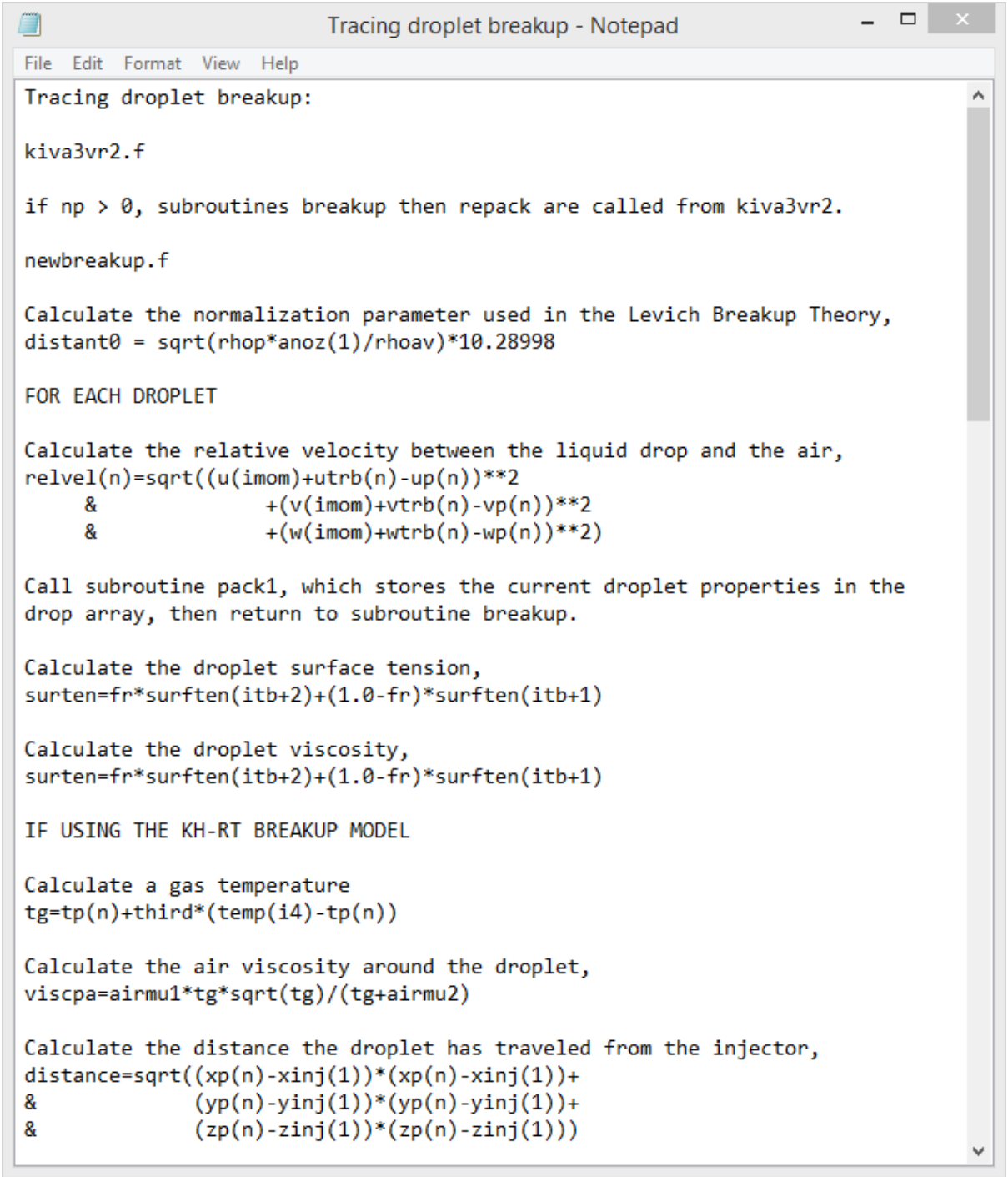

Tracing droplet breakup - Notepad

File Edit Format View Help

```
Calculate the distance the droplet has traveled from the injector,
distance=sqrt((xp(n)-xinj(1))*(xp(n)-xinj(1))+
&             (yp(n)-yinj(1))*(yp(n)-yinj(1))+
&             (zp(n)-zinj(1))*(zp(n)-zinj(1)))

Normalize the droplet distance by the Levich normalization parameter
calculated above (distant0),
distance=distance/distant0

Call the breakup subroutine (ercbum)

If the drop temperature is above its critical temperature, or there is no
relative velocity between the drop and its surroundings, or you are not using
the KH model, return to subroutine breakup,
if(tdrop.ge.tcrit) return
if(relvel.eq.0.)   return
if(ikh.eq.0) return

NOTE THAT IF VARIABLE IKH = 0, NEITHER THE KH, NOR THE RT MODELS WILL BE
USED.

Calculate the Reynolds number and the gas and liquid Weber numbers,
reynol =rdrop *relvel/xnu
weber  =relvel**2*rdrop /surten
weberg =roi4  *weber
weberl =rhop  *weber

Calculate the most unstable droplet surface wave and its growth rate,
wavlng = 9.02*(1.+0.45*ohn**0.5)*(1.+0.4*taylor**0.7)/denom
wavlng = wavlng*rdrop
growth = (0.34+0.385*weberg**1.5)/((1.+ohn)*(1.+1.4*taylor**0.6))
growth = growth*freq

Calculate the breakup time constant, which depends on whether or not the
droplet has hit a wall,
if(drop(kwalhit).gt.0.) then
         cnst2=cnst21
      else
         cnst2=cnst22
      endif

If the normalized distance the droplet has traveled (as calculated above, see
variable distance) is less than the model constant distant (which was input
from file itapeERC) and you are using the RT model (irt=1), call the RT
model,
if(distance.ge.distant.and.irt.eq.1) then
         call ercrt(visc,roi4,relvel,surten,drop,dt,iflag)
         if(iflag.eq.1) return
      endif

NOTE:  THE RT MODEL SUBROUTINE (ERCRT) WILL NOT BE INVESTIGATED AT THIS TIME.
```

Tracing droplet breakup - Notepad

File Edit Format View Help

```
variable distance) is less than the model constant distant (which was input
from file itapeERC) and you are using the RT model (irt=1), call the RT
model,
if(distance.ge.distant.and.irt.eq.1) then
         call ercrt(visc,roi4,relvel,surten,drop,dt,iflag)
         if(iflag.eq.1) return
      endif

NOTE:  THE RT MODEL SUBROUTINE (ERCRT) WILL NOT BE INVESTIGATED AT THIS TIME.

17. If the most unstable KH droplet surface wave as calculated above, is >=
the drop radius divided by a model constant (which was read in from itapeERC,
balpha) the droplet somehow gets larger,
a.      if (wavlng .ge.rdrop/balpha) then
         call erckhe(drop,relvel,dt,wavlng,growth)

NOTE:  DROPLET ENLARGEMENT WILL NOT BE COVERED AT THIS TIME.

18. Otherwise the droplet may breakup through the KH mechanism,
a.      else
         call erckhb(drop,dropnew,vrel,dt,wavlng,growth,new,surten)
      endif

            erckhb (source is inside ercbum.f)
19. Calculate the theoretical breakup time for the current droplet to breakup
completely into child size droplets (tshatt, which is a function of the
previously calculated fastest growing wavelength and growth rate, and the
drop radius),
a.      tshatt  = 3.788*cnst2*rdrop /(growth *wavlng )

20. Calculate the resulting child droplets size and number based on dt,
a.      radp   =(rdrop+dtshat*radeqb)/(1.+dtshat)

21. Calculate shed mass and some other stuff.

22. Determine wether or not to produce a new parcel.

23. If generating a new parcel, go into subroutine ercgnd and store droplet
characteristics in array dropnew and return to erckhb.

24. Return to newbreak

25. If a new parcel was made, go into pack2 and enter the droplet
characteristics from the drop array back into the global arrays.

NOTE:  THE PACK2 SUBROUTINE IS CALLED TWICE IN SUCCESSION.

26. Do the above for each parcel in subroutine breakup, then go back to
newkiva, then enter repack.

27. Repack parcel arrays.
```

REFERENCES

1. Gupta, H.N., Fundamentals of internal combustion engines. PHI Learning Pvt. Ltd. ISBN 812-0-34680-7, 2012.

2. Alagumalai, A., Internal combustion engines: Progress and prospects. Renewable and Sustainable Energy Reviews. Vol.38: p. 561-571, 2014.

3. Kalghatgi, G., Developments in internal combustion engines and implications for combustion science and future transport fuels. Proceedings of the combustion institute, Vol. 35(1): p. 101-115, 2015.

4. Institution of Mechanical Engineers, Internal Combustion Engines: Performance, Fuel Economy and Emissions. Elsevier Science. ISBN: 978-1-78242-183-2, 2014.

5. Wesseling, J., J. Faber, and M. Hekkert, How competitive forces sustain electric vehicle development. Technological Forecasting and Social Change, Vol.81: p. 154-164, 2014.

6. Mwasilu, F., J.J. Justo, E.-K. Kim, T.D. Do, and J.-W. Jung, Electric vehicles and smart grid interaction: A review on vehicle to grid and renewable energy sources integration. Renewable and Sustainable Energy Reviews, Vol.34: p. 501-516, 2014.

7. Hannan, M., F. Azidin, and A. Mohamed, Hybrid electric vehicles and their challenges: A review. Renewable and Sustainable Energy Reviews, Vol.29: p. 135-150, 2014.

8. Lynn Orr, Changing the World's Energy Systems, Stanford University Global Energy Project (after John EwardsAmerican Association of Petroleum Geologists); SRI Consulting, 2013.

9. U.S. Energy Information Administration (EIA), International energy outlook 2013. EIA Report Number: DOE/EIA-0484, 2013.

10. U.S. Energy Information Administration, International energy outlook 2014. EIA Report Number: DOE/EIA-0485, 2014.

11. U.S. Energy Information Administration (EIA), AEO2014 Early Release Overview, EIA Report Number: DOE/EIA-0383ER, 2014.

12. U.S. Energy Information Administration (EIA), Energy Information Administration, Monthly Energy Review, May, 2014.

13. Reitz, R.D., Directions in internal combustion engine research. Combustion and Flame, Vol.160(1): p. 1-8, 2013.

14. Ryley, T. and L. Chapman, Transport, Climate Change and the Environment. The SAGE Handbook of Transport Studies, p. 412, 2013.

15. Xinhuanet, Air pollution reports, 2013, Available from: <http://news.xinhuanet.com/politics/2013-01/14/c_124225848.htm> [20 March 2015].

16. Commission, E., Transport & Environment, Source available from: <http://ec.europa.eu/environment /air/transport/road.htm> [20 March 2015].

17. Transportation, I.C.o.C., EU CO2 emission standards for passenger cars and light-commercial vehicles. 2015.

18. David Sedgwick， Automotive News January 11, 2011. Available from <http://www.autonews.com/article/20110111/OEM06/1101098/direct-injection-gains-momentum> [20 March 2015].

19. Park, C., S. Kim, H. Kim, and Y. Moriyoshi, Stratified lean combustion characteristics of a spray-guided combustion system in a gasoline direct injection engine. Energy, Vol. 41(1): p. 401-407, 2012.

20. Zhao, H., Overview of gasoline direct injection engines. Advanced Direct Injection Combustion Engine Technologies and Development: Gasoline and Gas Engines, p. 1, 2014.

21. Zhao, H., Direct injection gasoline engines with autoignition combustion. Advanced Direct Injection Combustion Engine Technologies and Development: Gasoline and Gas Engines, p. 133, 2014.

22. Zhao, H., Advanced Direct Injection Combustion Engine Technologies and Development: Diesel Engines. Elsevier Vol. 2, 2009.

23. Pereira, C., Atomization and Combustion of Liquids. Masters thesis, Instituto Superior Técnico, Lisboa, Portugal, 2012.

24. O'Rourke, P. and F. Bracco, Modelling of drop interactions in thick sprays and a comparison with experiments. Proceedings of the Institution of Mechanical Engineers, p. 101-106, 1980.

25. Baumgarten, C., Mixture formation in internal combustion engines. Springer, 2006.

26. Faeth, G.M., L.P. Hsiang, and P.K. Wu, Structure and breakup properties of sprays. International Journal of Multiphase Flow, Vol. 21, Supplement(0): p. 99-127, 1995.

27. O'Rourke, P.J., Collective drop effects on vaporizing liquid sprays. Los Alamos National Lab., NM (USA). Report Number(s): LA-9069-T ON: DE82010958, 1981.

28. Hiroyasu, H. and M. Arai, Structures of fuel sprays in diesel engines. SAE Technical Paper 900475, 1990.

29. Klein-Douwel, R., P. Frijters, X. Seykens, L. Somers, and R. Baert, Gas Density and Rail Pressure Effects on Diesel Spray Growth from a Heavy-Duty Common Rail Injector†. Energy & Fuels, Vol. 23(4): p. 1832-1842, 2008.

30. Klein-Douwel, R., P. Frijters, L. Somers, W. De Boer, and R. Baert, Macroscopic diesel fuel spray shadowgraphy using high speed digital imaging in a high pressure cell. Fuel, Vol. 86(12): p. 1994-2007, 2007.

31. Naber, J.D. and D.L. Siebers, Effects of gas density and vaporization on penetration and dispersion of diesel sprays. SAE Technical Paper 960034, 1996.

32. Yule, A.J., P.R. Ereaut, and A. Ungut, Droplet sizes and velocities in vaporizing sprays. Combustion and Flame, Vol. 54(1–3): p. 15-22, 1983.

33. Zhao, H. and N. Ladommatos, Engine combustion instrumentation and diagnostics. Warrendale, PA: Society of Automotive Engineers, p. 842, 2001.

34. Araneo, L., V. Soare, R. Payri, and J. Shakal. Setting up a PDPA system for measurements in a Diesel spray. in Journal of Physics: Conference Series, IOP Publishing, 2006.

35. Tian, G., H. Li, H. Xu, Y. Li, and M. Satish, Spray characteristics study of DMF using phase doppler particle analyzer. SAE Int. J. Passeng. Cars – Mech. Syst. 3(1):948-958, 2010.

36. Li, H., li, C., Ma, X., TU, P. et al., Numerical Study of DMF and Gasoline Spray and Mixture Preparation in a GDI Engine, SAE Technical Paper 2013-01-1592, 2013.

37. Dantec-Dynamics, BSA Flow Software Version 4.10 Installation & User's Guide. 10th ed, 2006.

38. Hiroyasu, H., M. Arai, and M. Tabata, Empirical equations for the Sauter mean diameter of a Diesel spray. SAE Technical Paper 890464, 1989.

39. Estes, K.A. and I. Mudawar, Correlation of Sauter mean diameter and critical heat flux for spray cooling of small surfaces. International Journal of Heat and Mass Transfer, Vol. 38(16): p. 2985-2996, 1995.

40. Su, T., C. Chang, R.D. Reitz, P. Farrell, A. Pierpont, and T. Tow, Effects of injection pressure and nozzle geometry on spray SMD and DI emissions. SAE Technical Paper 952360, 1995.

41. Sauter, J., Die Grössenbestimmung der im Gemischnebel von Verbrennung skraftmaschinen vorhandenen Brennstoffteilchen. VDI-Verlag, 1926.

42. DeJuhasz, K.J., Dispersion of sprays in solid injection oil engines. Trans. ASME, Vol. 53: p. 65-77, 1931.

43. Castleman, R., The mechanism of atomization accompanying solid injection. US Government Printing Office, 1932.

44. Hiroyasu, H. Diesel engine combustion and its modeling. in Proceedings of 1st International Symposium on Diagnostics and Modeling of Combustion in internal Combustion Engines. Tokyo, Japan. 1985.

45. Hiroyasu, H., M. Shimizu, and M. Arai. The breakup of high speed jet in a high pressure gaseous atmosphere. in Proc. 2nd Int. Conf. on Liquid Atomization and Spray Systems. 1982.

46. Arai, M., M. Tabata, H. Hiroyasu, and M. Shimizu, Disintegrating process and spray characterization of fuel jet injected by a diesel nozzle. SAE Technical Paper 840275, 1984.

47. Chehroudi, B., S.-H. Chen, F.V. Bracco, and Y. Onuma, On the intact core of full-cone sprays. SAE Technical Paper 850126, 1985.

48. Wakuri, Y., M. Fujii, T. Amitani, and R. Tsuneya, Studies on the penetration of fuel spray in a diesel engine. Bulletin of JSME, p. 123-130, 1960. 3(9).

49. Reitz, R.D. and F. Bracco, On the dependence of spray angle and other spray parameters on nozzle design and operating conditions. SAE Technical Paper 790494, 1979.

50. Hiroyasu, H. and M. Arai, Fuel spray penetration and spray angle in diesel engines. Trans. JSAE, Vol. 21(5): p. 11, 1980.

51. Ruiz, F. and N. Chigier, The effects of design and operating conditions of fuel injectors on flow and atomization. SAE Technical Paper 870100, 1987.

52. Siebers, D.L., Liquid-phase fuel penetration in diesel sprays. SAE Technical Paper 980809, 1998.

53. Hiroyasu, H. and T. Kadota, Fuel droplet size distribution in diesel combustion chamber. SAE Technical Paper 740715, 1974.

54. Dodge, L.G., D.J. Rhodes, and R.D. Reitz, Drop-size measurement techniques for sprays: comparison of Malvern laser-diffraction and Aerometrics phase/Doppler. Applied Optics, Vol. 26(11): p. 2144-2154, 1987.

55. Tabata, M., M. Arai, and H. HlROYASU, Atomization of high viscosity liquid by a diesel nozzle. Bulletin of JSME, Vol. 29(252): p. 1795-1802, 1986.

56. Reitz, R.D., Atomization and other breakup regimes of a liquid jet. PhD thesis, 1978.

57. Reitz, R. and F. Bracco, Mechanism of atomization of a liquid jet. Physics of Fluids, p. 1730, 1982.

58. Tanner, F., Liquid jet atomization and droplet breakup modeling of non-evaporating diesel fuel sprays. SAE Technical Paper 970050, 1997.

59. Hwang, S., Z. Liu, and R.D. Reitz, Breakup mechanisms and drag coefficients of high-speed vaporizing liquid drops. Atomization and sprays, 1996.

60. Reitz, R.D., Modeling atomization processes in high-pressure vaporizing sprays. Atomisation Spray Technology, p. 309-337, 1987.

61. Lin, S. and R. Reitz, Drop and spray formation from a liquid jet. Annual Review of Fluid Mechanics, Vol. 30(1): p. 85-105, 1998.

62. Chigier, N. and R.D. Reitz, Regimes of jet breakup and breakup mechanisms- Physical aspects. Recent advances in spray combustion: Spray atomization and drop burning phenomena., p. 109-135, 1996.

63. Krzeczkowski, S.A., Measurement of liquid droplet disintegration mechanisms. International Journal of Multiphase Flow, p. 227-239, 1980.

64. Liu, A.B. and R.D. Reitz, Mechanisms of air-assisted liquid atomization. Atomization and sprays, 1993.

65. White, F.M. and I. Corfield, Viscous fluid flow. McGraw-Hill New York, Vol. 3, 1991.

66. Joseph, D.D., Stability of fluid motions. I, II. NASA STI/Recon Technical Report A, Vol. 77: p. 12423, 1976.

67. Bekdemir, C., L. Somers, and L. de Goey, Numerical modeling of diesel spray formation and combustion. PhD Thesis, Eindhoven University of Technology, Netherlands, 2008.

68. Ranz WE. On Sprays and Spraying. Department of Engineering Research. Pennsylvania State University. Bulletin, 1956.

69. Ohnesorge, W.V., Die bildung von tropfen an düsen und die auflösung flüssiger strahlen. ZAMM-Journal of Applied Mathematics and Mechanics/Zeitschrift für Angewandte Mathematik und Mechanik, Vol. 16(6): p. 355-358, 1936.

70. Torda, T., Evaporation of drops and breakup of sprays. Astronautica Acta, p. 383-393, 1973.

71. Amsden, A.A., P. Orourke, and T. Butler, KIVA-2: A computer program for chemically reactive flows with sprays. NASA STI/recon technical report N, p. 27975, 1989.

72. Amsden, A.A., KIVA-3V: A block-structured KIVA program for engines with vertical or canted valves. Los Alamos National Lab., NM (United States), 1997.

73. Amsden, A.A., KIVA-3: A KIVA program with block-structured mesh for complex geometries. Los Alamos National Lab., NM (United States), 1993.

74. Schweitzer, P., Mechanism of disintegration of liquid jets. Journal of Applied Physics, p. 513-521, 1937.

75. Grant, R.P. and S. Middleman, Newtonian jet stability. AIChE Journal, p. 669-678, 1966.

76. Phinney, R.E., The breakup of a turbulent liquid jet in a gaseous atmosphere. Journal of Fluid Mechanics, Vol. 60(04): p. 689-701, 1973.

77. Ruff, G., L. Bernal, and G. Faeth, Structure of the near-injector region of nonevaporating pressure-atomized sprays. Journal of Propulsion and Power, Vol. 7(2): p. 221-230, 1991.

78. Tseng, L.-K., G. Ruff, and G. Faeth, Effects of gas density on the structure of liquid jets in still gases. AIAA journal, Vol. 30(6): p. 1537-1544, 1992.

79. Wu, P.-K., R. Miranda, and G. Faeth, Effects of initial flow conditions on primary breakup of nonturbulent and turbulent round liquid jets. Atomization and sprays, 1995.

80. Huh KY, G.A., A Phenomenological Model of Diesel Spray Atomization. Proc Int Conf on Multiphase Flows ’91, Tsukuba, Japan, 1991.

81. Bergwerk, W., Flow pattern in diesel nozzle spray holes. Proceedings of the Institution of Mechanical Engineers, Vol. 173(1): p. 655-660, 1959.

82. Tamaki, N., M. Shimizu, and H. Hiroyasu, Enhancement of the atomization of a liquid jet by cavitation in a nozzle hole. Atomization and sprays, 2001.

83. Tamaki, N., M. Shimizu, K. Nishida, and H. Hiroyasu, Effects of cavitation and internal flow on atomization of a liquid jet. Atomization and sprays, 1998.

84. Park, B.S. and S.Y. Lee, An experimental investigation of the flash atomization mechanism. Atomization and sprays, 1994.

85. Giffen, E. and A. Muraszew, The atomisation of liquid fuels. Champman & Hall, 1953.

86. Rupe, J., Jet Properties. Liquid Propellant Rocket Combustion Instability, NASA SP-194, National Aeronautics and Space Administration, Washington DC, 1972.

87. Shkadov, V.Y., Wave formation on surface of viscous liquid due to tangential stress. Fluid Dynamics, p. 473-476, 1970.

88. Pilch, M. and C. Erdman, Use of breakup time data and velocity history data to predict the maximum size of stable fragments for acceleration-induced breakup of a liquid drop. International Journal of Multiphase Flow, Vol. 13(6): p. 741-757, 1987.

89. Wierzba, A., Deformation and breakup of liquid drops in a gas stream at nearly critical Weber numbers. Experiments in Fluids, p. 59-64, 1990.

90. Williams, F., Combustion theory: the fundamental theory of chemically reacting flow systems, Benjamin/Cummings Publishing Company, Inc., 1985.

91. Amsden, A.A., L.A.N. Laboratory, and P.J. O'Rourke, KIVA-II, a Computer Program for Chemically Reactive Flows with Sprays. Los Alamos National Laboratory, 1989.

92. Dukowicz, J.K., A particle-fluid numerical model for liquid sprays. Journal of Computational Physics, Vol. 35(2): p. 229-253, 1980.

93. Reitz, R.D., A photographic study of flash-boiling atomization. Aerosol Science and Technology, Vol. 12(3): p. 561-569, 1990.

94. Modeling Spray and Mixture Formation, in Mixture Formation in Internal Combustion Engine. Springer Berlin Heidelberg. p. 85-210, 2006.

95. Launder, B.E. and D. Spalding, The numerical computation of turbulent flows. Computer methods in applied mechanics and engineering, p. 269-289, 1974.

96. Arcoumanis, C., M. Gavaises, and B. French, Effect of fuel injection processes on the structure of diesel sprays. SAE Technical Paper 970799, 1997.

97. Som, S., Ramirez, A., Aggarwal, S., Kastengren, A. et al., "Development and Validation of a Primary Breakup Model for Diesel Engine Applications," SAE Technical Paper 2009-01-0838, 2009.

98. O'Rourke, P.J. and A.A. Amsden, The TAB method for numerical calculation of spray droplet breakup. Los Alamos National Lab., NM (USA), 1987.

99. Beale, J.C. and R.D. Reitz, Modeling spray atomization with the Kelvin-Helmholtz/Rayleigh-Taylor hybrid model. Atomization and sprays, 1999.

100. Rayleigh, On the instability of jets, University Press, Scientific Papers Vol. 3: 1887-1892, 1902.

101. Patterson, M.A. and R.D. Reitz, Modeling the Effects of Fuel Spray Characteristics on Diesel Engine Combustion and Emission. SAE Technical Paper 980131, 1998.

102. Belardini, P., C. Bertoli, and M. Cameretti, Numerical analysis of the influence of the jet breakup model formulation on diesel engine combustion computations. Atomization and sprays, 1998.

103. Bianchi, G., P. Pelloni, F. Corcione, L. Allocca, and F. Luppino, Modeling atomization of high-pressure diesel sprays. Journal of engineering for gas turbines and power, Vol. 123(2): p. 419-427, 2001.

104. Som, S. and S. Aggarwal, Effects of primary breakup modeling on spray and combustion characteristics of compression ignition engines. Combustion and Flame, Vol. 157(6): p. 1179-1193, 2010.

105. Amsden, A.A., KIVA-3V, release 2, improvements to KIVA-3V. Los Alamos National Laboratory, Los Alamos, NM, Report No. LA-UR-99-915, 1999.

106. Amsden, A.A., P. O'rourke, and T. Butler, KIVA-II: A computer program for chemically reactive flows with sprays. Los Alamos National Lab., NM (USA), 1989.

107. EnSight Ltd, CFD post-processing visualization and meshing tool, Manual, 2003.

108. Iwamoto, Y., K. Noma, O. Nakayama, T. Yamauchi, and H. Ando, Development of gasoline direct injection engine. SAE Technical Paper 970541, 1997.

109. Zhao, F., D.L. Harrington, and M.-C.D. Lai, Automotive gasoline direct-injection engines. Internal Combustion Engines, p. 02-12, 2014.

110. Binder, A., R. Ecker, A. Glaser, and K. Müller, Gasoline direct injection, in Gasoline Engine Management. Springer. p. 110-121, 2015.

111. Trinidad, O., Gasoline Direct Injection. Southern Illinois University Carbondale, Spring 3, 2011.

112. Zhao, F., M.-C. Lai, and D.L. Harrington, Automotive spark-ignited direct-injection gasoline engines. Progress in energy and combustion science, Vol. 25(5): p. 437-562, 1999.

113. North Hills Automotive, Greenville, S., Why Cleaning Fuel Induction/Injection Systems Is So Important! October, 2013.

114. Alkidas, A.C., Combustion advancements in gasoline engines. Energy Conversion and Management, Vol. 48(11): p. 2751-2761, 2007.

115. Preussner, C., C. Döring, S. Fehler, and S. Kampmann, GDI: interaction between mixture preparation, combustion system and injector performance. SAE Technical Paper 980498, 1998.

116. Kawajiri, K., T. Yonezawa, H. Ohuchi, M. Sumida, and H. Katashiba, Study of interaction between spray and air motion, and spray wall impingement. SAE Technical Paper 2002-01-0836, 2002.

117. Mitroglou, N., J. Nouri, M. Gavaises, and C. Arcoumanis, Spray characteristics of a multi-hole injector for direct-injection gasoline engines. International Journal of Engine Research, p. 255-270, 2006. 7(3).

118. Georjon, T., E. Bourguignon, T. Duverger, B. Delhaye, and P. Voisard, Characteristics of mixture formation and combustion in a spray-guided concept gasoline direct injection engine: an experimental and numerical approach. SAE Technical Paper 2000-01-0534, 2000.

119. Honda, T., M. Kawamoto, H. Katashiba, M. Sumida, N. Fukutomi, and K. Kawajiri, A study of mixture formation and combustion for spray guided DISI. SAE Technical Paper 2004-01-0046, 2004.

120. Peterson, B., D.L. Reuss, and V. Sick, On the ignition and flame development in a spray-guided direct-injection spark-ignition engine. Combustion and Flame, Vol. 161(1): p. 240-255, 2014.

121. Breuninger, T., J. Schmidt, H. Tschoeke, M. Hese, A. Kufferath, and F. Altenschmidt, Optical Investigations of the Ignition-Relevant Spray Characteristics from a Piezo-Injector for Spray-Guided Spark-Ignited Engines. SAE Int. J. Engines 8(1):89-100, 2015.

122. Whitaker, P., P. Kapus, M. Ogris, and P. Hollerer, Measures to Reduce Particulate Emissions from Gasoline DI engines. SAE Int. J. Engines 4(1):1498-1512, 2011.

123. Romoli, L., C.A.A. Rashed, and M. Fiaschi, Experimental characterization of the inner surface in micro-drilling of spray holes: A comparison between ultrashort pulsed laser and EDM. Optics & Laser Technology, Vol. 56(0): p. 35-42, 2014.

124. Smits, A.J., A physical introduction to fluid mechanics. John Wiley, 2000.

125. Dodge, L., Fuel preparation requirements for direct-injected spark-ignition engines. SAE Technical Paper 962015, 1996.

126. Echouchene, F., H. Belmabrouk, L. Le Penven, and M. Buffat, Numerical simulation of wall roughness effects in cavitating flow. International Journal of Heat and Fluid Flow, Vol. 32(5): p. 1068-1075, 2011.

127. Kalghatgi, G.T., P. Risberg, and H.-E. Ångström, Partially Pre-Mixed Auto-Ignition of Gasoline to Attain Low Smoke and Low NOx at High Load in a Compression Ignition Engine and Comparison with a Diesel Fuel. SAE Technical Paper 2007-01-0006, 2007.

128. Ciatti, S. and S.N. Subramanian, An experimental investigation of low-octane gasoline in diesel engines. Journal of engineering for gas turbines and power, Vol. 133(9): p. 092802, 2011.

129. Manente, V., P. Tunestål, and B. Johansson. Half load partially premixed combustion, PPC, with high octane number fuels. Gasoline and ethanol compared with diesel. in Symposium on International Automotive Technology: SIAT, 2009.

130. Zhang, F., H. Xu, J. Zhang, G. Tian, and G. Kalghatgi, Investigation into light duty dieseline fuelled partially-premixed compression ignition engine. SAE Int. J. Engines 4(1):2124-2134, 2011.

131. Zhang, F., H. Xu, S.Z. Rezaei, G. Kalghatgi, and S.-J. Shuai, Combustion and emission characteristics of a PPCI engine fuelled with dieseline. SAE Technical Paper 2012-01-1138, 2012.

132. Zeraati Rezaei, S., F. Zhang, H. Xu, A. Ghafourian, J.M. Herreros, and S. Shuai, Investigation of two-stage split-injection strategies for a Dieseline fuelled PPCI engine. Fuel, Vol. 107: p. 299-308, 2013.

133. Turner, D., G. Tian, H. Xu, M.L. Wyszynski, and E. Theodoridis, An experimental study of dieseline combustion in a direct injection engine. SAE Technical Paper 2009-01-1101, 2009.

134. Weall, A. and N. Collings, Investigation into partially premixed combustion in a light-duty multi-cylinder diesel engine fuelled with a mixture of gasoline and diesel. SAE Technical Paper 2007-01-4058, 2007.

135. Han, D., A.M. Ickes, S.V. Bohac, Z. Huang, and D.N. Assanis, Premixed low-temperature combustion of blends of diesel and gasoline in a high speed compression ignition engine. Proceedings of the combustion institute, Vol. 33(2): p. 3039-3046, 2011.

136. Kalghatgi, G., L. Hildingsson, and B. Johansson, Low NOx and Low Smoke Operation of a Diesel Engine Using Gasolinelike Fuels. Journal of engineering for gas turbines and power, Vol. 132(9): p. 092803-092803, 2010.

137. Pickett, L.M. and D.L. Siebers, Soot in diesel fuel jets: effects of ambient temperature, ambient density, and injection pressure. Combustion and Flame, Vol. 138(1): p. 114-135, 2004.

138. Pickett, L. and D. Siebers, Non-Sooting, Low Flame Temperature Mixing-Controlled DI Diesel Combustion. Combustion Research Facility, Sandia National Laboratories (US), 2003.

139. Payri, R., A. García, V. Domenech, R. Durrett, and A.H. Plazas, An experimental study of gasoline effects on injection rate, momentum flux and spray characteristics using a common rail diesel injection system. Fuel, Vol. 97: p. 390-399, 2012.

140. Smallwood, G. and O. Gulder, Views on the structure of transient diesel sprays. Atomization and sprays, p. 355-386, 2000.

141. Gulder, O.L. and G. Smallwood. Time-resolved structure of full cone diesel sprays. Proceedings of the Second International Workshop on Advanced Spray Combustion. 1998.

142. Lee, C.S. and S.W. Park, An experimental and numerical study on fuel atomization characteristics of high-pressure diesel injection sprays. Fuel, Vol. 81(18): p. 2417-2423, 2002.

143. Payri, F., J. Desantes, and J. Arregle, Characterization of DI Diesel sprays in high density conditions. SAE Technical Paper 960774, 1996.

144. Arcoumanis, C., M. Badami, H. Flora, and M. Gavaises, Cavitation in real-size, multi-hole diesel injector nozzles. SAE Technical Paper 2000-01-1249, 2000.

145. Serras-Pereira, J., Z. Van Romunde, P. Aleiferis, D. Richardson, S. Wallace, and R. Cracknell, Cavitation, primary break-up and flash boiling of gasoline, iso-octane and n-pentane with a real-size optical direct-injection nozzle. Fuel, Vol. 89(9): p. 2592-2607, 2010.

146. Lucchini, T., D'Errico, G., and Nordin, N., CFD Modelling of Gasoline Sprays, SAE Technical Paper 2005-24-086, 2005.

147. Costa, M., B. Iorio, U. Sorge, and S. Alfuso, Assessment of a numerical model for multi-hole gasoline sprays to be employed in the simulation of spark ignition GDI engines with a jet-guided combustion mode. SAE Technical Paper 2009-01-1915, 2009.

148. Allocca, L., F.E. Corcione, A. Fusco, F. Papetti, and S. SUCCI, Modeling of diesel spray dynamics and comparison with experiments. SAE Technical Paper 941895, 1994.

149. Park, S.W. and C.S. Lee, Investigation of atomization and evaporation characteristics of high-pressure injection diesel spray using Kelvin—Helmholz instability/droplet deformation and break-up competition model. Proceedings of the Institution of Mechanical Engineers, Part D: Journal of Automobile Engineering, Vol. 218(7): p. 767-777, 2004.

150. Li, Z.-H., B.-Q. He, and H. Zhao, Application of a hybrid breakup model for the spray simulation of a multi-hole injector used for a DISI gasoline engine. Applied Thermal Engineering, 2014.

151. Lai, M.-C., Y. Zheng, M. Shost, X. Xie, A. Matsumoto, J. Wang, X. Zhang, S. Moon, J. Gao, and K. Fezzaa, Characterization of Internal flow and Spray of Multihole DI Gasoline Spray using X-ray Imaging and CFD. SAE Technical Paper 2011-01-1881, 2011.

152. Brusiani, F., G.M. Bianchi, and A. Tiberi, Primary Breakup Model for Turbulent Liquid Jet Based on Ligament Evolution. Diesel Engine, p. 06-18, 2012.

153. Sallam, K. and G. Faeth, Surface properties during primary breakup of turbulent liquid jets in still air. AIAA journal, Vol. 41(8): p. 1514-1524, 2003.

154. Shinjo, J. and A. Umemura, Simulation of liquid jet primary breakup: Dynamics of ligament and droplet formation. International Journal of Multiphase Flow, Vol. 36(7): p. 513-532, 2010.

155. Nouri, J., N. Mitroglou, Y. Yan, and C. Arcoumanis, Internal flow and cavitation in a multi-hole injector for gasoline direct-injection engines. SAE Technical Paper 2007-01-1405, 2007.

156. Papoulias, D., E. Giannadakis, N. Mitroglou, M. Gavaises, and A. Theodorakakos, Cavitation in fuel injection systems for spray-guided direct injection gasoline engines. SAE Technical Paper 2007-01-1418, 2007.

157. Mitroglou, N., J. Nouri, Y. Yan, M. Gavaises, and C. Arcoumanis, Spray structure generated by multi-hole injectors for gasoline direct-injection engines. SAE Technical Paper 2007-01-1417, 2007.

158. Villermaux, E., P. Marmottant, and J. Duplat, Ligament-Mediated Spray Formation. Physical Review Letters, p. 074501, 2004.

159. Beale, J.C. and R.D. Reitz, Modeling spray atomization with the Kelvin-Helmholtz/Rayleigh-Taylor hybrid model. Atomization and sprays, p. 623-650, 1999.

160. Lee, C.S., M.S. Chon, and D.S. Kim, Spray structure and characteristics of high-pressure gasoline injectors for direct-injection engine applications. Atomization and sprays, 2001.

161. Lee, S. and S. Park, Experimental study on spray break-up and atomization processes from GDI injector using high injection pressure up to 30MPa. International Journal of Heat and Fluid Flow, p. 14-22, 2014.

162. Rotondi, R., G. Bella, C. Grimaldi, and L. Postrioti, Atomization of high-pressure diesel spray: Experimental validation of a new breakup model. Combustion, p. 10-05, 2014.

163. Desantes, J., R. Payri, F. Salvador, and J. De la Morena, Influence of cavitation phenomenon on primary break-up and spray behavior at stationary conditions. Fuel, Vol. 89(10): p. 3033-3041, 2010.

164. Jing, D., H. Xu, S.-j. Shuai, Z. Wang, and Y. Li, A Turbulence and Cavitation Induced Breakup Model for Fuel Spray Modeling. 2014, SAE Technical Paper 2014-01-2737, 2014.

165. Som, S., G. D'Errico, D. Longman, and T. Lucchini, Comparison and Standardization of Numerical Approaches for the Prediction of Non-reacting and Reacting Diesel Sprays. SAE Technical Paper 2012-01-1263, 2012.

166. S. Som, S.K. Aggarwal, E.M. El-Hannouny, D.E. Longman, ASME J. Eng. Gas Turb. Power Vol. 132 (4), p. 1-12, 2010.

167. Som, S., D. Longman, A. Ramirez, and S. Aggarwal, A comparison of injector flow and spray characteristics of biodiesel with petrodiesel. Fuel, Vol. 89(12): p. 4014-4024, 2010.

168. Soteriou, C., Direct Injection Diesel Spray and the Effect of Cavitation and Hydraulic Flip or Atomization. SAE Technical Paper 950080, 1995.

169. Som, S., E. El-Hannouny, D. Longman, and S. Aggarwal, Investigation of nozzle flow and cavitation characteristics in a diesel injector. Journal of engineering for gas turbines and power, Vol. 132(4): p. 042802, 2010.

170. Huh, K. and A. Gosman. A phenomenological model of diesel spray atomization. Proceedings of the international conference on multiphase flows, 1991.

171. Moin, P. and K. Mahesh, Direct numerical simulation: a tool in turbulence research. Annual Review of Fluid Mechanics, Vol. 30(1): p. 539-578, 1998.

172. FieldView image courtesy of Dr. Matsuo, Japan Aerospace Exploration Agency, or JAXA, 2012.

173. Maozhao, X., Mechanism and Modeling of Transcritical/Supercritical Fuel Spray and Mixture Formation in Internal Combustion Engines. Journal of Combustion Science and Technology, 2014.

174. Oefelein, J., R. Dahms, and G. Lacaze, Detailed modeling and simulation of high-pressure fuel injection processes in diesel engines. SAE Int. J. Engines 5(3):1410-1419, 2012.